Multiscale architected materials with tunable thermal expansion

by

Hang Xu

Department of Mechanical Engineering
McGill University

Montreal, Quebec, Canada

February 2018

A thesis submitted to McGill University in partial fulfillment of the requirements for a doctoral degree

Dedication

To my father **Hua Xu** *and my mother* **Guiyu Sun** *who give me life and all the support to explore the world*

To my beloved wife **Qiuyi Lyu** *and my lovely daughter* **Nina Jiameng Xu** *for their love and support*

Abstract

Systems in extreme thermal environments are susceptible to severe temperature changes. Variations in temperature can lead to undesired geometric changes in sensitive applications that require very fine precision, such as satellite antennas, space telescopes, and large array mirrors. These applications call for materials with zero coefficient of thermal expansion (CTE) to avoid unexpected thermal deformation. On the other hand, other applications require materials with large positive or negative CTE which make them capable to morph and adapt their geometry in response to variations in temperature. In these scenarios, materials that are able to provide tunable thermal expansion with high structural efficiency become crucially important.

It is known that the CTE of architected materials, as opposed to that of conventional solids, can be tuned by intentionally altering the geometry and material distribution of their dual-material architecture. Existing concepts, however, offer a limited range of CTEs, which is obtainable from a restricted palette of materials only. In addition, they feature an inherent coupling between their thermal and elastic properties, with high specific stiffness obtainable at the expense of CTE tunability, and vice versa. The overarching goal of this work is to address these intertwined issues so as to expand the CTE range that an architected material can offer without penalizing its specific stiffness.

The thesis introduces a class of planar and three dimensional architected materials with tunable thermal expansion. In 2D, hierarchical lattice materials are proposed to feature a theoretically unbounded range of CTE tunability, regardless of their constituent solids. An unbounded control on thermal expansion is achieved without incurring in severe loss of structural performance. Stretch-dominated bi-material diamonds with low- and high-CTEs are proposed as building blocks of hierarchical lattices, including those made of recursive unit cells, with the goal of decoupling thermal and elastic properties. In 3D, a unifying methodology based on thermoelastic behavior of dual-material tetrahedra is developed for the analysis and design of spatial lattices and truss structures with desired thermal expansion modes including unidirectional, transversely isotropic, and isotropic CTE. The method establishes a relationship between the unit cell symmetry and its corresponding thermoelastic response, which is expressed by introducing the thermal expansion vector of the building block in the unit cell. The methodology is exemplified through the application to a set of three dimensional lattices, such as the dual-material Octet-truss, which are proved not only to be stiffer and stronger than any other existing concepts, but also to offer a highly tunable CTE.

The method and concepts are obtained via a combination of thermoelastic mechanic theory, numeric simulations, and physical experiments on 3D fabricated prototypes with plan and spatial architecture. The material architectures are scale independent and can open up new avenues towards the development of multifunctional materials with customizable thermal expansion and mechanical properties. The novelty and simplicity of the proposed designs, as well as the ease in fabrication, make the concepts here introduced well-suited for a wide range of applications across the length scale, including satellite antennas, space optical systems, precision instruments, thermal actuators, and MEMS.

Résumé

Les systèmes dans des environnements extrêmes sont sujets à de larges variations de température. Ces écarts de température peuvent provoquer des changements de géométries non désirés pour des applications sensibles requérant une très grande précision, comme pour les antennes de satellites, les télescopes spatiaux ou les panneaux solaires. Ces applications nécessitent l'utilisation de matériaux possédant un coefficient d'expansion thermique (CET) nul afin d'éviter des déformations thermiques inattendues. Par ailleurs, d'autres applications requièrent des matériaux avec de grands CET, positifs ou négatifs, de manière à ce qu'ils puissent ainsi adapter leurs géométries en réponse aux variations de température. Dans ces scénarii, les matériaux dont il est possible de régler l'expansion thermique en gardant une grande efficacité structurelle deviennent de première importance.

Il est avéré que le CET de matériaux architecturés, à l'opposé de celui des solides conventionnels, peut être réglé en altérant de manière intentionnelle leurs géométries et leurs distributions, ce qui est rendu possible grâce à leur architecture duale. Les concepts préexistants n'offrent cependant qu'une plage limitée de CET, obtenue à partir d'une faible diversité de matériaux. De plus, il existe un couplage inhérent de leurs propriétés thermiques et élastiques, une grande raideur spécifique étant ainsi obtenue au dépend de la finesse du réglage du CET, et vice versa. Le but principal de cette étude est de traiter de cette problématique de couplage afin de faire en sorte qu'augmenter la plage de CET ne résulte pas en une raideur spécifique dégradée.

La thèse introduit une classe de matériaux architecturés dans le plan et tridimensionnels dont il est possible de régler l'expansion thermique. En 2D, des matériaux hiérarchisés avec une structure en treillis sont proposés pour représenter une plage théorique illimitée de réglage de CET, sans tenir compte des solides les constituant. Un contrôle illimité d'expansion thermique est atteint sans trop impacter les performances structurelles. Des diamants composés de deux matériaux à déformations axiales, avec des grands et des faibles CET sont proposés comme unité de base dans la structure des treillis hiérarchisés, incluant ceux fait de cellules récursives, dans le but de découpler les propriétés thermiques et élastiques. En 3D, une méthodologie universelle basée sur le comportement thermoélastique de tétrahedrons bi matériaux est développée pour l'analyse et le design de treillis dans l'espace et de structures en barreaux possédant des modes d’expansion thermiques recherchés, parmi lesquels les modes unidirectionnels, transverses isotropiques et isotropiques. La méthode établie une relation entre la symétrie de la cellule et la réponse thermoélastique correspondante, qui est exprimée en introduisant le vecteur d’expansion thermique de l’unité de base dans la cellule. Afin d’illustrer cette méthodologie, sont donnés des exemples de son application sur plusieurs structures en treillis tridimensionnels, comme l’Octet-truss bi matériaux, dont il est prouvé qu’il est non seulement plus rigides et plus résistants que n’ importe quel autre concept existant, mais qu’il offre aussi un CET réglable de manière très précise.

La méthode et les concepts sont obtenus via une combinaison de théorie mécanique thermoélastique, de simulations et d’expérimentations faites sur des prototypes tridimensionnels manufacturés avec des architectures planes ou spatiales. L’architecture des matériaux est échelonnée de façon indépendante et peut permettre d’ouvrir de nouvelles voies sur le développement de matériaux multifonctionnels possédant des expansions thermiques et des propriétés mécaniques personnalisables. Le caractère inédit et la simplicité des designs proposés, de même que le procédé simpliste de leurs fabrications, rendent ces concepts introduits ci-dessus bien adaptés pour de multiples applications à différents échelles, comme (pour) les antennes de satelites, les systems optiques spaciaux, les instruments de précisions, les actionneurs thermiques ou les systèmes microélectromécaniques.

Acknowledgement

I would like to take this chance to express my sincerest thanks to a group of people including my supervisor, my friends and family for their help and support. First, I would like to thank my PhD supervisor Professor Damiano Pasini. His kindness and enthusiasm encouraged me, his technical support and scientific guidance enlightened me, and his preciseness and dedication motivated me throughout my research explorations. He is a great teacher, a true mentor, and a family-oriented role model. He set the bar for me within school and beyond, both as an outstanding scholar as well as an exemplary father-figure for me in the future.

I appreciate the nice friends from "The Pasini Group" whom I was pleased to meet and know. Particularly, I wish to thank Purnendu Prithipaul, Emily Gogarty, and Sajad Khanoki who helped me so much in my first year, during my hardest moments. Thanks Amr Farag, Yingjun Wang, Jiazhen Leng, Daniel Fraschetti, and Joseph Lu whom I collaborated with. My other team members: Burnett Johnston, Abdolhamid Shafaroudi, Lu Liu, Ahmed Moussa, Xiao Shang, Chuan Qiao and many others, thank you for the good times.

I would like to say my deepest thanks to my beloved wife, Qiuyi Lyu, who accompanies me through all my adventures. I will always be indebted and grateful to you for all the sacrifices you made for me. I would like to express my special thanks to my parents and my parents-in-law for their encouragement, unconditional love, and continuous support. Nina, my lovely daughter, you taught me the meaning of responsibility, and your birth brought the whole family endless joy. This thesis and the rest of my life are dedicated to you.

Finally, I would like to thank the China Scholarship Council (CSC), the National Sciences and Engineering Research Council of Canada (NSERC), and the McGill Engineering Doctoral Award (MEDA) for their collaborative financial support for this project.

Table of contents

List of figures

List of tables

Contributions of the author

This is a manuscript-based thesis consisting of three journal articles. The title of the articles, name of the authors, and their contributions are listed below:

1) Multilevel hierarchy in bi-material lattices with high specific stiffness and unbounded thermal expansion

Hang Xu, Amr Farag, and Damiano Pasini
Department of Mechanical Engineering, McGill University,
817 Sherbrooke St. West, Montreal, QC H3A 0C3, Canada
Acta Materialia, 2017. 134: p. 155-166.

***Author contributions**:*

H. Xu: Developed hierarchical architectures, derived closed form expressions, designed and performed the experiments, analyzed the data and wrote the manuscript.

A. Farag: Developed the Finite element model, performed the simulation, editing the text.

D. Pasini: Supervised the research and review processes, gave technical and scientific advice, and edited the figures and the text.

2) Routes to program thermal expansion in three-dimensional lattice metamaterials built from tetrahedral building blocks

Hang Xu, Amr Farag, and Damiano Pasini
Department of Mechanical Engineering, McGill University,
817 Sherbrooke St. West, Montreal, QC H3A 0C3, Canada
Journal of the Mechanics and Physics of Solids, 2018. 117: p. 54-87.

***Author contributions**:*

H. Xu: Developed spatial architected materials, derived closed form expressions, designed and performed the experiments, analyzed the data and wrote the manuscript.

A. Farag: Developed the Finite element model, performed the simulation, editing the text.

D. Pasini: Supervised the research and review processes, gave technical and scientific advice, and edited the figures and the text.

3) Structurally Efficient Three-dimensional Metamaterials with Controllable Thermal Expansion

Hang Xu and Damiano Pasini
Department of Mechanical Engineering, McGill University,
817 Sherbrooke St. West, Montreal, QC H3A 0C3, Canada
Scientific Reports, 2016. 6: p. 34924.

Author contributions:
H. Xu: Developed spatial architected materials, derived closed form expressions, designed and performed the experiments, analyzed the data and wrote the manuscript.

D. Pasini: Supervised the research and review processes, gave technical and scientific advice, and edited the figures and the text.

Chapter 1

Introduction and literature review

Chapter 1: Introduction and literature review

1.1 Introduction

1.1.1 Thermal expansion

Thermal expansion, the change in shape, length, area, and volume upon heating under constant pressure, is assumed to be normal in our daily live [1]. Materials usually expand in response to heating and contract in response to cooling. For example, the contraction of air in a cooling jar widens the gap between internal-external air pressures and causes the jar lid to tighten. However, there are a growing number of materials, synthetic and naturally occurring, that can maintain their dimension(s) or can even contract upon heating within certain temperature ranges, thus exhibiting a zero or negative thermal expansion [2]. For instance, ice-cold water contracts as it is warmed up to 4℃ and then expands above this temperature. Hence, the negative thermal expansion of water vanishes at 4℃ and then becomes positive. In everyday life, thermal expansion is a typical requirement to meet in several applications. In medical applications, for example, mercury expands in a thermometer showing the body temperature. In the transportation field, hot air balloons fly when the air inside expands and becomes less dense than the air surrounding it. However, in some cases, thermal expansion is viewed by engineers as a nuisance, which must be compensated for. For example in the rail transportation industry, gaps must be left between successive lengths of train tracks to allow for thermal expansion on hotter days. Without the gaps, the tracks would thermally buckle, thereby hindering the safety of train passengers.

1.1.2 The definition of coefficient of thermal expansion

Subjected to an increase in temperature, most naturally occurring materials uniformly expand. This uniform expansion has been considered an inherent property of the material and it cannot be modified [3]. The coefficient of thermal expansion (CTE) describes this inherent property, i.e. how the size of an object would change in response to a change in temperature, a phenomenon associated with the anharmonicity of the interatomic potential energy in the crystalline lattice. The CTE quantifies the tendency of matter to change in length, area, or volume in response to a change in temperature. The linear definition of CTE is:

$$\alpha = \frac{\Delta l}{l_0 \cdot \Delta T} \tag{1.1}$$

where l_0 is the representative length of an element at reference temperature T_0, $\Delta T = T - T_0$ is the change of temperature and Δl is the change in length.

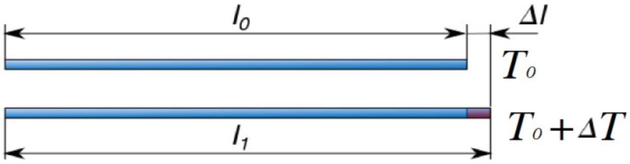

Figure 1-1: Linear thermal expansion of a straight bar.

1.1.3 Thermal expansion requirements in engineering applications

Materials with unconventional thermal expansion behaviors (e.g. near zero, large positive or negative CTE) are particularly advantageous in a large assortment of applications that maintain precise dimensional tolerances or require responsive deformations under given changes in temperature [4-6]. On one hand, in extreme thermal environments, sensitive applications that require very fine precision call for materials with low-to-zero thermal expansion so as to avoid undesired thermal deformation. For example, systems in outer space are particularly vulnerable to large temperature changes when passing in and out of sunlight. Variations in temperature can lead to undesired geometric changes in sub-reflector supporting struts, satellite antennas, space telescopes, and large array mirrors [7, 8]. These geometric changes cause systems to be susceptible to large thermal stress, thermo-mechanical fatigue, and thermal buckling. To suppress such failures, materials with a zero CTE over a wide range of temperature are desired.

On the other hand, there are other applications requiring materials with large positive or negative thermal expansion, which make them capable of morphing and adapting their geometry in response to variations in temperature. This temperature change is often, but not always, dictated by the surrounding environment [9]. For instance, large positive/negative CTE materials can be used in smart lightweight structures that possess morphing (e.g. self-shaping, self-folding, and deployable [10-12]) functions, which may have broad applications in self-assembly [13], packaging [11, 12], actuation [14], structural adaptivity [10, 14, 15], and biological devices [12], among many others. In bioengineering, for instance, the mismatch of thermal expansion between a restorative material and a tooth may cause stress at their interface, thus leading to microleakage [16]. In order to avoid the possibility of the microleakage, the restorative material should have a large negative CTE, as near as possible to the CTE of human dentin, which is $-66.03\times10^{-6}/°\text{C}$ in a dry condition [16].

In addition to providing desired zero, large positive, or negative CTEs, there exists a large number of applications that require materials subjected to other design requirements, such as high stiffness, high strength, and resistance to thermal fatigue [17]. Among many, examples of multifunctional materials include those that can maintain precise dimensional tolerances under large temperature fluctuations and high structural efficiency (e.g. stiffness/mass and strength/mass), which are very appealing, especially in aerospace where minimum mass is of critical importance [2]. Specifically, the supporting struts of the subreflector are required to have high stiffness to obtain a high natural frequency far from any excitation frequency that could cause structural failure.

1.1.4 Materials with intrinsically zero or large positive/negative CTE

In general, low to zero thermal expansion can be achieved with the use of intrinsically low or negative expansion materials [18], such as ZrW_2O_8 and related ceramics [19-21] or Invar and related metals (as shown in Figure 1-2) [22, 23], alone or in a composite form [24, 25]. Solids having low, or even negative, CTE exist, but all possess characteristics which limit their use in applications requiring robustness and durability over large temperature changes. One of their drawbacks is the narrow range in which they can operate, which is problematic when large temperature swings, from -150°C to 150°C as in outer space, occur. Invar ($Fe_{65}Ni_{35}$) and $Fe_{68}Pd_{32}$ are robust, although the low thermal expansion they can provide (shown in Figure 1-2a) is strongly dependent on the temperature they operate with [22, 23]. For example, $Fe_{68}Pd_{32}$ provides near-zero CTE only at temperatures near 327℃ (600K) as shown in Figure 1-2a. Hence, if the temperature conditions vary outside this range during the service life of the material/structure, there will be undesired dimensional changes. For ZrW_2O_8 and related ceramics [19, 20], the brittleness and abrupt failure upon peaks of thermal stresses limit their use in applications requiring robustness and durability over a large temperature range. Low to zero CTE can also be achieved with solids in a composite form such as fiber-reinforced composites.

However, the interface thermal strain and failure caused by the large difference of CTEs between fiber and matrix restrict their application range [26].

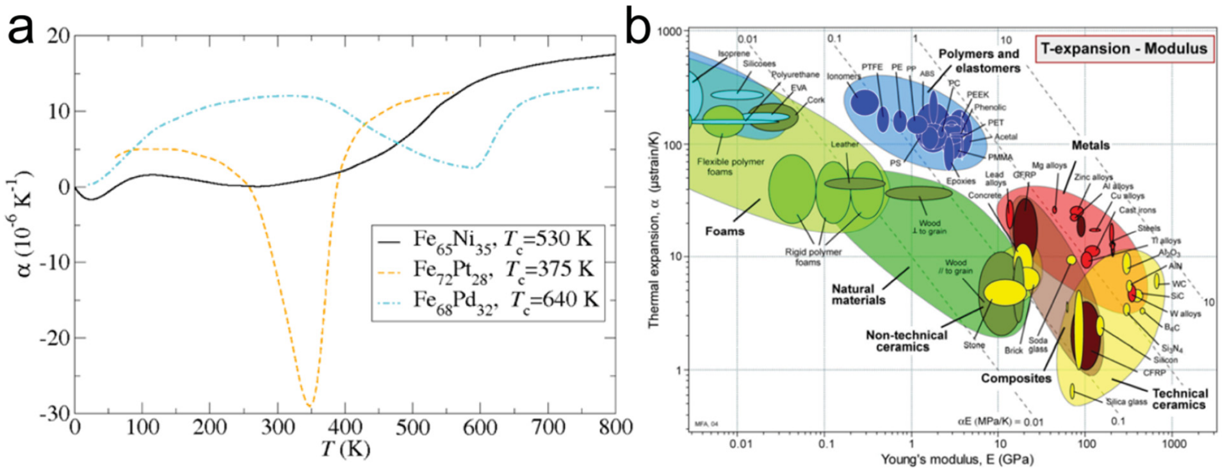

Figure 1-2: (a) The linear CTEs of ferromagnetic disordered $Fe_{65}Ni_{35}$, $Fe_{72}Pt_{28}$ and $Fe_{68}Pd_{32}$ alloys as a function of temperature, according to experiments [22, 23, 27]. The value of the Curie temperature of each system is denoted as Tc [28]. (b) Ashby Chart: the linear expansion coefficient, α , plotted against Young's modulus, E [29].

Similarly, for applications requiring large CTEs, solid materials can feature intrinsically positive or negative CTEs, such as $Fe_{72}Pt_{28}$ shown in Figure 1-2a. However, the available range of CTE these materials can offer remain too narrow (about -10^1 ppm /℃ to 10^3 ppm /℃ as shown in Figure 1-2b [29]) to induce responsive and large deformations, such as those required for morphing and other applications [10, 14]. Furthermore, the CTE is proportional to the reciprocal of Young's moduli (1/E) [30], i.e. the increase of the CTEs of solids is accompanied by the reduction of the elastic moduli. For example, as depicted in Figure 1-2b, ceramics, with the lowest coefficients of expansion, have the highest moduli; elastomers which expand the most have the lowest moduli. Hence, the coupled thermoelastic properties of solids distribute in a zone from top left to bottom right and leave broad blank spaces in the thermal expansion–modulus chart (Figure 1-2b). The absence of combinations of thermal expansions and Young's moduli that lay in the unpopulated regions manifested by the trends shown in Figure 1-2b limits designers to meet the diverse design requirements of various engineering applications.

1.1.5 The main target of this PhD work

Where solids have limitations, architected materials have been proposed to overcome the issues above. The main target of this PhD work is to design architected materials with specific thermomechanical properties, notably zero, large positive or negative CTE with desired structural efficiency. More particularly, the aim is to introduce materials with tailored thermal distortion for applications where thermal management and low mass are important requirements.

The next section, literature review, starts first to recall the basic concepts of micro-architected lattice materials. The corresponding structural performance of stretch- and bend-dominated structures to meet mechanical requirements of engineering applications is then analyzed before reviewing the literature of architected materials with tunable CTE.

1.2 Literature review

1.2.1 Micro-architected lattice materials

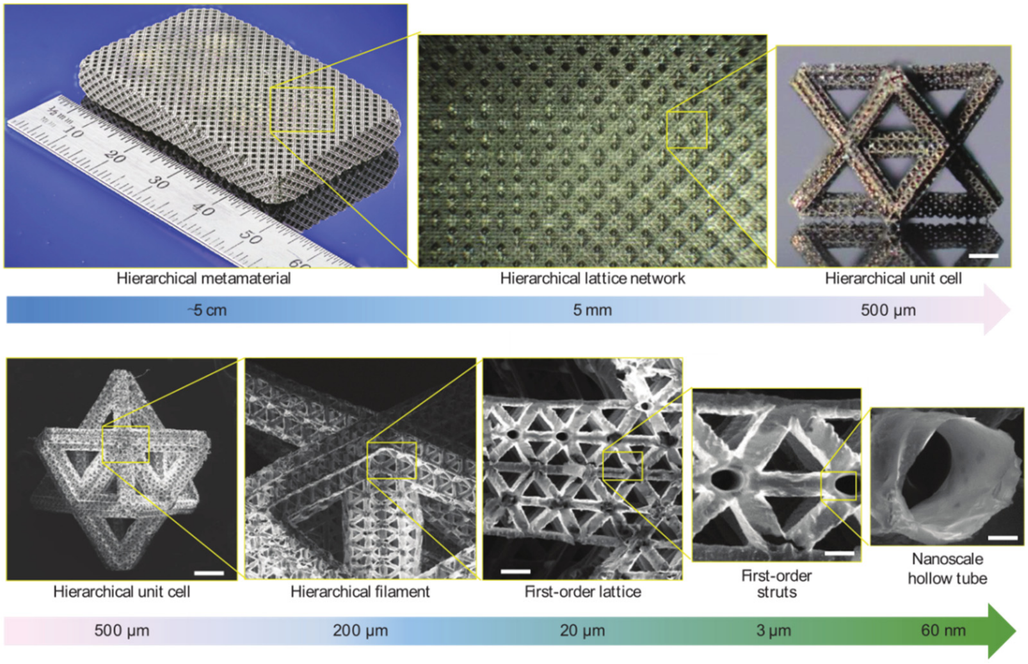

Figure 1-3: Nickel alloy hierarchical metamaterial and critical features across seven orders of magnitude in length scale. [31]

Architected materials (also known as mechanical metamaterials) are man-made designer matter that obtains their effective properties by structure rather than composition [32]. Via introducing voids to the material, e.g., as illustrated in Figure 1-3, highly regular cellular materials can be designed by tessellating a large number of unit cells comprising slender beams or tubes, leading to micro-architected lattice materials [33]. The multiscale metallic lattices in Figure 1-3 display structural hierarchy, which means materials exhibit a given structure on more than one length scale and contain structural elements which themselves have structure [34]. Structural hierarchy has been recognized as one crucial factor governing high stiffness, strength, and toughness in both natural and bio-inspired materials [34-36].

Architected materials can be designed to elicit extreme mechanical properties, often beyond those of existing solids [37]. In the applications of these properties, the target to maximize might be either structural, through attaining for example minimum mass at maximum stiffness [31, 38], or functional, such as thermal dimension control [4], heat transfer [39], band gaps [40], mechanical biocompatibility [41], and others [37]. Among these, tunable thermal expansion has been the recent focus of intense research [6, 42] aiming at obtaining large positive, zero or negative CTE via material architecture tuning. Recent works have shown that the CTE of architected materials made of two solids can be tuned by purposefully designing the architecture of their repeating units and proper selection of the constituent materials [4, 17, 18, 43-48]. These architected materials can accommodate thermal expansion through the thermally-mismatched deformation of the component materials they are made of.

1.2.2 Bending versus stretching dominated architectures

Architected materials can deform through either bending (Figure 1-4a) or stretching (Figure 1-4b) of their constituent members. While most architected materials are bend-dominated, those that are stretch-dominated are more weight-efficient and thus suitable in structural applications [49]. Figure 1-4 depicts the difference in the deformation modes of bend- and stretch-dominated architectures under given loading condition. In Figure 1-4a, the applied load, F, induces bending moments at the rigid joints of the architecture, and these cause the beam elements to bend. The collapse load of this bend-dominated architecture is dictated mainly by the flexural strength of the beam elements. However, when loaded, although the beam elements of the architecture in Figure 1-4b slightly bend, the constituent members mainly support axial loads: tensile in some, compressive in others. Thus, the frame in Figure 1-4b is stretch-dominated and the collapse load is dictated largely by the axial strength of the beam elements. The architected materials that are stretch-dominated are more efficient from a weight standpoint; for example, a stretch-dominated architected material is expected to be about ten times as stiff and about three times as strong as a bending-dominated one for a relative density $\rho^* = 0.1$ (relative density is expressed by the ratio of the density of the architected material, ρ, and that of the solid component, ρ_s) [49].

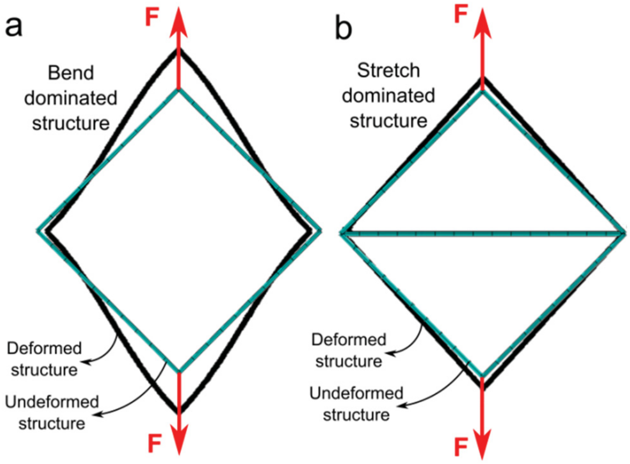

Figure 1-4: Deformation modes of architectures: (a) bend-dominated structure and (b) stretch-dominated structure with their undeformed and deformed structures.

1.2.3 Architected materials with tunable CTEs

In the realm of thermal control, architected materials made of two solids with distinct CTEs have been proposed as a potential family of CTE tunable materials. Many attempts have been made to design architected materials capable of exploiting thermal management applications with the respective concepts shown in Figure 1-5 to 11. All of them incorporate two materials with positive CTEs: one high and the other low.

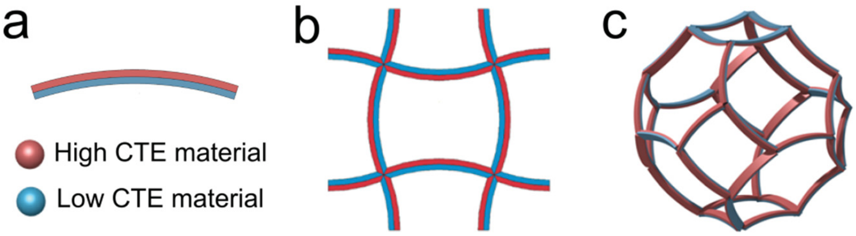

Figure 1-5: Architected material concepts constructed via bi-material strips [50, 51]: (a) a bi-material strip building block with controllable CTE in the horizontal direction [43]; (b) a unit cell

in 2D [43]; and (c) a unit cell in 3D [52]. Red and blue constituents represent materials with high and low CTE respectively.

Lakes has described periodic foams in 2D (Figure 1-5b) and 3D (Figure 1-5c) built from bi-material strips (Figure 1-5a) that are dominated by bending, a characteristic that lowers structural efficiency, and brings about unbounded thermal expansion [43, 52]. When the temperature changes, the individual bi-material strips (Figure 1-5a) flex or flatten due to the in-plane shear stress caused by thermal expansion mismatch between the two layers. The change in curvature of an individual load-free strip induces a positive, zero or even a negative overall CTE of the lattice structure, depending on the relative thermal expansion of each layer. Given this bi-material strip concept, several investigators have constructed dual-material architected lattices that can exhibit large positive, zero or large negative thermal expansion via distinct tessellation algorithm in both 2D and 3D including Wu et al. [53] and Qu et al. [54]. However, all the planar and spatial lattices assembled by winding strips deform with a bend-dominated mode, whose stiffness and strength to weight ratios are less than that obtainable with stretch-dominated lattices.

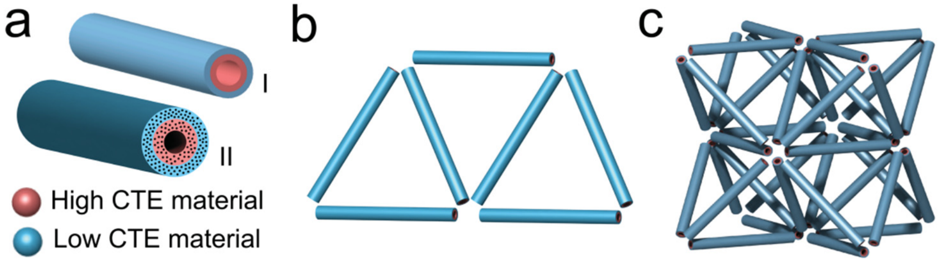

Figure 1-6: Architected material concept constructed via nested double-barrelled struts [44, 47]: (a) building block: a bi-material nested double-barrelled strut with controllable CTE in the axial direction without (I) and with (II) structural hierarchy; (b) a unit cell in 2D; and (c) a unit cell in 3D. Red and blue constituents represent materials with high and low CTE respectively.

More recently, Lehman and Lakes [44, 47] have proposed stretch-dominated lattices in both 2D (Figure 1-6b) and 3D (Figure 1-6c) made of nested double-barrelled struts (Figure 1-6a) with high structural efficiency but limited adjustable CTE range. Their tunable CTE range is limited due to the relatively modest mechanism of CTE accommodation, i.e. Poisson's effect, their struts can attain. The Poisson's effect can be explained as Poisson's contraction in the longitudinal direction that is achieved by the transversal mismatch of thermal expansion of two nested concentric tubes made of different materials [47]. These nested double-barrelled concepts have then been developed to contain structural hierarchy (Figure 1-6a-II), i.e. the nested double-barrelled struts in the concept contain oriented porosity at a length scale one order smaller [44]. This gives rise to improved strength and stiffness, and provides additional design flexibility associated with anisotropy. However, the limited adjustable CTE range the nested double-barrelled concept can obtain restricts its application.

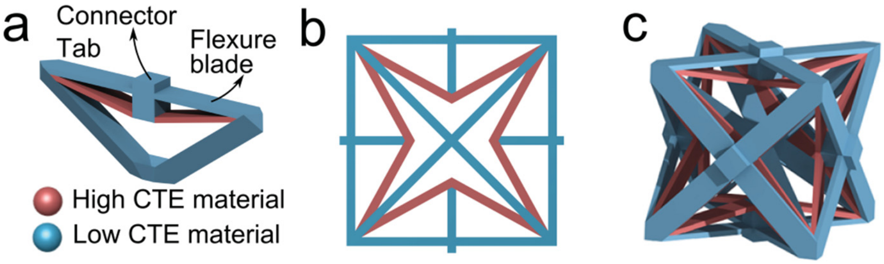

Figure 1-7: Architected material concepts constructed via flexure-blades building blocks [45, 48, 55]: (a) a flexure-blades building block with controllable CTE in the vertical direction; (b) a unit cell in 2D; and (c) a unit cell in 3D. Red and blue constituents represent materials with high and low CTE respectively.

Hopkins et al. demonstrated an architected material with tunable CTE designed by the principles of freedom, actuation, and constraint topologies (FACT) approach [48]. The FACT approach can be applied to the synthesis, analysis, and optimization of microarchitectures that possess extreme or unusual thermal expansion properties (e.g. zero or large negative thermal expansion coefficients). From its successful application, the 2D and 3D concepts (Figure 1-7b and c, respectively) constructed via flexure-blades building blocks (Figure 1-7a) have low specific stiffness but can attain large negative CTEs for the given pair of constituents: photocurable poly (ethylene glycol) diacrylate (PEGDA) and reinforced PEGDA [45]. In the Hopkins' concepts, a negative CTE is achieved by means of flexure blade deforming [45]. Consider the building block shown in Figure 1-7a, when heated, two red beam elements will expand more, due to their higher CTE, than blue elements and pull toward the blue cell-to-cell connector tab, which crosses the center of each unit cell wall. As the temperature increases, the cells expand into the void spaces and the connector tabs pull inward causing the entire architecture to contract along the two orthogonal axes for planar concept or three orthogonal axes for spacial concept.

The FACT synthesis approach provides designers with a comprehensive library of geometric shapes from which they can rapidly visualize and consider a large number of solutions, such as multiple cell topologies of lattices with low CTE [48, 55]. Furthermore, the FACT approach combined with topology optimization has claimed to help designers identify the most optimal concepts with greater confidence than either approach alone [48]. Owing to its diversity and optimality of cell topologies, Hopkins' concepts can also use irregular unit cells to fit irregular boundaries [55]. However, because of the significant stress concentrations at the small and slender cell-to-cell connector tabs, the strength and stiffness of this concept under given material and geometric conditions is lower than stretch dominated concepts.

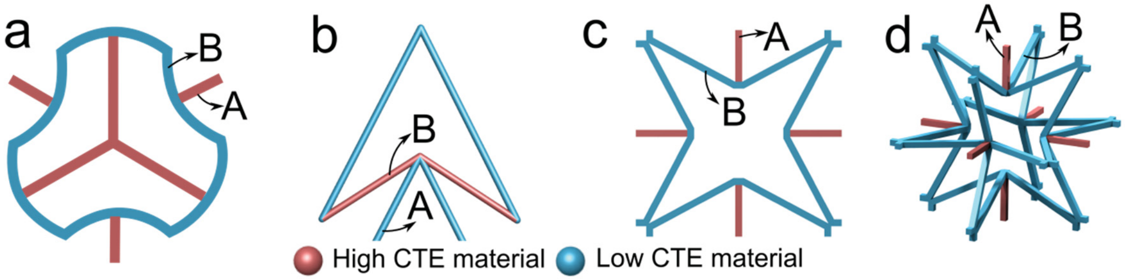

Figure 1-8: CTE-tunable concepts with re-entrant architecture: (a) Jefferson et al. [18, 56], (b) Ng et al. [57], (c) the 2D concept of Ai et al. [58], and (d) the 3D concept of Ai et al [42]. The two elements of a re-entrant architecture are marked as: (A) intercellular straight connector and (B) a curved beam. Red and blue constituents represent materials with high and low CTE respectively.

Bend-dominated concepts with controllable CTE also include those designed via re-entrant architecture, a well-known mechanism for negative Poisson's ratio [59]. With Jefferson's concept (Figure 1-8a), near-zero-CTE and isotropic negative expansion designs are achieved by creating compliant re-entrant architectures, where the overall expansion is compensated by internal bending deformation. A continuous honeycomb-like structure is fabricated out of one material. A second material with dissimilar CTE is inserted into each cell as shown in Figure 1-8a. As the structure undergoes a temperature increase, the inserts expand more than the honeycomb and thus the faces experience bending. The shortening of the faces due to bending effectively cancels out the overall expansion; thus, with appropriate specification of materials and geometry, a zero or other design target of effective thermal expansion can be achieved [18]. Jefferson also found that, for the lattice structure made up of this unit cell, the edge effect is quite small and can be neglected [18]. In addition, the thermal expansion of the structure resulting from a uniform temperature change shows that this essential behavior is maintained even with a substantial asymmetry in the temperature distribution. Similar re-entrant architecture can be found in the concepts of Ng et al. [57] (Figure 1-8b) and Ai et al. [42, 58] (Figure 1-8c and d) with negative Poisson's ratio. However, all concepts with re-entrant architecture are bend-dominated and have lower structural efficiency than stretch-dominated architected materials.

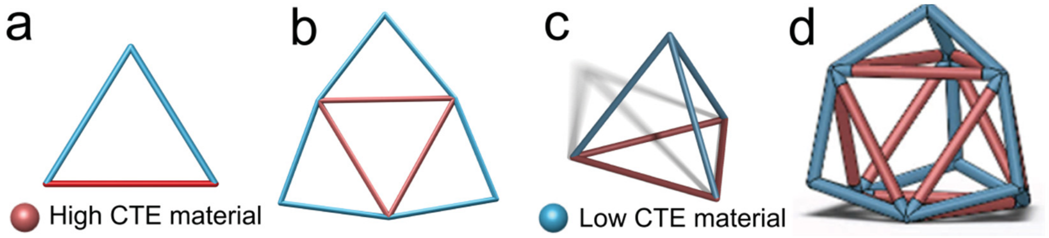

Figure 1-9: Architected material concept constructed via bi-material triangles and tetrahedra [17, 60, 61]: (a) the planar building block: a bi-material triangle with controllable CTE in the vertical direction; (b) a unit cell in 2D; (c) the spacial building block: a bi-material tetrahedron with controllable CTE in the vertical direction; and (d) a unit cell in 3D. Red and blue constituents represent materials with high and low CTE respectively.

Steeves et al. introduced a family of robust stretch-dominated bi-material lattices which combine low (or zero) thermal expansion with high stiffness over wide temperature ranges [17, 60, 61]. The thermal expansion of the Steeves' concepts is accommodated by rotations of elements at the nodes. With a temperature increase, the height rise of the dual-material triangle in Figure 1-9a, triggered by the blue elements with low CTE, is compensated by the sinking of its top vertex due to the higher thermal expansion of the red bar with high CTE. Similarly, in a spatial building block (Figure 1-9c), with a temperature increase, the height rise, i.e. the thermal expansion in the vertical direction triggered by the blue elements, is counteracted by the sinking of its apex due to the higher thermal expansion of the high-CTE red base. The assembly of the dual-material triangular and tetrahedral building blocks creates Steeves' concepts in 2D (Figure 1-9b) and 3D (Figure 1-9d) with planar and spatial isotropic controllable CTE, respectively. It is also significant that, by choosing the skewness of the low-CTE elements and the combination of components, Steeves' concepts can ensure a controllable CTE over the desired wide temperature range, while keeping high structural efficiency due to the axial deformation endured by its members [17]. Comparable results, i.e. planar and spatial lattice concepts constructed via multi-material triangle, tetrahedra or pyramids, with controllable CTE and high structural efficiency, have been obtained by Schuerch [62], Vandeperre et al. [63], Aboudi et al. [64], Grima et al. [65, 66], Miller et al. [67], Berger et al. [68], Palumbo et al. [4], Lim et al. [69, 70], Yamamoto et al. [5], and Wei et al. [71, 72]. However, the desired flexural deformation that a large thermal deformation would require is generally antagonist to the high specific stiffness that is distinctive of a structurally efficient architecture. This indicates that preserving high specific stiffness is in conflict with the need of enhancing thermal deformation control, as manifest in stretch-dominated unit cells constructed by dual-material triangles (2D) or tetrahedra (3D), which offer a remarkable structural performance, but cannot achieve the sizeable CTE tunability of bend-dominated architectures. Another main drawback which reduces the thermal expansion performance lies in the significant stress concentrations at the connections of different materials [18].

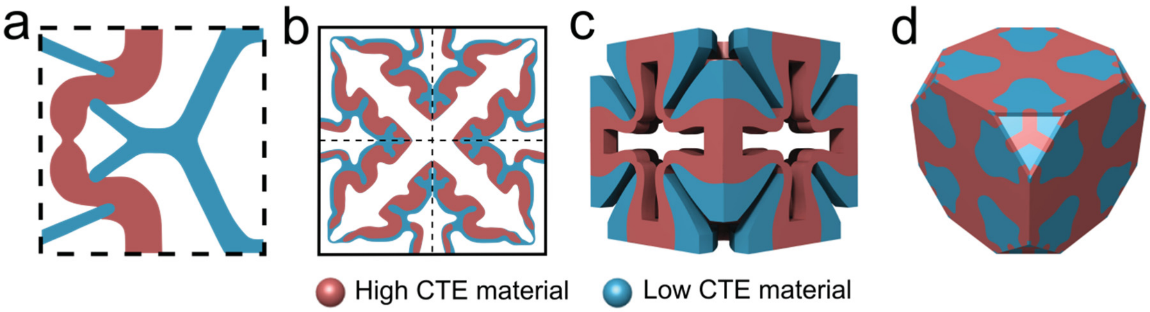

Figure 1-10: Concepts developed by topology optimization: (a) concept with zero thermal expansion and maximized bulk modulus [46, 73, 74]; (b) optimized concepts with the forced void domain for maintaining the deformation range [75]; (c) a low bulk modulus, high thermal expansion concept [76]; and (d) the maximal modulus design [76]. Red and blue constituents represent materials with high and low CTE respectively.

The numerical topology optimization method is applied to find the distribution of materials within a unit cell envelop that achieves the predefined thermoelastic properties subject to certain constraints, such as the volume fraction of different phases in a periodic base cell [74]. The optimization procedure yields the distribution of two material phases with dissimilar bulk moduli and a void phase [74]. Sigmund and Torquato [46, 73, 74] used topology optimization to design three-phase composites with zero thermal expansion while maximizing the bulk modulus (Figure 1-10a). The concepts are used to design 2D composites with extremal or unusual thermal expansion behavior. However, although the bulk modulus was optimized, the in-plane uniaxial stiffness is poor. In addition, the two materials should be of similar stiffness, with widely differing thermal expansions [46]. This is another aspect that contributes to narrowing the choice of materials. Several other three-phase concepts that exhibit tailorable CTEs have also been carried out via topology optimization: Takezawa et al. [75] considered planar concepts with a forced void domain for maintaining the deformation range (Figure 1-10b); Watts et al. [76] considered spatial concepts with constraints on both modulus and thermal expansion (Figure 1-10c and d); Oruganti et al. demonstrated an NTE Ni-Cr cellular structure [77]; Wang et al. applied level-set method for design [78]; and Hirota et al. obtained optimal design via mixed integer programming [79]. Although the aforementioned concepts have optimized performance under corresponding constraints, the complex configuration and bended geometry of the unit cell also limit their application in stiff lightweight components due to challenges in manufacturing. Nevertheless, the merit of topology optimization is to obtain the performance boundary, which can be used as a benchmark to compare different unit cells.

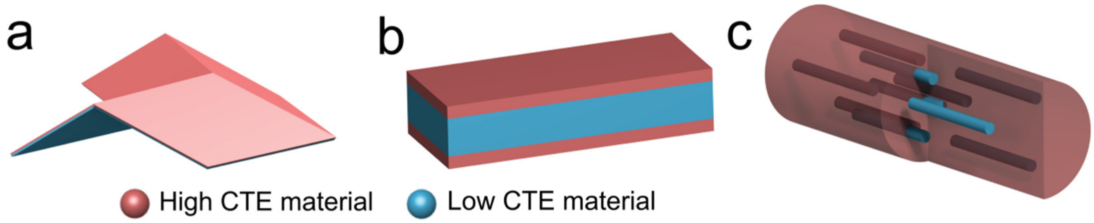

Figure 1-11: Laminates and particulate composites with controllable CTEs: (a) origami laminates for tunable thermal expansion [80]; (b) laminated plate with in-plane controllable CTEs [26, 81-86]; and (c) particulate composites for thermal stress management [87, 88]. Red and blue constituents represent materials with high and low CTE respectively.

Differently from all previously reported systems, the combination of two materials with dissimilar CTEs may form nonporous laminates or particulate composites having positive, near-zero or even negative thermal expansion. When heated, the thermal expansion mismatch of different components induces thermal stress on the interface between two distinct materials. The thermally induced shear stress deforms the architecture anisotropically, such as plate tuning of origami (Figure 1-11a) [80], as well as the Poisson effect of laminates (Figure 1-11b) [26, 81-86] and particulate composites (Figure 1-11c) [87, 88]. These anisotropic deformations compensate the thermal expansion of architected materials in specific directions leading to a low-to-zero or even negative effective CTE. For example, Boatti et al. demonstrated that origami architected materials provide a platform for the design of systems with a wide range of CTEs by tuning the geometrical parameters of the origami structure and the arrangement of plates and creases [80]. Grima et al. proposed that a negative CTE can be obtained via the Poisson's effect of multilayered systems constructed by a combination of thin layers of stiff materials, having a high positive CTE, bonded with thicker layers of a soft material, having low CTE and high Poisson's ratio (Figure 1-11b) [85]. However, architected materials with porosity provide a larger range of attainable CTEs than nonporous ones, while also allowing both isotropic and anisotropic behaviour. This is due to the empty regions in the architecture in which a large amount of anisotropic displacement is possible. The large interlayer stress concentration which leads to failures including thermal buckling, matrix crack, delamination, and fiber break, restricts the application of laminates and particulate composites with controllable CTEs.

1.2.4 Challenges for design of architected materials

It can be concluded from this survey of literature that current concepts belong to either i) bend-dominated architecture with low structural efficiency but wide adjustable CTE range or ii) stretch-dominated architecture with high structural efficiency but restricted adjustable CTE range. The existing concepts fail to simultaneously meet requirements in engineering applications (section 1.1.3): i) high structural efficiency and ii) wide, ideally unbound, obtainable CTE scope covering large negative to positive including zero CTEs. The high structural efficiency, e.g. stiffness to mass ratio with small deformation when mechanically loaded, and ample freedom to tune the effective CTE, e.g. sufficient deformation can be obtained to adjust the thermal expansion of components leading to zero effective CTE, are two conflicting requirements, which current available concepts are unable to ideally reconcile.

The conflict existing between structural efficiency and adjustable CTE range has also been identified in the seminal work of Lehman and Lakes, who attempted to find a trade-off design of stiff lattices with zero CTE via rib cross section optimization [44]. In their approach, however, the architectures with enhanced stiffness still deform mainly by bending. As a result the whole set of trade-off designs are bend-dominated and cannot meet the aforementioned application requirements. A very small set of architectures, on the other hand, are stretch dominated with high specific stiffness, but these concepts can generate only a narrow range of CTE. Steebes et al. attempted to extend the controllable CTE range of their stretch-dominated concepts via tuning the geometrical parameters at the cost of decreasing the structural efficiency [61]. The trade-off between CTE tunability and structural efficiency is currently unresolved with current concepts achieving wide, or even unbounded, adjustable CTE range only at the expense of a dramatic loss in their specific stiffness and specific strength [18, 48, 50, 52], and vice versa [2, 17, 44, 47, 64, 67, 69, 70].

As discussed above, the first issue we want to address in this thesis: how to enlarge adjustable CTE range in stiff bi-material concepts, with the ultimate goal of obtaining any desired CTE starting from any pair of materials with different CTEs, up to a theoretical unbounded CTE range. The second issue associated with the first is the coupling between mechanical properties and thermal properties. This is typical of existing dual-materials concepts, for which CTE tailoring through architecture manipulation may result in severe reduction of mechanical performance. Hence, the second question: how to reduce the penalty that an increase in the adjustable CTE range will bring on the elastic properties, so as to obtain the best out of them.

In addition, several methodologies in the literature have been developed to use existing building blocks with CTE tuning mechanisms to design a class of architected materials with desired thermal expansion [2, 17, 47, 52, 55, 67]. However, they only investigate individual special cases of periodic lattice layouts while the underlying relationships between controllable thermal expansion of building blocks, structural symmetry of unit cells, and the effective thermoelastic properties of periodic trusses have not been reported. Thus a systematic methodology for designing and evaluating unlimited number of lattices with controllable CTE is necessary in order to meet a great diversity of application requirements.

In this thesis, therefore, the overarching goal is to address these intertwined issues so as to expand the CTE range an architected material can offer without penalizing its specific stiffness. The proposed research will focus primarily on developing and validating concepts for stiff, strong, and CTE tunable lattice materials that can overcome the deficiencies of the material and structural concepts currently available in literature.

1.3 Thesis objectives

The overall objective of this thesis is to contribute to the field of architected materials with tunable thermal expansion and desirable mechanical performance. The specific objectives of this thesis are to:

- Enlarge adjustable CTE range in stiff bi-material concepts, with the ultimate goal of obtaining a theoretical unbounded CTE range starting from any pair of materials with different CTEs, without penalizing their mechanical performance.
- Decouple the tailoring process of thermal and mechanical characteristics of architected materials to simultaneously realize a wide adjusted CTE range and high structural efficiency, e.g. specific stiffness and specific strength.
- Investigate relationships between controllable thermal expansion of building blocks, structural symmetry of unit cells, and the effective thermoelastic properties of periodic trusses. Then, develop and validate a systematic methodology for designing and evaluating architected materials with controllable CTE and high structural efficiency.
- Exemplify the design methodology through the application to a set of architected materials that are not only stiffer and stronger than existing concepts, but also offer a highly controllable CTE.

1.4 Structure of the thesis

The present thesis is manuscript based and is composed of five chapters. The current chapter (Chapter 1) briefly introduced the general background of thermal expansion, followed by a detailed review of CTE tunable architected materials. Requirements in the engineering applications are characterized, and the significance of utilizing architected materials is analyzed. In particular, Chapter 1 points out three main requirements of thermal expansion control: materials with zero CTE to avoid severe thermal distortion, large positive/negative CTEs to morph as a response to changes in ambient temperatures, and high structural efficiency to meet mechanical requirements such as high load-bearing capacity and low mass. A survey of existing concepts and design guidelines for CTE tunable architected materials indicates their merits and limitations. The challenges of existing concepts in the literature to tailor thermal and mechanical performance are evaluated and discussed. In the end, the overall objective of this thesis is proposed.

Chapter 2 of this thesis proposes two-dimensional hierarchical lattices that feature a theoretically unbounded range of CTE tunability, regardless of the constituent solids provided that their CTEs are different, and enables thermal expansion control without incurring a severe loss of structural performance. Bi-material diamonds with low- and high-CTEs have been proposed as building blocks of hierarchical lattices with the goal of decoupling the thermal and elastic properties to allow for separate tuning of their performances in different length scales. The obtainable CTE range increases with the order of hierarchy, so as to theoretically approach an unbounded value for unlimited hierarchical order. Through derived closed-form expressions, simulations, and experiments on fabricated proof-of-concepts, it is found that hierarchical architectures, including those made of recursive unit cells, can be tailored to provide theoretically unbounded CTE tunability with CTE values ranging from large positive, zero, to large negative.

Chapter 3 reports routes to systematically engineer thermally responsive architected materials that are built from dual-material tetrahedral units that are stiff and strong. Drawing from concepts of vector analysis, crystallography, and tessellation, a scheme is presented for three-dimensional lattices to program desired magnitude and spatial directionality of thermal expansion. All the material permutations that can occur in the struts of a dual-material tetrahedron are analyzed and three tetrahedra are selected as building blocks to construct unit cells. The relationship between the geometric symmetry of the unit cell and its thermal expansion is elucidated, and then systematic routes to assemble truss materials with desired magnitude and directionality of thermal expansion are proposed. The framework is applied to nine concepts that can meet three thermal expansion requirements including unidirectional, transverse isotropic, and isotropic. A range of investigations covering theoretical and computational analysis along with thermal testing on fabricated samples is carried out to assess their thermal expansion and elastic properties, e.g. Young’s modulus, as well as the trade-off existing between them.

Chapter 4 exemplifies the introduced design methodology through the application to a set of three-dimensional lattices, such as the dual-material Octet-truss, which are proven to not only be stiffer and stronger than any other existing concepts, but also offer a highly tunable CTE. Pretension snap-fits were used to fabricate all the three versions of the Octet cell, which resolve the trade-off between CTE tunability and structural efficiency, and extend the pin-jointed concept in Chapter 3 to bonded-joint lattices. Via a combination of numerical simulations and physical experiments on 3D fabricated prototypes, this work demonstrates how the Octet lattice can generate a large range of CTE values, including negative, zero, or positive, with no loss in structural efficiency. The novelty and simplicity of the proposed design as well as the ease in fabrication, make this bi-material architecture well-suited for a wide range of applications, including satellite antennae, space optical systems, precision instruments, thermal actuators, and MEMS.

Finally, Chapter 5 highlights the main results and the main contributions of this research. At the end, a few guidelines for future works are also recommended.

1.5 Reference

1. Takenaka, K., *Negative thermal expansion materials: Technological key for control of thermal expansion.* Science and Technology of Advanced Materials, 2012. **13**(1).
2. Palumbo, N.M.A., *Trusses with reduced thermal expansion: Their design, and mass and stiffness penalties*. 2013, University of Exeter: UK. p. 260.
3. Lakes, R. *Materials with negative or extremal unbounded thermal expansion.* 2014; Available from: http://silver.neep.wisc.edu/~lakes/NegAlpha.html.
4. Palumbo, N., C. Smith, W. Miller, and K. Evans, *Near-zero thermal expansivity 2-d lattice structures: Performance in terms of mass and mechanical properties.* Acta Materialia, 2011. **59**(6): p. 2392-2403.
5. Yamamoto, N., E. Gdoutos, R. Toda, V. White, H. Manohara, and C. Daraio, *Thin films with ultra-low thermal expansion.* Advanced Materials, 2014. **26**(19): p. 3076-3080.
6. Wei, K., Y. Peng, K. Wang, S. Duan, X. Yang, and W. Wen, *Three dimensional lightweight lattice structures with large positive, zero and negative thermal expansion.* Composite Structures, 2018. **188**: p. 287-296.

7. Imbriale, W.A., S. Gao, and L. Boccia, *Space antenna handbook*. 2012: Wiley.

8. Gilmore, D.G., *Spacecraft thermal control handbook: Fundamental technologies*. 2002, United States: Aerospace Press.

9. Yong, Z. and C. Tzu-Hsuan, *A review of microelectromechanical systems for nanoscale mechanical characterization.* Journal of Micromechanics and Microengineering, 2015. **25**(9): p. 093001.

10. Zhang, Q., J. Wommer, C. O'Rourke, J. Teitelman, Y. Tang, J. Robison, G. Lin, and J. Yin, *Origami and kirigami inspired self-folding for programming three-dimensional shape shifting of polymer sheets with light.* Extreme Mechanics Letters, 2017. **11**(Supplement C): p. 111-120.

11. Breger, J.C., C. Yoon, R. Xiao, H.R. Kwag, M.O. Wang, J.P. Fisher, T.D. Nguyen, and D.H. Gracias, *Self-folding thermo-magnetically responsive soft microgrippers.* ACS Applied Materials & Interfaces, 2015. **7**(5): p. 3398-3405.

12. Stoychev, G., N. Puretskiy, and L. Ionov, *Self-folding all-polymer thermoresponsive microcapsules.* Soft Matter, 2011. **7**(7): p. 3277-3279.

13. Tibbits, S., *Design to self-assembly.* Architectural Design, 2012. **82**(2): p. 68-73.

14. Mao, Y., Z. Ding, C. Yuan, S. Ai, M. Isakov, J. Wu, T. Wang, M.L. Dunn, and H.J. Qi, *3d printed reversible shape changing components with stimuli responsive materials.* Scientific Reports, 2016. **6**: p. 24761.

15. Ding, Z., C. Yuan, X. Peng, T. Wang, H.J. Qi, and M.L. Dunn, *Direct 4d printing via active composite materials.* Science Advances, 2017. **3**(4): p. e1602890.

16. Lopes, M.B., Z. Yan, S. Consani, A. Gonini Júnior, A. Aleixo, and J.F. McCabe, *Evaluation of the coefficient of thermal expansion of human and bovine dentin by thermomechanical analysis.* Brazilian Dental Journal, 2012. **23**: p. 03-07.

17. Steeves, C.A., S.L. dos Santos e Lucato, M. He, E. Antinucci, J.W. Hutchinson, and A.G. Evans, *Concepts for structurally robust materials that combine low thermal expansion with high stiffness.* Journal of the Mechanics and Physics of Solids, 2007. **55**(9): p. 1803-1822.

18. Jefferson, G., T.A. Parthasarathy, and R.J. Kerans, *Tailorable thermal expansion hybrid structures.* International Journal of Solids and Structures, 2009. **46**(11-12): p. 2372-2387.

19. Korthuis, V., N. Khosrovani, A.W. Sleight, N. Roberts, R. Dupree, and W.W. Warren, Jr., *Negative thermal expansion and phase transitions in the zrv2-xpxo7 series.* Chemistry of Materials, 1995. **7**(2): p. 412-417.

20. Mary, T.A., J.S.O. Evans, T. Vogt, and A.W. Sleight, *Negative thermal expansion from 0.3 to 1050 kelvin in zrw2o8.* Science, 1996. **272**(5258): p. 90-92.

21. Evans, J.S.O., T.A. Mary, and A.W. Sleight, *Negative thermal expansion materials.* Physica B, 1998. **241-243**: p. 311-316.

22. Matsui, M. and S. Chikazumi, *Analysis of anomalous thermal expansion coefficient of fe–ni invar alloys.* Journal of the Physical Society of Japan, 1978. **45**(2): p. 458-465.

23. Sumiyama, K., M. Shiga, M. Morioka, and Y. Nakamura, *Characteristic magnetovolume effects in invar type fe-pt alloys.* Journal of Physics F: Metal Physics, 1979. **9**(8): p. 1665.

24. Lommens, P., C. De Meyer, E. Bruneel, K. De Buysser, I. Van Driessche, and S. Hoste, *Synthesis and thermal expansion of zro2/zrw2 o8 composites.* Journal of the European Ceramic Society, 2005. **25**(16): p. 3605-3610.

25. Jacquot, P.M., M. Lehmann, and X.C. de Lega. *Deformation analysis of a communication telescope structure under nonuniform heating using holographic interferometry*. in *Practical Holography XII*. 1998. International Society for Optics and Photonics.

26. Ito, T., T. Suganuma, and K. Wakashima, *A micromechanics-based analysis for tailoring glass-fiber-reinforced thermoplastic laminates with near-zero coefficients of thermal expansion.* Composites Science and Technology, 2000. **60**(9): p. 1851-1861.

27. Matsui, M., T. Shimizu, H. Yamada, and K. Adachi, *Magnetic properties and thermal expansion of fe-pd invar alloys.* Journal of Magnetism and Magnetic Materials, 1980. **15**: p. 1201-1202.

28. Liot, F.c., *Thermal expansion and local environment effects in ferromagnetic iron-based alloys-a theoretical study*, in *Department of Physics, Chemistry and Biology*. 2009, Linoping University: Sweden. p. 61.

29. Ashby, M.F., *Materials selection in mechanical design*. Fourth ed. 2011, Oxford: Butterworth-Heinemann.

30. Cottrell, A.H., *The mechanical properties of matter*. 1964: Wiley.

31. Zheng, X., W. Smith, J. Jackson, B. Moran, H. Cui, D. Chen, J. Ye, N. Fang, N. Rodriguez, T. Weisgraber, and C.M. Spadaccini, *Multiscale metallic metamaterials.* Nature Materials, 2016. **15**(10): p. 1100-1106.
32. Overvelde, J.T.B., J.C. Weaver, C. Hoberman, and K. Bertoldi, *Rational design of reconfigurable prismatic architected materials.* Nature, 2017. **541**: p. 347.
33. Fleck, N.A., V.S. Deshpande, and M.F. Ashby, *Micro-architectured materials: Past, present and future.* Proceedings of the Royal Society A: Mathematical, Physical and Engineering Science, 2010. **466**(2121): p. 2495-2516.
34. Lakes, R., *Materials with structural hierarchy.* Nature, 1993. **361**(6412): p. 511-515.
35. Vigliotti, A. and D. Pasini, *Mechanical properties of hierarchical lattices.* Mechanics of Materials, 2013. **62**: p. 32-43.
36. Banerjee, S., *On the mechanical properties of hierarchical lattices.* Mechanics of Materials, 2014. **72**(0): p. 19-32.
37. Ashby, M.F. and Y.J.M. Bréchet, *Designing hybrid materials.* Acta Materialia, 2003. **51**(19): p. 5801-5821.
38. Lee, M.G., J.W. Lee, S.C. Han, and K. Kang, *Mechanical analyses of "shellular", an ultralow-density material.* Acta Materialia, 2015. **103**: p. 595-607.
39. Lu, T.J., H.A. Stone, and M.F. Ashby, *Heat transfer in open-cell metal foams.* Acta Materialia, 1998. **46**(10): p. 3619-3635.
40. Wang, P., J. Shim, and K. Bertoldi, *Effects of geometric and material nonlinearities on tunable band gaps and low-frequency directionality of phononic crystals.* Physical Review B - Condensed Matter and Materials Physics, 2013. **88**(1): p. 014304.
41. Khanoki, S.A. and D. Pasini, *Multiscale design and multiobjective optimization of orthopedic hip implants with functionally graded cellular material.* Journal of biomechanical engineering, 2012. **134**(3): p. 031004.
42. Ai, L. and X.L. Gao, *Three-dimensional metamaterials with a negative poisson's ratio and a non-positive coefficient of thermal expansion.* International Journal of Mechanical Sciences, 2018. **135**: p. 101-113.
43. Lakes, R., *Cellular solid structures with unbounded thermal expansion.* Journal of Materials Science Letters, 1996. **15**(6): p. 475-477.

44. Lehman, J. and R.S. Lakes, *Stiff, strong, zero thermal expansion lattices via material hierarchy.* Composite Structures, 2014. **107**: p. 654-663.

45. Wang, Q., J.A. Jackson, Q. Ge, J.B. Hopkins, C.M. Spadaccini, and N.X. Fang, *Lightweight mechanical metamaterials with tunable negative thermal expansion.* Physical Review Letters, 2016. **117**(17): p. 175901.

46. Sigmund, O. and S. Torquato, *Composites with extremal thermal expansion coefficients.* Applied Physics Letters, 1996. **69**(21): p. 3203-3205.

47. Lehman, J. and R. Lakes, *Stiff, strong zero thermal expansion lattices via the poisson effect.* Journal of Materials Research, 2013. **28**(17): p. 2499-2508.

48. Hopkins, J.B., K.J. Lange, and C.M. Spadaccini, *Designing microstructural architectures with thermally actuated properties using freedom, actuation, and constraint topologies.* Journal of Mechanical Design, Transactions of the ASME, 2013. **135**(6): p. 061004.

49. Deshpande, V.S., M.F. Ashby, and N.A. Fleck, *Foam topology: Bending versus stretching dominated architectures.* Acta Materialia, 2001. **49**(6): p. 1035-1040.

50. Lehman, J. and R. Lakes, *Stiff lattices with zero thermal expansion.* Journal of Intelligent Material Systems and Structures, 2012. **23**(11): p. 1263-1268.

51. Lehman, J. and R. Lakes, *Stiff lattices with zero thermal expansion and enhanced stiffness via rib cross section optimization.* International Journal of Mechanics and Materials in Design, 2013. **9**(3): p. 213-225.

52. Lakes, R., *Cellular solids with tunable positive or negative thermal expansion of unbounded magnitude.* Applied Physics Letters, 2007. **90**(22): p. 221905.

53. Wu, L., B. Li, and J. Zhou, *Isotropic negative thermal expansion metamaterials.* ACS Applied Materials & Interfaces, 2016. **8**(27): p. 17721-17727.

54. Qu, J., M. Kadic, A. Naber, and M. Wegener, *Micro-structured two-component 3d metamaterials with negative thermal-expansion coefficient from positive constituents.* Scientific Reports, 2017. **7**: p. 40643.

55. Spadaccini, C. and J. Hopkins, *Lattice-structures and constructs with designed thermal expansion coefficients*. 2013, Google Patents: US.

56. Jefferson, G., R.J. Kerans, and T.A. Parthasarathy, *Bi-material composite structure with reduced thermal expansion*. 2012, Google Patents.

57. Ng, C.K., K.K. Saxena, R. Das, and E.I. Saavedra Flores, *On the anisotropic and negative thermal expansion from dual-material re-entrant-type cellular metamaterials.* Journal of Materials Science, 2016: p. 1-14.

58. Ai, L. and X.L. Gao, *Metamaterials with negative poisson's ratio and non-positive thermal expansion.* Composite Structures, 2017. **162**: p. 70-84.

59. Lakes, R., *Foam structures with a negative poisson's ratio.* Science, 1987. **235**(4792): p. 1038-1040.

60. Steeves, C.A., C. Mercer, E. Antinucci, M.Y. He, and A.G. Evans, *Experimental investigation of the thermal properties of tailored expansion lattices.* International Journal of Mechanics and Materials in Design, 2009. **5**(2): p. 195-202.

61. Steeves, C.A. and A.G. Evans, *Optimization of thermal protection systems utilizing sandwich structures with low coefficient of thermal expansion lattice hot faces.* Journal of the American Ceramic Society, 2011. **94**(SUPPL. 1): p. S55-S61.

62. Schuerch, H.U., *Thermally stable macro-composite structures*. 1972, Washington, D.C.: National Aeronautics and Space Administration.

63. Vandeperre, L.J. and W.J. Clegg, *Tailoring strains through microstructural design.* MRS Online Proceedings Library, 2003. **785**: p. D11.4.1.

64. Aboudi, J. and R. Gilat, *Micromechanical analysis of lattice blocks.* International Journal of Solids and Structures, 2005. **42**(15): p. 4372-4392.

65. Grima, J.N., P.S. Farrugia, R. Gatt, and V. Zammit, *A system with adjustable positive or negative thermal expansion.* Proceedings of the Royal Society A: Mathematical, Physical and Engineering Science, 2007. **463**(2082): p. 1585-1596.

66. Grima, J.N., P.S. Farrugia, R. Gatt, and V. Zammit, *Connected triangles exhibiting negative poisson's ratios and negative thermal expansion.* Journal of the Physical Society of Japan, 2007. **76**(2): p. 025001.

67. Miller, W., D.S. Mackenzie, C.W. Smith, and K.E. Evans, *A generalised scale-independent mechanism for tailoring of thermal expansivity: Positive and negative.* Mechanics of Materials, 2008. **40**(4–5): p. 351-361.

68. Berger, J., C. Mercer, R.M. McMeeking, and A.G. Evans, *The design of bonded bimaterial lattices that combine low thermal expansion with high stiffness.* Journal of the American Ceramic Society, 2011. **94**: p. s42-s54.

69. Lim, T.-C., *Negative thermal expansion in transversely isotropic space frame trusses.* Physica Status Solidi (b), 2013. **250**(10): p. 2062-2069.

70. Lim, T.-C., *Negative thermal expansion structures constructed from positive thermal expansion trusses.* Journal of Materials Science, 2012. **47**(1): p. 368-373.

71. Wei, K., H. Chen, Y. Pei, and D. Fang, *Planar lattices with tailorable coefficient of thermal expansion and high stiffness based on dual-material triangle unit.* Journal of the Mechanics and Physics of Solids, 2016. **86**: p. 173-191.

72. Wei, K., Y. Peng, W. Wen, Y. Pei, and D. Fang, *Tailorable thermal expansion of lightweight and robust dual-constituent triangular lattice material.* Journal of Applied Mechanics, 2017. **84**(10): p. 101006.

73. Sigmund, O. and S. Torquato, *Design of smart composite materials using topology optimization.* Smart Materials and Structures, 1999. **8**(3): p. 365-379.

74. Sigmund, O. and S. Torquato, *Design of materials with extreme thermal expansion using a three-phase topology optimization method.* Journal of the Mechanics and Physics of Solids, 1997. **45**(6): p. 1037-1067.

75. Takezawa, A. and M. Kobashi, *Design methodology for porous composites with tunable thermal expansion produced by multi-material topology optimization and additive manufacturing.* Composites Part B: Engineering, 2017. **131**: p. 21 - 29.

76. Watts, S. and D.A. Tortorelli, *Optimality of thermal expansion bounds in three dimensions.* Extreme Mechanics Letters, 2017. **12**(Supplement C): p. 97-100.

77. Oruganti, R., A. Ghosh, and J. Mazumder, *Thermal expansion behavior in fabricated cellular structures.* Materials Science and Engineering: A, 2004. **371**(1): p. 24-34.

78. Wang, X., Y. Mei, and M.Y. Wang, *Level-set method for design of multi-phase elastic and thermoelastic materials.* International Journal of Mechanics and Materials in Design, 2004. **1**(3): p. 213-239.

79. Hirota, M. and Y. Kanno, *Optimal design of periodic frame structures with negative thermal expansion via mixed integer programming.* Optimization and Engineering, 2015. **16**(4): p. 1-43.

80. Boatti, E., N. Vasios, and K. Bertoldi, *Origami metamaterials for tunable thermal expansion.* Advanced Materials, 2017. **29**: p. 1700360.

81. Ito, T., T. Suganuma, and K. Wakashima, *Glass fiber/polypropylene composite laminates with negative coefficients of thermal expansion.* Journal of Materials Science Letters, 1999. **18**(17): p. 1363-1365.

82. Landert, M., A. Kelly, R. Stearn, and P. Hine, *Negative thermal expansion of laminates.* Journal of materials science, 2004. **39**(11): p. 3563-3567.

83. Kelly, A., L. McCartney, W. Clegg, and R. Stearn, *Controlling thermal expansion to obtain negative expansivity using laminated composites.* Composites Science and Technology, 2005. **65**(1): p. 47-59.

84. Kelly, A., R.J. Stearn, and L.N. McCartney, *Composite materials of controlled thermal expansion.* Composites Science and Technology, 2006. **66**(2): p. 154-159.

85. Grima, J.N., L. Oliveri, B. Ellul, R. Gatt, D. Attard, G. Cicala, and G. Recca, *Adjustable and negative thermal expansion from multilayered systems.* Physica Status Solidi (RRL)-Rapid Research Letters, 2010. **4**(5 - 6): p. 133-135.

86. Lim, T.C., *Coefficient of thermal expansion of stacked auxetic and negative thermal expansion laminates.* Physica Status Solidi (b), 2011. **248**(1): p. 140-147.

87. Grima, J.N., B. Ellul, D. Attard, R. Gatt, and M. Attard, *Composites with needle-like inclusions exhibiting negative thermal expansion: A preliminary investigation.* Composites Science and Technology, 2010. **70**(16): p. 2248-2252.

88. Miller, W., C. Smith, P. Dooling, A. Burgess, and K. Evans, *Tailored thermal expansivity in particulate composites for thermal stress management.* Physica Status Solidi (b), 2008. **245**(3): p. 552-556.

Chapter 2

Multilevel hierarchy in bi-material lattices with high specific stiffness and unbounded thermal expansion

Chapter 2: Multilevel hierarchy in bi-material lattices with high specific stiffness and unbounded thermal expansion

Hang Xu, Amr Farag, and Damiano Pasini*
Department of Mechanical Engineering, McGill University,
817 Sherbrooke St. West, Montreal, QC H3A 0C3, Canada
*Corresponding author. Tel: +1 (514) 398-6295 Fax: +1 (514) 398-7365
Email: damiano.pasini@mcgill.ca

Acta Materialia, 2017. 134: p. 155-166.

Reproduced with permission from Elsevier

2.1 Abstract

Dual-material concepts that expand or contract as desired upon changes in temperature exist but have their limitations. One upon which we focus here is the trade-off caused by the inherent thermo-elastic coupling that they feature, a condition that makes desired changes in thermal expansion penalize elastic stiffness, and vice versa. In this chapter, we present hierarchical bi-material lattices that are stiff and can be designed to attain a theoretically unbounded range of thermal expansion without (i) impact onto elastic moduli and (ii) severe penalty in specific stiffness. Through a combination of theory, numerical simulations and experiments, we demonstrate the thermomechanical performance of eight hierarchical lattices, including two fractal-like hierarchical lattices with self-repeating units that are built from dual-material diamond shapes with low and high coefficients of thermal expansion (CTE). Results show that the achievable range of CTE can be enlarged by 66% through the addition of one order of hierarchy only, and that for a given CTE range the specific stiffness can be at least 1.4 times larger than that of existing stretch-dominated concepts. The concepts here introduced can open up new avenues towards multifunctional devices and structurally efficient materials with simultaneously customized thermal expansion and mechanical properties.

Keywords: Thermal expansion tunability, Thermoresponsive materials, Cellular solids, Composites, Mechanical properties.

2.2 Introduction

Architected materials can be designed to elicit extreme mechanical properties, often beyond those of existing solids [1]. They are very appealing for use in several fields of engineering including aerospace, automotive and biomedical [2-4]. In these applications, the target to maximize might be either structural, through attaining for example minimum mass at maximum stiffness [5, 6], or functional, such as thermal dimension control [2], heat transfer [7], band gaps [8], mechanical biocompatibility [9], and others [1]. For lightweight structural applications, high stiffness is desired for preserving the structural integrity and resisting a variety of loading conditions. In contrast, high compliance is required to adapt under other loading conditions for more functional applications, such as energy absorption [10]. For functional applications, the coefficient of thermal expansion (CTE) has been the recent focus of intense research [11, 12] aiming at obtaining large positive, zero or negative CTE via material architecture tuning.

The design freedom to adjust thermal expansion is particularly advantageous in a large assortment of applications. On one hand, in extreme thermal environments, sensitive applications that require very fine precision, such as satellite antennas, space telescopes, and large array mirrors [4, 13], call for materials with zero CTE so as to avoid undesired thermal deformation. On the other hand, there are other applications requiring materials with large positive or negative CTEs. These materials must induce responsive and desirable deformations under given changes in temperature [14], often, but not always, dictated by the surrounding environment, such as in morphing and adaptive structures [15, 16], as well as MEMS [17]. The potential of periodic architected materials is also appealing because their repeating cell can be designed to concurrently maximize multiple performance requirements, notably structural and functional. Among many, examples of multifunctional lattices include those developed for aerospace components that can maintain precise dimensional tolerances under large temperature fluctuations and specific stiffness requirements [2, 18].

This chapter focuses on multifunctional lattices designed with the goal of providing unique control of thermal expansion and structural performance, at levels currently unmet by existing concepts. As with previous works [2, 11, 18-22], we deal with material architectures made of two materials, which can be designed to compensate the mismatched thermal deformation generated by each of the two materials. If exploited, this strategy enables the attainment of an overall thermal deformation that can be large positive, zero or large negative. Since dual material architectures achieve a tunable CTE through a purely mechanical, and thus temperature-independent, mechanism [4], their CTE is extremely dependent on the unit cell architecture and on the difference in CTE of their constituent solids [12, 18]. To assess the potential of a given architected material in providing a range of CTE values via tailored selection of its material constitutes and its cell topology, we need a quantitative metric. CTE tunability, (ΔCTE), can be used [23] to measure the maximum range of CTE values that a concept can achieve upon changes of its unit cell geometry from a given pair of materials. Whereas a single material has only one CTE value, hence no ΔCTE, the CTE of dual material concepts can be adjusted by geometric manipulation of the building block with the result of obtaining a range of CTE values. The difference between the minimum and maximum CTE that an architected material can offer is defined as ΔCTE. For a given concept, a large ΔCTE indicates ample freedom to tune the unit cell geometry, an asset that can release the dependence on the CTE ratio of the constituents (see Supplementary Material Section 2.7.1).

Several dual-material concepts have been proposed in the literature, most notably by Lehman and Lakes [19, 24], Steeves et al. [18], Hopkins et al. [25], Jefferson et al. [20], Sigmund et al. [22], and Xu et al. [23]. A number of these concepts, such as Lakes concept [26], while successful in demonstrating theoretically unbounded CTE tunability, feature a trade-off in structural efficiency [27]. The compromise between them emphasizes an inherent coupling between mechanical properties and thermal properties. This is typical of existing dual-materials concepts (See Supplementary Material Section 2.7.1), for which CTE tailoring through architecture manipulation may result in severe reduction of mechanical performance. For example, some existing concepts show that the desired flexural deformation that a large CTE tunability would require is generally antagonist to the high specific stiffness that is distinctive of a structurally efficient architecture. This indicates that preserving high specific stiffness is in conflict with the need of enhancing ΔCTE, as manifest in stretch-dominated unit cells constructed by dual-material triangle (2D) or tetrahedron (3D), which offer a remarkable structural performance [2, 18], but cannot achieve the sizeable CTE tunability of bend-dominated architectures [11, 26]. Hence, the main issue we want to address in this chapter: how to reduce the penalty that an increase in ΔCTE will generate on the elastic properties, so as to obtain the best compromise out of them.

This work proposes hierarchical lattice materials which feature enhanced CTE tunability regardless of the choice of the constituent solids, and enable thermal expansion control without incurring in severe loss of structural performance. Structural hierarchy is not new and for a long time now has been recognized as one crucial factor governing high stiffness, strength, and toughness in both natural and bio-inspired materials [28-30], and even more recently in the field of thermal expansion [19]. However, what has not been so far explored yet is how to exploit it to, first, amplify CTE tunability in architected materials, and then to decouple physical properties that are in conflict. The method adopted in this chapter, as explained in Section 2.3, combines solid mechanics theory, finite element simulations and experiments on proof-of-concept lattices. The results presented in Section 2.4 demonstrate that initially coupled properties can be individually tuned in distinct hierarchical orders to obtain large CTE tunability without sensible loss in structural performance. Section 2.5 discusses the concept performance by drawing a comparison with a set of existing architected materials that are stretch and bend dominated.

2.3 Methodology

Our focus here is on bi-material unit cells (Figure 2-1) with high and low CTE, which are used to build hierarchical lattices (HL) including those made of self-repeating unit cells, i.e. fractal-like hierarchical lattices (fractal-like HL) and hierarchical lattices which feature at least two unit cells with different topologies, thus making the hierarchical lattice of a hybrid-type (hybrid-type HL) (Figure 2-2). The following provides closed-form expressions and computational results of their thermomechanical properties, along with details on sample fabrication and CTE testing.

2.3.1 Unit cell model with a bi-material diamond shape

Figure 2-1a-I shows the diamond that can attain a low-CTE performance (LD). Upon a uniform increase of temperature, red (α_{s1}) and blue (α_{s2}) elements in a LD deform at different rates, visualized in Figure 2-1a-II as unbonded for explanation purpose. Figure 2-1a-II displays the height increase, ΔH_{l1}, caused solely by thermal expansion in the blue elements. In the final configuration (Figure 2-1a-III), rigid connections at the nodes cause a higher expansion in the red horizontal bar that turns the blue struts. As a result, the top vertex of the diamond springs back by ΔH_{l2}, a displacement that if desired can be conveniently designed to compensate ΔH_{l1}. By harnessing the values of α_{s1} and α_{s2}, or the skewness of the blue elements, θ, the CTE of a LD can be tuned to zero, or even negative, in the *y*-direction. Similarly, Figure 2-1b-I shows the complementary version of the diamond in Figure 2-1a-I, where the switched material distribution yields a high-CTE diamond (HD). In Figure 2-1b-II, the expansion of the red elements bring about a height increase, ΔH_{h1}, and a width-wise gap, ΔW_h, which would appear if the blue bar, which exhibits less expansion, were visualized as unconnected. Also in this case, rigid connections (Figure 2-1b-III) would compensate the visualized horizontal gap, ΔW_h, by a height increase of ΔH_{h2}, adding on to ΔH_{h1}, and this value of ΔH_{h2} can also be tuned by manipulating α_{s1}, α_{s2} and θ. From this explanation, we gather that the CTE in the *y*-direction depends on the thermal expansion ratio of the constituent materials, $\xi = \alpha_{s2}/\alpha_{s1}$, and the skewness angle, θ. If θ is given, the smaller the ξ, the lower (for LD) or higher (for HD) the CTE [18]; hence the greater the CTE distinction of the constituent solids, the higher the CTE tunability.

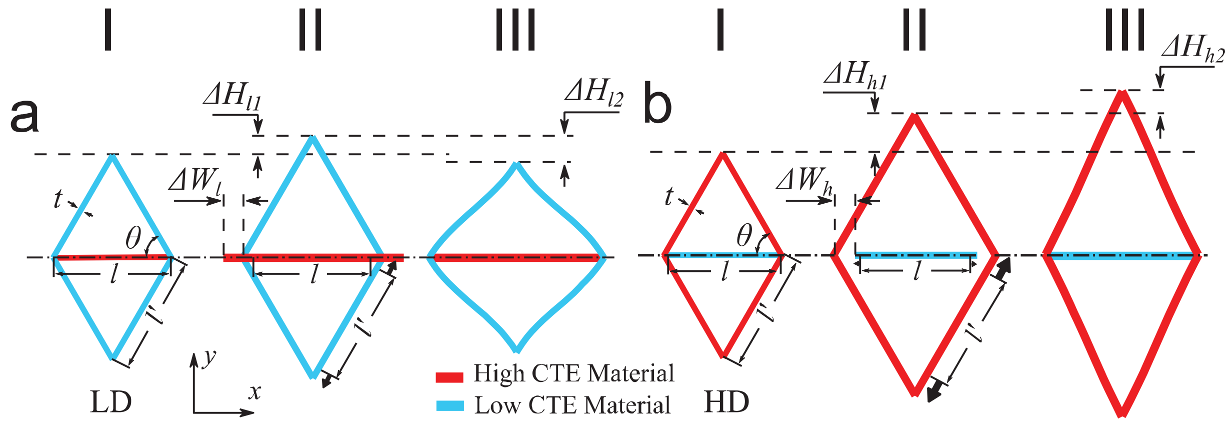

Figure 2-1: Deformation of a unit cell in a diamond shape with low, LD (a-I), and high, HD (b-I), CTE, strut thickness t, horizontal bar length l, sloped bar length l', and skew angle θ. (II) Deformation of hypothetically unconnected elements and their corresponding dimensional changes. (III) Actual deformation of rigidly connected elements along with change in dimensions due to rigid nodal connectivity.

We now examine the general case of a LD (Figure 2-1a-I) with an arbitrary skew angle, θ, and we derive its Young's moduli, from which those for HD can also be easily obtained. A small thickness ratio is considered, $t/l < 1/8$, that gives LD a low relative density, ρ^*/ρ_s, which is defined as the ratio of its real density over the density of the solid. For a generic dual-material unit cell, the relative density can be expressed as a function of the volume fractions of the constituents (Supplementary Material Section 2.7.2), and more specifically for a LD (details in Supplementary Material Section 2.7.3) can be written as:

$$\frac{\rho^*}{\rho_s} = \frac{\cos\theta + 2}{\sin\theta}\frac{t}{l} \tag{2-1}$$

Using structural mechanics [31], the in-plane Young's moduli can be derived as (Supplementary Material Section 2.7.3):

$$\frac{E_y^*}{E_{s2}} = \left(\frac{1}{2\sin^3\theta} + \frac{E_{s2}/E_{s1}}{\tan^3\theta}\right)^{-1}\frac{t}{l} \tag{2-2}$$

$$\frac{E_x^*}{E_{s2}} = \frac{E_{s1}/E_{s2}}{\tan\theta}\frac{t}{l} \tag{2-3}$$

where E_{s1} and E_{s2} are the Young's modulus for solid materials 1 and 2, respectively. We note that although Eqs. (2-2) and (2-3) are valid for a defect-free lattice in a fully undeformed state, the thermal deformation and fabrication imperfections, which are less than ±1% of the bar length deviation, will not significantly reduce the elastic moduli (no more than 5% [32]). Even under the largest achievable temperature changes considered in this article ($\Delta T = 50°\mathrm{C}$), the thermal deformation remains small, thereby causing no significant impact on the elastic moduli.

Since the thermal expansion mismatch between the constituent materials cause bar bending, the effective CTE in the *y*-direction can be written (Supplementary Material Section 2.7.3) as:

$$\alpha_y^* = \alpha_{s2} + \left(\frac{\cos\theta}{2} - \frac{1}{8\cos\theta\left(t/l\right)^2}\right)\frac{\alpha_{s1} - \alpha_{s2}}{\sin^2\theta\Big/\left(8\cos^3\theta\left(t/l\right)^2\right) + \cos\theta/2 + \left(E_{s1}/E_{s2}\right)^{-1}} \tag{2-4}$$

Similarly in the *x*-direction, the effective CTE is (Supplementary Material Section 2.7.3):

$$\alpha_x^* = \alpha_{s1} - \frac{\alpha_{s1} - \alpha_{s2}}{\left(\sin^2\theta\left(E_{s1}/E_{s2}\right)\right)\Big/\left(8\cos^3\theta\left(t/l\right)^2\right) + \cos\theta\left(E_{s1}/E_{s2}\right)/2 + 1} \tag{2-5}$$

Eq. (2-4) can be simplified as:

$$\alpha_y^* = \alpha_{s2} + k_{CTE}(\alpha_{s1} - \alpha_{s2}) \tag{2-6}$$

where $k_{CTE} = \left(\cos\theta/2 - \left(8\cos\theta\left(t/l\right)^2\right)^{-1}\right)\left(\sin^2\theta/8\cos^3\theta\left(t/l\right)^2 + \cos\theta/2 + \left(E_{s1}/E_{s2}\right)^{-1}\right)^{-1}$ has always a negative value. The LD and HD cases can be specified by the difference in values of the two solid CTEs. If $\alpha_{s1} > \alpha_{s2}$, α_y^* is less than the lowest CTE of the two solids (i.e. α_{s2}), thus representing LD (Figure 2-1a-I). On the other hand, if $\alpha_{s2} > \alpha_{s1}$, then α_y^* is larger than the highest CTE - in this instance α_{s2} - which corresponds to the HD case (Figure 2-1b-I).

In Eqs. (2-4) and (2-5) above, the effective CTE is also governed by the geometric parameters of the lattice, namely t/l and θ. The stiffness can also be expressed similarly to the CTE, since they are contingent on the same set of geometric parameters (i.e. t/l and θ in the Eqs. (2-2) and (2-3)). From this, it is evident that a change of this set of parameters would make both the CTE and stiffness vary, as further demonstrated in Supplementary Material Section 2.7.1. How to avoid this thermo-elastic coupling is illustrated later in this section, after we first explain below how to enlarge ΔCTE in architectures made of any pair of materials.

The LD and HD unit cells introduced above can be used as building blocks to create multiscale self-repeating lattices (fractal-like HL) with potentially unbounded range of CTE without severe penalty in specific stiffness. This can provide better trade-off between thermal and mechanical performance. This performance is achieved with neither change of their constituent materials nor manipulation of their skew angles. The underlying principle here is that by replacing the solid constituents with unit cells with higher (HD) and lower (LD) CTE values than those of their base materials, we amplify ΔCTE. Figure 2-2a shows a low-CTE example of fractal-like HL with two hierarchical orders, each constructed through the tessellation of LD and HD with prescribed internal angle $\theta = 60°$. The reverse performance case, i.e. higher CTE, can be obtained by a switch of HD and LD positions. Higher orders can be introduced to reduce or enlarge the effective CTE in desired directions with high structural efficiency (E/ρ) originating from the stretch-dominated cell this fractal-like HL is built from.

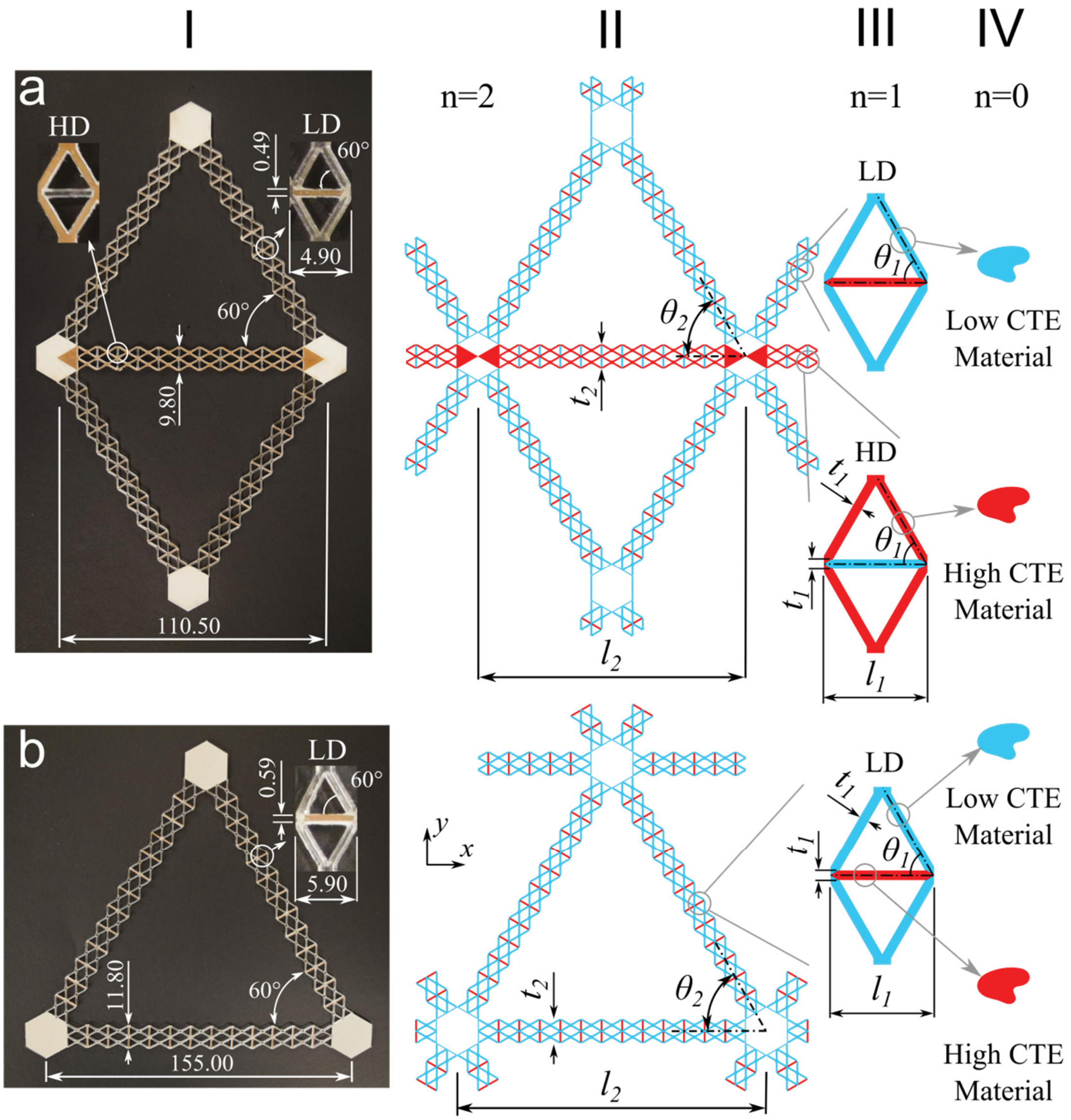

Figure 2-2: Multiscale lattices with second-order hierarchy (n=2). (a-I) Fabricated fractal-like HL with low-CTE, (b-I) hybrid-type HL with low-CTE with specified dimensions denoted in mm. (a-II) and (b-II) geometric models of second-order hierarchy with cell-wall thickness, t_2, and length, l_2. (a-III) and (b-III) first order unit cell models with low- and high-CTE shaped-diamond, i.e. LD and HD, and their respective cell-wall thickness, t_1, and length, l_1. θ_n with $\theta_n \in \left(0, 90^\circ\right)$ is the angle between the inclined cell wall and the *x*-direction. (a-IV) and (b-IV) constituent materials colour-coded to illustrate low and high CTEs. All lattices are planar with prismatic units of identical out-of-plane thickness.

For the analysis, we consider the general case of n^{th} order fractal-like HL of density ρ_n^*, effective Young's modulus E_n^*, and effective CTE α_n^*. The cell walls consist of LD and HD cells of density, ρ_{n-1}^*, effective Young's modulus, E_{n-1}^*, and effective CTE, α_{n-1}^*. The skew angle θ is given and common to all hierarchical orders, whereas the thickness ratios t_i/l_i are different. The relative density for the general case of fractal-like HL with n orders is:

$$\frac{\rho_n^*}{\rho_s} = \left(\frac{\cos\theta + 2}{\sin\theta}\right)^n \left(\frac{t_n}{l_n}\right)\cdots\left(\frac{t_2}{l_2}\right)\left(\frac{t_1}{l_1}\right) = \left(\frac{\cos\theta + 2}{\sin\theta}\right)^n \prod_{i=1}^{n}\left(\frac{t_i}{l_i}\right) \tag{2-7}$$

The Young's modulus of the high- and low-CTE fractal-like HL in the y-direction can be expressed as:

$$\begin{cases} \dfrac{E^*_{l,\mathrm{y},i}}{E^*_{l,\mathrm{y},i-1}} = \left(\dfrac{1}{2\sin^3\theta} + \dfrac{E^*_{l,\mathrm{y},i-1}\big/E^*_{h,\mathrm{y},i-1}}{\tan^3\theta}\right)^{-1}\dfrac{t_i}{l_i} \\ \dfrac{E^*_{h,\mathrm{y},i}}{E^*_{l,\mathrm{y},i-1}} = \left(\dfrac{E^*_{l,\mathrm{y},i-1}\big/E^*_{h,\mathrm{y},i-1}}{2\sin^3\theta} + \dfrac{1}{\tan^3\theta}\right)^{-1}\dfrac{t_i}{l_i} \end{cases} \quad \begin{pmatrix} 1\le i\le n, \\ E^*_{h,\mathrm{y},0} = E_{sh}, \\ E^*_{l,\mathrm{y},0} = E_{sl} \end{pmatrix} \tag{2-8}$$

where h and l represent the high- and low-CTE, respectively, and i represents the hierarchical order, such that $E^*_{l,\mathrm{y},i}$ is the effective Young's modulus of the low-CTE element in the i^{th} order and the y-direction. Their effective CTEs are given by:

$$\begin{cases} \alpha^*_{l,y,\mathrm{i}} = \alpha^*_{l,y,i-1} + \left(\dfrac{\cos\theta}{2} - \dfrac{1}{8\cos\theta\left(t_{i-1}/l_{i-1}\right)^2}\right)\dfrac{\alpha^*_{h,y,i-1} - \alpha^*_{l,y,\mathrm{i}-1}}{\sin^2\theta\left(t_{i-1}/l_{i-1}\right)^{-2}\big/8\cos^3\theta + \cos\theta/2 + E^*_{l,y,i-1}\big/E^*_{h,y,i-1}} \\ \alpha^*_{h,y,\mathrm{i}} = \alpha^*_{h,y,i-1} + \left(\dfrac{\cos\theta}{2} - \dfrac{1}{8\cos\theta\left(t_{i-1}/l_{i-1}\right)^2}\right)\dfrac{\alpha^*_{l,y,i-1} - \alpha^*_{h,y,\mathrm{i}-1}}{\sin^2\theta\left(t_{i-1}/l_{i-1}\right)^{-2}\big/8\cos^3\theta + \cos\theta/2 + E^*_{h,y,i-1}\big/E^*_{l,y,i-1}} \end{cases} \tag{2-9}$$

with $1\le i\le n$, $\alpha^*_{h,y,0} = \alpha_{sh}$, $\alpha^*_{l,y,0} = \alpha_{sl}$, $E^*_{h,y,0} = E_{sh}$, and $E^*_{l,y,0} = E_{sl}$.

The relations above show that fractal-like HL of any hierarchical order possesses anisotropic thermo-elastic properties that are coupled. Isotropic (planar) behaviour can be attained by changing cell shapes among structural order, i.e. by creating hierarchical lattices, with shapes that exhibit isotropy. Below we apply this strategy and consider self-repeating lattices that are shaped at the last order with cell geometry dissimilar than those of the preceding orders, so as to create hybrid-type HL.

Figure 2-2b illustrates an example of hybrid-type HL with two levels of hierarchy. A change in unit cell shape, i.e. a triangle, is implemented at $n = 2$ to show how hierarchy can be effective in not only decoupling but also tuning thermo-elastic properties. As opposed to the fractal-like HL in Figure 2-2a-I, which contains both LD and HD, in Figure 2-2b-I only LD is used at $n = 1$ to create a triangle hierarchical lattice with low-CTE, whereas its high-CTE counterpart can be obtained by swapping the material position. We shape hybrid-type HL at $n = 2$ with a triangle to infer isotropic (planar) mechanical properties and control thermal expansion with LD at $n = 1$. This simple strategy is effective in achieving desired levels of property decoupling which can be readily extended to lattices of higher hierarchical order and beyond CTE and stiffness, such as CTE and strength, CTE and Poisson's ratio, thermal-conductivity and Poisson's ratio, and others.

Let's examine hybrid-type HL with $n = 2$. If the 2nd order consists of LD only (Figure 2-2b-I), then its overall effective CTE, α_2^*, is equal to the CTE of LD in the axial direction (*y*-direction in the current case), which can be simply expressed as $\alpha_2^* = \alpha_{1y}^*$. This shows that α_2^* is not dependent on any changes in geometry at the 2nd order, such that θ_2 and t_2/l_2 have no influence on the effective CTE of the overall hybrid-type HL. However, any geometric changes at the first order, such as the skew angle, will affect not only α_{1y}^* but also the CTE of the overall hybrid-type HL, i.e. α_2^*. With respect to elastic stiffness for hybrid-type HL, the normalized effective Young's modulus E_2^*/E_1^* of the 2nd order, which is mainly a function of unit cell topology, nodal connectivity, cell wall angle, and relative density, ρ_2^*/ρ_1^*, can be expressed through the wall thickness ratio, t_2/l_2 as:

$$\frac{E_2^*}{E_1^*} = k_2 \left(\frac{t_2}{l_2} \right)^q \tag{2-10}$$

k_2 is a function of the cell topology adopted at the 2nd order of hybrid-type HL; q depends on the cell wall deformation mode of the 2nd order - stretching or bending - and can assume values that depend on the scaling condition applied to the cell wall cross-section [33-35]. If E_1^* is given, the stiffness of the 2nd order is merely a function of the geometry at the 2nd order and any geometric change at this order will not influence the overall CTE of hybrid-type HL.

The thermal and mechanical 2D isotropic behaviour of the hybrid-type HL in Figure 2-2b derives from the shape of the unit cell, in this case a triangle. The relevant properties of hybrid-type HL at $n=1$ are given in Eqs. (2-1), (2-2), and (2-4), and the mechanical properties at $n=2$ ($\theta_2 = 60°$) in Eqs. (2-11) and (2-12). Since the CTE of the last order hybrid-type HL, α_2^*, is equivalent to that of the preceding order, in this example the CTE of LD, or HD for the high-CTE case, the thermomechanical properties of hybrid-type HL are given by:

$$\frac{\rho_2^*}{\rho_1^*} = 2\sqrt{3}\frac{t_2}{l_2} \qquad (2\text{-}11) \qquad \frac{E_2^*}{E_{1y}^*} = \frac{2\sqrt{3}}{3}\frac{t_2}{l_2} \qquad (2\text{-}12) \qquad \alpha_2^* = \alpha_{1y}^* \qquad (2\text{-}13)$$

To demonstrate CTE tuning that brings no change in the elastic properties of hybrid-type HL, we seek in its first order a set of pairs for the skew angle θ_1 and t_1/l_1 that can satisfy the condition of constant E_{1y}^*. This can be achieved by rearranging Eq. (2-4) to find the expression of E_{1y}^* that is governed by t_1/l_1 and θ_1, and whose solution provides CTE values at the first order, α_1^*, that change with the skew angle but leave E_{1y}^* unaltered. This strategy preserves the Young's moduli in the second order and allows CTE tuning in the first order. Furthermore, this scheme enables to construct hybrid-type HL with tunable stiffness via changing wall thickness at the second order, t_2/l_2, while keeping the overall CTE α_2^* constant, hence allowing thermo-elastic decoupling.

The explanation given above is of course demonstrative for hybrid-type HL of 2 orders. If $n > 2$ and hybrid-type HL has the triangle at the last (n th) order, the scheme still holds and enables to decouple CTE from elastic stiffness. In this case, the first order to the $(n\text{-}1)$ th order are made of low-CTE fractal-like HL; and the relative density and thermo-elastic properties of the highest order can be expressed using Eqs. (2-11) to (2-13) by simply replacing 2nd order terms with n th order terms and 1st order with $(n\text{-}1)$ th order. The effective properties ρ_{n-1}^*, E_{n-1}^*, and α_{n-1}^* in those general equations can be calculated through Eqs. (2-7), (2-8) and (2-9), respectively.

2.3.2 Experimental validation

Three sets of experimental validation (Figure 2-3 to 5) for the prediction models presented earlier are performed on laser cut prototypes of hierarchical lattices. Given the scheme presented here is material selection free, a representative pair of materials is chosen to fabricate the samples: Teflon® Polytetrafluoroethylene (PTFE, DuPont, USA), and acrylic plastic (Polymethyl Methacrylate (PMMA), Reynolds Polymer, Indonesia) (materials properties in Table 2-1). Nevertheless, the experimental validation here provided can be applied to lattices made of any pair of solids including metals, such as Al6061 and Ti-6Al-4V, and for hierarchical orders above 2. The first set of experiments aims at validating the fractal-like HL model that can predict CTE values and its tunability (Eq. (2-9)), where the low-CTE of a representative lattice is tested in the *y*-direction. The second set is designed to measure CTE tunability for hybrid-type HL with $n = 2$ (Eqs. (2-4) and (2-13)), and the third to demonstrate thermo-elastic properties decoupling (Eqs. (2-4) and (2-13)).

Material	Measured CTE (DIC)	Measured CTE (TMA Q400)	CTE provided by the supplier	Difference (%)	Young's Modulus (GPa)	Density (g/cm^3)
Acrylic (Low CTE component)	67.0 ±0.5	-	69.0	2.9%	3.2	1.2
Teflon® PTFE (High CTE component)	123.0 ±0.9	-	120.0	2.5%	0.475	2.2
Al6061	22.6 ±0.4	23.0	-	1.7%	-	-

Table 2-1: Predicted and experimentally measured CTE values ($\times 10^{-6}/°C$) for solid materials.

Sheets of 1.59 mm thickness of each material were laser cut (TROTEC Laser GmbH, Austria) to build 2nd order fractal-like and hybrid-type HL. Laser cutter was calibrated to provide planar deviations within ±0.05 mm. Bar elements were individually embedded to diamond-shaped cells and epoxy glue (Gel Epoxy Syringe Glue, LePage) was applied to provide adherence between materials. The epoxy glue thickness was about 0.1 mm, 2% of the typical length of a lattice element; the epoxy CTE ($65\times 10^{-6}/°C$) was similar to the CTE of acrylic, thus providing negligible influence on the CTE measurements of HL samples.

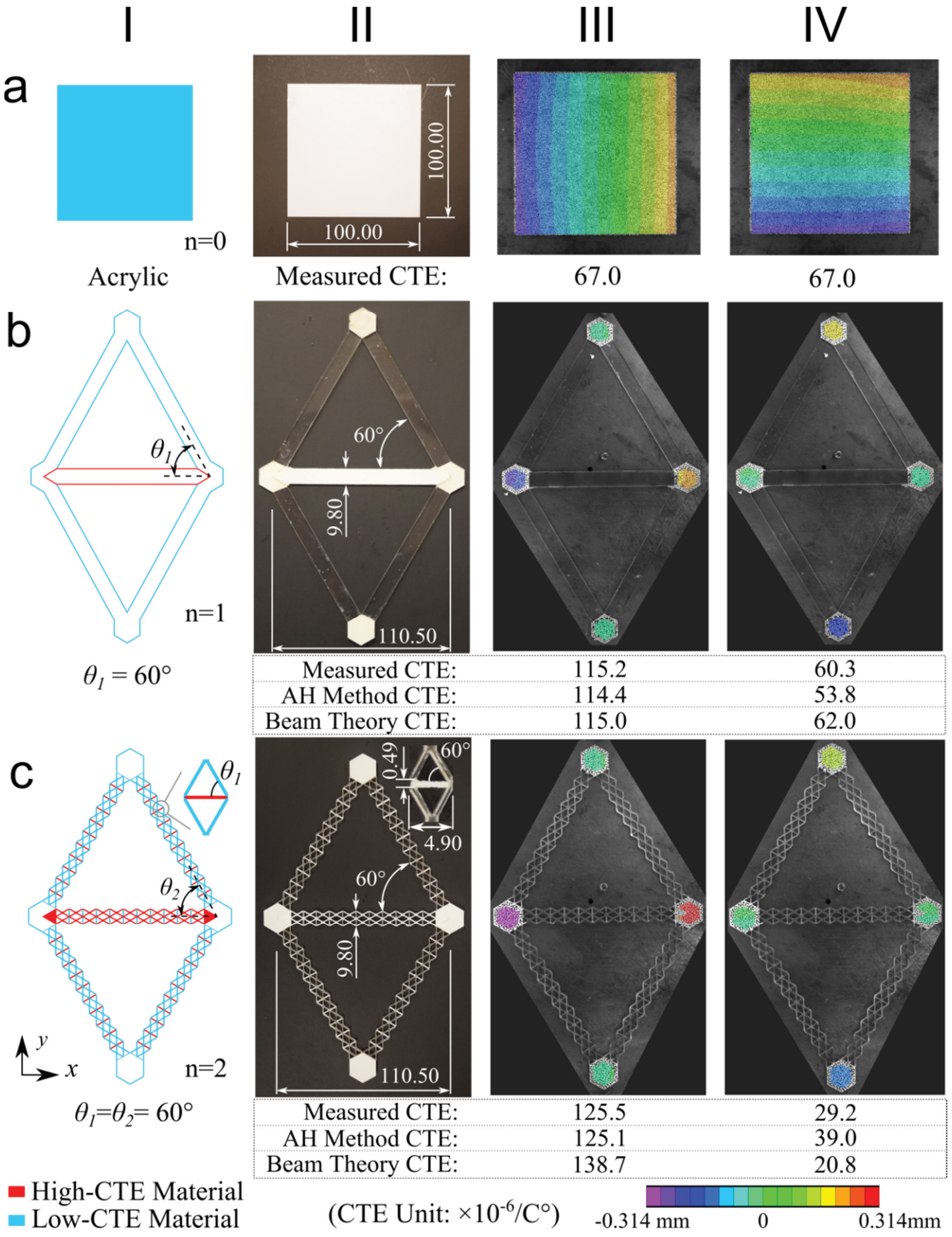

a	III	IV
Measured CTE:	67.0	67.0

b	III	IV
Measured CTE:	115.2	60.3
AH Method CTE:	114.4	53.8
Beam Theory CTE:	115.0	62.0

c	III	IV
Measured CTE:	125.5	29.2
AH Method CTE:	125.1	39.0
Beam Theory CTE:	138.7	20.8

Figure 2-3: Thermal experiment of fractal-like HL with: $n = 0$ (a); $n = 1$ (b); and $n = 2$ (c), and thermal deformation field shown in column (III) for x-direction and column (IV) for y-direction. To perform DIC, black and white speckles were applied randomly and uniformly across the nodes to each hybrid-type and fractal-like HL samples, for thermal displacement measurements.

Columns (I) and (II) illustrate respectively initial configurations for designed and fabricated samples. Obtained CTE values along with theoretical and simulated values are summarized along their corresponding columns. Computational values are obtained via asymptotic homogenization.

A 3D digital image correlation (DIC) set-up with a temperature controlled heating chamber (See Supplementary Material Section 2.7.4 for details) was assembled and used to assess the CTE of each set of HLs. In total, 3 sets of DIC experiments were undertaken for a total of 9 tests, 3 for each set. In the first group (Figure 2-3), DIC was applied to solid bars of acrylic and 2 fractal-like HLs, one with 1 order of hierarchy and the other with $n = 2$. The skew angle ($\theta = 60°$) as well as the wall thickness ratio (about $t/l = 0.1$) of the fractal-like HL were kept identical. The joints were shaped in hexagons to preserve strut connectivity (six) at each node. The second set (Figure 2-4) features DIC results for 2nd order hybrid-type HL samples with varying skew angles (55°, 60° and 65°) and hexagonal nodes of dimensions identical to those of the first set. To prove CTE tunability of hybrid-type HL for constant Young's modulus, E^*_{y1}, the geometry of the three hybrid-type HL samples was kept identical with the exception of their skew angles, θ_1, and wall thickness, t_1, in the first order. The last set of samples in Figure 2-5, second order hybrid-type HL, were built with varying strut thickness to assess the impact of t_2/l_2 on their effective CTE. Here the geometric parameters of all samples were kept identical except the thickness ratio of the second order ($n = 2$) chosen as the only variable. The number of LD along the thickness direction varied from $M = 1$ to $M = 3$ as shown in Figure 2-5a, b, and c. All samples were tested five times through the thermal cycle to ensure test repeatability, and on each occasion the thermal displacement was measured to provide statistical context to the results.

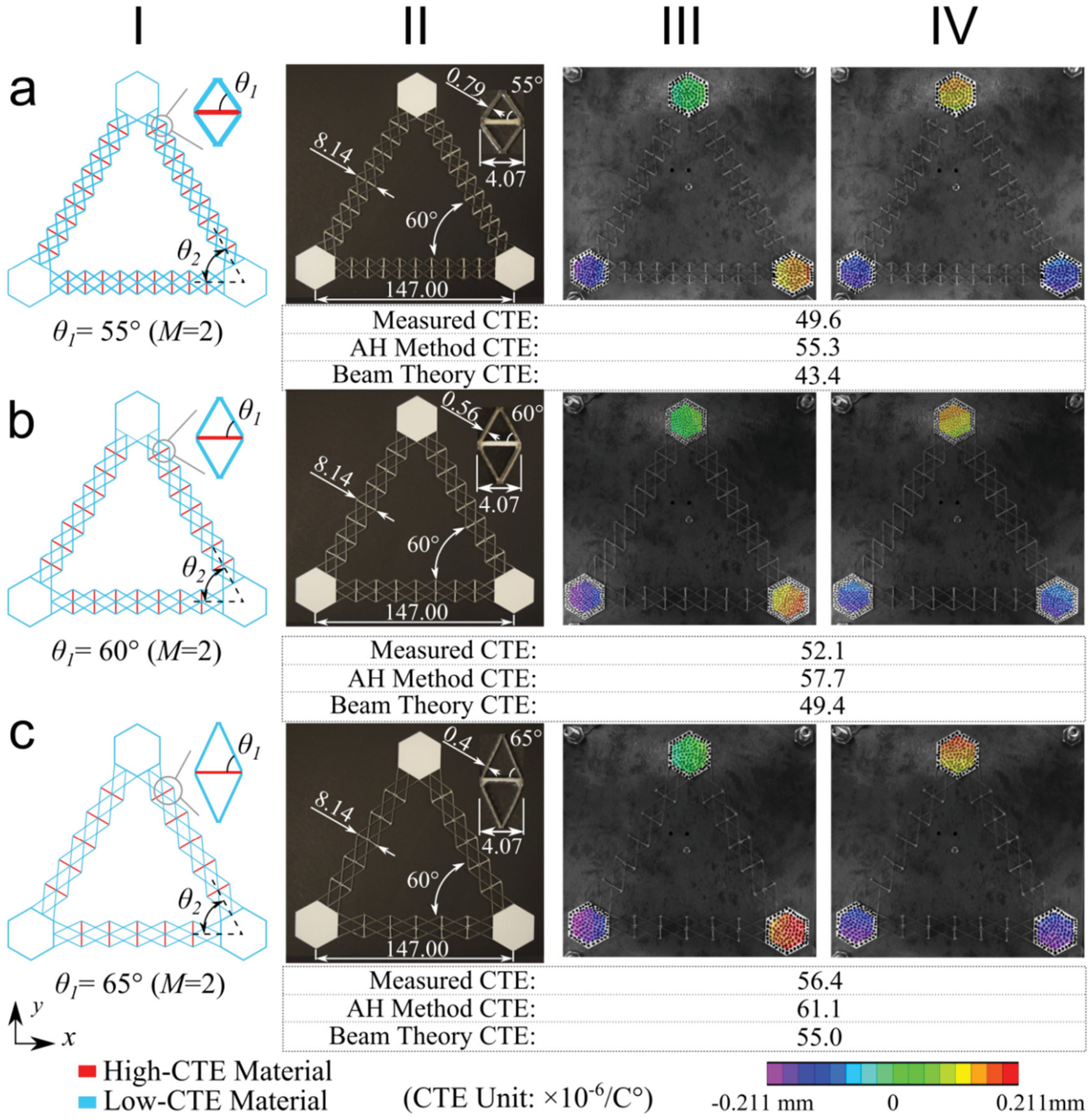

Measured CTE:	49.6
AH Method CTE:	55.3
Beam Theory CTE:	43.4

Measured CTE:	52.1
AH Method CTE:	57.7
Beam Theory CTE:	49.4

Measured CTE:	56.4
AH Method CTE:	61.1
Beam Theory CTE:	55.0

(CTE Unit: ×10^{-6}/C°)

Figure 2-4: Thermal experiment of hybrid-type HL with skew angles of 55° (a), 60° (b), and 65° (c) and thermal deformation field shown in column (III) for *x*-direction and column (IV) for *y*-direction. Columns (I) and (II) illustrate respectively initial configurations for designed and fabricated samples. Obtained CTE values along with theoretical and simulated values are summarized along their corresponding columns. Computational values are obtained via asymptotic homogenization.

Testing temperature was monitored and managed from 25℃ to 75℃ through a PID (proportion-integration-differentiation) controller (CN7800, Omega, US). DIC system calibration ensured an epipolar projection error below 0.01 pixels, i.e. the average error between the position where a target point was found in the image and the theoretical position where the mathematical calibration model located the point. A CCD (charge coupled device) camera (PointGrey, Canada) was used to focus on an area of $240 \times 200\ \mathrm{mm}^2$ with a resolution of 2448×2048 pixels; based on the image resolution, any deformation smaller than 0.98 μm (0.01 pixels) was merged by the epipolar projection error. Finally the accuracy of the whole testing system was verified with measures taken from a commercial thermomechanical analyzer, TMA Q400 (TA Instr., US).

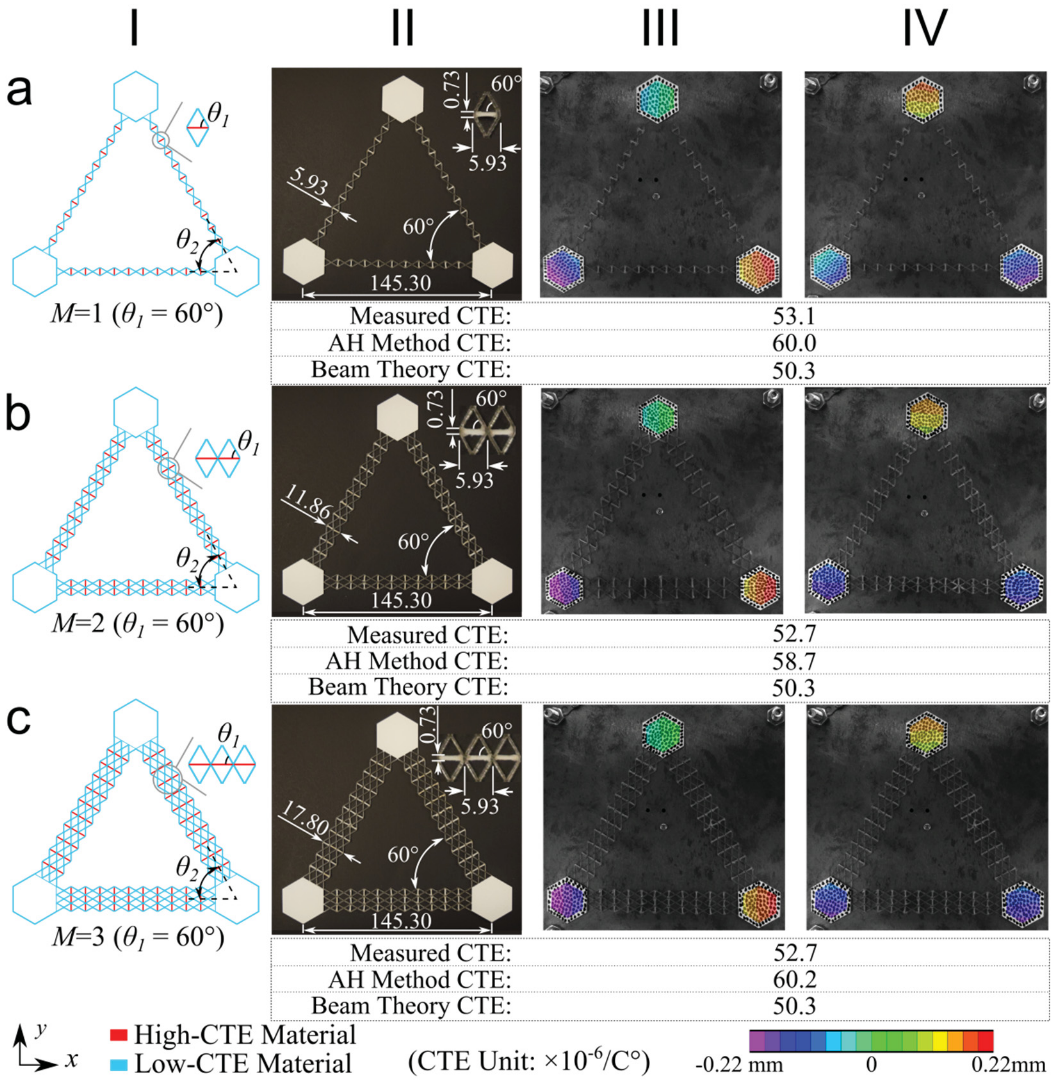

Measured CTE:	53.1
AH Method CTE:	60.0
Beam Theory CTE:	50.3

Measured CTE:	52.7
AH Method CTE:	58.7
Beam Theory CTE:	50.3

Measured CTE:	52.7
AH Method CTE:	60.2
Beam Theory CTE:	50.3

Figure 2-5: Thermal experiment of hybrid-type HL with wall layers of $M = 1$ (a); $M = 2$ (b); and $M = 3$ (c) and thermal deformation field shown in column (III) for *x*-direction and column (IV) for *y*-direction. Columns (I) and (II) illustrate respectively initial configurations for designed and fabricated samples. Obtained CTE values along with theoretical and simulated

values are summarized along their corresponding columns. Computational values are obtained via asymptotic homogenization.

2.4 Results

2.4.1 System calibration

The testing system was calibrated on three solid materials, Al6061, acrylic and PTFE. Table 2-1 shows a comparison of their measured and predicted mean CTE along with their standard deviations, with errors below 3%. The epipolar projection error is at 0.98 μm, which governs the smallest measured CTE value of the samples, i.e. 0.27×10^{-6}/°C. The low magnitude of these errors warrants the required accuracy for the DIC system used in this work.

2.4.2 Testing results

Figure 2-3a-III and IV show thermal deformation maps for the solid material, acrylic, in both *x*- and *y*-directions, respectively. The tested CTE is observed isotropically in all directions in the 2D plane. While their thermal deformation is shown in Figure 2-3 to Figure 2-5-III and -IV in both *x*- and *y*-directions, mean CTE from testing are summarized in Table 2-2, along with their standard deviation and CTE predictions. The error associated with testing results only go as high as 5%, and the difference between tests and the computational values obtained via asymptotic homogenization (AH) (see Supplementary Material Section 2.7.5) are generally within 10% error, with the exception of fractal-like HL ($n=2$) sample, where the amplified low-CTE behaviour also amplifies the deviation between both results.

Figure 2-3b-IV illustrates that LD (Figure 2-3b-I, $n=1$ with $\theta=60°$) without structural hierarchy can reduce the CTE along the *y*-direction from 67.0×10^{-6}/°C ($n=0$, i.e. the component material, acrylic, as shown in Figure 2-3a-I) to 60.3×10^{-6}/°C. However, for increasing hierarchical order, fractal-like HL (Figure 2-3c-I, $n=2$) can further reduce the effective CTE in the *y*-direction to 29.2×10^{-6}/°C, result obtained with no change in material selection nor skew angle. By adding hierarchical orders from $n=1$ to $n=2$, fractal-like HL shows a CTE tunability up to 31.1×10^{-6}/°C. Figure 2-4-III and IV show for hybrid-type HL the decrease of the effective CTE from 56.4×10^{-6}/°C ($\theta_1=65°$) to 49.6×10^{-6}/°C ($\theta_1=55°$), which emphasizes a much smaller CTE tunability (6.8×10^{-6}/°C) in comparison with adding hierarchical orders (31.1×10^{-6}/°C). The combination of varying skew angles and adding hierarchical orders appears to be proficient in tuning the effective CTE. For the last set of specimens, however, the effective stiffness relative to an hybrid-type HL with $M = 1$ is expected to double for $M = 2$ and triple for $M = 3$; the overall effective CTE displays a tendency of remaining constant around 53×10^{-6}/°C. These results experimentally show that thermo-elastic properties can be decoupled in hybrid-type HL, as explained in more detail in the following section.

Sample	Predicted CTE (Beam Theory, $\times10^{-6}$/°C)		Measured CTE ($\times10^{-6}$/°C)		Error	
	x	y	x $\pm \sigma_x$	y $\pm \sigma_y$	x	y
Fractal-like HL (n=1)	115.0	62.0	115.2±0.3	60.3 ±2.4	0.2%	2.8%
Fractal-like HL (n=2)	138.7	20.8	125.5±1.3	29.2 ±0.9	10.5%	28.8%
Hybrid-type HL (55°, M=2)	43.4		49.6 ±1.3		12.5%	
Hybrid-type HL (60°, M=2)	49.4		52.1 ±0.6		5.2%	
Hybrid-type HL (65°, M=2)	55.0		56.4 ±2.9		2.5%	
Hybrid-type HL (60°, M=1)	50.3		53.1 ±1.3		5.3%	
Hybrid-type HL (60°, M=2)	50.3		52.7 ±1.6		4.2%	
Hybrid-type HL (60°, M=3)	50.3		52.7 ±1.6		4.2%	

Table 2-2: Predicted and experimentally measured CTE values for fractal-like and hybrid-type HL (σ_x and σ_y indicate standard deviation).

2.4.3 Model predictions

Figure 2-6a illustrates the CTE values for low- and high-CTE fractal-like HL in the *y*-direction as a function of hierarchical order. Each of the plotted lines, obtained from Eq. (2-9), represents CTE values for a given skew angle, θ, and starts from $n = 0$, solid materials, through $n = 1$, the HD and LD, followed by fractal-like HLs with increasing hierarchical order $n \geq 2$. We recall that these predictions represent discrete values of CTE, each obtained for a given *n*, although the trends are shown as continuous to ease their interpretation within each figure. Assuming the CTE of PTFE and acrylic as the high and low CTE values, respectively, we observe that as the order increases from 0 to 1, the effective CTE of HD is higher than that of PTFE, whereas the CTE of the LD is lower than that of acrylic. The gap between these two CTE spectra, i.e. LD and HD, taking $\theta = 60°$ as an example, enlarges from 56×10^{-6}/°C (initial gap between solid materials) to 93×10^{-6}/°C, meaning an increase of 165% in ΔCTE. As the order changes from 1 to 2, the gap increases even more drastically to 154.7×10^{-6}/°C (275% of the initial gap) and larger once more from order 2 to 3, reaching 257.3×10^{-6}/°C (460% of the initial gap). CTE tunability (ΔCTE) increases with the order of hierarchy, so as to theoretically approach an unbounded value for unlimited n.

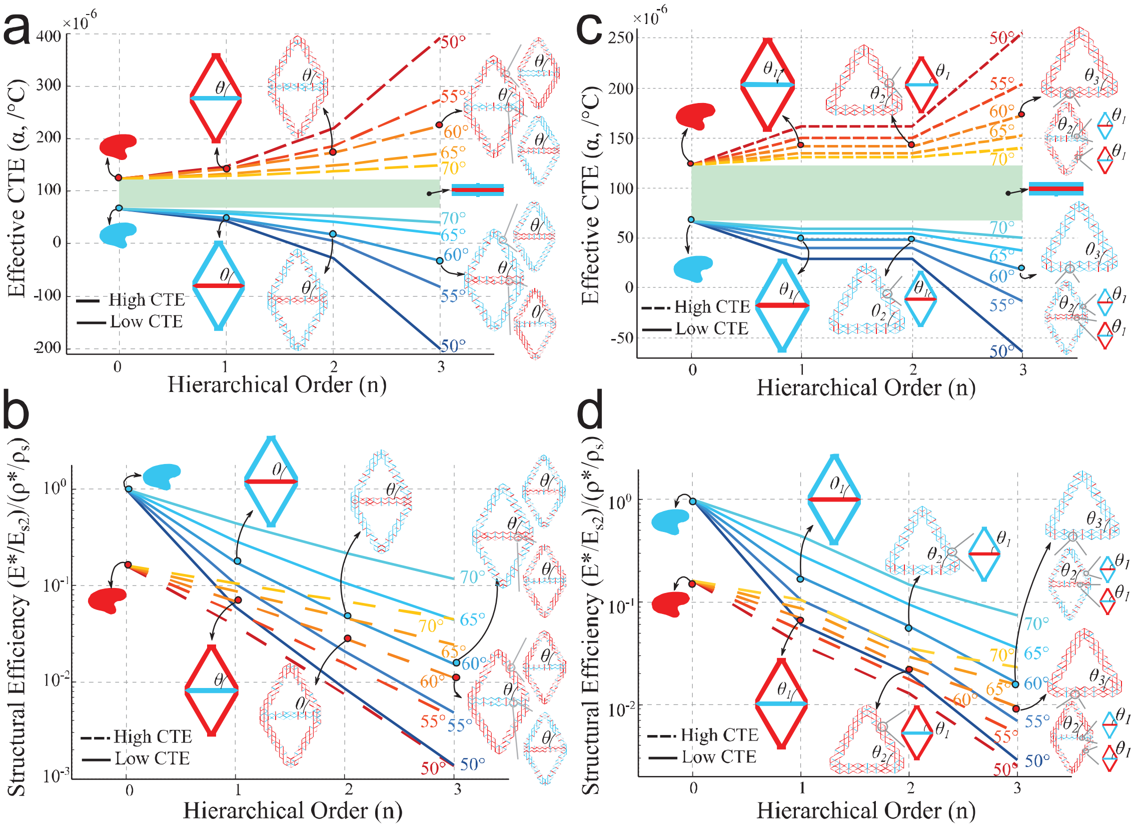

Figure 2-6: CTE (a) and structural efficiency (b) of fractal-like HL in the *y*-direction as a function of n, the number of hierarchical order; CTE (c) and structural efficiency (d) of hybrid-type HL in the *y*-direction, respectively, with respect to n. Lines of given skew angle are visualized for hybrid-type HL and fractal-like HL, and shaded regions (green) in (a) and (c) are depicted to represent by-layer laminates of solid materials ($\theta = 0$). CTE trends shown as continuous connect discrete values calculated via the models presented in Section 2.3.

We also note the shaded region in Figure 2-6a, where the lattice collapses to a by-layer laminate. This concept can cover CTE values between the CTEs of the constituent solids by changing their layer thickness ratio. Furthermore, Figure 2-6b illustrates structural efficiency – a metric expressed here as the ratio of the specific stiffness of the lattice to that of the solid materials – in the y-direction of low- and high-CTE fractal-like HL versus hierarchical order. For normalization purposes, solid acrylic (blue in figure) is considered as benchmark with 100% structural efficiency. With the increase of hierarchical order, the structural efficiency of fractal-like HL decreases. This is expected as stretch dominated lattices become more compliant with higher order of hierarchy, but nevertheless this drop is less than that of bend dominated lattices [29]. Another insight that we gain from Figure 2-6a and b is that the thermo-elastic properties of fractal-like HL are coupled, and CTE changes as structural efficiency does. How to avoid this coupling is shown below where results obtained from models described in Section 2.3 are presented.

Figure 2-6c, d show the predicted CTE and structural efficiency for hybrid-type HL as a function of the hierarchical order and the skew angle, θ_1, in the range $50° - 70°$, which is representatively chosen here to visualize the effect of varying skewness. In Figure 2-6c, the first order ($n = 1$) allows some degree of CTE tailoring with a gap increase between the low and high CTE spectra from 56×10^{-6}/°C to 93×10^{-6}/°C. With the addition of the second order ($n = 2$), this time hybrid-type HL, as opposed to fractal-like HL, allows stiffness modulation without thermal expansion variation. Hence CTE remains insensitive, i.e. ΔCTE between the first two orders is constant, despite a drop of structural efficiency.

The trends shown in Figure 2-6c and d between $n = 1$ and $n = 2$ are now used as example to show how hybrid-type HL can be effective in decoupling thermal and mechanical properties. To do so, we first show that CTE and Young's modulus for LD are inherently coupled and hence no independent tuning is possible. This is shown in Figure 2-7a, b where Eqs. (2-1) to (2-5) are plotted in dash style along with results obtained from AH (continuous style), here included to provide a further element of validation to the analytic models presented therein. Figure 2-7a shows that for prescribed t_1/l_1, a reduction of the skew angle brings a decrease of both the CTE and Young's modulus in the y-direction. On the other hand, if the skew angle is given and t_1/l_1

varies (Figure 2-7b), both the CTE and Young's modulus in the *y*-direction show a monotonic increase for rising relative density. Hence Figure 2-7a, b visualise the thermo-elastic coupling that exists in diamond lattices. In the next step, we show separate property tuning through hybrid-type HL. Figure 2-7c, d show results for CTE and Young's modulus obtained from Eqs. (2-12) and (2-13) for hybrid-type HL of two orders (Figure 2-2b-I). Also in this case, results from closed-form expressions are reported along with those obtained computationally via AH. Figure 2-7c shows that a changed θ_1 in the first order of hybrid-type HL enables CTE tuning for both orders, while causing no impact in the Young's modulus, as shown by its unchanging trend. Likewise in the mechanical spectrum, Figure 2-7d shows that the effective Young's modulus can be varied with relative density with no effect on the CTE. It is the thickness ratio of the second order, t_2/l_2, that, in this case, is the variable empowering the Young's modulus modulation for inviolate values of CTE. Figure 2-7, thus, gives a visual summary of model predictions validated through experiments for thermo-elastic coupling, which appears to have been bypassed with hybrid-type HL.

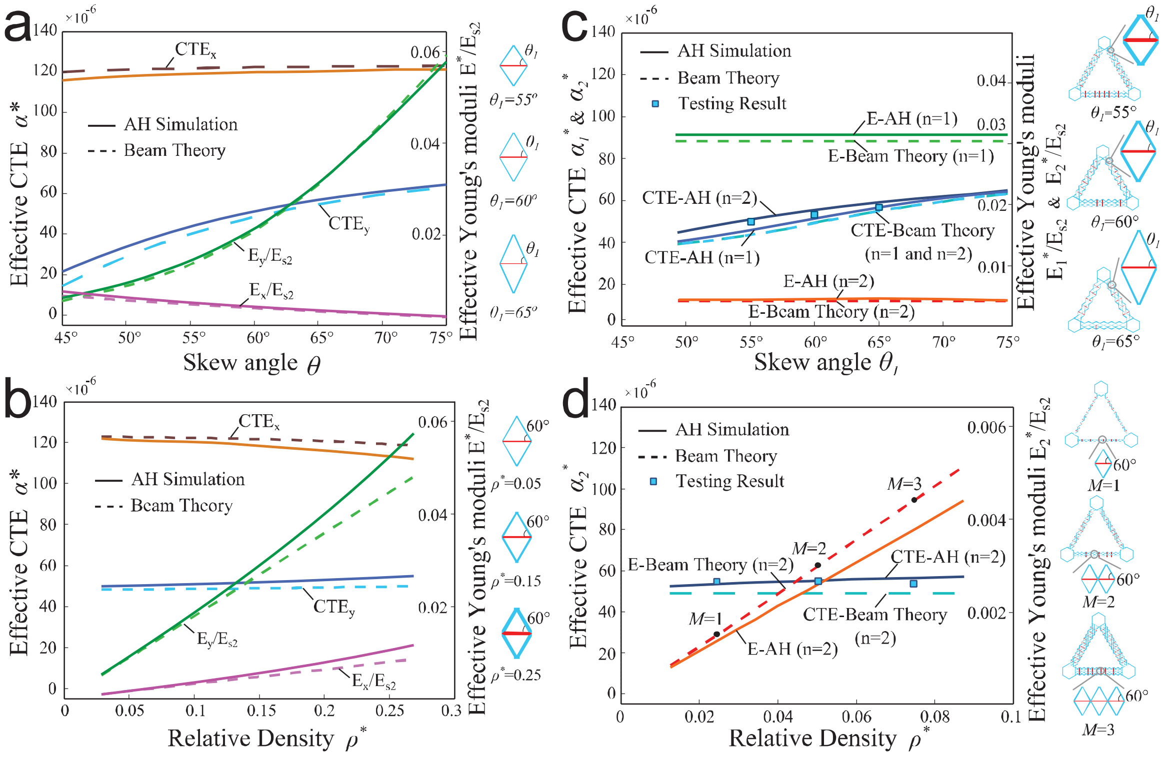

Figure 2-7: Visualization of properties coupling and decoupling for LD unit and hierarchical lattices. A change in skew angle (a) and relative density (b) in LD affects both thermal (a_x^* and

a_y^*) and elastic properties (E_x^*/E_{s2}^* and E_y^*/E_{s2}^*). On the other hand for hybrid-type HL (c and d), a_1^* and a_2^* of the first and the second order, as well as their effective Young's modulus, are tuned to preserve constant either the Young's modulus (E_{1y}^*) in (c) or the CTE (α_2^*) in (d). This is achieved in (c) through changing both the skew angle of the first order, θ_1, and t_1/l_1, and in (d) by keeping these parameters constant and varying the relative density of the second order, ρ_2^*/ρ_s^*.

2.5 Discussion

This chapter proposes to use LD and HD as building blocks of fractal-like and hybrid-type HL with the goal of attaining a CTE range that can be theoretically unbound, and if desired this boost can be obtained with no penalty in elastic stiffness. Experimental results with specifics illustrated in Figure 2-3, 2-4, 2-5, are reported in Figure 2-7c and d and provide validation to the trends obtained via closed-form expressions presented in Section 2.3 and numerically via AH. Thermo-elastic properties of fractal-like HL in Figure 2-6 demonstrate that the addition of only one order of hierarchy enlarges the CTE tunability by 66%, which is up to five times higher than what can be obtained through a change in skew angle. On the other hand, hybrid-type HL allows an increase in structural efficiency equal to 0.0585 of 20.6% (Figure 2-6 at $n = 2$) with respect to that of fractal-like HL (0.0485) at the identical order. Validated models of hybrid-type HL suggest that concepts with higher orders can offer much larger CTE tunability than stretch-dominated lattice benchmarks [18] and superior mechanical performance than baseline concepts that are bend-dominated [26], in addition to their decoupled, planar isotropic thermo-elastic properties.

To compare the thermo-elastic performance of fractal-like and hybrid-type HL ($n \le 5$) with the existing ones, in particular L-Concept [26] and S-Concept [18], we plot in Figure 2-8a bars of their specific stiffness, a measure of structural efficiency, and of ΔCTE, the CTE tunability defined as the maximum range of CTE values a concept can offer. The magnitude of a given performance metric is represented by the bar height. All concepts are compared on an equal basis, as they are generated from the same pair of materials (PTFE and acrylic). With respect to the (orange) bars of CTE tunability in Figure 2-8a, ΔCTE is calculated for each concept and for a given value of Young's modulus, which is representatively considered here as 1 MPa. From the bar rises, we gather that fractal-like HL dominates with the largest CTE range (534×10^{-6}/°C), whereas ΔCTE for the S-Concept is the smallest (169×10^{-6}/°C). ΔCTE for hybrid-type HL (331.1×10^{-6}/°C) is as high as that of L-Concept (332.6×10^{-6}/°C), which is claimed to provide unbounded ΔCTE. This is quite unique, as the L-Concept relies on bend-dominated cells, whereas the proposed hybrid-type HL can obtain a similar result using a much stiffer structure. Similarly with respect to structural efficiency (green bars), Figure 2-8a provides a visual comparison of the specific stiffness of each concept for a representative CTE value that is here assumed as half the average of the materials' CTE (47.5×10^{-6}/°C). From the bars, we observe that fractal-like HL has the highest specific stiffness in the *y*-direction (349.2 KPa×m^3/Kg) followed by hybrid-type HL (116.5 KPa×m^3/Kg), both of which outperform the existing concepts. More specifically, focusing on planar isotropic materials, hybrid-type HL provides a 42% increase in structural efficiency compared to the stiff, yet dense, S-Concept (82 KPa×m^3/Kg), while demonstrating twice the specific stiffness of the L-Concept (51.7 KPa×m^3/Kg).

A more comprehensive comparison of the concepts is illustrated in Figure 2-8b, where CTE tunability is plotted versus specific stiffness. The curves are created from a parametric study of the unit cells, where the skewness angle and the thickness-to-length ratio are the active variables for given materials. hybrid-type and fractal-like HL are compared with L-Concept and S-Concept, the benchmarks. While both high- and low-CTE cases (Figure 2-6) can be plotted, Figure 2-8b displays only the low-CTE concepts which are sufficient to capture the potential of hierarchical lattices. We recall that, in this low-CTE case, ΔCTE is defined by the range between the lowest CTE value of a given low-CTE concept, at the calculated structural efficiency, and the CTE of the solid material with lower thermal expansion (i.e. 67×10^{-6}/°C of acrylic).

While S- and L-Concepts show curves that describe the change of ΔCTE with structural efficiency, hybrid-type and fractal-like HL are represented by two domains (blue for hybrid-type HL and green for fractal-like HL). These shaded regions represent the possible set of curves that are obtained with varying hierarchical orders. For both cases, the first hierarchical order that makes up the concept ($n=1$ for fractal-like HL and $n=2$ for hybrid-type HL) provides the most optimal curve (closest to the top-right corner). The following hierarchical orders (the second for fractal-like HL, and the third for hybrid-type HL) provide the least optimal curve, while higher orders lie in between. Higher hierarchical orders are predicted to approach the curve of the first order ($n=1$ for fractal-like HL and $n=2$ for hybrid-type HL) with increasing n .

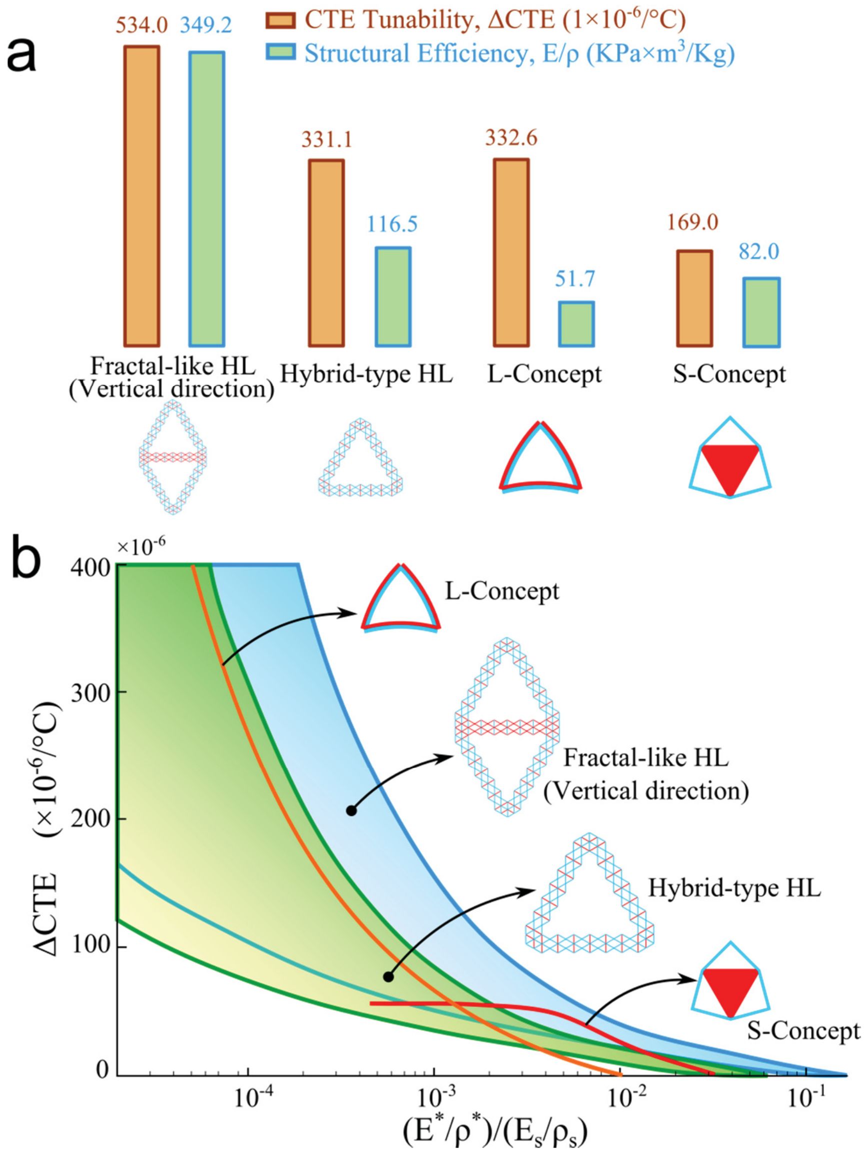

Figure 2-8: (a) Comparison of proposed and existing bi-material concepts on the basis of (i) CTE tunability ($\Delta CTE =$ Max CTE – Min CTE) for prescribed stiffness of 1 MPa, visualized as orange bars, and (ii) specific stiffness (Young's modulus / Density: E/ρ) for given CTE (47.5× 10^{-6}/°C), in green. (b) CTE tunability plotted versus structural efficiency of existing concepts along with hybrid-type and fractal-like HL for increasing hierarchical order ($n=1, 2, \ldots$). Results

are obtained from a parametric study of unit cell geometry, where the list of possible sets of properties for each concept are sorted by increasing structural efficiency, and then grouped based on a range of similar values of E/ρ. The minimum CTE value is selected from each group to calculate ΔCTE for a given E/ρ. This value, the median structural efficiency of each group, is plotted as a point on the graph with the corresponding ΔCTE value on the ordinate axis.

In general, Figure 2-8b shows a Pareto-front for the existing concepts, thus showing trade-offs between metrics: an attempt of increasing structural efficiency results in a reduced ΔCTE. This trade-off is not only influenced by the relation between geometric parameters and effective properties, but also by the design requirements. For example, the L-Concept is the ideal candidate to attain large CTE tunability, whereas the S-Concept is ideal for structural efficiency, as both are designed for different specifications. When considering the concepts presented in this chapter, a better overall performance can be observed compared to the existing baselines. The curves derived from both fractal-like and hybrid-type HL are offsets of the L- and S-Concept toward the top right corner on the figure, where both high CTE tunability and high structural efficiency are achieved; hence their domains show higher potential of hierarchical lattices to attain better trade-offs between ΔCTE and E/ρ.

While the work here presented show promises for planar lattices, the strategy can be applied also to 3D hierarchical concepts. Nevertheless, their potential should always be confronted with the capabilities of current practices. For example, while the concepts are scale independent and material selection free, increasing the order of structural hierarchy has to account for the limits that a given manufacturing process poses [6]. The fabrication of hierarchical structures can be highly time consuming, and to the best of authors' knowledge, only structures with up to three orders of hierarchy have been physically realized, even recently, such as multi-material shape memory structures (two orders) [36] and multiscale metallic metamaterials which feature three orders of hierarchy [6]. Given the fast development of multiple material additive manufacturing [37, 38], we can infer that higher level of hierarchy in dual material lattices might be achieved in the near future. In addition, while thermal expansion and stiffness have been here investigated, other structural properties, such as yield strength and toughness, might not perform equally well in practice as adding hierarchy alone reduces strength further due to high stress concentrations that stem at the joints of dissimilar materials [30].

2.6 Conclusion

In this chapter, stretch-dominated bi-material unit cells with low- and high-CTE have been proposed as diamond shaped building blocks of hierarchical lattices with the goal of improving CTE tunability and structural performance, as well as allowing separate tuning of their thermo-elastic properties. Through simulations, derived closed-form expressions and experiments on fabricated proof-of-concepts, we have shown that hybrid-type HL architecture including those made of self-repeating unit cells, i.e. fractal-like HL, can be tailored to concurrently provide high specific stiffness and theoretically unbounded CTE tunability with CTE values ranging from large positive, zero to large negative. The hallmark of fractal-like and hybrid-type HL is that they can reduce the penalty that an increase in ΔCTE will generate on the elastic properties, so as to obtain the best compromise out of them. In addition, their stretch-dominated behaviour provides higher specific stiffness than existing concepts that are bend-dominated. Another benefit of hybrid-type HL is that they can be exploited to decouple initially coupled thermo-elastic properties so as to provide the individual property tailoring that current concepts have not been proven to attain yet. The strategy presented in this work can pave the way to the multifunctional design of bi-material hierarchical lattices with properties that can be independently tuned and exploited to the most of their potential. It can thus be extended to potentially address other conflicting properties to finally generate trade-off solutions for multifunctional applications, including thermal expansion control, MEMS, biomedical sensors and space optical systems.

2.7 Supplementary material

2.7.1 Architected material baselines

Two benchmarks from the field of controllable thermal expansion are here considered from Lakes' [26] and Steeves' [18]. As shown in Figure 2-9, Lakes' concept is a curved bilayer beam with distinct solid materials of dissimilar coefficients of thermal expansion (CTE) such that the overall CTE of the structure can be tailored by changing the curvature of the beam. The curvature of the beam is defined by the angle of the arc, or included angle (θ_L). On the other hand, Steeves' concept, is constructed by a bi-material low-CTE triangle that can be tuned by altering the skew angle, θ_S. Lakes relies on a bending dominated topology to achieve a quite large range of CTE values, while Steeves' concept is stretching dominated and can attain a smaller range of low-CTE values. The thermo-elastic properties of both concepts are mainly dependent on two geometric parameters: the wall-thickness ratio and the angles defining the curvature or skewness of the cell geometry. Figure 2-9 illustrates the effects of varying one of these variables, while keeping the other constant, on the effective CTE and Young's modulus of each topology. Steeves' stretch dominated concept (solid line), in Figure 2-9, demonstrates significantly higher Young's Modulus compared to Lakes' bilayer beam (dashed line) at every point. However, Steeves' design cannot attain a wide range of CTE values as that observed in Lakes' design. Finally, it is evident that changing each variable results in a pronounced modification to both the CTE and Young's Modulus of both structures. Therefore, the thermo-elastic properties are coupled and neither of them can be tailored independently.

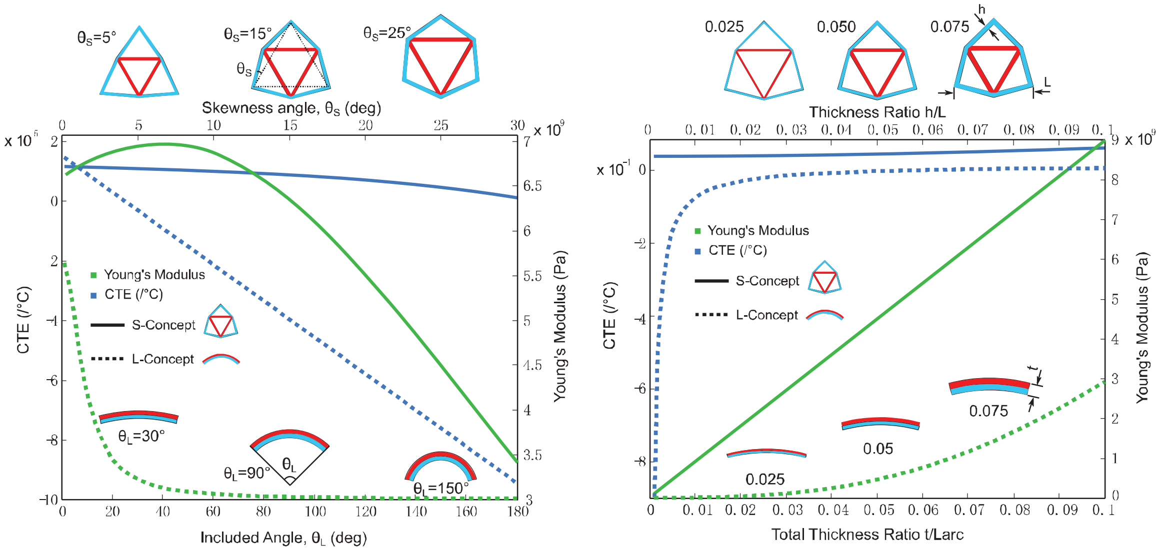

Figure 2-9: Lakes' and Steeves' low-CTE concepts with structural hierarchy. [18, 26]

Figure 2-10 presents the effect of the CTE ratio between the two constituents, α_1/α_2, on the CTE tunability (ΔCTE) of the two benchmarks considered in our work. On one hand, each concept offers its own ΔCTEs for a given pair of materials. As shown in Figure 2-10, when the structural efficiency is higher than 0.002 (line AB in Figure 2-10), the S-concept offers a larger

ΔCTE than the L-concept. However, when the structural efficiency is lower than 0.002, the L-concept has a larger (up to an unbounded) CTE tunability than the S-concept. Difference in CTE tunability depends on cell topology, whether the building block is bend- or stretch-dominated. On the other hand, for a given concept, especially those with limited CTE tunability, each α_1/α_2 offers its own ΔCTE s. This is demonstrated in Figure 2-10 below, where as we change α_1/α_2 from 2 to 10, the ΔCTE of the S-concept increases. Similar reasoning applied for the L-concept. From this figure we gather that for a given concept to achieve a specified ΔCTE and structural efficiency, there is a limitation on the α_1/α_2 , i.e. a limit on the difference in expansion of the material constituents. Hence, having a large ΔCTE indicates ample freedom to tune the unit cell geometry, which is an advantage that can release the dependence on the CTE ratio of the material constituents.

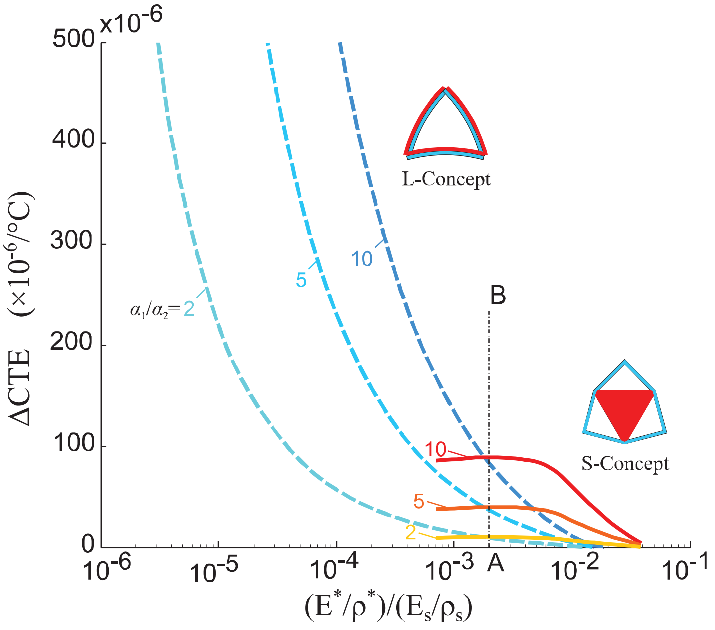

Figure 2-10: Thermal and mechanical performance of Lakes' and Steeves' low-CTE concepts with different CTE ratio (α_1/α_2) of the constituent materials. [18, 26]

2.7.2 Definition of relative density, fractal, and hierarchical lattice

Definition of Relative Density:

The unit cell volume can be defined as:

$$V_{unit\ cell} = V_{void} + V_{mat1} + V_{mat2} \tag{2-14}$$

where $V_{unit\ cell}$ is the volume occupied by the unit cell, in particular by its envelope defined by the unit cell size. V_{mat1} and V_{mat2} are the volumes occupied by the first and the second kind of constituent materials separately.

$$Ro = \frac{V_{mat1} + V_{mat2}}{V_{unit\ cell}} \tag{2-15}$$

$$V_{f1} = \frac{V_{mat1}}{V_{mat1} + V_{mat2}} \tag{2-16}$$

$$V_{f2} = \frac{V_{mat2}}{V_{mat1} + V_{mat2}} \tag{2-17}$$

where: Ro is the volume fraction of the unit cell, in particular the volume of the solids normalized by the volume occupied by the unit cell. V_{f1} and V_{f2} are the volume fraction of material 1 and material 2 separately with respect to the sum of the volumes of the two constituent solids. The relative density can be defined as following:

$$\rho_{relative} = \frac{\rho_{lattice\ unit\ cell}}{\rho_{solid\ composite}} \tag{2-18}$$

where $\rho_{relative}$ is the relative density of a bi-material lattice unit cell. $\rho_{lattice\ unit\ cell}$ is the density of the bi-material lattice unit cell (the ratio of the mass of the lattice material to the unit cell volume ($V_{unit\ cell}$)). $\rho_{solid\ composite}$ is the combined density of the bi-material solids based on their volume fractions without considering the volume of the voids in the bi-material lattice. If we also define the density of the solid material ρ_{mat1} (the density of the solid constituent material 1) and ρ_{mat2} (the density of the solid constituent material 2), we can derive:

$$\rho_{lattice\ unit\ cell} = \frac{\left(V_{mat1} \times \rho_{mat1}\right) + \left(V_{mat2} \times \rho_{mat2}\right)}{V_{unit\ cell}} \tag{2-19}$$

$$\rho_{solid\ composite} = \frac{\left(V_{unit\ cell} \times V_{f1} \times \rho_{mat1}\right) + \left(V_{unit\ cell} \times V_{f2} \times \rho_{mat2}\right)}{V_{unit\ cell}} \tag{2-20}$$

$$Ro \times V_{f1} = \frac{V_{mat1} + V_{mat2}}{V_{unit\ cell}} \times \frac{V_{mat1}}{V_{mat1} + V_{mat2}} = \frac{V_{mat1}}{V_{unit\ cell}} \tag{2-21}$$

We find:

$$V_{unit\ cell} \times V_{f1} = \frac{V_{mat1}}{Ro} \tag{2-22}$$

Similarly:

$$V_{unit\ cell} \times V_{f2} = \frac{V_{mat2}}{Ro} \tag{2-23}$$

By substituting Eqs. (2-22) and (2-23) into Eq. (2-20):

$$\begin{aligned} \rho_{solid\ composite} &= \frac{V_{mat1}/Ro \times \rho_{mat1} + V_{mat2}/Ro \times \rho_{mat2}}{V_{unit\ cell}} \\ &= \frac{1}{Ro} \times \frac{V_{mat1} \times \rho_{mat1} + V_{mat2} \times \rho_{mat2}}{V_{unit\ cell}} = \frac{1}{Ro}\rho_{lattice\ unit\ cell} \end{aligned} \tag{2-24}$$

Thus the relative density of a bi-material lattice is:

$$\rho_{relative} = \frac{\rho_{lattice\ unit\ cell}}{\rho_{solid\ composite}} = Ro \tag{2-25}$$

Eq. (2-25) shows that the relative density of a bi-material periodic lattice can be represented by the volume fraction, as defined Eq. (2-15).

2.7.3 Thermo-elastic properties of dual-material diamond-shaped lattice

Figure 2-11a shows a unit cell of a dual-material diamond shape with all cell walls at a constant thickness, t, and the width of each cell is l. We now evaluate the moduli for a general honeycomb at an arbitrary skew angle, θ, with depth (into the page) of c. We assume that the honeycomb has a low relative density, ρ^*/ρ_s , so that t/l is small (e.g. $t/l < 0.1$); simple geometry gives the relation between the two as:

$$\frac{\rho^*}{\rho_s} = \frac{\cos\theta + 2}{\sin\theta}\frac{t}{l} \tag{2-26}$$

We also assume that deformations are sufficiently small such that changes in the geometry can be neglected. Using standard method of stress analysis [31], consider the equilibrium of an elemental cuboid cut of a diamond-celled honeycomb as outlined in the dashed region of Figure 2-11. The honeycomb is subject to the applied stresses, σ_x and σ_y , which are in-plane and tensile. The tension distributions that exist in the cell walls are shown as T_1 and T_2 . It is necessary to consider two separate in-plane loading cases as they give rise to two different tension distributions within the cell wall.

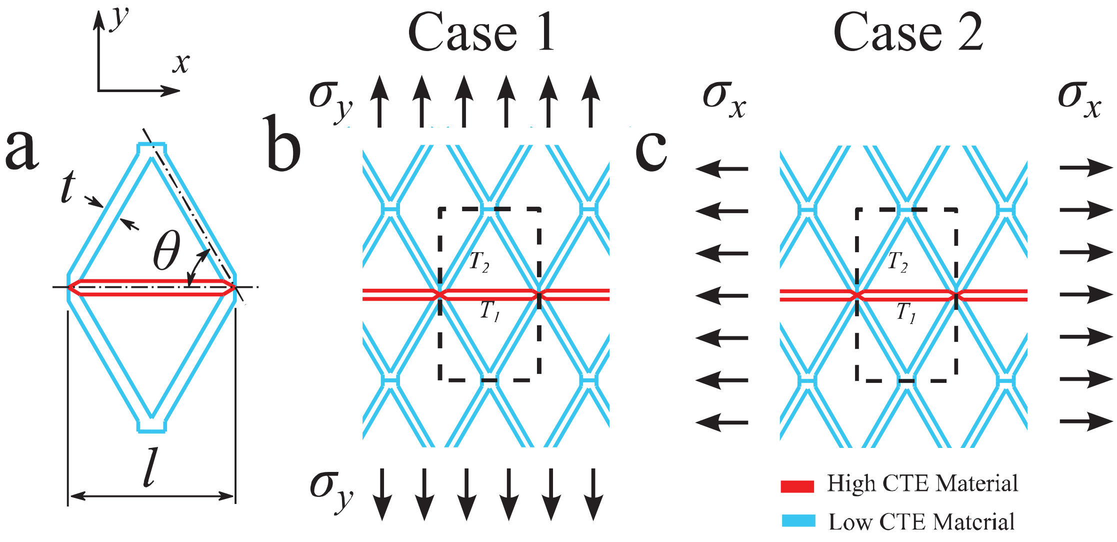

Figure 2-11: Stress distribution in a diamond-celled honeycomb. Case 1 has the applied stress in the y-direction while case 2 has the applied stress in the *x*-direction.

Since the cell walls behave as rigid structures when the joints between the cell walls are replaced by pins, the cell wall deformation of diamond-celled honeycombs is stretch-dominated under axial loading. Calculation of tension distribution assumes that all joints are pinned joints – that is, they cannot sustain any bending moments. In this way, simple equilibrium of joints can be applied and tensile stresses are calculated in the cell walls. The force acting on the two boundaries of the elemental cuboids shown in the dashed region gives rise to the following equilibrium equations:

Case 1

external force internal tensions

$$y\text{-direction} \qquad \sigma_y cl = 2T_2 \sin\theta \tag{2-27}$$

$$x\text{-direction} \qquad 0 = T_1 + 2T_2 \cos\theta \tag{2-28}$$

Case 2

external force internal tensions

$$y\text{-direction} \qquad 0 = 2T_2 \sin\theta \tag{2-29}$$

$$x\text{-direction} \qquad \sigma_x cl \tan\theta = T_1 + 2T_2 \cos\theta \tag{2-30}$$

From these equilibrium equations, the corresponding wall tensions are

Case 1

$$T_1 = -\frac{\sigma_y cl}{\tan\theta} \tag{2-31}$$

$$T_2 = \frac{\sigma_y cl}{2\sin\theta} \tag{2-32}$$

Case 2

$$T_1 = \sigma_x cl \tan\theta \tag{2-33}$$

$$T_2 = 0 \tag{2-34}$$

It is known for lattices made up of slender struts that the deflection of the structure is not influenced greatly by the encasement of the joints. This phenomenon introduces an error on the order of a few percent when calculating deflections. It is therefore acceptable to use a pin-jointed framework analysis for estimating elastic moduli, as these are calculated from the load required to achieve a given deflection (this assumption will be verified later).

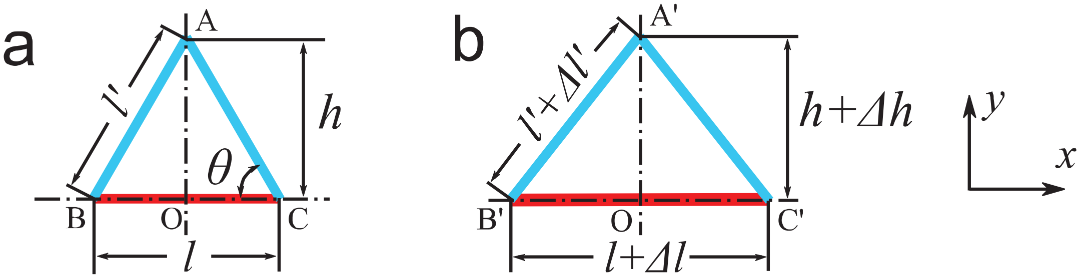

Figure 2-12: Deformed isosceles triangles for calculating elastic moduli. The corners are assumed to be pin-jointed as the effect of encasement on deflections is of second order.

It is important to emphasize the direct extension and the lateral contraction of an isosceles triangular cell when it is stretched during deformation. Consider an isosceles triangle of skew angle θ as shown in Figure 2-12a. If its sides extend by small amounts of Δl and $\Delta l'$ then the two sides have length $l'+\Delta l'$ each, and the base length becomes $l+\Delta l$. The stretched height of the triangle is $h+\Delta h$, and by using Pythagoras' theorem we obtain:

$$\left(\frac{l+\Delta l}{2}\right)^2+\left(h+\Delta h\right)^2=\left(l'+\Delta l'\right)^2 \tag{2-35}$$

Ignoring terms of second order for small extensions, and using the results $l'=l/2\cos\theta$ and $h=l\tan\theta/2$ we get:

$$\frac{\Delta h}{h}=\frac{1}{\sin^2\theta}\left(\frac{\Delta l'}{l'}\right)-\frac{1}{\tan^2\theta}\left(\frac{\Delta l}{l}\right) \tag{2-36}$$

The quantities $\Delta l/l$ and $\Delta l'/l'$ are simply the strains of the sides under tension T_1 and T_2 given by $T_1/E_{s1}t$ and $T_2/E_{s2}t$, respectively, where E_{s1} and E_{s2} are the Young's modulus of solid material 1 and 2. The strains in cases 1 and 2 can therefore be represented as:

Case 1

y-direction:

$$\varepsilon_{y1}=\frac{\Delta h}{h}=\frac{\sigma_x l}{2\sin^3\theta\,E_{s2}t}+\frac{\sigma_x l}{\tan^3\theta\,E_{s1}t} \tag{2-37}$$

Case 2

x-direction:
$$\varepsilon_{x2} = \frac{\Delta l}{l} = \frac{\sigma_y l \tan\theta}{E_{s1} t} \tag{2-38}$$

From Eqs. (2-37) to (2-38) the in-plane Young's moduli for the honeycomb are derived as:

$$\frac{E_y^*}{E_{s1}} = \frac{\sigma_x / \varepsilon_{y1}}{E_{s1}} = \frac{1}{\frac{E_{s1}/E_{s2}}{2\sin^3\theta} + \frac{1}{\tan^3\theta}} \frac{t}{l} \tag{2-39}$$

$$\frac{E_x^*}{E_{s1}} = \frac{\sigma_y / \varepsilon_{x2}}{E_{s1}} = \frac{1}{\tan\theta} \frac{t}{l} \tag{2-40}$$

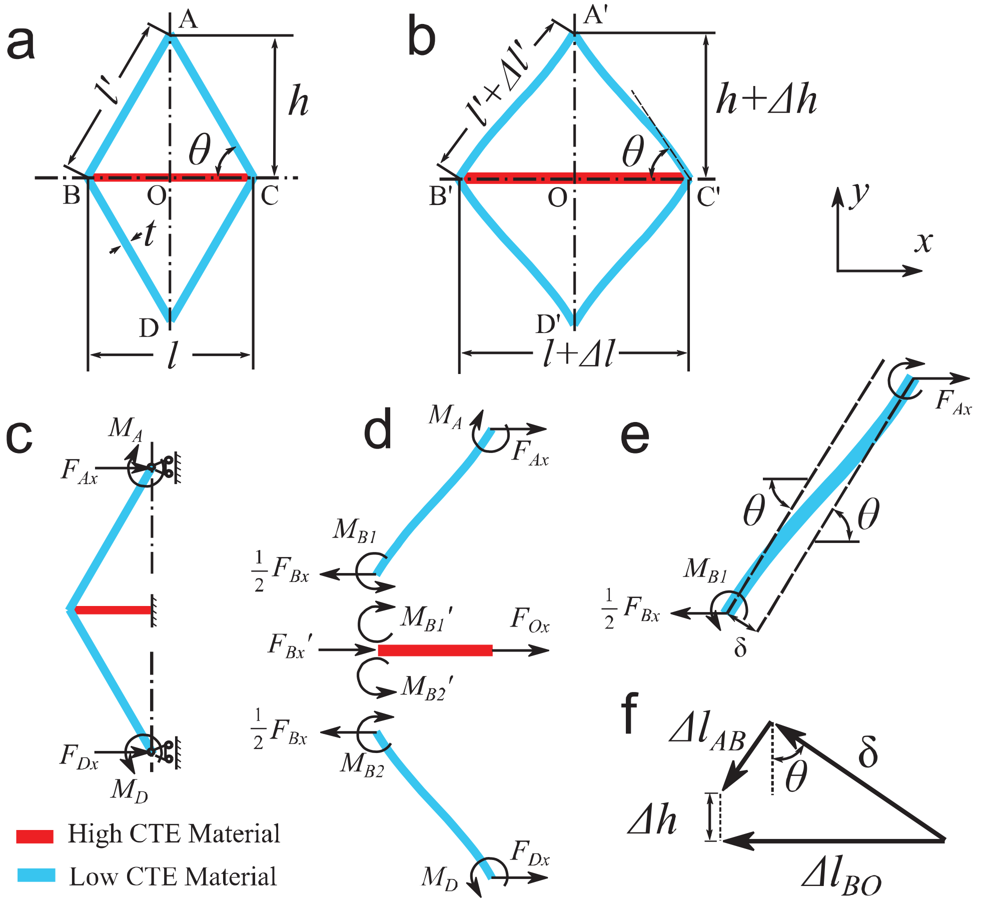

Figure 2-13: Cell thermal deformation: (a) undeformed diamond-celled honeycomb; (b) deformation caused by thermal expansion; (c) left half of the unit cell, which is here examined further; (d) force diagram of beam elements; (e) geometric constraint of inclined beam against rotation; and (f) geometric coordinate condition.

Unlike the calculation above for elastic deflection, the coefficient of thermal expansion is influenced significantly by the behaviour of the joints as a result of bending stresses induced in the cell walls. The bending moment is caused by the thermal expansion mismatch of different component materials. In contrast, a unit cell modelled with pin joints will not experience any thermal stresses under significant temperature changes. Therefore under thermal load, joint type has a significant impact on the stress distribution. Since the lattices built in this work were connected with rigid joints, the rigid-jointed model can evaluate the effective thermal expansion more accurately than a pin-jointed model. Figure 2-13b shows the defected shape of the rigid-joint unit cell (Figure 2-13a) when experiencing an increase in temperature. The deflected shape of the cell walls emerges from the assumption that the embedded angle (e.g. $\angle ACB$) at the joints is maintained at θ. Due to symmetry, we only analyse the left half of the diamond unit cell as shown in Figure 2-13c.

Because of the rigid joint at point B, the embedded angle $\angle ABO$ is maintained (Figure 2-13e). First, we express $I = ct^3/12$ as the second moment of area of the cell wall and $A = ct$ as the cross-sectional area. Then, given $\phi = Fl^2 / 2E_s I$ for the angular displacement caused by $\frac{1}{2}F_{Bx}$ and $\phi = Ml / E_s I$ for the angular displacement caused by M_{B1} on a fixed-fixed beam, the angle of rotation of beam AB at point B can be derived from:

$$0 = \frac{\frac{1}{2}F_{Bx}\sin\theta l'^2}{2E_{s2}I_2} - \frac{M_{B1}l'}{E_{s2}I_2} \tag{2-41}$$

considering $l' = l/2\cos\theta$, Eq. (2-41) becomes

$$M_{B1} = \frac{1}{8}\tan\theta F_{Bx} l \tag{2-42}$$

Using $\delta = Fl^3 / 3E_s I$ for the deflection of $\frac{1}{2}F_{Bx}$ and $\delta = Ml^2 / 2E_s I$ for the deflection of M_{B1} on a fixed-fixed beam, the total deflection of beam AB is calculated as:

$$\delta = \frac{\frac{1}{2} F_{Bx} \sin\theta l'^3}{3E_{s2} I_2} - \frac{M_{B1} l'^2}{2E_{s2} I_2} \tag{2-43}$$

To satisfy the deformation compatibility condition in the horizontal direction (Figure 2-13f):

$$\delta \sin\theta + \Delta l_{AB} \cos\theta = \Delta l_{BO} \tag{2-44}$$

where Δl_{AB} and Δl_{BO} are the elongation of beams AB and BO:

$$\Delta l_{BO} = \alpha_1 \cdot \frac{1}{2} l \cdot \Delta T - \frac{F_{Bx}^{'} \cdot \frac{1}{2} l}{E_{s1} A_1} \tag{2-45}$$

$$\Delta l_{AB} = \alpha_2 \cdot l' \cdot \Delta T + \frac{\frac{1}{2} F_{Bx} \cos\theta l'}{E_{s2} A_2} \tag{2-46}$$

From (2-42) to (2-46) we can find:

$$F_{Bx} = \frac{(\alpha_1 - \alpha_2)\Delta T}{\frac{1}{96} \frac{\sin^2\theta \, l^2}{\cos^3\theta \, E_{s2} I_2} + \frac{\cos\theta}{2E_{s2} A_2} + \frac{1}{E_{s1} A_1}} \tag{2-47}$$

Then, from Figure 2-13f, Δh can be obtained as:

$$\Delta h = \Delta l_{AB} \sin\theta - \delta \cos\theta \tag{2-48}$$

from which the effective CTE parallel to y-direction is simply $\alpha_y^* = \Delta h / (h \Delta T)$. Since $h = \frac{1}{2} \tan\theta l$, we obtain:

$$\alpha_y^* = \alpha 2 + \left(\frac{\cos\theta}{2E_{s2} A_2} - \frac{l^2}{96 \cos\theta E_{s2} I_2} \right) \frac{\alpha_1 - \alpha_2}{\frac{\sin^2\theta \, l^2}{96 \cos^3\theta \, E_{s2} I_2} + \frac{\cos\theta}{2E_{s2} A_2} + \frac{1}{E_{s1} A_1}} \tag{2-49}$$

The effective CTE parallel to *x*-direction is $\alpha_x^* = \Delta l_{BO} / \left(\frac{1}{2} l \Delta T\right)$, giving:

$$\alpha_x^* = \frac{\Delta l_{BO}}{\frac{1}{2} l \Delta T} = \alpha_1 - \frac{F_{Bx} l}{E_{s1} A_1 \Delta T} = \alpha_1 - \frac{\frac{\alpha_1 - \alpha_2}{E_{s1} A_1}}{\frac{\sin^2 \theta \, l^2}{96 \cos^3 \theta \, E_{s2} I_2} + \frac{\cos\theta}{2 E_{s2} A_2} + \frac{1}{E_{s1} A_1}} \tag{2-50}$$

With $I_1 = I_2 = ct^3/12$ and $A_1 = A_2 = ct$, the coefficients of thermal expansion are given by:

$$\alpha_y^* = \alpha_2 + \left(\frac{\cos\theta}{2} - \frac{1}{8\cos\theta \left(t/l\right)^2} \right) \frac{\alpha_1 - \alpha_2}{\frac{\sin^2\theta}{8\cos^3\theta \left(t/l\right)^2} + \frac{\cos\theta}{2} + \frac{1}{E_{s1}/E_{s2}}} \tag{2-51}$$

$$\alpha_x^* = \alpha_1 - \frac{\alpha_1 - \alpha_2}{\frac{\sin^2\theta \left(E_{s1}/E_{s2}\right)}{8\cos^3\theta \left(t/l\right)^2} + \frac{\cos\theta \left(E_{s1}/E_{s2}\right)}{2} + 1} \tag{2-52}$$

2.7.4 Testing setup

Figure 2-14 shows the schematic of the experimental set-up built to test the thermal expansion of lattice materials. It consists of a heating chamber and a DIC system. The former with dimensions of 200(L)×200(W)×150(H) mm is made of borosilicate glass to provide an unobstructed view for DIC measurements. A 200 Watt strip heater was placed under the copper plate in the heating chamber. The copper plate is supported by four leveling mounts which were used for horizontal adjustment. The temperature was controlled by a feedback system, which included a K-type thermocouple attached to the copper plate and a proportion integration differentiation (PID) (OMEGA CN7800) temperature controller. The controllable temperature range was from 25°C to 200°C. The temperature-time data in the PID controller were imported through a RS-485 interface. A NI cDAQ 9174 data acquisition system was used to collect the other three thermocouples from different locations in the chamber and to measure the temperature heterogeneity. A fan in the chamber mixes the air to provide a uniform ambient temperature. The temperature inhomogeneity was regulated within 5% of the real-time temperature through the application of a rotational air fan. Testing samples were covered by a black and white pattern and were set on the copper plate with thermal transfer grease between the two. The thermal strain was measured by DIC using images that were captured through two CCD cameras (Grasshopper 5.0 MP with Fujinon HF25SA-1 lens). Using the DIC correlation software, Vic-3D (Correlate

Solution Inc.), virtual extensometers were placed on the reference image and tracked through the images to measure the displacement between pairs of pixel subsets. The strain field was obtained from the relative displacement between these pairs of subsets. The average CTE was calculated from thermal strain and temperature change.

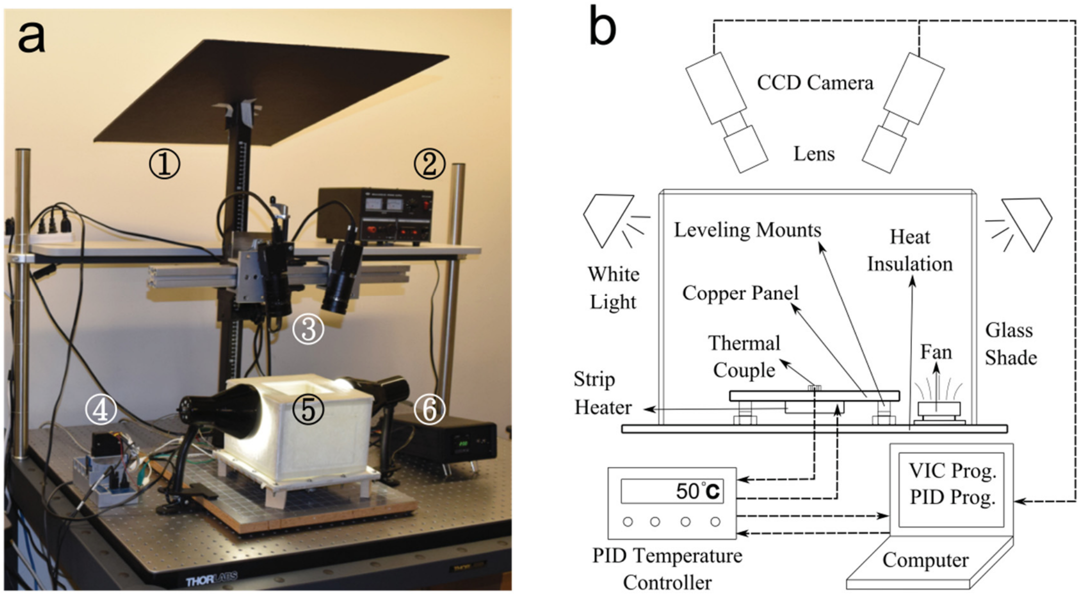

Figure 2-14: Experimental set-up used to measure thermal expansion: (a) 1) Light shield; 2) Power source; 3) CCD cameras; 4) DAQ system; 5) Heating chamber; and 6) PID controller, and (b) schematic of the apparatus.

2.7.5 Asymptotic homogenization method

A lattice material can be considered as a periodic structure comprised of solids and voids. Asymptotic homogenization (AH) is one homogenization method where, in a periodic domain, the mechanical (including thermo-elastic) properties of a heterogeneous material can be accurately predicted to consistently align with results obtained from experiments. This homogenization method represents different length scale behaviors in composite materials by an asymptotic expansion to determine the effective values. AH replaces the periodic composite with an equivalent material model and has been demonstrated to provide accurate predictions of thermo-elastic properties for any type of cell topology and for the whole range of relative density.

AH assumes that each field quantity depends on two different scales: one on the macroscopic level x and the other on the microscopic level, $y = x/\varepsilon$. ε is a magnification factor that scales the dimensions of the unit cell to the dimensions of the material at the macroscale. It also assumes that the corresponding boundary value problem for any field quantity, such as displacement and temperature, can be described with an asymptotic expansion [39]:

$$u^{\epsilon}(x) = u^{0}(x,y) + \epsilon^{1} u^{1}(x,y) + \epsilon^{2} u^{2}(x,y) + \ldots \tag{2-53}$$

where the functions $u^{0}, u^{1}, u^{2} \ldots$ are Y-periodic with respect to the local coordinate y, which means they yield identical values on the opposing sides of the unit cell. When this expansion is replaced into the governing equations of equilibrium, it allows for the derivation of the effective properties of the material [40, 41]. Considering the microstructure effects, the governing equations (weak form) of the thermal stress problems can be described, respectively, by

$$\begin{aligned} &\int_{\Omega^{\epsilon}} E_{ijkl}^{H} \frac{\partial u_{k}^{0}(x)}{\partial x_{l}} \frac{\partial \upsilon_{i}(x)}{\partial x_{j}} d\Omega = \\ &\int_{\Omega^{\epsilon}} b_{i}(x) \upsilon_{i}(x) d\Omega + \int_{\Gamma_{t}} t_{i}(x) \upsilon_{i}(x) d\Gamma + \int_{\Omega} E_{ijkl}^{H} \alpha_{kl}^{H} \left(T^{0} - T_{0}\right) \frac{\partial \upsilon_{i}(x)}{\partial x_{j}} d\Omega \quad \forall \boldsymbol{\upsilon} \in V_{\Omega} \end{aligned} \tag{2-54}$$

where Ω is assumed to be an open subset of $\mathbb{R}^{3}$ with a smooth boundary on Γ and Ω^{ϵ} is the solid part of the domain. b_{i} and t_{i} denote the body force and the traction on boundary Γ_{t} and T_{0} is the initial temperature. V_{Ω} is the kinematically admissible virtual displacement field. The temperature and displacement fields are expressed using an asymptotic expansion as follows:

$$u^{\epsilon}(x) = u^{0}(x,y) + \epsilon^{1} u^{1}(x,y) + \ldots \tag{2-55}$$

$$T^{\epsilon}(x) = T^{0}(x,y) + \epsilon^{1} T^{1}(x,y) + \ldots \tag{2-56}$$

The homogenized elastic tensor E_{ijkl}^{H} and thermal expansion coefficient α_{kl}^{H} are derived as follows:

$$E_{ijkl}^{H}(x)=\frac{1}{|Y|}\int_{Y}\left(E_{ijkl}-E_{ijpq}\frac{\partial\chi_{p}^{kl}}{\partial y_{q}}\right)dY \tag{2-57}$$

$$\alpha_{ij}^{H}(x)=C_{ijpq}^{H}\frac{1}{|Y|}\int_{Y}E_{pqkl}\left(\alpha_{kl}-\frac{\partial\phi_{k}}{\partial y_{l}}\right)dY \tag{2-58}$$

where Y is the base cell of the cellular body and $|Y|$ denotes the volume of the unit cell. E_{ijkl} is the elastic tensor and C_{ijpq}^{H} is the homogenized compliance tensor. χ_{p}^{kl} is the characteristic function tensor of microstructure. ϕ_{k} represents the characteristic displacement vector due to the traction t_i and the thermal expansion [42].

Periodic boundary conditions (PBC), can be generally applied on the base cell. PBC implies that, each unit cell in the composite has identical deformation modes and no separation or overlap between neighboring unit cells exists after deformation. This means all boundary nodes separated by the periods $Y1$ and $Y2$ along the coordinate directions should follow the following displacement constraints:

$$u_i(x_1;x_2)=u_i(x_1\pm k_1Y_1;x_2\pm k_2Y_2) \tag{2-59}$$

where u_i is the displacement vector at node i and k_1 and k_2 are integers.

AH results have been validated experimentally in a series of studies to prove the accuracy and reliability of the method in predicting the effective mechanical properties, large deformation behavior and failure mechanisms of heterogeneous periodic materials. That, along with its flexibility in application, emphasizes the noteworthy advantage of AH as a theoretical tool, used in the study to further validate the closed-form expressions obtained from beam theory.

2.8 References

1. Ashby, M.F. and Y.J.M. Bréchet, *Designing hybrid materials.* Acta Materialia, 2003. **51**(19): p. 5801-5821.
2. Palumbo, N., C. Smith, W. Miller, and K. Evans, *Near-zero thermal expansivity 2-d lattice structures: Performance in terms of mass and mechanical properties.* Acta Materialia, 2011. **59**(6): p. 2392-2403.
3. Arabnejad, S., B. Johnston, M. Tanzer, and D. Pasini, *Fully porous 3d printed titanium femoral stem to reduce stress-shielding following total hip arthroplasty.* Journal of Orthopaedic Research, 2016: p. 1-10.
4. Yamamoto, N., E. Gdoutos, R. Toda, V. White, H. Manohara, and C. Daraio, *Thin films with ultra-low thermal expansion.* Advanced Materials, 2014. **26**(19): p. 3076-3080.
5. Lee, M.G., J.W. Lee, S.C. Han, and K. Kang, *Mechanical analyses of "shellular", an ultralow-density material.* Acta Materialia, 2015. **103**: p. 595-607.
6. Zheng, X., W. Smith, J. Jackson, B. Moran, H. Cui, D. Chen, J. Ye, N. Fang, N. Rodriguez, T. Weisgraber, and C.M. Spadaccini, *Multiscale metallic metamaterials.* Nature Materials, 2016. **15**(10): p. 1100-1106.
7. Lu, T.J., H.A. Stone, and M.F. Ashby, *Heat transfer in open-cell metal foams.* Acta Materialia, 1998. **46**(10): p. 3619-3635.
8. Wang, P., J. Shim, and K. Bertoldi, *Effects of geometric and material nonlinearities on tunable band gaps and low-frequency directionality of phononic crystals.* Physical Review B - Condensed Matter and Materials Physics, 2013. **88**(1): p. 014304.
9. Khanoki, S.A. and D. Pasini, *Multiscale design and multiobjective optimization of orthopedic hip implants with functionally graded cellular material.* Journal of biomechanical engineering, 2012. **134**(3): p. 031004.
10. Wang, Z., L. Jing, J. Ning, and L. Zhao, *The structural response of clamped sandwich beams subjected to impact loading.* Composite Structures, 2011. **93**(4): p. 1300-1308.
11. Wang, Q., J.A. Jackson, Q. Ge, J.B. Hopkins, C.M. Spadaccini, and N.X. Fang, *Lightweight mechanical metamaterials with tunable negative thermal expansion.* Physical Review Letters, 2016. **117**(17): p. 175901.

12. Wei, K., H. Chen, Y. Pei, and D. Fang, *Planar lattices with tailorable coefficient of thermal expansion and high stiffness based on dual-material triangle unit.* Journal of the Mechanics and Physics of Solids, 2016. **86**: p. 173-191.

13. Gilmore, D.G., *Spacecraft thermal control handbook: Fundamental technologies*. 2002, United States: Aerospace Press.

14. Monroe, J.A., D. Gehring, I. Karaman, R. Arroyave, D.W. Brown, and B. Clausen, *Tailored thermal expansion alloys.* Acta Materialia, 2016. **102**: p. 333-341.

15. Naficy, S., R. Gately, R. Gorkin, H. Xin, and G.M. Spinks, *4d printing of reversible shape morphing hydrogel structures.* Macromolecular Materials and Engineering, 2017. **302**(1): p. 1600212.

16. Mao, Y., Z. Ding, C. Yuan, S. Ai, M. Isakov, J. Wu, T. Wang, M.L. Dunn, and H.J. Qi, *3d printed reversible shape changing components with stimuli responsive materials.* Scientific Reports, 2016. **6**: p. 24761.

17. Yong, Z. and C. Tzu-Hsuan, *A review of microelectromechanical systems for nanoscale mechanical characterization.* Journal of Micromechanics and Microengineering, 2015. **25**(9): p. 093001.

18. Steeves, C.A., S.L. dos Santos e Lucato, M. He, E. Antinucci, J.W. Hutchinson, and A.G. Evans, *Concepts for structurally robust materials that combine low thermal expansion with high stiffness.* Journal of the Mechanics and Physics of Solids, 2007. **55**(9): p. 1803-1822.

19. Lehman, J. and R.S. Lakes, *Stiff, strong, zero thermal expansion lattices via material hierarchy.* Composite Structures, 2014. **107**: p. 654-663.

20. Jefferson, G., T.A. Parthasarathy, and R.J. Kerans, *Tailorable thermal expansion hybrid structures.* International Journal of Solids and Structures, 2009. **46**(11-12): p. 2372-2387.

21. Sigmund, O. and S. Torquato, *Composites with extremal thermal expansion coefficients.* Applied Physics Letters, 1996. **69**(21): p. 3203-3205.

22. Sigmund, O. and S. Torquato, *Design of smart composite materials using topology optimization.* Smart Materials and Structures, 1999. **8**(3): p. 365-379.

23. Xu, H. and D. Pasini, *Structurally efficient three-dimensional metamaterials with controllable thermal expansion.* Scientific Reports, 2016. **6**: p. 34924.

24. Lehman, J. and R. Lakes, *Stiff, strong zero thermal expansion lattices via the poisson effect.* Journal of Materials Research, 2013. **28**(17): p. 2499-2508.

25. Hopkins, J.B., Y. Song, H. Lee, N.X. Fang, and C.M. Spadaccini, *Polytope sector-based synthesis and analysis of microstructural architectures with tunable thermal conductivity and expansion.* Journal of Mechanical Design, 2016. **138**(5): p. 051401.

26. Lakes, R., *Cellular solid structures with unbounded thermal expansion.* Journal of Materials Science Letters, 1996. **15**(6): p. 475-477.

27. Lehman, J. and R. Lakes, *Stiff lattices with zero thermal expansion and enhanced stiffness via rib cross section optimization.* International Journal of Mechanics and Materials in Design, 2013. **9**(3): p. 213-225.

28. Lakes, R., *Materials with structural hierarchy.* Nature, 1993. **361**(6412): p. 511-515.

29. Vigliotti, A. and D. Pasini, *Mechanical properties of hierarchical lattices.* Mechanics of Materials, 2013. **62**: p. 32-43.

30. Banerjee, S., *On the mechanical properties of hierarchical lattices.* Mechanics of Materials, 2014. **72**(0): p. 19-32.

31. Hunt, H.E.M., *The mechanical strength of ceramic honeycomb monoliths as determined by simple experiments.* Chemical Engineering Research and Design, 1993. **71a**: p. 257 - 266.

32. Romijn, N.E.R. and N.A. Fleck, *The fracture toughness of planar lattices: Imperfection sensitivity.* Journal of the Mechanics and Physics of Solids, 2007. **55**(12): p. 2538-2564.

33. Pasini, D., *Shape transformers for material and shape selection of lightweight beams.* Materials & Design, 2007. **28**(7): p. 2071-2079.

34. Pasini, D., *Shape and material selection for optimizing flexural vibrations in multilayered resonators.* Journal of Microelectromechanical Systems, 2006. **15**(6): p. 1745-1758.

35. Pasini, D., D.J. Smith, and S.C. Burgess, *Selection of arbitrarily scaled cross-sections in bending stiffness design.* Proceedings of the Institution of Mechanical Engineers, Part L: Journal of Materials: Design and Applications, 2003. **217**(2): p. 113-125.

36. Ge, Q., A.H. Sakhaei, H. Lee, C.K. Dunn, N.X. Fang, and M.L. Dunn, *Multimaterial 4d printing with tailorable shape memory polymers.* Scientific Reports, 2016. **6**: p. 31110.

37. Vaezi, M., S. Chianrabutra, B. Mellor, and S. Yang, *Multiple material additive manufacturing – part 1: A review.* Virtual and Physical Prototyping, 2013. **8**(1): p. 19-50.

38. Momeni, F., S. M.Mehdi Hassani.N, X. Liu, and J. Ni, *A review of 4d printing.* Materials & Design, 2017. **122**: p. 42-79.

39. Hassani, B. and E. Hinton, *Homogenization and structural topology optimization: Theory, practice, and software*. 1999: Springer.

40. Hassani, B. and E. Hinton, *A review of homogenization and topology optimization i—homogenization theory for media with periodic structure.* Computers & Structures, 1998. **69**(6): p. 707-717.

41. Guedes, J. and N. Kikuchi, *Preprocessing and postprocessing for materials based on the homogenization method with adaptive finite element methods.* Computer Methods in Applied Mechanics and Engineering, 1990. **83**(2): p. 143-198.

42. Cheng, C.-H., *Modeling of the thermal elasto-plastic behavior for composite materials using the homogenization method*, in *Mechanical Engineering*. 1992, The University of Michigan: Michigan. p. 229.

Link between chapter 2 and chapter 3

In the previous chapter, the thesis proposed two-dimensional hierarchical lattices that feature a theoretically unbounded range of CTE tunability, regardless of the constituent solids, provided that their CTEs are different, and enables thermal expansion control without incurring a severe loss of structural performance. However, the bi-material diamond with low- and high-CTEs is the only building block that has been proposed for hierarchical lattices with the goal of decoupling the thermal and elastic properties to allow for separate tuning of their performances in different length scales. In order to extend concepts from 2D to 3D with a variety of building blocks to program CTE directionality, Chapter 3 reports routes to systematically engineer thermally responsive architected materials that are built from nine dual-material tetrahedral building blocks that are stiff and strong. Drawing from concepts of vector analysis, crystallography, and tessellation, a scheme is presented for three-dimensional lattices to program desired magnitude and spatial directionality of thermal expansion. All the material permutations that can occur in the struts of a dual-material tetrahedron are analyzed. The relationship between the geometric symmetry of the unit cell and its thermal expansion is elucidated, and then systematic routes to assemble truss materials with desired magnitude and directionality of thermal expansion are proposed. The framework is applied to nine concepts that can meet three thermal expansion requirements including unidirectional, transverse isotropic, and isotropic. A range of investigations covering theoretical and computational analysis along with thermal testing on fabricated samples is carried out to assess their thermal expansion and elastic properties, e.g. Young's modulus, as well as the trade-off existing between them.

Chapter 3

Routes to program thermal expansion in three-dimensional lattice metamaterials built from tetrahedral building blocks

Chapter 3: Routes to program thermal expansion in three-dimensional lattice metamaterials built from tetrahedral building blocks

Hang Xu, Amr Farag, and Damiano Pasini*

Department of Mechanical Engineering, McGill University, 817 Sherbrooke Street West,
Montreal, Quebec H3A 0C3 Canada

*Corresponding author: (damiano.pasini@mcgill.ca)

Journal of the Mechanics and Physics of Solids, 2018. 117: p. 54-87.

Reproduced with permission from Elsevier

3.1 Abstract

Thermal expansion can be problematic in manifold applications that require thermal stability, yet it can also be purposely exploited to meet specific directional requirements of thermal deformation. Opportunities to tailor thermal expansion in architected materials exist, but design options that are stiff and provide full directional authority on thermal expansion are currently limited by the structural characteristics of existing concepts. In this work, we report routes to systematically engineer thermally responsive lattice materials that are built from dual-material tetrahedral units that are stiff and strong. Drawing from concepts of vector analysis, crystallography, and tessellation, a scheme is presented for three-dimensional lattices to program desired magnitude and spatial directionality, such as unidirectional, transverse isotropic, or isotropic, of thermal expansion. Demonstrations on thermal expansion and mechanical properties include theoretical, computational, and experimental studies of nine representative concepts, from tetrahedral building blocks to compound unit cells that can tessellate structurally efficient lattices with tunable magnitude and prescribed directionality of thermal expansion.

Keywords: thermal expansion, three-dimensional lattices, mechanical metamaterials, structural efficiency.

3.2 Introduction

Systems in extreme thermal environments are susceptible to severe temperature changes. Variations in temperature can lead to undesirable geometric changes in sensitive applications that require very fine precision during their working conditions, such as satellite antennas, space telescopes, and large array mirrors [1, 2]. As shown in Figure 3-1a, systems that operate in space need to be thermally stable and dismiss unexpected thermal deformation, a feature that calls for material with zero coefficient of thermal expansion (CTE) [1, 3]. In other applications, on the other hand, thermal deformation is highly desired, and here the quest shifts to material systems that can deliberately deform in response to a temperature swing dictated by the surrounding environment. This scenario generally translates into a demand for large, positive or negative, CTE [4-6]. Examples stemming from a broad and diversely wide range of applications include morphing, e.g. self-shaping, self-folding, and deployable systems [7-9], self-assembly [10], packaging [8, 9], actuation [11], structural adaptivity [4, 7, 11] and biological devices [9].

In general, low to zero CTE can be achieved with intrinsically low or negative expansion materials [12], used as standalone solid or in a composite form without voids [13]. As shown in Figure 3-1a, ZrW_2O_8 and related ceramics [14, 15] or Invar have low, or even negative, CTE. But most of all have shortcomings that limit their use in applications requiring robustness and durability over a large temperature range. Their faults generally correlate with the material type, and examples include: for ceramics, the brittleness and abrupt failure upon peaks of thermal stresses; for Invar-36 and other metals (e.g. $Fe_{68}Pd_{32}$) with low CTE, their limited range of temperature (Figure 3-1a) [3]; and for fibre-reinforced composites, the interface thermal strain and failure caused by the large difference of CTEs between fibre and matrix [16]. Similarly, for applications requiring large CTEs, solid materials can feature intrinsically positive or negative CTEs, such as $Fe_{72}Pt_{28}$ shown in Figure 3-1a. However, the available range of CTE these materials can offer remain too narrow (about -10^1 ppm /℃ to 10^3 ppm /℃ [17]) to induce responsive and large deformations, such as those required for morphing and other applications [7, 11]. An effective alternative to all solids listed above are architected materials made of two solids with distinct CTEs. The rational tuning of their structural geometry and/or selection of their components can generate desired values of CTE from large positive to negative including zero.

Different concepts exist in the literature of CTE tunable architected materials. Each has its own characteristics and performance, and CTE tunability (ΔCTE) is a metric that can be used to discriminate between the potential of their architecture; ΔCTE measures the range of CTE attainable via geometric manipulation of a concept for a given pair of constituents. Whereas no ΔCTE exists for a single material system, dual material concepts can attain a range of CTE values, and the difference between the upper and lower bound represents ΔCTE. The larger ΔCTE, the broader the prospect of manipulating the material architecture to meet given CTE requirements. In the literature, the majority of concepts are in 2D [2, 3, 18-29] and can accommodate only in-plane thermal deformation, including those resorting to origami [6]. Others are three-dimensional [3, 20, 24, 25, 30-35] and, compared to the planar concepts, have a range of advantages including the ability to provide low density space filling in a protective medium [36], remarkable heat exchange with larger contact area [37], CTE tunability in all spatial directions to yield desired thermal behaviour, such as spatial isotropic expansion [24, 38], and others. The lower part of Figure 3-1 also shows the main 3D concepts that can use one building block to construct a series of unit cell topologies with controllable CTE. Figure 3-1g is a periodic foam built from bi-material strips (Figure 3-1b) that are dominated by bending, a characteristic that lowers structural efficiency (i.e. stiffness/mass and strength/mass), and brings about unbounded ΔCTE [27, 31]. Figure 3-1h is a stretch-dominated lattice made of nested double-barrelled struts (Figure 3-1c) with high structural efficiency but low ΔCTE due to the relatively modest Poisson effect their struts can attain, i.e. transversal mismatch of thermal expansion brings longitudinal contraction [32]. Another concept in Figure 3-1i has low specific stiffness [30] but can attain high CTE tunability mainly in the negative range (as shown in Figure 3-1a for the given pair of constituents Al and Ti). Concepts built from a bi-material tetrahedron as building block (Figure 3-1j), on the other hand, are able to ensure a sizeable CTE tunability, while keeping high structural efficiency due to the axial deformation endured by its members [3, 20, 38, 39]. While the concepts listed above are introduced by a number of researchers, others are generated via topology optimization [28, 40], and feature a fairly complex structure. As shown by some illustrative examples in Figure 3-1f and k, their architecture is generally bend-dominated, thus highlighting a uniaxial specific stiffness that is lower than that of stretch dominated, truss-like concepts.

The majority of the 3D building blocks discussed in the literature (Figure 3-1b-e), except those developed via topology optimization (Figure 3-1f and k) [40], can tailor the CTE in only one specific direction (horizontal direction for Figure 3-1b, axial direction for Figure 3-1c, and vertical direction for Figure 3-1d and e). A more diverse performance with a multitude of tunable CTE directions, such as isotropic CTE, can be obtained by assembling several building blocks into a unit cell (as demonstrated in Figure 3-1g-j). This can be achieved by studying the relationships between building block symmetry, tessellation patterns, and effective thermoelastic properties, a research path yet to be systematically explored in the context of architected materials. While mechanisms for tessellating building blocks into unit cells via reflection and translation are available in the literature [20], only special cases have been so far examined, with those inspired by multi-fold rotational symmetry in crystallography able to attain only isotropic CTE [23]. However, other directional requirements of thermal expansion, such as unidirectional and transverse isotropic, might be desirable in certain engineering applications.

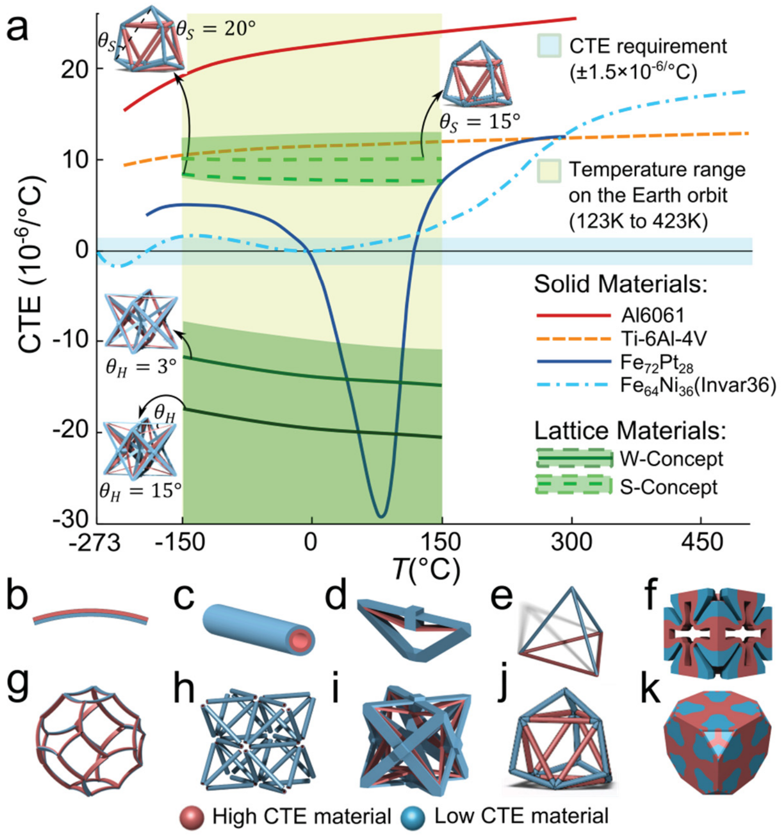

Figure 3-1: (a) CTE versus temperature for selected solids and architected materials: W-concept [30], S-concept [3], Al6061 [41], Ti-6Al-4V [41], and two iron alloys [42]. The temperature

range on the earth orbit and the CTE requirement for materials used in communication satellites are also shown. Since CTEs of component materials, i.e. Al6061 and Ti-6Al-4V, selected here for demonstrative purposes, change with temperature, the effective CTE of the W-concept and S-concept is also a function of temperature, and its value has been numerically obtained for the temperature range -150°C to 150°C. (b-e) CTE tunable building blocks in the literature: (b) a bi-layer strip concept [27], (c) a nested double-barrelled concept [27], (d) a flexure blade concept [30], and (e) a tetrahedron concept with a stationary node [3]. The corresponding unit cells in 3D are shown in (g) to (j). Concepts constructed via topology optimization: (f) a low-bulk modulus, high thermal expansion design and (k) the maximal modulus design [40]. We also note that a change of the constitutive materials can yield values of the CTE that differ from those in the figure, which are obtained for the given pair of materials: Al6061 and Ti-6Al-4V; prescribing the pair of materials enables a consistent comparison among the relative performance endowed by the architecture of each concept.

The aim of the investigation reported here is twofold: (i) to provide a fundamental understanding of the mechanisms of thermal expansion in spatial lattices built from dual-material tetrahedron building blocks, and (ii) to offer systematic routes to program their thermal expansion in given directions as required by the application. Concepts of vector analysis are used to express thermal expansion of building blocks and compound units along their principal, or any other, directions. In addition, notions of crystal symmetry are borrowed from crystallography to elucidate the relationship between geometric symmetry and thermal expansion of bi-material lattices assembled from either building blocks or compound units. The proposed framework enables the attainment of three sets of distinct behaviour of directional CTE: (i) unidirectional, (ii) transverse isotropic, and (iii) isotropic. In addition to CTE tunability, closed form expressions are provided for the Young's modulus, shear modulus, buckling and yielding strength of unit cells, here introduced to attain a high level of both CTE tunability and structural efficiency. A total of 21 proof-of-concepts are built and their effective CTE tested via three-dimensional digital image correlation (3D DIC) for model validation; in particular, 12 proof-of-concepts are metallic tetrahedra built from Al6061, Ti-6Al-4V, and Invar-36, and 9 are polymer unit cell specimens made of PTFE (Polytetrafluoroethylene), acrylic, and ABS (Acrylonitrile Butadiene Styrene).

Concluding the chapter is a discussion that gauges the trade-off between CTE tunability and specific stiffness, a paramount insight to elucidate for aerospace and other applications.

3.3 3D lattice with low-CTE tetrahedra

In this section, we draw from concepts of vector analysis to reframe thermal expansion of periodic trusses as a relationship between the material length vector and the thermal displacement vector. These concepts are first applied to the tetrahedron building block with the goal of studying thermal expansion in a three-dimensional space. Then we borrow concepts from crystallography to show how typical relations of symmetry can be used to create unit cells with desired thermal expansion, such as unidirectional, transverse isotropic, or isotropic. These can be further tessellated into spatial trusses or lattices exhibiting prescribed thermoelastic behaviour.

3.3.1 Definition of material length vector and thermal displacement vector

In a solid, a change in temperature can cause the material to change in shape, length, area and volume. Here we show that via the application of the thermal displacement vector, it is possible to draw a simple analogy between the thermal deformation triggered in a solid material and that appearing in a bi-material building block. Below, the basic concepts for a solid material are briefly summarized and then extended to a truss system.

Figure 3-2a-I shows the *material length vector*, $\mathbf{M}$, whose direction defines a referential direction along which the thermal expansion is measured, and whose magnitude describes the initial length, l_0, i.e. the initial distance between two points, e.g. A and B, in a spatial domain. If point A is selected as a stationary reference, with a change in temperature (ΔT), point B can move away from its original location to reach a generic point B' (Figure 3-2a-II), creating the vector, $\mathbf{N}$, which is defined as the *thermal displacement vector*. Assuming there is no rigid-body translation or rotation of the material in the domain $\mathrm{A}x_1x_2x_3$, we can represent the thermal strain by the second-order tensor, $\left[\varepsilon_{ij}\right]$:

$$N_i = \varepsilon_{ij} M_j \qquad \left(i, j = 1,2,3\right), \tag{3-1}$$

where the subscript follows the Einstein notation. If ΔT takes place uniformly throughout the solid (i.e. ΔT is a scalar), the deformation is uniform, and all the components of $\left[\varepsilon_{ij}\right]$ are proportional to ΔT such that:

$$\varepsilon_{ij} = \alpha_{ij} \Delta T, \tag{3-2}$$

where α_{ij} is the CTE along the direction *ij*. Since $\left[\varepsilon_{ij}\right]$ is a symmetrical second-order tensor, so is $\left[\alpha_{ij}\right]$, which is given in its three-dimensional form by:

$$\alpha_{ij} = \begin{bmatrix} \alpha_{11} & \alpha_{12} & \alpha_{13} \\ \alpha_{21} & \alpha_{22} & \alpha_{23} \\ \alpha_{31} & \alpha_{32} & \alpha_{33} \end{bmatrix}. \tag{3-3}$$

In the most general case where the solid material can freely expand in any direction, **N** has components both parallel ($N_{\parallel}$) and transverse ($N_{\perp}$) to $\mathbf{M}$. The magnitude of the CTE in the direction of $\mathbf{M}$ is given by measuring $N_{\parallel}/(M\Delta T)$, where M is the length of $\mathbf{M}$ and $N_{\parallel} = |\mathbf{N}|\cos(\beta)$ (Figure 3-2-a) is identical to the length change, Δl. Then the CTE in the $\mathbf{M}$ direction, $\alpha_{\mathbf{M}}$, can be expressed as:

$$\alpha_{\mathbf{M}} = \frac{\mathbf{M} \cdot \mathbf{N}}{M^2 \Delta T}, \tag{3-4}$$

where "$\cdot$" represents the dot product. Eq. (3-4) shows that for a unit change in temperature the CTE in any arbitrary direction is the thermal extension or contraction, per unit length of a line drawn originally in that direction. If the thermal expansion tensor is conveniently expressed with respect to its mutually orthogonal principal axes, then the tensor (Eq. (3-3)) simplifies to:

$$\alpha_{ij} = \begin{bmatrix} \alpha_1 & & \\ & \alpha_2 & \\ & & \alpha_3 \end{bmatrix}, \tag{3-5}$$

where α_1, α_2, and α_3 are the principal CTEs in the x_1, x_2, and x_3 directions. For the remainder of the chapter, the material length and the thermal displacement vectors are now abbreviated to

ML and TD vectors, respectively, and mathematically expressed as $\mathbf{M}$ and $\mathbf{N}$, respectively.

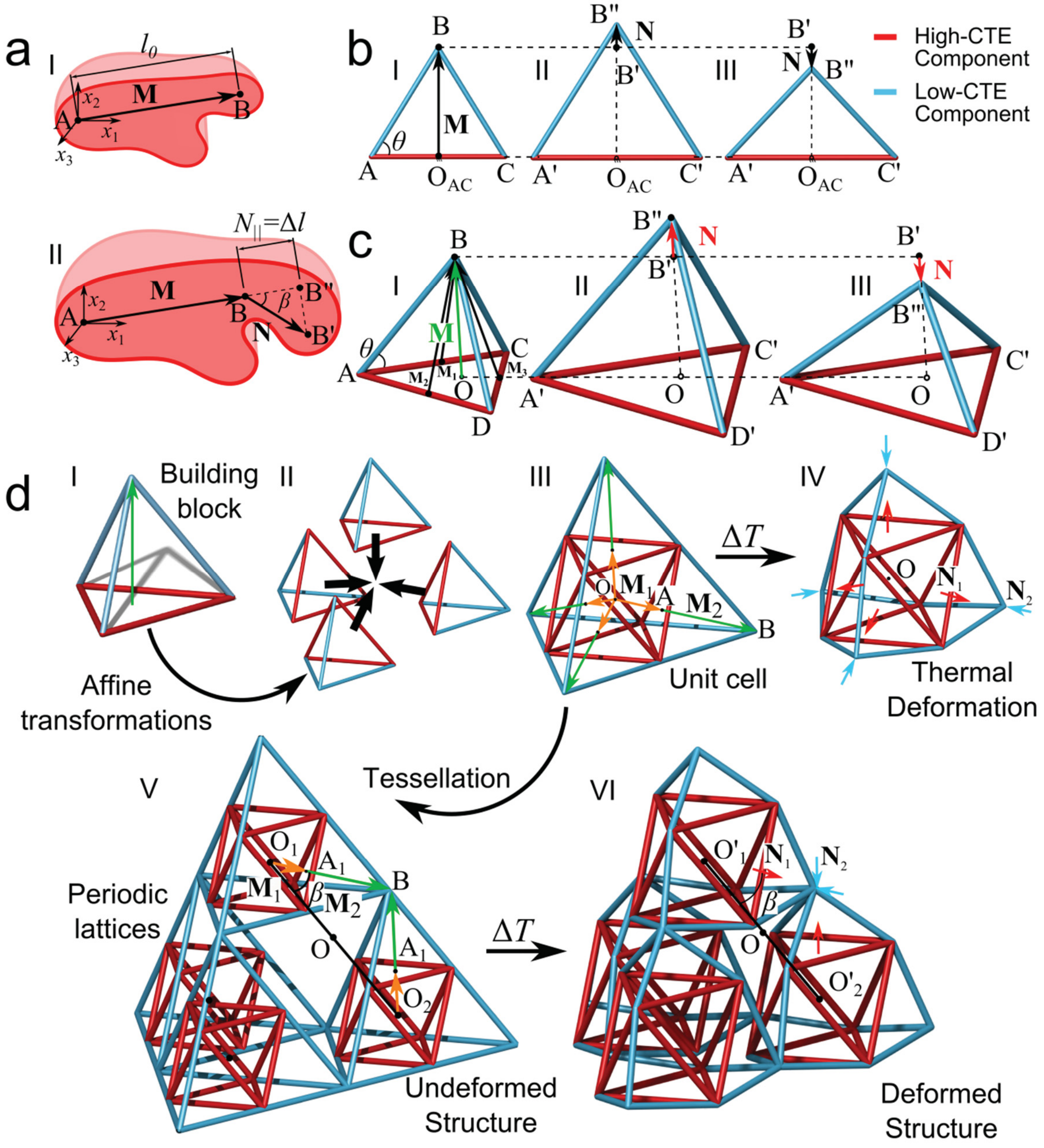

Figure 3-2: (a) Material length vector, $\mathbf{M}$, and thermal displacement vector, $\mathbf{N}$, for a solid material under a temperature change. Definition of $\mathbf{M}$ and $\mathbf{N}$ vectors on building blocks in 2D and 3D: (b) 2D low-CTE triangle and (c) 3D low-CTE tetrahedron. (d) $\mathbf{M}$ and $\mathbf{N}$ vectors for an assembled unit cell (d-I to d-IV) and a tessellated system of unit cells (d-V and d-VI) before and after thermal deformation [3]. Deformations are visualized considerably larger than the true ones, which are small and within the linear elastic regime.

The simple concepts for ML and TD vectors described above for a solid material (Figure 3-2a), can be extended to a dual-material triangle truss in 2D (Figure 3-2b) and further to a tetrahedron truss in 3D (Figure 3-2c). With a temperature increase, the height rise of the dual-material triangle in Figure 3-2b, triggered by the blue elements with low CTE is compensated by the sinking of its top vertex (Point B) due to the higher thermal expansion of the red bar with high CTE. In Figure 3-2b-I, the ML vector describes the direction of thermal expansion between the midpoint of the base (O_{AC}, taken here as the reference point) and the apex (point B), which is the only CTE tunable direction in the triangle. By harnessing the CTE values of the solid components, α_{s1} and α_{s2}, or the skewness of the blue elements, θ, we can tailor the CTE of the dual-material triangle in the vertical direction, so as to assume one of the following value: positive (Figure 3-2b-II) with codirectional ML and TD vectors; negative (Figure 3-2b-III) with ML and TD vectors in the opposite direction; or zero with a zero TD vector.

Similarly in 3D, the $\mathbf{M}$ vector of the dual-material tetrahedron (Figure 3-2c-I, [20]) is defined by the apex (point B) and the centroid of the base triangle (point O, taken as the reference point). With a temperature increase, the height rise, i.e. the thermal expansion in the $\mathbf{M}$ direction, triggered by the blue elements is counteracted by the sinking of its apex due to the higher thermal expansion of the red base (△ACD). In this case, all lateral faces (i.e. △BAC, △BAD, and △BCD) of the dual-material tetrahedron are low-CTE triangles (Figure 3-2b-I), and the resultant of all three ML vectors of the low-CTE triangles (i.e. $\mathbf{M}_1$, $\mathbf{M}_2$, and $\mathbf{M}_3$ in Figure 3-2c-I) passes through points O and B. Thus, the direction of the resultant vector given by the sum of $\mathbf{M}_1$, $\mathbf{M}_2$, and $\mathbf{M}_3$ (each representing the only CTE tunable direction in 2D) is equidirectional to the $\mathbf{M}$ vector of the tetrahedron (green vector in Figure 3-2c-I, representing the only CTE tunable direction in 3D). This observation highlights a directional relationship of CTE between a tetrahedron and its triangular faces: the resultant of the 2D ML vectors of the triangles specifies the CTE tunable direction of the tetrahedron, chosen here as the direction of the 3D ML vector. In other words, the direction of the tunable thermal expansion in the triangular faces governs that of the overall tetrahedron. This rule is also useful for locating the ML vector direction of other types of dual-material tetrahedra, along with the CTE tunable directions, as explained in the following section. As per the magnitude, the effective CTE in 3D, similar to the 2D case, can be tailored to be positive (Figure 3-2c-II), negative (Figure 3-2c-III), and zero through a change in θ and/or α_{s1}/α_{s2}. In both 2D and 3D cases, the apex point B can be termed as stationary node [3], since for the zero-CTE case its position relative to the reference point can remain stationary during thermal expansion.

The ML and TD vectors can also express the CTE of an assembly of building blocks, such as the unit cell shown in Figure 3-2d-III [3]. Here in this exemplifying case, simple affine transformations, in particular translation and rotation (Figure 3-2d-II), are used to assemble the dual-material building block (Figure 3-2d-I) into a unit cell with multiple subunits (Figure 3-2d-II). The assembly of the four tetrahedra in Figure 3-2d-II creates a high CTE octahedron core within the unit cell (Figure 3-2d-III). The ML vectors, $\mathbf{M}_1$ in orange for the octahedron core, and $\mathbf{M}_2$ in green for the tetrahedron (Figure 3-2d-III), can be defined between the center of the unit cell, point O, taken as the reference point, and the vertex B, separated by point A (Figure 3-2d-III). The overall thermal expansion behaviour between O and B is given by the sum of the corresponding vectors, $\mathbf{M}_1$, $\mathbf{M}_2$, and the TD vectors, $\mathbf{N}_1$ and $\mathbf{N}_2$, of these two thermally distinct parts, OA and AB. Hence the thermal expansion of the assembled unit cell in Figure 3-2d-III can be simply expressed as:

$$\alpha_{\mathbf{M}} = \frac{\sum_k \left(\mathbf{M}_k \cdot \mathbf{N}_k / M_k\right)}{\Delta T \sum_k M_k} \quad \left(k = 1, 2\right). \tag{3-6}$$

We now show that the above ML and TD vectors can also be applied to desired 3D tessellations of compound units. Figure 3-2d-V shows an example with a periodic truss assembled with the compound cell of Figure 3-2d-III. The distance between the centers of any adjacent unit cells, such as between centers O_1 and O_2, can be accessed via ML and TD vectors, as shown in Figure 3-2d-V and VI. In this case, the thermal expansion of the spatial truss can be simply expressed as:

$$\alpha_{\mathrm{O}_1\mathrm{O}_2} = \frac{\sum_k N_{\parallel k}}{\Delta T \sum_k M_{\parallel k}} \quad \left(k = 1, 2\right), \tag{3-7}$$

where $N_{\|k}$ and $M_{\|k}$ are the components of $\mathbf{N}_k$ and $\mathbf{M}_k$ parallel to $\mathrm{O_1O_2}$, respectively. We remark here that since the projection cosine of both $N_{\|k}$ and $M_{\|k}$, i.e. $\cos\beta$, is identical, the terms containing the directional angle, β in Figure 3-2d-V and VI, cancel out in both the numerator and denominator of Eq. (3-7). No matter which direction is considered, the CTE for this cell topology is identical in all directions, thus equaling the effective CTE evaluated by Eq. (3-6), i.e. $\alpha_{\mathrm{O_1O_2}} = \alpha_{\mathbf{M}}$. We can conclude that since the thermal expansions between centers of any adjacent unit cells are identical, the overall CTE of the truss material shown in Figure 3-2d-V is thermally isotropic and the magnitude can be evaluated by the vector analysis explained above.

The concept presented in Figure 3-2c and d are given as examples to show the handiness of using vectors to visualize and analyze thermal expansion of a periodic truss built from single units as well as a more complex assembly of compound units. In both cases, the primitive building block is a tetrahedron that features a distinct arrangement of solids in its bars. But this is just one among other material layouts that are feasible. The following sections examine all the possible material arrangements that can appear in the strut of a dual-material tetrahedron, each defining a building block with its own CTE profile.

3.3.2 Exploration of dual-material tetrahedra

The simplest 3D hinged structure that is free to deform upon temperature changes is a tetrahedron. Six types of rods can make up its frame, and different combinations of component materials or dimensions are possible. Below we examine all the material permutations that can occur in the struts of a dual-material tetrahedron, and study the relation that each of these has with the CTE along its principal axes. The goal here is to provide a foundational basis to understand other, more complicated, truss-like materials.

3.3.2.1 Thermal deformation mode of dual-material tetrahedra

Let us consider a tetrahedron made of six rods, each made of a material with either low or high CTE, but both positive. Figure 3-3 shows all the possible material permutations that can appear by simply switching the position of red rods with high-CTE, α_{s1}, and blue rods with low-CTE, α_{s2}. In total, there are eleven possible arrangements, each visualized by a tetrahedron from Figure 3-3a-k. For monomaterial tetrahedra (e.g. Figure 3-3a and k), the thermal expansion is uniform; as there is no thermal mismatch, no opportunity exists to tailor the CTE. For the remaining tetrahedra, on the other hand, CTE tunability is possible as the effective CTE can be adjusted in one or more directions. To ease the CTE assessment, we propose to classify the nine tetrahedra into three groups:

I. Low-CTE tetrahedra (Figure 3-3b-e), which can yield an effective CTE that is lower than the CTEs of both the component materials;

II. Intermediate-CTE tetrahedron (Figure 3-3f), the only one able to attain the effective CTE of a value between the CTEs of the two components only;

III. High-CTE tetrahedra (Figure 3-3g-j), with effective CTEs higher than both the CTEs of the components.

For the sake of simplicity, the main body of the chapter examines only the low-CTE cases (Figure 3-3b-e), as the analysis of high-CTE cases can be easily completed by switching the material properties. The analysis of the second group (Figure 3-3f) is given in Supplementary Material Section 3.8.1.

The $\mathbf{M}$ and $\mathbf{N}$ vectors introduced in the previous section now become handy in evaluating the thermal expansion of all tetrahedra in Figure 3-3. The direction of the 3D $\mathbf{M}$ vector with CTE tunability is controlled by the resultant of the 2D ML vectors of its triangular faces, and can be purposely chosen to align along one of the principal axes of a tetrahedron. As explained in later sections, this choice eases the assembly of building blocks in spatial lattices and helps identify the direction of CTE tunability.

Figure 3-3b-I shows a tetrahedron in which one of the rods possesses high-CTE as opposed to the rest with low-CTE. Two low-CTE triangles equivalent to those in Figure 3-2b can be found in Figure 3-3b-I, $\triangle ACD$ (purple face) and $\triangle BCD$ (yellow face), where only the undeformed configuration is shown to emphasize their ML vector, $\mathbf{M}_1$ and $\mathbf{M}_2$ (marked as black vectors), whose resultant sets the direction of the $\mathbf{M}$ (green arrow) and $\mathbf{N}$ vector (red arrow) for this tetrahedron. The $\mathbf{M}$ vector visualized in Figure 3-3b-I is aligned with the direction of CTE tunability, i.e. the local coordinate axis z, and show the thermal expansion direction of the deformed tetrahedron (Figure 3-3bII). For the zero-CTE case, points A and B are stationary nodes with respect to the line CD in the low-CTE triangles. Analogously, the relative position, including the minimum distance and skew angle between the two skewed lines, AB and CD, can be constant under a temperature change. We can thus name the pair of lines AB and CD as stationary lines (SL), and call the tetrahedron shown in Figure 3-3b as a tetrahedron with stationary lines (TL-1). Under the pin-jointed assumption, through Eq. (3-4) we can obtain its effective CTEs as:

$$\begin{cases} \alpha_x = \alpha_{s1} \\ \alpha_y = \alpha_{s2} \\ \alpha_{z,TL-1} = \dfrac{\alpha_{s2} - (\alpha_{s1} + \alpha_{s2})\cos^2\theta_{TL-1}}{1 - 2\cos^2\theta_{TL-1}} \end{cases}, \theta_{TL-1} \in \left(45^\circ, 90^\circ\right). \tag{3-8}$$

Figure 3-3c and d shows two other possible ways by which we can permute the positions of high- and low-CTE bars. Here two high-CTE bars and four low-CTE bars make up the unit: the high-CTE bars of the former meet at one of their vertices, while the high-CTE bars of the latter are not in contact. Let us first examine Figure 3-3c, where the tetrahedron has two low-CTE triangles: $\triangle \mathrm{ABC}$ and $\triangle \mathrm{ACD}$. We consider $\mathbf{O'A}$, the resultant of the two corresponding 2D ML vectors ($\mathbf{M}_1$ and $\mathbf{M}_2$), as the direction of $\mathbf{M}$, and O as the fixed reference point. After thermal expansion, the deformation mode in Figure 3-3c shows the tetrahedron is no longer a regular triangular pyramid. The $\mathbf{N}$ vector, i.e. the change of the relative location between point A and the base $\triangle \mathrm{BCD}$, indicates the CTE in the vertical direction can be tuned, only while being subjected to shear deformation due to the thermally asymmetric nature of this tetrahedron. For this reason, its thermoelastic properties are given in Supplementary Material Section 3.8.1.

We now turn to the tetrahedron in Figure 3-3d, where all four triangles have low CTE. Here, the resultant vector of their four 2D ML vectors passes through the midpoints of the two high-CTE bars. Similar to the case shown in Figure 3-3b, for the zero-CTE case, the relative location, including the minimum distance and the skew angle between lines AB and CD, can be kept stationary during thermal expansion (Figure 3-4b). Thus, the tetrahedron in Figure 3-3d has a pair of SLs that can be used for CTE tailoring. The effective CTEs of this tetrahedron with stationary lines (TL-2) can be obtained by applying Eq. (3-4) under the pin-jointed assumption as:

$$\begin{cases} \alpha_x = \alpha_y = \alpha_{s1} \\ \alpha_{z,\,TL-2} = \dfrac{\alpha_{s2} - 2\alpha_{s1}\cos^2\theta_{TL-2}}{1-2\cos^2\theta_{TL-2}}, \theta_{TL-2} \in \left(45^\circ, 90^\circ\right). \end{cases} \tag{3-9}$$

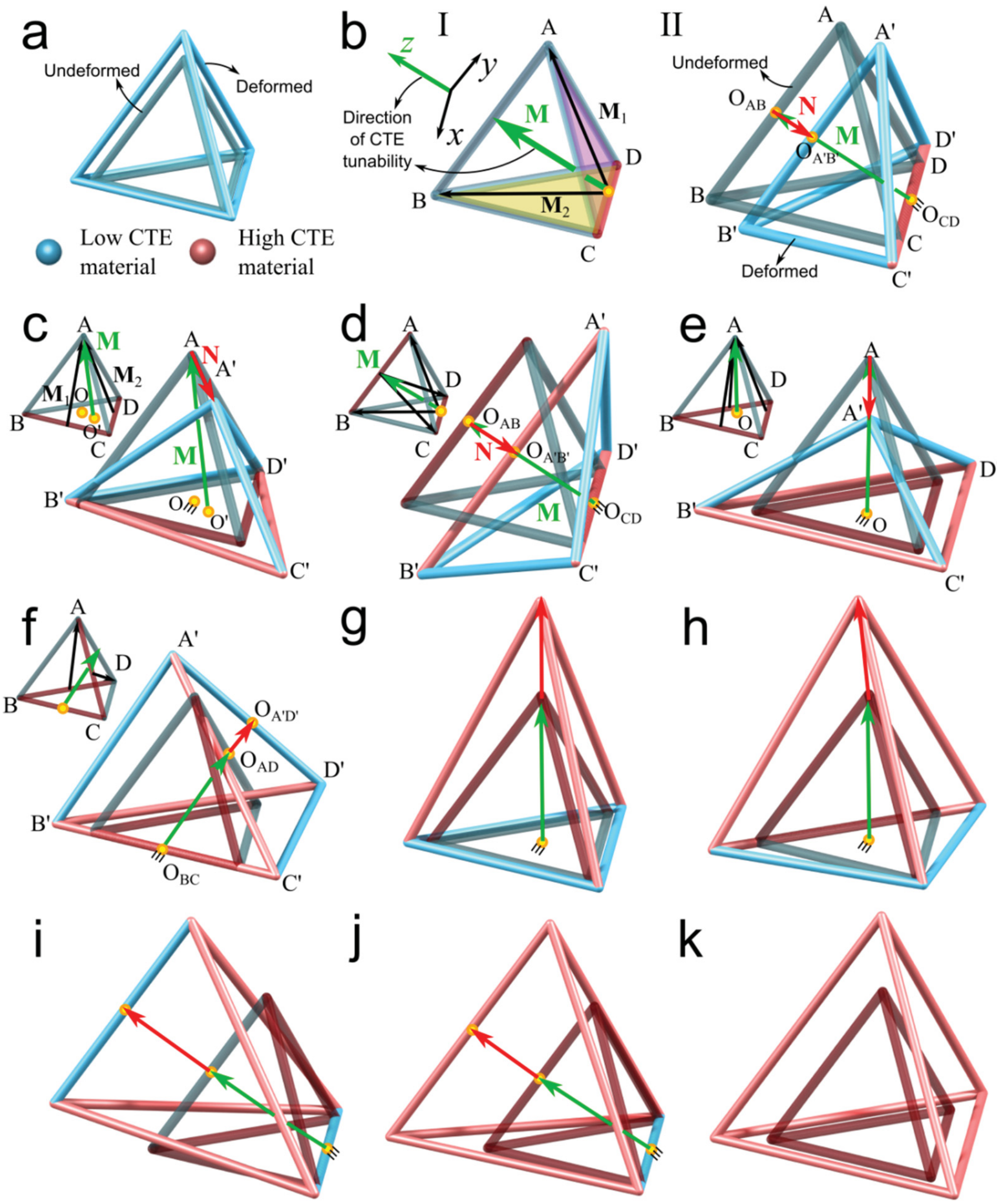

Figure 3-3: Exploration of dual-material tetrahedra made of permutations of low (blue) and high (red) CTE bars. (a): monomaterial low-CTE tetrahedra with no CTE tunability; (b) to (e): tetrahedra with low-CTE; (f): a tetrahedron with intermediate CTE; and (g) to (j): tetrahedra with high-CTE; (k): monomaterial high-CTE tetrahedra with no CTE tunability. Both undeformed and

deformed structures are depicted in each subfigure from (a) to (k). Black arrows represent 2D ML vectors. Green arrows represent 3D $\mathbf{M}$ vectors along the direction of CTE tunability, and red arrows $\mathbf{N}$.

For a tetrahedron with three high-CTE bars and three low-CTE bars, there are three possible ways by which bars can be arranged (Figure 3-3e-g). In the arrangement shown in Figure 3-3e, the high-CTE bars are connected in a loop. During thermal expansion, the relative location between point A and the base $\Delta\,\mathrm{BCD}$ can be kept stationary, as discussed in the previous section. Thus, point A is a stationary node (SN), and Figure 3-3e shows a tetrahedron with a stationary node (TN). The effective CTEs of TN under the pin-jointed assumption can be expressed as:

$$\begin{cases} \alpha_x = \alpha_y = \alpha_{s1} \\ \alpha_{z,TN} = \dfrac{3\alpha_{s2} - 4\alpha_{s1}\cos^2\theta_{TN}}{3 - 4\cos^2\theta_{TN}}, \theta_{TN} \in \left(30^\circ, 90^\circ\right). \end{cases} \tag{3-10}$$

The case where the high-CTE bars and low-CTE bars are in series, as in Figure 3-3f (group two: intermediate tetrahedron), is also given in Supplementary Material Section 3.8.1. Figure 3-3g shows the opposite configuration of Figure 3-3e, and hence this building block is used to obtain high-CTE. Similarly, Figure 3-3j, h and i are the counterparts of Figure 3-3b, c, and d, and thus these tetrahedra are viable for high-CTE systems. The close-form equations for the CTE evaluation of high-CTE group can be obtained via switching α_{s1} and α_{s2} in the equations of the low-CTE group.

3.3.2.2 CTE of low-CTE tetrahedron

The CTE of the regular tetrahedra presented above can be adjusted by manipulating both material and geometric variables, in given directions. Evidently, the pin-jointed assumption used to derive Eqs. (3-8)-(3-10) reduces the CTE-dependent variables to only the skew angle and the CTE of the components. This section examines the role of these two CTE-dependent variables on the effective CTE of building blocks for both high- and low-CTE concepts (considering Figure 3-3g-j are the counterparts of c to f). We examine three CTE-tunable building blocks with different linear-dominant thermal deformation modes along the principal direction: TL-1 (Figure 3-3c), TL-2 (Figure 3-3e), and TN (Figure 3-3f). The zero-CTE cases of these building blocks are also visualized in Figure 3-4a-c before and after thermal expansion; each tetrahedron is orientated to keep the $\mathbf{M}$ (green) vector along the vertical direction, demonstrating the concepts of stationary line and stationary node.

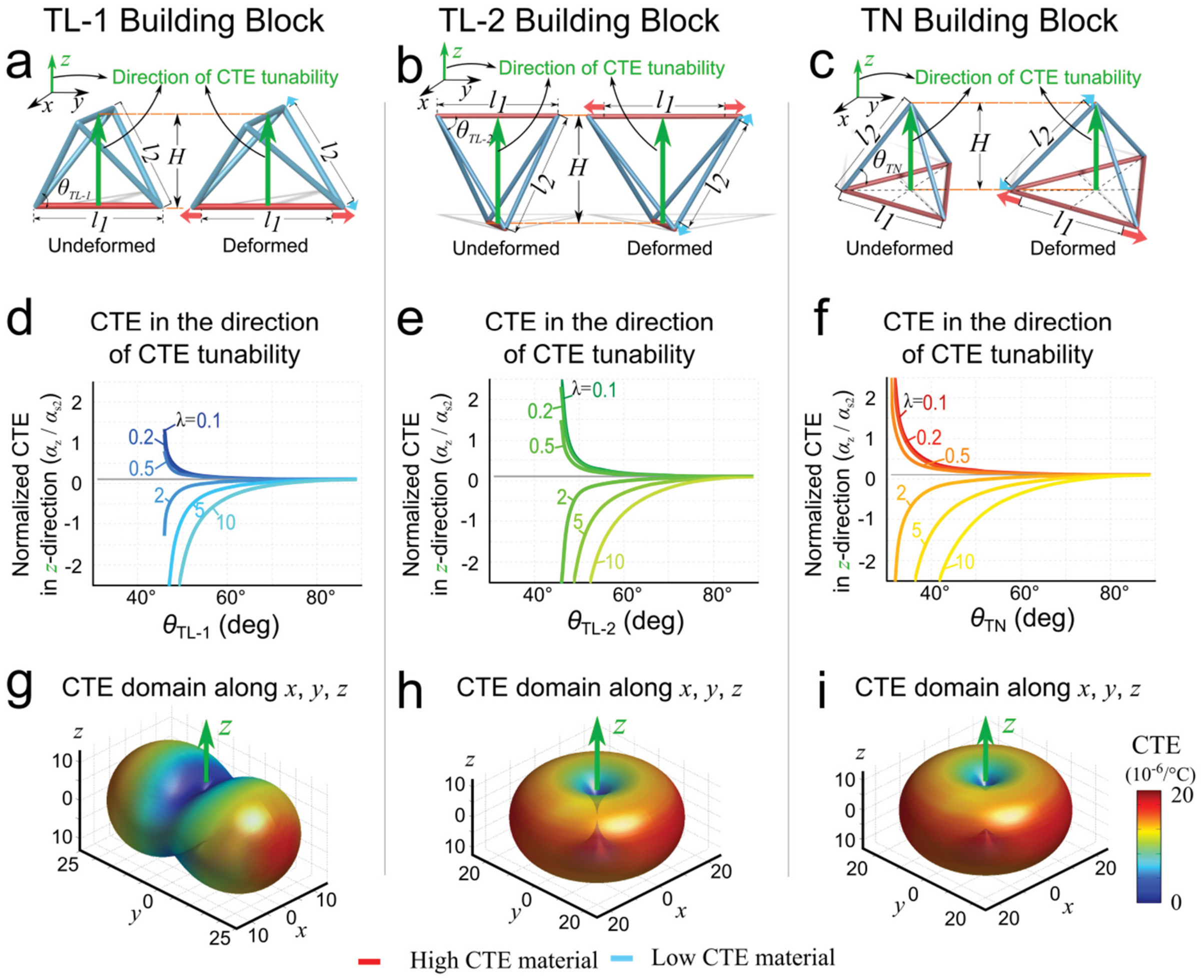

Figure 3-4: Tetrahedra with zero CTE in the principal direction (z-direction): (a) TL-1, (b) TL-2, and (c) TN with undeformed frame on the left and thermal deformations with zero CTE on the z-direction on the right. The normalized CTEs of Low-CTE tetrahedra along the vertical direction vary with respect to the skew angle and ratio of the component CTE ($\lambda = \alpha_{s1}/\alpha_{s2}$): (d) TL-1, (e) TL-2, and (f) TN. CTE magnitude plotted in polar coordinate system with respect to the principal directions, i.e. x, y, and z; the semi-axes of each ellipsoid are the CTE coefficients, $|\alpha_x|$, $|\alpha_y|$, and $|\alpha_z|$ of the corresponding tetrahedra with $\lambda = 2$ (A high-CTE material of $\alpha_{s1} = 20\times10^{-6}$ / °C and a low-CTE material of $\alpha_{s2} = 10\times10^{-6}$ / °C are taken here as representative components): (g) TL-1, (h) TL-2, and (i) TN.

Figure 3-4d-f shows the effective CTEs of both low- and high-CTE tetrahedra along the *z*-direction (shown in Figure 3-4a-c) against the skew angles. From previous section, we recall that the $\mathbf{M}$ vector direction (green arrow), i.e. *z*-direction, is the only CTE tunable principle direction while along the others the CTE is that of the constituent solids. As depicted in Figure 3-4d-f, α_z of the building blocks can be tuned by changing the skew angles to cover a large range of values, from large negative/positive to approximately zero, demonstrating a sizeable CTE tunability. Figure 3-4d-f also demonstrates that the CTE in the *z*-direction depends on the CTE ratio of the constituent materials, $\lambda = \alpha_{s1}/\alpha_{s2}$. If the skew angle, θ, is given, the larger/smaller the λ , the lower (for low CTE concept, Figure 3-3b, d, and e) or higher (for high CTE concept, Figure 3-3g, i, and j) the effective CTE, respectively. Hence the greater the CTE distinction of the constituent solids, the higher the CTE tunability. The magnitude of the three ellipsoids shown in Figure 3-4g-i illustrates that the direction of the tetrahedron $\mathbf{M}$ vector (*z*-direction), i.e. the direction of CTE tunability, follows the direction of a principal axis, i.e. the direction that can yield the lowest CTE magnitude for the case of $\lambda = 2$ (whereas the highest CTE magnitude will be for $\lambda < 1$). The aforementioned building blocks distinguished by their own tunable characteristics lay the foundation for designing spatial lattices with tunable CTE, as shown in the following section.

3.3.3 Generation of 3D bi-material lattices with desired thermal expansion

Here, we propose a scheme that systematically uses the building blocks, TL-1, TL-2, or TN, along with their $\mathbf{M}$ and $\mathbf{N}$ vectors in the CTE tunable direction to program thermal expansion in spatial lattices. Notions of crystal symmetry, in particular from the crystallographic point groups, are applied to the building blocks and used to assemble more complex truss systems that can meet desired CTE requirements. To illustrate the scheme, Sections 3.3.3.1 to 3.3.3.3 present nine examples of lattices that are engineered to attain unidirectional, transverse isotropic, or isotropic controllable CTE. Before doing so, though, we first elucidate the relation between the geometric symmetry in a unit cell and the directions of its thermal expansion, which are typically set a priori by a given application.

In a general case, the thermal expansion requirements a system should attain can be specified by: (i) the magnitude and sign of its CTE, which can be large positive, near zero, or negative, and/or

(ii) the thermal expansion directionality, defining its anisotropic or isotropic behaviour. The former is a requirement mainly governed by the geometry and components of the building blocks, as elucidated in Sections 3.3.2.1 and 3.3.2.2. The latter correlates to the directions of the CTE properties that are governed by the assembly rules of tetrahedral building blocks, such as orientation, symmetry operations, and relative position, as explained below.

System	Characteristic Symmetry	Number of independent coefficients	Tensor referred to axes in the conventional–orientation
Cubic	4 3-fold axes	1	$\begin{bmatrix} \alpha & & \\ & \alpha & \\ & & \alpha \end{bmatrix}$
Tetragonal	1 4-fold axes	2	$\begin{bmatrix} \alpha_1 & & \\ & \alpha_1 & \\ & & \alpha_3 \end{bmatrix}$
Hexagonal	1 6-fold axes		
Trigonal	1 3-fold axes		
Orthorhombic	3 mutually perpendicular 2-fold axes; no axes of higher order	3	$\begin{bmatrix} \alpha_1 & & \\ & \alpha_2 & \\ & & \alpha_3 \end{bmatrix}$
Monoclinic	1 2-fold axes	4	$\begin{bmatrix} \alpha_1 & & \alpha_{13} \\ & \alpha_2 & \\ \alpha_{13} & & \alpha_{33} \end{bmatrix}$
Triclinic	A center of symmetry or no symmetry	6	$\begin{bmatrix} \alpha_{11} & \alpha_{12} & \alpha_{13} \\ \alpha_{12} & \alpha_{22} & \alpha_{23} \\ \alpha_{13} & \alpha_{23} & \alpha_{33} \end{bmatrix}$

Table 3-1: Relation between crystal symmetry and the thermal expansion tensor $\boldsymbol{\alpha}$, specified with respect to the principal directions (i.e. conventional orientations) of the crystals in cubic, tetragonal, hexagonal, trigonal, and orthorhombic systems. Crystals in a monoclinic system have only one fixed principal axis, i.e. the direction of 2-fold axis (with respect to the x_2 direction). Crystals in triclinic system have no fixed principal axis, thus the $\boldsymbol{\alpha}$ tensor is expressed as a general form in the last column. Groups without higher-order axes denote groups containing only 2-fold axes, mirror planes, and inversion center, e.g. orthorhombic, monoclinic, and triclinic systems. [43]

There is a direct relation between the geometric symmetry of building blocks in the unit cell and the symmetry of elements of its thermal expansion tensor. To understand this, notions of crystallographic point groups become handy here. As the crystal properties are governed by the crystal symmetry, analogously the CTE properties of a lattice can be inferred by the geometric relationships of symmetry between building blocks. Following the *Neumann's Principle: if a crystal is invariant with respect to certain symmetry operations, its physical properties must also be invariant with respect to the same symmetry operations*. This is shown in Table 3-1 for several systems, where the effect of crystal symmetry on the second-rank tensor properties is described by the reduction of independent components in its symmetrical tensor. For example, for a crystal with cubic symmetry that is invariant with respect to four 3-fold axes, the CTE can be expressed by a second-rank tensor, $\boldsymbol{\alpha}$, where the number of independent coefficients decreases from six to one; hence the CTE is isotropic. Another example is for a crystal with trigonal symmetry (Figure 3-5a), where the number of independent coefficients decreases to two.

The last column of Table 3-1 illustrates the CTE tensor of the corresponding crystal having its principal directions aligned along the axes defining the reference coordinate system of the crystal, i.e. x_1, x_2, and x_3. In this case, the CTE of a trigonal crystal, taken here as example, can be simply expressed as

$$\alpha_{ij} = \begin{bmatrix} \alpha_1 & & \\ & \alpha_1 & \\ & & \alpha_3 \end{bmatrix}, \tag{3-11}$$

where α_1 and α_3 refer to the CTE along the principal directions. If the reference axes are rotated with respect to the principal directions, the components of $\boldsymbol{\alpha}$ can be just obtained by applying a transformation law for second-rank tensor, through the matrix, $\left(l_{ij}\right)$, such as:

$$\alpha'_{mn} = l_{mi} l_{nj} \alpha_{ij}, \tag{3-12}$$

where the CTE tensor α'_{mn} refers to the coordinate system after transformation, and l_{mi} and l_{nj} represent the components in the transformation matrix $\left(l_{ij}\right)$. The CTE value in any specific direction can then be evaluated through:

$$\alpha = \alpha_{ij} l_i l_j, \tag{3-13}$$

where l_i and l_j are the direction cosines of the original axes with respect to the new rotated axes.

By analogy, the symmetry systems reported above can be readily transferred to assess the CTE of dual-material lattices built from tetrahedral building blocks. In particular during the assembly of building blocks, the symmetrical arrangement of tetrahedra in a unit cell can be chosen to match that of a point group of a crystal. Figure 3-5a and b shows an example for a trigonal system with a 3-fold axes. The screw geometry illustrates that this system relies on a 3-fold axes in which a single geometry is replicated twice through rotation about the axis at $2\pi/3$ intervals. By analogy, Figure 3-5c shows that the trigonal system can be enforced to assemble 4 TNs. The result is the repeating unit in Figure 3-5d, where three TNs form the base of the 3D lattice, and upon their apexes rests the fourth one. All the building blocks have 3-fold axes of symmetry, which is also the rule of symmetry of their spatial arrangement. Hence, the correspondence between the symmetry relationship of the building blocks within the unit cell and that of the crystal system used to assemble them, makes the CTE tensor of the overall lattice feature physical characteristics identical to those of a trigonal crystal. For the lattice in Figure 3-5d, the CTE in Eq. (3-11) is defined by only two independent coefficients, i.e. α_1 and α_3, with only α_3 having CTE tunability. Hence the unit cell holds a unidirectional CTE tunability along the principal direction x_3. Therefore, the calculation of the CTEs along the principal directions reduces to the mere appraisal of the $\mathbf{M}$ and $\mathbf{N}$ vectors of its building block, and the CTEs in any other directions can be obtained via Eq. (3-13).

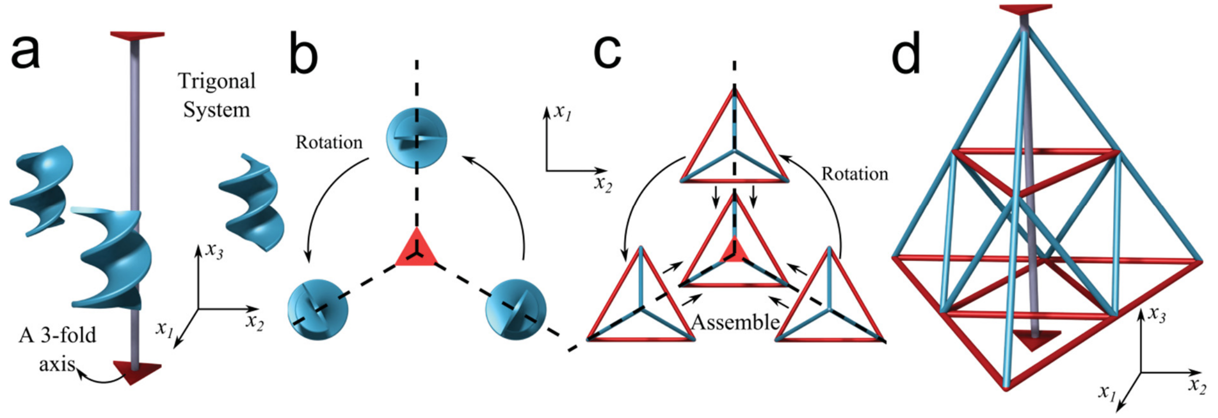

Figure 3-5: Trigonal crystallographic symmetry group applied to the generation of a spatial bi-material lattice with two independent coefficients, α_1 and α_3, of the CTE tensor: (a) screw geometry illustrating the 3-fold axes of symmetry with its top view shown in (b), (c) top view of building blocks assembled with 3-fold axes, and (d) axonometric view of the resulting unit cell.

The simple example above focusing on one symmetry system has demonstrated how the crystallographic point groups can guide the relative arrangement of building blocks in the repeating unit. This is just one, among others, of the possible systems listed in Table 3-1. When one of these symmetry systems is enforced to arrange building blocks in a unit cell, then a direct correlation emerges between the geometric symmetry of the building block and the symmetry of the elements of its CTE tensor. The elements in the CTE tensor that are independent represent the CTEs of the overall lattice in the principal directions, which can be evaluated via $\mathbf{M}$ and $\mathbf{N}$ vector analysis. This is shown in the following sections, where a crystal symmetry system is used to assemble building blocks into a repeating unit that can satisfy prescribed CTE requirements.

3.3.3.1 Unidirectional CTE requirement

There is theoretically an infinite number of unit cells that can be proposed to meet the unidirectional requirement of CTE. Figure 3-6a-c shows three of them, each constructed with its own building block and a specific relation of symmetry, but all have unidirectional CTE tunability in the vertical direction (x_3).

The first unit cell in Figure 3-6a consists of eight TL-1 building blocks assembled via reflection and rotational transformations to make each adjacent block appear in an upside-down position. In this unit cell, there are only three mutually perpendicular 2-fold axes with an inversion center but no axes of higher order, e.g. 3-fold or 4-fold axes; hence, the unit cell has an orthorhombic symmetry (Figure 3-6g). All ML vectors of TL-1s in Figure 3-6a are parallel with the vertical direction and therefore the CTE-tunable mechanism of TL-1 governs the thermal deformation of the unit cell in the vertical direction. As revealed in Table 3-1, the CTE tensor of an orthorhombic unit cell has three independent components with values equivalent to the principal CTEs. Although the overall CTE is orthotropic, the entire lattice shows unidirectional CTE tunability with magnitude of $\alpha_3 = \alpha_{z,TL-1}$ (Eq. (3-8)) that is tunable in the vertical direction only. Along the other two principal directions $\alpha_1 = \alpha_{s1}$ and $\alpha_2 = \alpha_{s2}$, the periodic lattice can uniformly expand with the CTE of its components. The second unit cell shown in Figure 3-6b is structured with eight TL-2 building blocks via only rotation around, and translation along, the vertical direction. This unit cell has a 4-fold axis with a middle mirror plan, and thus classed as tetragonal symmetry. In its CTE tensor (Table 3-1), there are only two independent coefficients: $\alpha_1 = \alpha_{s1}$ and $\alpha_3 = \alpha_{z,TL-2}$ (Eq. (3-9)). This unit cell, although obtained with symmetry relationship different from that of the previous model, still keeps all ML vectors of the building blocks along the vertical direction and therefore results in a unidirectional CTE controllable in the vertical direction. The unit cell in Figure 3-6c uses the TN tetrahedron, which has a trigonal symmetry (Figure 3-5b and Figure 3-6i). As discussed above, the only two independent coefficients are $\alpha_1 = \alpha_{s1}$ and $\alpha_3 = \alpha_{z,TN}$ (Eq. (3-10)), thereby demonstrating unidirectional CTE tunability.

The three concepts in Figure 3-6 feature dissimilar symmetry systems constructed via different affine transformations, however, they all keep the $\mathbf{M}$ vectors in the CTE tunable direction along direction x_3. The direction x_3 of each concept follows the direction of the 2-fold, 3-fold, and 4-fold axes, which are principal directions. Each unit cell, therefore, inherits the CTE tunability of its building block in the principal direction x_3. Figure 3-6p-r illustrates their omnidirectional CTEs in a spherical coordinate system, from which a pertinent symmetry in thermal expansion appears for each case. The direction with the lowest CTE (dark blue in the legend), i.e. a single vertical axis for each unidirectional concept, is the principal direction of CTE tunability. No CTE tunability is viable along the other principal directions, i.e. plane $x_1 - x_2$.

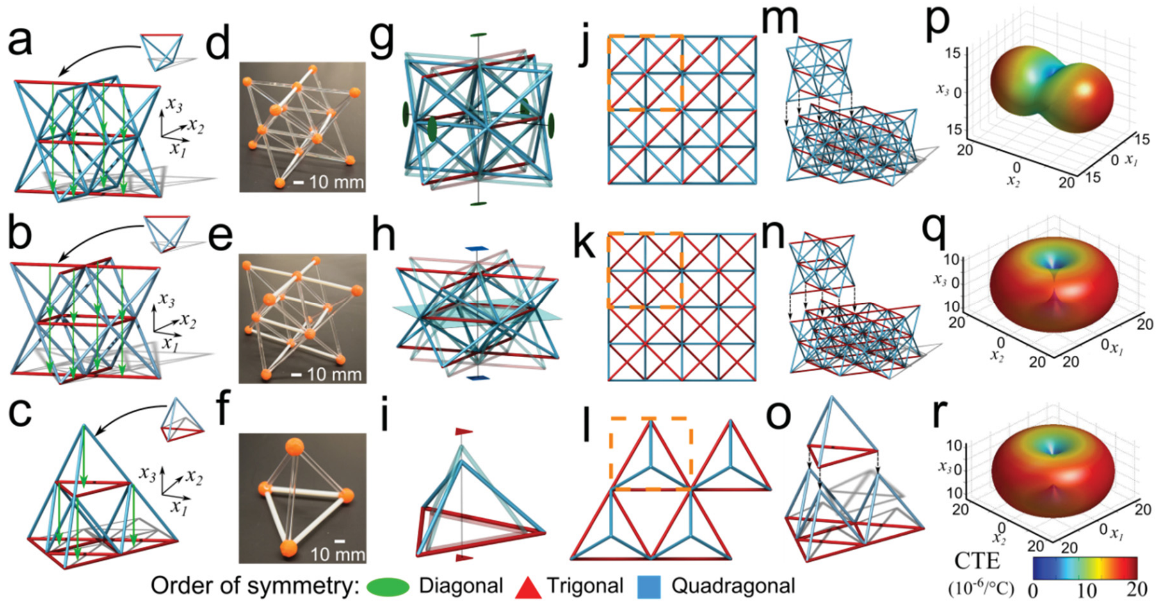

Figure 3-6: Unit cells with unidirectional CTE tunability: (a) TL-1 concept, (b) TL-2 concept, and (c) TN concept. Green arrows represent the ML vectors of the building blocks, all oriented along the x_3 direction. (d), (e), and (f) are images of their physical ball-and-stick models. (g), (h), and (i) show the deformed and undeformed concepts with the main characteristic symmetry of the building block arrangement. The order of rotational symmetry is given by one of the three graphical symbols: a cusped oval, a triangle, and a square. (j), (k), and (l) are the top view of the unit cell assembly. (m), (n), and (o) show an axonometric view of the unit cell assembly. (p), (q), and (r) show CTE magnitude plotted in polar coordinate system with respect to the principal directions, i.e. x_1, x_2, and x_3; the semi-axes of each CTE ellipsoid are the CTE coefficients, $|\alpha_1|$, $|\alpha_2|$, and $|\alpha_3|$ of the corresponding unit cell.

3.3.3.2 Transverse isotropic CTE requirement

Figure 3-7a-c shows three unit cells, each assembled with its own building block but all have trigonal symmetry to meet transverse isotropic CTE requirement. In the first example (Figure 3-7a), low-CTE stationary lines of six TL-1s form the inner core with two sets of triadic building blocks at the same altitude (x_3) arranged with equal angular spacing. On the middle mirror plane (Figure 3-7g), three additional low-CTE bars are added, combined with the six low-CTE stationary lines, forming a central triangular bipyramid. This operation, considered along with the periodic tessellation in Figure 3-7m, is enforced to lock any mechanism as well as to make the unit able to perform as a pin-jointed structure. As shown in Figure 3-7g, the unit cell consists of 3-fold rotational symmetry, analogous to the trigonal crystal, it has only two independent components in the CTE tensor, α_1 and α_3. All TL-1 ML vectors deviate outward from the vertical direction by an identical deviation angle, γ ($\gamma \in \left(0^\circ, 90^\circ\right)$ with $\gamma = 75^\circ$ in Figure 3-7a), which, together with the skew angle and component CTEs, controls the horizontal effective CTE with in-plane isotropic CTE tunability ($\alpha_1 = \alpha_2$). In the out-of-plane principal direction, i.e. x_3, if the tessellation of unit cells (shown in Figure 3-7j and m only along plane $x_1 - x_2$ for visual simplicity) allows connection only at the peaks of the triangular bipyramid, there is no CTE tunability, resulting in $\alpha_3 = \alpha_{s2}$. Thus, the overall effective CTEs of the unit cell in Figure 3-7a are expressed as:

$$\begin{cases} \alpha_1 = \alpha_2 = \dfrac{\alpha_{s2}\cos\theta\tan^{-1}\gamma + \left[\alpha_{s2} - \left(\alpha_{s1} + \alpha_{s2}\right)\cos^2\theta\right]\big/\xi}{\cos\theta\cot\gamma + \xi} \\ \alpha_3 = \alpha_{s2} \end{cases}, \tag{3-14}$$

where $\xi = \left(1 - 2\cos^2\theta\right)^{1/2}$.

Similarly, for the second example in Figure 3-7b, TL-1s are replaced by TL-2 building blocks to construct a unit cell with transverse isotropic controllable CTE. A triangular bipyramid core is constructed via six high-CTE stationary lines and three high-CTE bars added in the middle mirror plane. All TL-2s have an identical γ ($\gamma \in \left(0^\circ, 90^\circ\right)$ with $\gamma = 75^\circ$ in Figure 3-7b). The symmetry relationship of the building blocks within the unit cell in Figure 3-7b is identical to that of TL-1 concept (Figure 3-7a), and the unit cell has thermal expansion behaviour expressed as:

$$\begin{cases} \alpha_1 = \alpha_2 = \dfrac{\alpha_{s1}\cos\theta\tan^{-1}\gamma + \left(\alpha_{s2} - 2\alpha_{s1}\cos^2\theta\right)\big/\xi}{\cos\theta\cot\gamma + \xi} \\ \alpha_3 = \alpha_{s1} \end{cases}. \tag{3-15}$$

The third example in Figure 3-7c shows that TN building blocks can also be manipulated to construct a unit cell with transverse isotropic CTE. Six TNs deviate from the vertical direction by γ ($\gamma \in \left(0^\circ, 90^\circ\right]$ with $\gamma = 90^\circ$ in Figure 3-7c) and round up their high-CTE base members, together with the three high-CTE bars added on the middle mirror plane, to form the edges of a central polyhedron. Figure 3-7i shows the unit cell in a 3-fold rotational symmetry, analogous to a trigonal crystal, resulting in only two independent components in the CTE tensor, α_1 and α_3. Within the horizontal plane, the concept has in-plane isotropic CTE tunability ($\alpha_1 = \alpha_2$). The out-of-plane tessellation (along plane $x_1 - x_2$ in Figure 3-7o) reveals a mere connection via the high-CTE cores, yielding $\alpha_3 = \alpha_{s1}$ with no CTE tunability in the vertical direction. For this reason, the thermal expansion behaviour of the unit cell in Figure 3-7c is expressed by:

$$\begin{cases} \alpha_1 = \alpha_2 = \dfrac{\left(3\alpha_{s2} - 4\cos^2\theta\alpha_{s1}\right)/\zeta + \alpha_1 \cos\theta}{2\sqrt{3}\cos^2\theta + \zeta} \\ \alpha_3 = \alpha_{s1} \end{cases}, \tag{3-16}$$

where $\zeta = \left(3 - 4\cos^2\theta\right)^{1/2}$.

We remark that the top views shown in Figure 3-7j, k, and l are the 3D analogues of previous 2D concepts [23]. The assembly of other spatial unit cells can be inspired by other 2D cell topologies in the literature [3, 20]. Furthermore, as shown in the examples of Supplementary Material Section 3.8.1, the vertical direction (x_3) can also possess CTE tunability by decreasing the deviation angle, γ. Figure 3-7p-r show the omnidirectional CTEs of the concepts in a spherical coordinate system. A central horizontal plane circularly shaped (dark blue in Figure 3-7p to r) shows principal directions with CTE tunability for each transverse isotropic concept. Contour plot symmetry in Figure 3-7p-r also reflects the symmetry in thermal expansion, such as no CTE tunability is viable in the vertical direction.

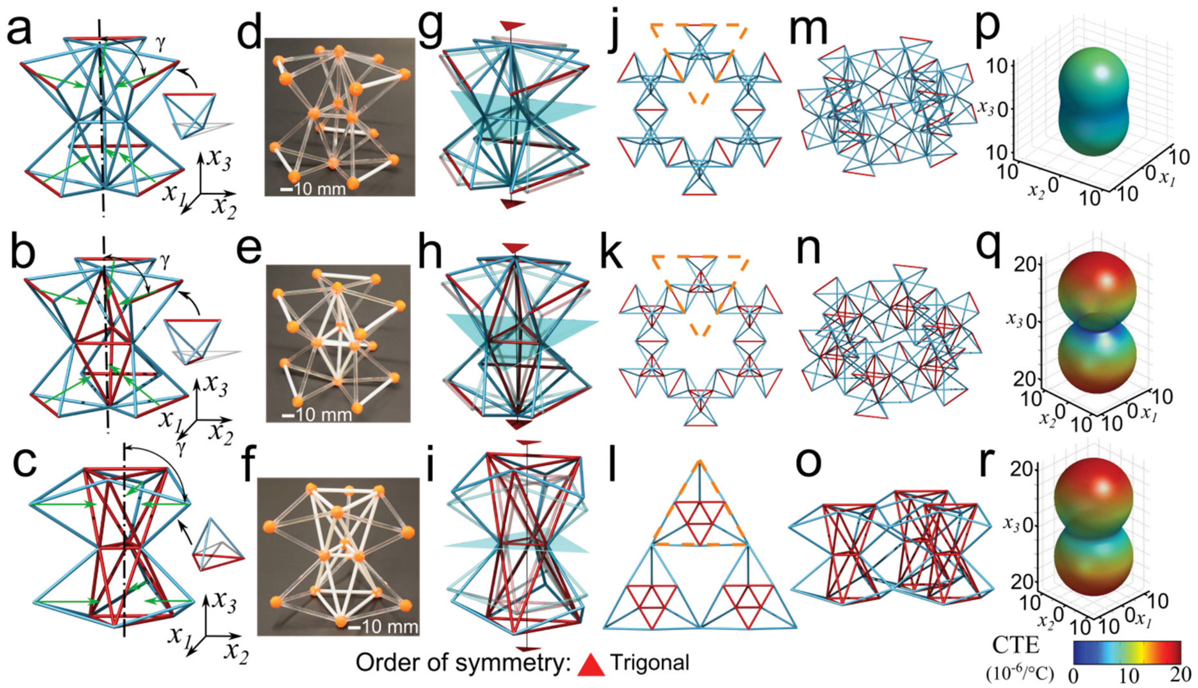

Figure 3-7: Low-CTE unit cells with transverse isotropic CTE tunability: (a) TL-1 concept, (b) TL-2 concept, and (c) TN concept. Green arrows represent the ML vectors of the building blocks. (d), (e), and (f) are images of their physical ball-and-stick models. (g), (h), and (i) show the deformed and undeformed concepts with main characteristic symmetry of the building block arrangement. The order of three-fold rotational symmetry is given by the triangle symbol. (j), (k), and (l) are the top view of the unit cell assembly; (m), (n), and (o) show an axonometric view of the unit cell assembly. (p), (q), and (r) show CTE magnitude plotted in polar coordinate system with respect to the principal directions, i.e. x_1, x_2, and x_3; the semi-axes of each CTE ellipsoid are the CTE coefficients, $|\alpha_1|$, $|\alpha_2|$, and $|\alpha_3|$ of the corresponding unit cell.

3.3.3.3 Isotropic CTE requirement

Figure 3-8 shows three unit cells, one for each row, possessing isotropic controllable CTE, with TL-1s, TL-2s, and TNs as their building blocks, respectively. A regular octahedron core is constructed by either stationary lines of TL building blocks or high-CTE base triangles of TNs. This monolithic core has a uniform thermal expansion in all directions and connects all building blocks via identical distance to the center of each unit cell for given angular space. All the unit cells have a cubic envelope as the unit cell domain. Along the four body diagonal directions of the cubic domain, four 3-fold axes can be found for each unit cell (Figure 3-8g-i), thus showing a cubic symmetry. Analogous to the cubic crystal, there is only one independent coefficient in the CTE tensor of each concept, and therefore each unit cell has identical thermal expansion in all directions. Hence, the tessellated periodic lattices, with all unit cells connected by either stationary nodes or stationary lines (Figure 3-8j-o), feature a CTE that is isotropic with adjustable magnitude given by:

$$\alpha_{Iso-TL-1} = \frac{\alpha_{s2}\cos\theta + \left[\alpha_{s2} - \left(\alpha_{s1} + \alpha_{s2}\right)\cos^2\theta\right]/\xi}{\cos\theta + \xi}, \qquad \text{for Figure 3-8-a;} \qquad (3\text{-}17)$$

$$\alpha_{Iso-TL-2} = \frac{\alpha_{s1}\cos\theta + \left(\alpha_{s2} - 2\alpha_1\cos^2\theta\right)/\xi}{\cos\theta + \xi}, \qquad \text{for Figure 3-8-b;} \qquad (3\text{-}18)$$

$$\alpha_{Iso-TN} = \frac{\alpha_{s1}\sqrt{2}\cos\theta + \left(\alpha_{s2} - 4/3\,\alpha_{s1}\cos^2\theta\right)/\zeta}{\sqrt{2}\cos\theta + \zeta}, \qquad \text{for Figure 3-8-c.} \qquad (3\text{-}19)$$

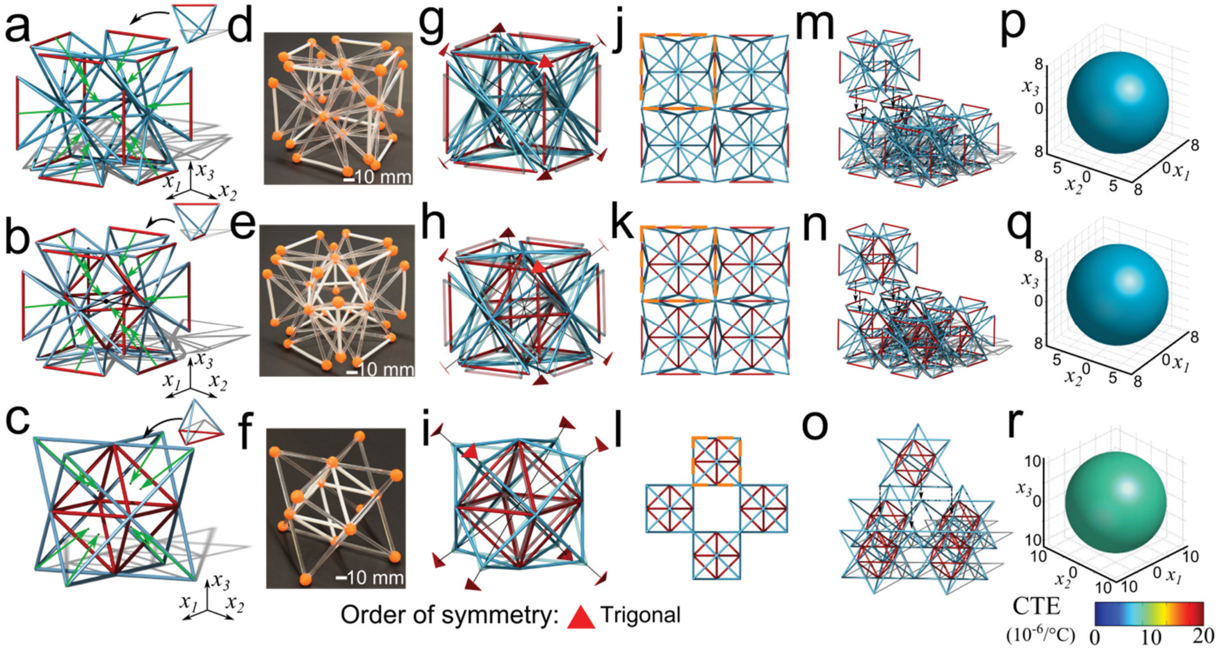

Figure 3-8: Unit cells with isotropic CTE tunability: (a) TL-1 concept, (b) TL-2 concept, and (c) TN concept. Green arrows represent the ML vectors of the building blocks. (d), (e), and (f) are images of their physical ball-and-stick models. (g), (h), and (i) show the deformed and undeformed concepts with the main characteristic symmetry of the building block arrangement. The order of three-fold rotational symmetry is given by the triangle symbol. (j), (k), and (l) are

the top view and assembly. (m), (n), and (o) show an axonometric view of the unit cell assembly. (p), (q), and (r) show CTE magnitude plotted in polar coordinate system with respect to the principal directions, i.e. x_1, x_2, and x_3; the semi-axes of each CTE ellipsoid are the CTE coefficients, $|\alpha_1|$, $|\alpha_2|$, and $|\alpha_3|$ of the corresponding unit cell.

The unit cells examined in Figure 3-8 are some among many other possibilities. Figure 3-2d shows another example of a unit with isotropic CTE tunability, previously studied in the literature [3]; this cell has an analogous spatial structure of carbon atoms in a diamond, i.e. cubic symmetry. More examples are shown in Supplementary Material Section 3.8.1. Figure 3-8p-r indicates the omnidirectional CTEs of the concepts in a spherical coordinate system. Evidently, the isotropic CTEs are described by monocoloured spheres, reflecting the symmetry in thermal expansion. The principal directions can be randomly selected within the entire spherical space, yet obtaining the identical lowest CTE for each unit cell.

3.3.3.4 Geometrical constraints of compound unit cells

For the nine concepts illustrated in Figure 3-6 to 8, the effective CTEs in the principal direction can be tuned through a change of the skew angle, θ, of the building block. The range of θ is restricted by certain values that preserve the tetrahedral shape of the building block, as well as avoid causing collision between adjacent unit cells during thermal expansion. For concepts with transverse isotropic CTE, the range of θ is also governed by γ. Table 3-2 shows the allowable range of θ for each cell topology with φ representing the packing factor of the lattice. A packing factor correlates to a given tessellation. For example, a packing factor of 100% is shared by the unit cells shown in Figure 3-6m-o. In contrast, for the unit cells with isotropic CTE given ranges of their skew angles result in tessellations with lower packing factors, such as 50% for the tessellation shown in Figure 3-8o ($\theta = 60°$). Differences in the packing factor are controlled by the requirement of the inner polyhedron, e.g. octahedron in Figure 3-8c, to thermally expand without touching adjacent cells.

	Unidirectional	Transverse Isotropic	Isotropic
TL-1 and TL-2	$\left(45^\circ, 90^\circ\right)$ $\varphi = 100\%$	$\left(45^\circ, \arccos\left(1+\csc^2\gamma\right)^{-\frac{1}{2}}\right]$, $\varphi = 50\%$	$\left(45^\circ, \arccos\left(\sqrt{3}/3\right)\right]$ $\varphi = 50\%$
		$\left(\arccos\left(1+\csc^2\gamma\right)^{-\frac{1}{2}}, 90^\circ\right)$, $\varphi = 100\%$	$\left(\arccos\left(\sqrt{3}/3\right), 90^\circ\right)$ $\varphi = 100\%$
TN	$\left(30^\circ, 90^\circ\right)$ $\varphi = 100\%$	$\left(30^\circ, \arccos\left(\frac{\left(3-\cos\gamma\right)^2}{3\sin^2\gamma}+\frac{4}{3}\right)^{-\frac{1}{2}}\right)$, $\varphi = 50\%$	$\left(30^\circ, 60^\circ\right]$, $\varphi = 50\%$
		$\left(\arccos\left(\frac{\left(3-\cos\gamma\right)^2}{3\sin^2\gamma}+\frac{4}{3}\right)^{-\frac{1}{2}}, 90^\circ\right)$, $\varphi = 100\%$	$\left(60^\circ, 90^\circ\right)$, $\varphi = 100\%$

Table 3-2: Admissible range of the skew angle, θ, for the building blocks of the concepts visualized in Figure 3-6 to 8. γ and φ represent the deviation angle and packing factor respectively.

3.3.3.5 Summary points for prescribing thermal expansion in spatial lattices

There are plentiful ways to construct 3D lattices from tetrahedral building blocks. Below, the key notions explained above are summarized to help assemble tetrahedron-based lattices that can meet given magnitude and directional requirements of thermal expansion. The distinguishing features are the building blocks with the definition of their ML and TD vectors, and the symmetry construction operations used to assemble them in the repeating unit.

- *Building blocks with their thermal expansion.* The bi-material tetrahedron is the smallest building block chosen here for generating a periodic 3D lattice. Nine relevant material permutations are available (Figure 3-3b-j), among which the most practical are those with stationary lines, TL-1 and TL-2, and with stationary node, TN. For each of them, the material length vector, ML, and the thermal displacement vector, TD, provide a visual and handy description of the magnitude and direction of their thermal expansion. They assist in meeting requirements of given CTE magnitude and closed form expressions are given in Section 3.3.2 to quantify them.

- *Unit cell construction for prescribed CTE behaviour.* Building blocks can be used to assemble complex compound units either with unidirectional CTE tunability (e.g. Figure 3-6a) or with a number of tunable CTE directions (e.g. Figure 3-8c), as prescribed by the application requirements. The crystal systems in Table 3-1 can assist their arrangement to satisfy directional requirements. If the symmetry relations of one crystal system transfer to the geometrical arrangement of building blocks in a unit cell, analogously the independent tensor components of that crystal system return into the CTE tensor of the overall lattice. Here, the tensor components of the unit cell represent the CTEs in the principal directions, either with or without CTE tunability, of the overall lattice. By following this strategy the overall thermal expansion of a spatial lattice built from compound units can be assessed through the ML and TD vectors of its constitutive building blocks (Section 3.3.2).

In this summary, we also remark that unit cell construction should also meet tessellation requirements, such as those ensuring minimum static and kinematic determinacy, among others. If the assembly process leads to an unstable mechanism, additional members are necessary to lock in any mechanism, and additional struts can be inserted to match the CTE of its surrounding elements so as to avoid altering the direction(s) of CTE-tunability. In addition, because there are multiple tetrahedral building blocks and numerous relations of symmetry to choose from, the number of 3D tessellations capable of satisfying given CTE requirements can be countless. This work has presented nine of them (Figure 3-6 to 3-8) obtained by implementing the scheme presented here, and the following section describes their proof-of-concept fabrication and thermal testing. Additional concepts showing the viability of the method are given in Supplementary Material Section 3.8.1.

3.4 Fabrication and experimental validation

3.4.1 Component materials

This section presents the fabrication and CTE testing of (i) the building blocks, TN and TL-2, made from metallic constituents, and (ii) the nine lattice concepts shown in Figure 3-6 to 3-8, made from polymers. The six constituent materials selected are: Al6061, Ti-6Al-4V, and Invar-36 as metallic constituents; and acrylic, Teflon® PTFE, and ABS as polymer constituents. Table 3-3 shows their relevant properties.

Material	Al 6061	Ti-6Al-4V	Invar-36	Acrylic	PTFE	ABS
Young's modulus (GPa)	70.8	113.8	140.0	3.2	0.475	2.6
CTE ($\times 10^{-6}$/℃)	23.0	11.5	1.5	67.0	123.0	94.5

Table 3-3: Properties of solid materials for proof-of-concept fabrication [41]

3.4.2 Engineering of specimens

3.4.2.1 Fabrication of building block samples

Testing samples of building blocks were fabricated via pin-jointed metallic bars (Figure 3-9a-d). Ti-6Al-4V shafts (low-CTE) were cut and sanded to the desired length (Figure 3-9b and d) with each end shaped into a crevice. A flake in the shape of a ring tongue terminal was fastened in the crevice of bars by interference fit and strengthened via administering epoxy glue (LePage Epoxy Gel, Henkel, Canada) to serve as a hinge axle sleeve for pinned joints. As shown in Figure 3-9, Al6061 shafts (high-CTE) are thicker (diameter of 6.4 mm) than the Ti-6Al-4V bars (diameter of 3.2 mm) so as to construct a stable base with through-holes drilled directly to serve as hinge axle sleeves. All the high CTE bars have given length of 50mm (Figure 3-9b and d), and the length of low-CTE bars vary for modifying the skew angle at given values. Then the assembly of the different tetrahedral samples were completed using bolts, screw nuts and washers. Since only rotation occurs and no bending moment appears at the joints, the tested CTE of pin-jointed building blocks are validated via closed-form equations in Section 3.3.3 relying on the pin-jointed assumption. Furthermore, in the fabricated prototypes shown in Figure 3-9, the length of the flakes (totalling about 12 mm at both ends), compared with the typical length of the shaft (about 40-55 mm), is not negligible. Thus, the thermal effect of flakes on the overall effective CTE of lattices is taken into account to amend the analytical model as further explained in Supplementary Material Section 3.8.2.

3.4.2.2 Fabrication of unit cell specimens

To ease the understanding of the spatial arrangement of building blocks in all unit cells, we built ball-and-stick models as proof-of-concepts (Figure 3-6 to 3-8). Connection balls (10 mm diameter) have several blind holes (with a 1.6 mm diameter and 2 mm depth) in different orientations on the surface (Figure 3-9g) to connect sticks (Figure 3-9e and f). All the spheres are 3D printed (printer: Original Prusa i3 MK2) by ABS. The sticks were laser cut into different lengths, all from 1.6-mm-diameter rods made from either PTFE (high-CTE) or acrylic (low-

CTE). Both ends of the sticks were plugged into the blind holes of spheres and then rigidly fixed by resin glue (LePage Epoxy Gel, Henkel, Canada). The thickness of the resin adhesive layer was very thin making the thermal expansion of resin glue negligible. In contrast, the ABS connection ball had a non-negligible thermal expansion, and this deviation is considered in a later section validating experimental measures against theoretical and simulation results.

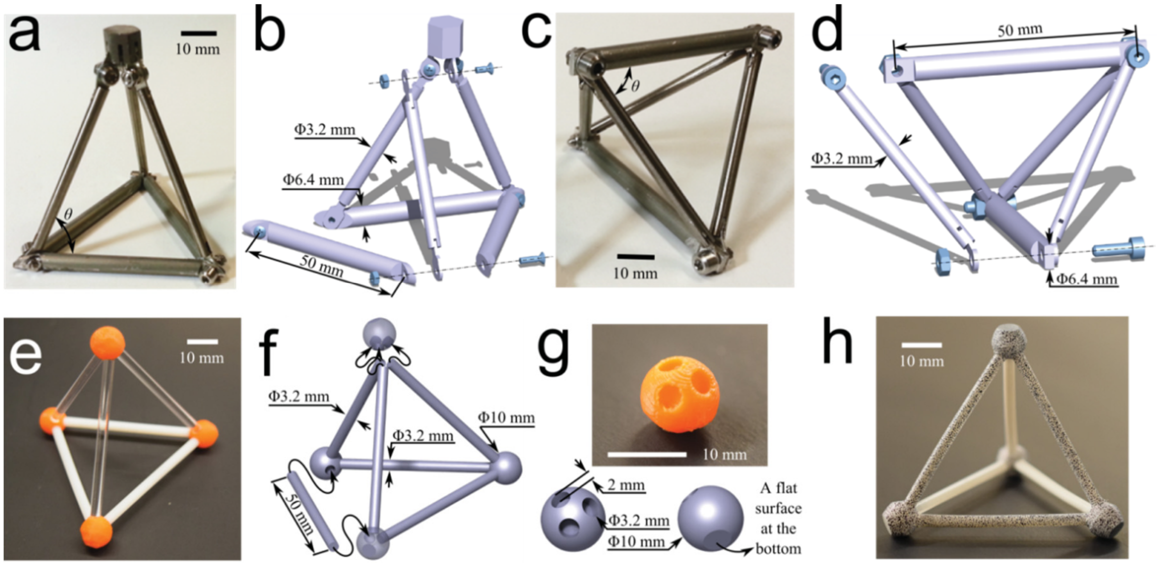

Figure 3-9: Testing samples: (a) TN (components: Al6061 and Ti-6Al-4V); (b) assembly drawing of a TN; (c) TL-2 (components: Al6061 and Ti-6Al-4V); (d) assembly drawing of a TL-2; (e) TN concept with rigid joints (components: acrylic and PTFE for bars and ABS for joints); (f) assembly drawing of proof-of-concepts with rigid joints; (g) ball for rigid joint (a flat surface at the bottom is used to ensure continuous contact with the carrier of the 3D printer); (h) testing sample with black and white pattern for DIC testing.

Moreover, since the CTE properties of the concepts here introduced are primarily dependent on the unit cell geometry besides the CTEs of the constituent solids, the principles can be applied to systems across a wide range of length scales, and hence fabricated with both conventional and advanced methods. Additive manufacturing is a viable method that can be effortlessly used to assemble in large volume bi-material lattices with smaller element size, as demonstrated by recent works appeared in the literature on this topic [30, 35, 44].

3.4.3 Experimental method

Both tetrahedral building blocks (Figure 3-9) and compound unit cells (Figure 3-6 to 8) were experimentally investigated to validate their CTEs. For the former, 12 physical samples were tested to verify the respective theoretical models of TL-2 and TN building blocks (Eqs. (3-9) and (3-10) in Section 3.3.2.1) with two dissimilar pair of material combinations and three different skew angles (see Supplementary Material Section 3.8.2 for the images of the physical samples of the building blocks). The first material combination consisted of Al6061 and Ti-6Al-4V (i.e. Al/Ti), and the second consisted of Al6061 and Invar (i.e. Al/Invar). In all cases, Al was the high CTE material while Invar and Ti were the low CTE materials. The three skew angles of the building blocks for each material combination varied between 53° and 65° with approximately equal angle difference. For example, if the 12 samples were organized into four sets of three, the first set would consist of three TL-2 samples made from Al/Ti with skew angles 53.5°, 61.7° and 63.7°, respectively. Besides building blocks, nine physical samples of the compound unit cells were tested, one for each of the concepts shown in Figure 3-6 to 8 (see Supplementary Material Section 3.8.2 for the images of the compound unit samples). The skew angles of all samples were set to 60°, and the CTEs along the principal directions were measured by assessing the relative thermal displacement of the connection balls.

3D DIC tests (schematic setup shown in Supplementary Material Section 3.8.2) were performed to measure the thermal displacement of all samples with randomly distributed black and white pattern painted on the surface (Figure 3-9h). DIC testing consists of capturing images, before and after heating the sample within a heating chamber, at selected temperatures so that elongation can be measured. Testing temperature was monitored and managed from 25℃ to 75℃ (for polymer samples) or to 150℃ (for metallic samples) through a PID (proportion-integration-differentiation) controller (CN7800, Omega, US). A data acquisition system (NI cDAQ 9174) was used to measure the temperature heterogeneity via collecting three thermocouples from different locations in the chamber. The temperature heterogeneity was regulated within 5% of the real-time temperature through the application of a rotational air fan. DIC system calibration ensured an epipolar projection error below 0.01 pixel, i.e. the average error between the position where a target point was found in the image and the theoretical position where the mathematical calibration model located the point. Two CCD (charge coupled device) cameras (PointGrey, Canada) were used to focus on an area of 240×200 mm^2 with a resolution of 2448×2048 pixel; based on the image resolution, any deformation smaller than 0.98 μm (0.01 pixel) was merged with the epipolar projection error. Using the DIC correlation software, Vic-3D (Correlate Solution Inc.), virtual extensometers were placed on the reference image and tracked through the images to measure the displacement between pairs of pixel subsets. The thermal deformation field (Figure 3-10) was obtained from the relative displacement between these pairs of subsets. The effective CTE was calculated from thermal strain and temperature change. Finally, the accuracy of the whole testing system was verified with CTE measurements of a solid material, Al6061, taken from a commercial thermomechanical analyzer, TMA Q400 (TA Instrument, US). A comparison of their measured (22.6×10^{-6}/°C) and DIC predicted mean CTE (23.0×10^{-6}/°C) shows an error of 1.7%. The epipolar projection error is at 0.98 μm, which governs the smallest measured CTE value of the samples, i.e. 0.27×10^{-6}/°C. Hence, the low magnitude of these errors warrants the required accuracy for the DIC system used in this work.

3.4.4 Experimental results

The thermal testing results of both the building blocks and compound unit cells are here compared with results from either numerical analysis (Figure 3-10) or closed-form expressions (Figure 3-11). The role of component materials and skew angle on the effective CTE is emphasized. In addition, the effect of connection type, either pin-joint (building blocks) or rigid-joint (unit cells), is assessed to validate the pin-jointed assumption of the closed-form expressions derived for ideal building blocks and compound unit cells.

As shown in Figure 3-10a-h, a TL-2 and a TN, both pin-jointed with similar θ and identical components of Al/Ti, are taken as representatives to illustrate the tunable thermal displacement that each tetrahedron can provide along the principal directions. The horizontal thermal displacement shown in Figure 3-10 (a and b for TL-2 with $\theta = 61.7^{\circ}$, e and f for TN with $\theta = 63.3^{\circ}$) indicates that for both building blocks, the effective CTE is high and positive (23×10^{-6}/°C), identical to that of the high-CTE constituent Al, i.e. no CTE tunability. In the vertical direction of TL-2 (Figure 3-10c and d), the nearly alike light-green colour on nodes used for CTE measurement (i.e. nodes B1 and B2 in Figure 3-10d) indicates a near zero distance change. Thus, the effective CTE of TL-2 specimen in the vertical direction is almost vanishing ($3.70 \times$

10^{-6}/°C). In contrast, along the vertical direction of TN (Figure 3-10g and h), the distance between the two corresponding nodes, D1 and D2 in Figure 3-10h used for CTE measurement, increases during thermal expansion, which results in a positive effective CTE (8.42×10^{-6}/°C), a value below those of its constituents Al (23×10^{-6}/°C) and Ti (11.5×10^{-6}/°C). Thus for similar skew angle and identical constituents, TL-2 can attain a lower CTE than TN.

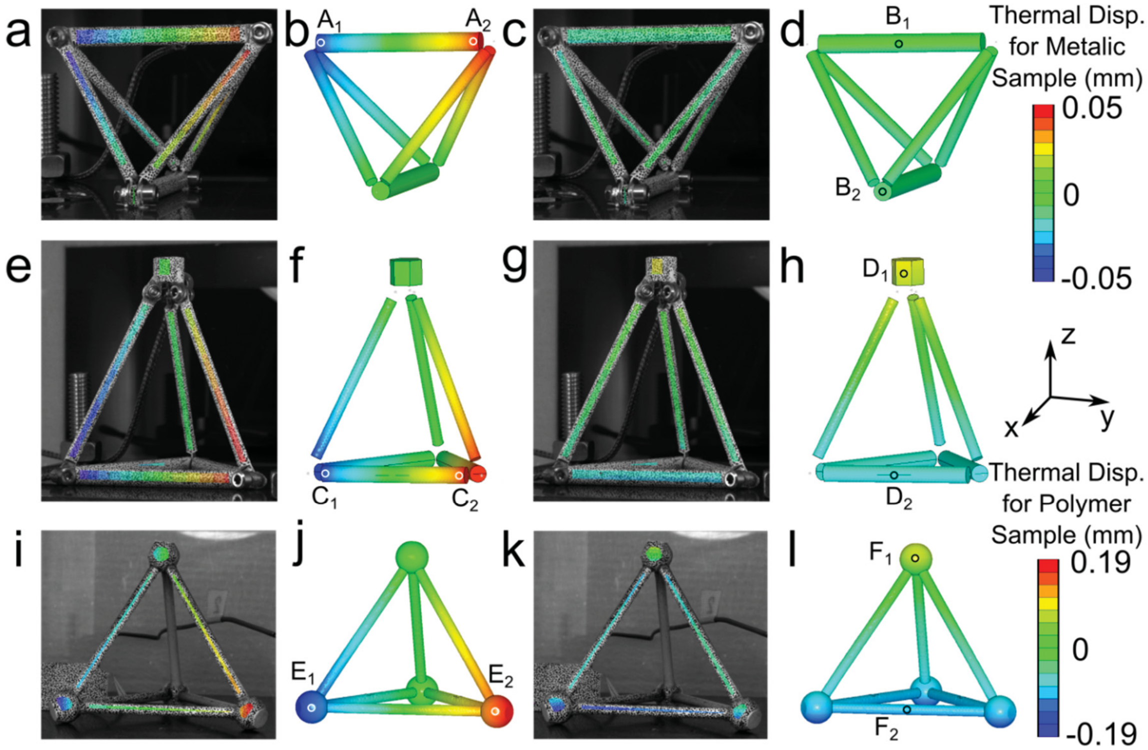

Figure 3-10: Thermal displacement distribution in a pin-jointed TL-2 ($\theta = 61.7^\circ$, Al/Ti) measured experimentally (a and c), and computationally (b and d), in the horizontal and vertical directions, respectively. Thermal displacement distribution in pin-jointed TN ($\theta = 63.3^\circ$, Al/Ti) and rigid-jointed TN ($\theta = 60^\circ$, acrylic/Teflon) tested (for pinned: e and g; for rigid: i and k) and computed numerically (for pinned: f and h; for rigid: j and l) in the horizontal and vertical directions, respectively.

To assess the assumption of the unit cell connections, pin- versus rigid-joints, we compare the results shown in Figure 3-10e-h, to those in Figure 3-10i-l illustrating the tested thermal displacement distribution of a unit cell specimen (Figure 3-6f). In both directions, the thermal distribution of the former made of Al and Ti, parallel that of the latter, made of acrylic and PTFE, despite the difference in magnitude caused by each given pair of constituent materials.

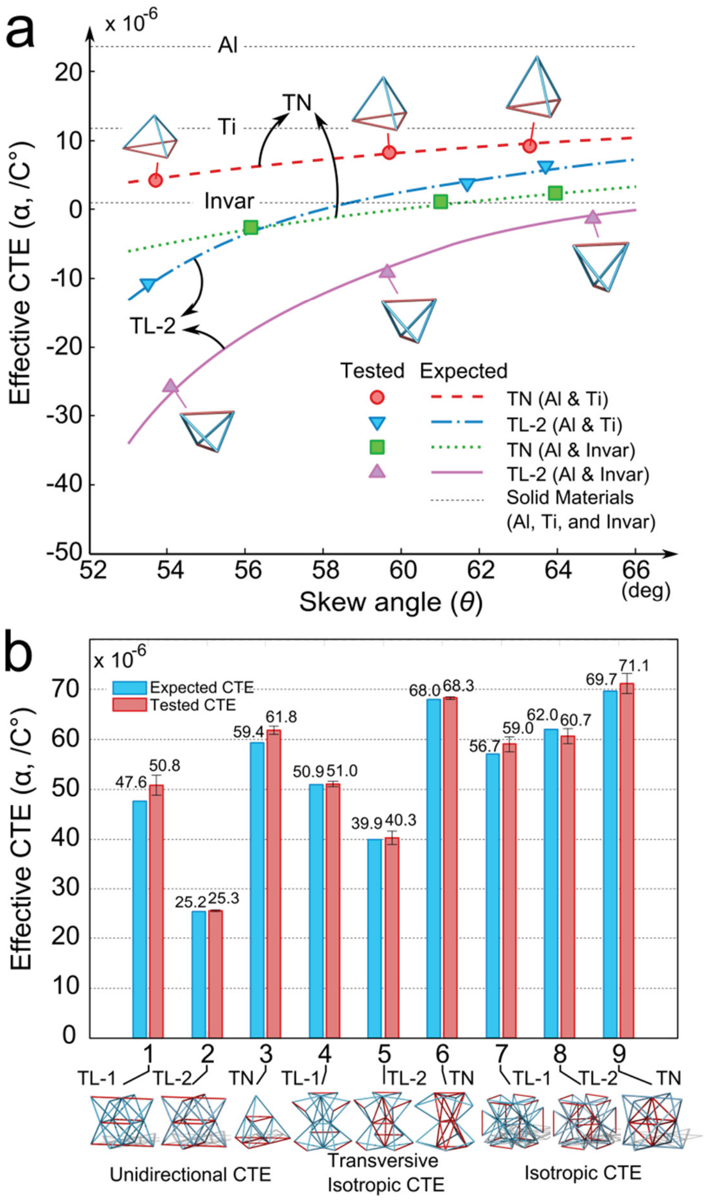

Figure 3-11: (a) Predicted curve and experimental results of effective CTE for Al/Ti and Al/Invar building blocks (TL-2 and TN) within a range of skewness, along with the CTE of the solid materials. (b) Predicted and experimental CTE results along the principal direction/s: vertical direction (x_3) for the concepts with unidirectional CTE and principal directions within the plane $x_1 - x_2$ for other concepts here examined.

Figure 3-11a illustrates the impact of the skew angle, building block type, and component material on the effective CTE of building blocks. For all sets of samples, the CTE reduces significantly with decreasing skew angle, whereas for high values the CTE is less sensitive; nevertheless, CTE tuning across the range of skew angle here considered can be achieved for both TN and TL-2. In addition, for prescribed pair of materials, i.e. (Al/Ti) and (Al/Invar), the red and green curves show the CTE trend of TN with respect to the skew angle, and the blue and violet curves that of TL-2. The results show that the CTE of TL-2 can be tuned to a smaller value than that of TN, hence the ΔCTE of TL-2 is larger in the given range of skew angle. Another insight that can be gained from Figure 3-11a pertains to the role of the CTE ratio of the constituents, i.e. $\lambda = \alpha_{s1}/\alpha_{s2}$. The greater the CTE distinction of the constituent solids ($\lambda_{\text{Al-Invar}} \approx 15.3$ which is higher than $\lambda_{\text{Al-Ti}} = 2.0$), the larger the CTE tunability of a building block. We also remark that the largest negative CTE a building block can reach in all experiments of this work is -26.2$\times 10^{-6}$/°C (Al/Invar TL-2 with $\theta = 54.1^{\circ}$) which is well below the CTE values of its components.

Figure 3-11b compares the experimental (specimens with rigid-joints) and theoretical (closed-form expressions with pin-joints) results for the CTE of all the compound units. The relatively small errors associated with the testing results, which go as high as 6.3%, validate the CTEs under pin- and rigid-joint assumptions displaying small deviations, hence respecting the small deformation assumption. Another insight concerns the effective CTE of the building blocks here investigated. As shown in Figure 3-11b, comparing the three concepts with unidirectional CTE tunability (i.e. specimens 1, 2, and 3 in Figure 3-11b), specimens with stationary lines (TL-1 and TL-2) have smaller effective CTE values than that of specimens with stationary nodes. The conclusion up to this point is summarized as TL concepts have larger CTE tunability than TN concepts which also applies to the concepts with identical transverse isotropic or isotropic CTEs. The comparison between three concepts made of TL-1s (i.e. specimens 1, 4, and 7 in Figure 3-11b), or other concepts made of the identical building block, show an increase in the effective CTE when the CTE-tunable directionality increases from unidirectional (one principal direction) to transvers isotropic (two principal directions) and then to isotropic CTE (three principal directions). An increase of CTE-tunable directionality is accompanied by the presence and size increase of the monomaterial core of concepts. For example, unidirectional cells contain no monomaterial core, but transverse-isotropic cells have small cores compared to isotropic cells' large cores. The presence and size of a monomaterial core make the effective CTEs increase with the size of the core. However, TL-2 concepts are more significantly affected by the high-CTE (red) cores than TL-1 concepts with low-CTE (blue) cores. Thus in Figure 3-11b, with a triangular bipyramid core, specimen 4 has a larger CTE than specimen 5, while in contrast, specimen 7 has a smaller CTE than specimen 8 when an octahedron core is constructed for the isotropic concepts. The fabrication and testing method reported in this work can also be applied to building blocks with effective CTEs higher than that of the constituents (i.e. high-CTE cases as shown in Figure 3-3) as well as concepts with more complex architecture.

3.5 Mechanical properties

To understand how a programmable CTE truss-system behaves as a bulk material with effective properties, we adopt here a classical continuum-based approach that relates the stress-strain behaviour of the unit cell to that of the global level. In doing so, we assume that the characteristic length of the unit cell is at least one or two orders of magnitude below the characteristic length of the truss-system. This scale separation between the global response and that of the unit cell allows us to calculate the effective properties through a continuum model [45]. For three dual-material unit cells with unidirectional CTE tunability (TL-1, TL-2 and TN concepts shown in Figure 3-6), we present in the main body of the text closed-form expressions of their elastic properties, and in Supplementary Material Section 3.8.4 their buckling and yielding strength. For unit cells with transverse isotropic or isotropic CTEs (concepts shown in Figure 3-7 and 8), a numeric approach is used to obtain their elastic properties.

3.5.1 Relative density

Table 3-4 lists the relative density ρ^*, i.e. the volume fraction, of all nine unit cells. ρ^* is given by the ratio of the volume of the solid components, V_{solid}, to the volume of the unit cell, $V_{unit\ cell}$: $\rho^* = V_{solid} / V_{unit\ cell}$. The expressions rely on the assumption that all high- and low-CTE bars have a circular cross-section with radius a, and bars made of identical material have identical length.

	TL-1 & TL-2	TN
Unidirectional CTE	$\frac{4\pi a^2\left(\cos\theta+1\right)}{l_1^2\xi}$ (3-20)	$\frac{6\pi a^2\left(2\cos\theta+1\right)}{l_1^2\zeta}$ (3-21)
Transverse Isotropic CTE	$\frac{2\pi a^2\left(3+4/\cos\theta+\sqrt{3}\cos\gamma\right)}{\sqrt{3}\sin^3\theta l_1^2\left(\tan^{-1}(\gamma)+\xi/\cos\theta\right)^2}$ (3-22)	$\frac{4\pi a^2\left(11+6/\cos\theta+\cos\gamma\right)}{\sin\gamma l_1^2\left(1+\cos\gamma+\sin\gamma\zeta/\cos\theta\right)^2}$ (3-23)
Isotropic CTE	$\frac{6\sqrt{2}\pi a^2\left(5+8/\cos\theta\right)}{l_1^2\left(1+\xi/\cos\theta\right)^3}$ (3-24)	$\frac{162\pi^2\left(1+1/\cos\theta\right)}{l_1^2\left(\sqrt{2}+\zeta/\cos\theta\right)^3}$ (3-25)

Table 3-4: Relative density of all nine unit cells, where l_1 is the length of high-CTE bars with circular cross section of radius a, γ is the deviation angle (Figure 3-7), $\zeta=\left(3-4\cos^2\theta\right)^{1/2}$, and $\xi=\left(1-2\cos^2\theta\right)^{1/2}$.

3.5.2 Elastic stiffness

The continuum-based modeling approach offers a practical and efficient method for analyzing a periodic medium [45, 46]. It is based on the substitution of the discrete model with an equivalent continuum. A number of approaches, such as those relying on standard mechanics and asymptotic homogenization theory [47], have been proposed for developing continuum models, and for determining the appropriate constitutive relations [46]. Using the standard mechanics approach [48] (see Supplementary Material Section 3.8.3 for more details), here we examine the three unit cells with unidirectional CTE tunability (Figure 3-6a-c) for demonstration purposes. The macroscopic stiffness tensor for the TL-1 concept:

$$\overline{C_{TL-1}}=\frac{\pi a^2}{l_1^2\xi}\begin{pmatrix} \frac{E_{s1}\cos\theta}{2}+8E_{s2}\cos^4\theta+\frac{E_{s2}}{4} & \frac{E_{s1}\cos\theta}{2}+\frac{E_{s2}}{4} & 4E_{s2}\cos^2\theta\xi^2 & 0 & 0 & \frac{E_{s1}\cos\theta}{2}+\frac{E_{s2}}{4} \\ & \frac{E_{s1}\cos\theta}{2}+8E_{s2}\cos^4\theta+\frac{E_{s2}}{4} & 4E_{s2}\cos^2\theta\xi^2 & 0 & 0 & \frac{E_{s1}\cos\theta}{2}+\frac{E_{s2}}{4} \\ & & 4E_{s2}\xi^4 & 0 & 0 & 0 \\ & & & 4E_{s2}\cos^2\theta\xi^2 & 0 & 0 \\ & \mathit{Symm.} & & & 4E_{s2}\cos^2\theta\xi^2 & 0 \\ & & & & & \frac{E_{s1}\cos\theta}{2}+\frac{E_{s2}}{4} \end{pmatrix},\tag{3-26}$$

where $\overline{C_{TL-1}}$ is the effective stiffness matrix of TL-1 concept and E_{s1}, E_{s2} are Young's modulus of two components, respectively. The stiffness matrix in Eq. (3-26) shows a typical material in an orthorhombic system referring to the coordinate system shown in Supplementary Material Section 3.8.3. Analogously, for the TL-2 concept the stiffness tensor is:

$$\overline{C_{TL-2}} = \frac{\pi a^2}{l_1^2 \xi} \begin{pmatrix} E_{s1}\cos\theta + 8E_{s2}\cos^4\theta & E_{s1}\cos\theta & 4E_{s2}\cos^2\theta\xi^2 & 0 & 0 & 0 \\ & E_{s1}\cos\theta + 8E_{s2}\cos^4\theta & 4E_{s2}\cos^2\theta\xi^2 & 0 & 0 & 0 \\ & & 4E_{s2}\xi^4 & 0 & 0 & 0 \\ & & & 4E_{s2}\cos^2\theta\xi^2 & 0 & 0 \\ & Symm. & & & 4E_{s2}\cos^2\theta\xi^2 & 0 \\ & & & & & E_{s1}\cos\theta \end{pmatrix}, \tag{3-27}$$

which shows a typical material in a tetragonal system. The macroscopic stiffness tensor for the TN concept can be written as:

$$\overline{C_{TN}} = \frac{2\pi a^2}{l_1^2 \zeta} \begin{pmatrix} \frac{9E_{s1}\cos\theta}{4} + 2E_{s2}\cos^4\theta & \frac{3E_{s1}\cos\theta}{4} + \frac{2E_{s2}\cos^4\theta}{3} & \frac{2}{3}E_{s2}\cos^2\theta\zeta^2 & 0 & \frac{2E_{s2}\cos^3\theta\zeta}{3} & 0 \\ & \frac{9E_{s1}\cos\theta}{4} + 2E_{s2}\cos^4\theta & \frac{2}{3}E_{s2}\cos^2\theta\zeta^2 & 0 & -\frac{2E_{s2}\cos^3\theta\zeta}{3} & 0 \\ & & \frac{1}{9}E_{s2}\zeta^4 & 0 & 0 & 0 \\ & & & \frac{2}{3}E_{s2}\cos^2\theta\zeta^2 & 0 & -\frac{2E_{s2}\cos^3\theta\zeta}{3} \\ & \text{Symm.} & & & \frac{2}{3}E_{s2}\cos^2\theta\zeta^2 & 0 \\ & & & & & \frac{3E_{s1}\cos\theta}{4} + \frac{2E_{s2}\cos^4\theta}{3} \end{pmatrix}, \tag{3-28}$$

which is the stiffness tensor of a typical material in a trigonal system. The homogenized stiffness matrix relates the macroscopic strains to the macroscopic stresses of the homogenized material. Table 3-5 reports the closed form expressions of the effective Young's modulus of the three concepts in the vertical direction (i.e. the principal direction with CTE tunability, x_3) and shear modulus in the $x_1 - x_2$ plane.

Unidirectional CTE Concepts	E_{33}	G_{12}
TL-1	$\frac{E_{s1}E_{s2}\xi^{4}}{\left(E_{s1}+4E_{s1}\cos^{4}\theta+2E_{s2}\cos^{3}\theta\right)\left(\cos\theta+1\right)}\rho^{*}$	$\frac{E_{s1}E_{s2}\cos\theta}{2\left(\cos\theta+1\right)\left(E_{s2}+2E_{s1}\cos\theta\right)}\rho^{*}$
TL-2	$\frac{E_{s1}E_{s2}\xi^{4}}{\left(E_{s1}+4E_{s2}\cos^{3}\theta\right)\left(\cos\theta+1\right)}\rho^{*}$	$\frac{E_{s1}\cos\theta}{4\left(\cos\theta+1\right)}\rho^{*}$
TN	$\frac{E_{s1}E_{s2}\zeta^{4}}{\left(9E_{s1}+8E_{s2}\cos^{3}\theta\right)\left(2\cos\theta+1\right)}\rho^{*}$	$\frac{E_{s1}\cos\theta}{4\left(2\cos\theta+1\right)}\rho^{*}$

Table 3-5: Effective Young's modulus (in direction x_3) and shear modulus (on the x_1-x_2 plane) for TL-1, TL-2, and TN concepts with unidirectional CTE tunability.

Similar to the CTE maps presented in Section 3.3.2.2 for the three building blocks, TL-1, TL-2 and TN, Figure 3-12 visualizes the spatial variation of the Young's moduli in spherical coordinates for their corresponding unidirectional concepts. The symmetries of the surfaces shown in Figure 3-12 also feature the geometrical symmetry of each concept: Figure 3-12a for the orthorhombic system, Figure 3-12b for the tetragonal system, and Figure 3-12c for the trigonal system.

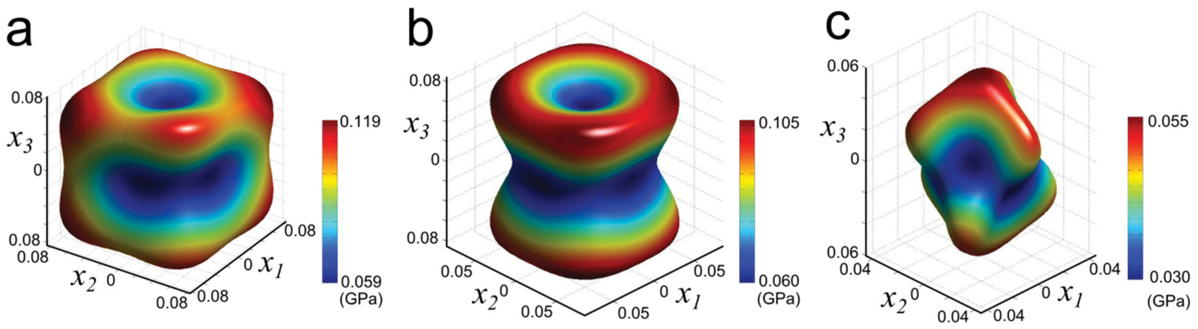

Figure 3-12: Three-dimensional surfaces showing the variation of Young's moduli along the principal directions for (a) TL-1, (b) TL-2 and (c) TN concepts. The length of the radius vector is the Young's moduli of each concept taken Al/Ti as components. All concepts have identical beam length to diameter ratio of 0.04.

As shown in Figure 3-13, for concepts with unidirectional CTE tunability, the normalized specific Young's moduli and shear moduli change with the skew angle and Young's modulus ratio of components (i.e. Young's moduli of low-CTE material over high-CTE material:

E_{s2}/E_{s1}). In Figure 3-13, an increase in skew angle causes rising Young's modulus and falling shear modulus due to concept degeneration. For all the three concepts, the normalized vertical Young's moduli gradually converge to 1 and the normalized shear moduli gradually converge to 0. Figure 3-13a and b also indicate that, for each concept, the effective stiffness, including both Young's and shear moduli, increases with the stiffness ratio of the components. This is caused by the low-CTE material (material two in this work) predominantly located along the x_3 direction with stiffness (E_{s2}) increasing with the component stiffness ratio. Comparing concepts of given skew angle, the TN concept generally has Young's moduli in the vertical direction higher than those of stationary lines. In contrast, concepts constructed via TL-1 and TL-2 have similar vertical Young's moduli. As shown in Figure 3-13b, no concept is absolutely superior to others for all skew angles, as the shear moduli converge at different rates to zero with θ approaching 90°. In addition to stiffness, buckling and yielding strength, other properties that pertain to structural efficiency, are derived and summarized in Supplementary Material Section 3.8.4.

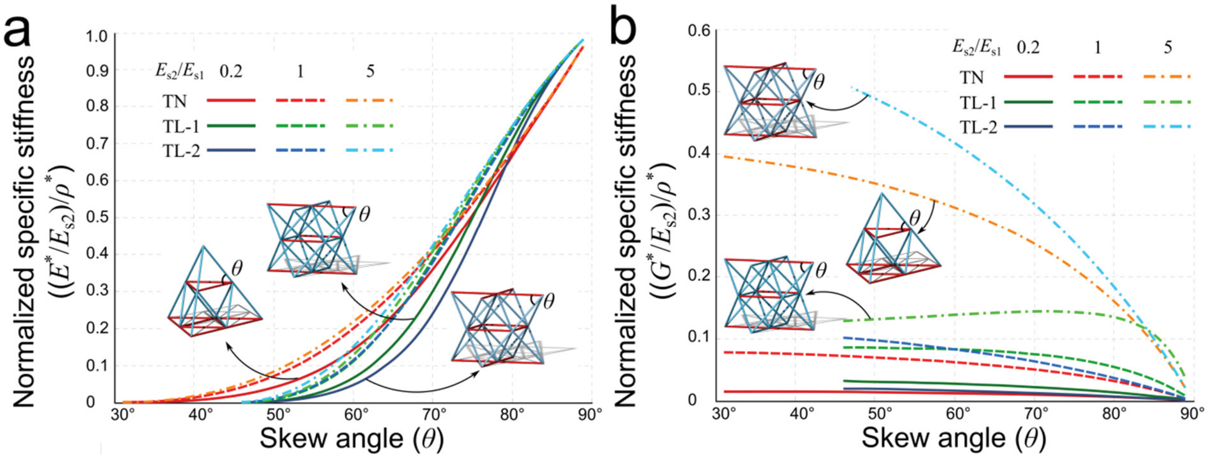

Figure 3-13: Normalized specific stiffness in the vertical direction for TL-1, TL-2, and TN building blocks as a function of the skew angle for selected values of the stiffness ratio of the components (E_{s2}/E_{s1}): (a) Young's modulus and (b) shear modulus. ρ^* represents relative density.

3.6 Discussion on thermal expansion, specific stiffness, and their trade-off

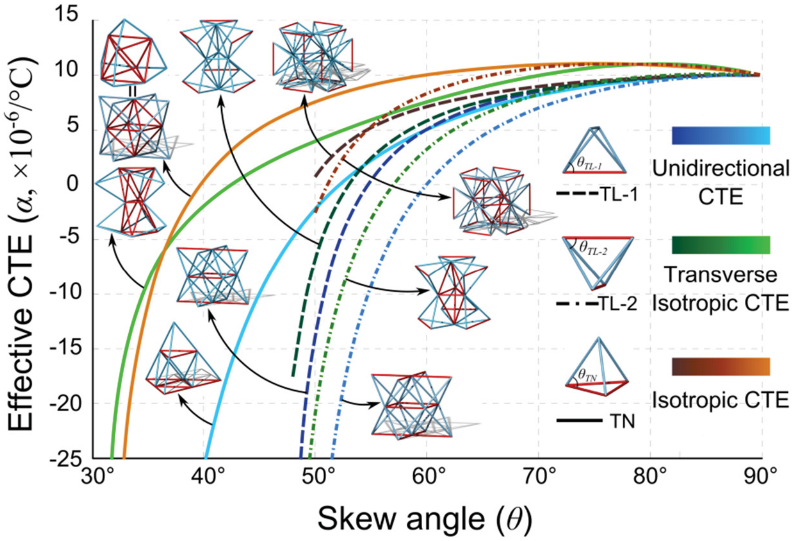

Figure 3-14: Relation between CTEs and skew angle for the nine unit cells here under investigation. A high-CTE material of $\alpha_{s1} = 20\times10^{-6}$ / °C and a low-CTE material of $\alpha_{s2} = 10\times10^{-6}$ / °C are taken here as representative components. For unit cells with unidirectional low CTE, the CTE refers to the vertical direction (x_3). For unit cells with transverse isotropic and isotropic low CTE, the effective CTE refers to the principal directions in the plane $x_1 - x_2$. Each line style indicates one of the three building blocks which a unit cell is built from. The CTE of a benchmark isotropic concept [3] with identical effective CTE to the isotropic TN concept is also shown in purple for comparison.

Thermal expansion. The CTE of bi-material lattice materials depends on the CTE mismatch of materials, the skew angle, i.e. the interplay of the structural members, as well as the stiffness mismatch of materials and joints. Figure 3-14 reveals the role of the skew angle in the thermal expansion performance of each low-CTE unit cell. As a general trend, we observe that as the skew angle increases from the minimum to the maximum value of θ range (Table 3-2), the CTEs for all units converge gradually to that of the low-CTE solid material (10×10^{-6} / °C in Figure 3-14). The similar upper bound indicates the largest ΔCTE comes from the concept obtaining the lowest CTE value. As shown in Figure 3-14, with a given range of skew angles and given directional behaviour (i.e. unidirectional, transverse isotropic, or isotropic), the lowest effective

CTE a TL-1 and TL-2 concept can achieve is generally lower than that of the TN concept. This demonstrates that concepts with stationary lines have a better CTE tunability, because the CTE tunability of TL-1 and TL-2 building blocks is higher than that of the TNs (Figure 3-4). Similarly, when comparing TL-1 with TL-2 concepts, the latter has generally a larger ΔCTE, especially for concepts with small or no monomaterial core (i.e. transverse-isotropic and unidirectional, respectively). However, for isotropic concepts, above $\theta = 53^\circ$ TL-2 has higher CTE values than TL-1, as the influence of TL-2 high-CTE octahedron core is far larger than that of the low-CTE core of the TL-1 concept. For lattices assembled with a given building block, TL-1, TL-2, or TN, the CTE tunability is often the smallest for unit cells with isotropic CTE, followed by unit cells with transverse isotropic CTE. This can also be attributed to the influence of larger single-material core (octahedron) of isotropic-concepts than the core (triangular bipyramid) of the transverse-isotropic concepts; the former is more effective in counteracting the CTE tunability via larger monomaterial core and hence impairing CTE tunability. On the other hand, the largest CTE tunability in the principal direction can be achieved by unit cells which have unidirectional CTE with no monomaterial core.

The experimental results in Section 3.3.4 show that the CTEs under the pin- and rigid-jointed assumptions deviate marginally from each other. Under the pin-jointed assumption, the stiffness mismatch of the component materials has no effect on the effective CTE, as opposed to the case of the rigid-jointed assumption, where the stiffness mismatch of the components can play a role on CTE tunability. A relative comparison between the three factors here examined shows that the effect of the stiffness mismatch is secondary to the influence of the other two, namely the interplay of structures and the CTE mismatch of materials. Section 3.8.1 reports additional results on the CTE of rigid-jointed bi-material lattices obtained for a number of Young's modulus ratio of the constituent solids.

Specific stiffness. As per the sensitivity of the elastic properties, Figure 3-15 shows computational results of their normalized Young’s modulus in the direction of CTE tunability, versus both ρ^*, relative density, and θ, skew angle. The relative density ranges from 0 to 0.2. Different representative fields of the skew angle are selected for each concept to indicate the variation trend of unit cell stiffness. Along the vertical axes, sketches show the variation of the unit cell geometry with the skew angle.

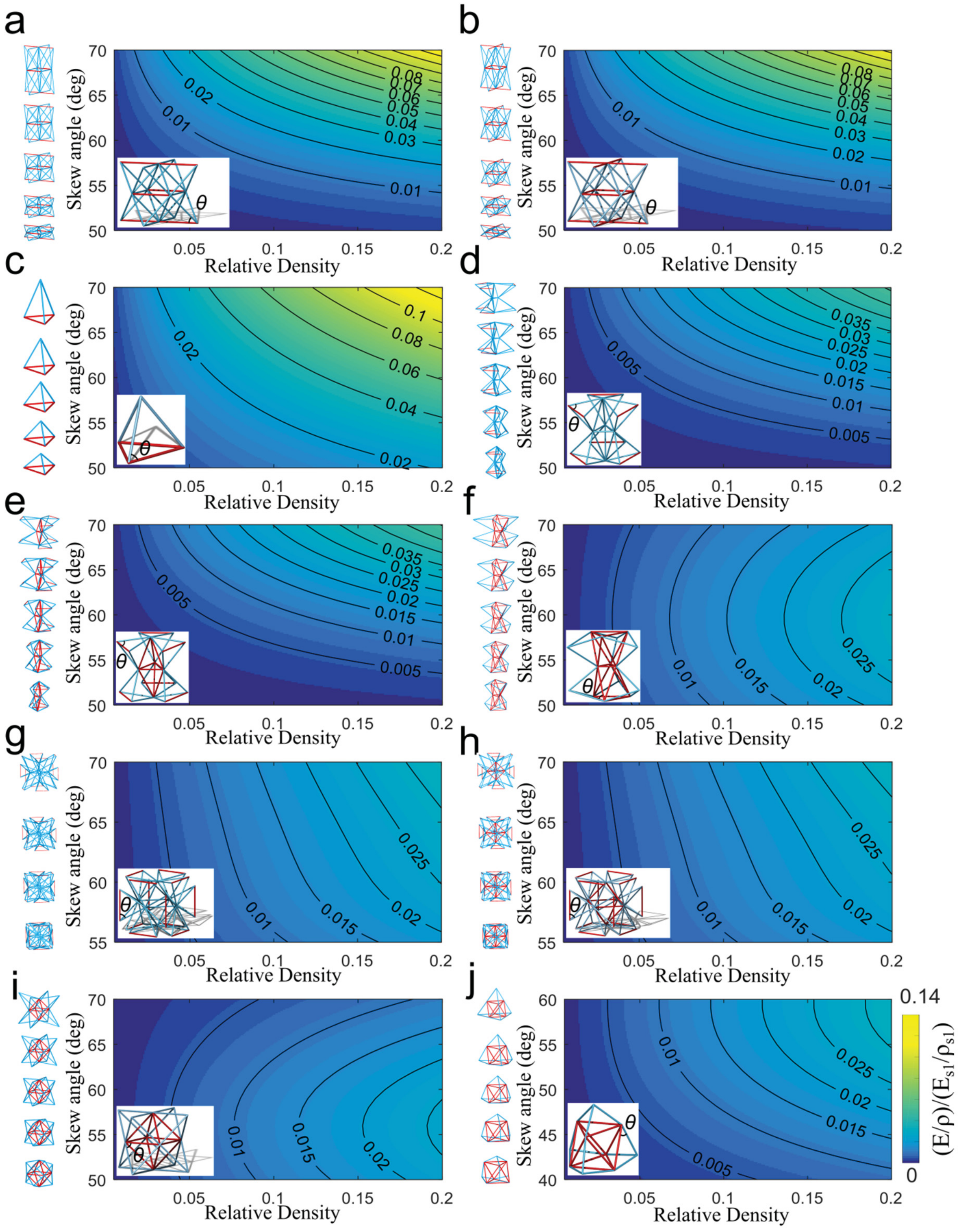

Figure 3-15: Contour plots for specific stiffness ($\left(E/\rho\right)/\left(E_{s1}/\rho_{s1}\right)$ with E representing the effective stiffness in the CTE tunable direction and ρ representing the density of the lattice) versus skew angle and relative density: Young's modulus in the vertical direction of cell

topologies with unidirectional CTE: (a) TL-1, (b) TL-2, and (c) TN concept; Young's modulus in the horizontal direction of cell topologies with transverse isotropic CTE: (d) TL-1, (e) TL-2, and (f) TN concept; and Young's modulus of cell topologies with isotropic CTE: (g) TL-1, (h) TL-2, and (i) TN concept. S-concept [3] is plotted as a benchmark in (j) to compare elastic performances.

The specific stiffness of all concepts increases linearly with ρ^*. For increasing θ with constant ρ^*, the Young's modulus is also observed to raise for unidirectional concepts (Figure 3-15a to c), while a parabolic effect appears for the remaining concepts (e.g. Figure 3-15f and i), i.e. a rise is followed by declining modulus. This can be attributed to the changing alignment of the high-stiffness component (i.e. low-CTE Ti bars) along the loading direction: (i) for unidirectional concepts, increasing θ results in an incremental alignment along x_3; (ii) for both transverse-isotropic and isotropic concepts, the same incremental alignment is initially experienced along the loading direction, before beginning to deviate from the loading direction above a specific θ value. The parabolic effect can also be observed for Figure 3-15d, e, g, h, and j when a larger range of θ is plotted.

For given ρ^* and θ, Figure 3-15 highlights also similarities between the stiffness of TL-1 and TL-2 concepts. Compared to TL-2 concepts, TL-1 concepts feature slightly higher values of specific stiffness, due to presence of more Ti bars. However, TN concepts generally outperform the others in stiffness, especially for transverse-isotropic (Figure 3-15f) and isotropic concepts (Figure 3-15i) where the parabolic effect is observed at $\theta \approx 60^\circ$, resulting in a much higher specific stiffness than TL concepts with identical θ, ρ^*, and CTE directionality. Figure 3-15j plots also the specific stiffness values for the benchmark [3]. Compared to this baseline, we notice that unidirectional and transverse-isotropic concepts produce higher stiffness along the direction of CTE tunability, but the isotropic concepts are comparable for given geometric and constituent parameters.

Trade-off between CTE tunability and specific stiffness. The results above give an indication of existing trade-offs between the properties of the concepts here studied: ΔCTE and specific stiffness. To better understand these trade-offs, Figure 3-16a shows bars of ΔCTE and specific stiffness simultaneously, and in Figure 3-16b ΔCTE is plotted versus specific stiffness to demonstrate Pareto-fronts, both for all concepts made of Al and Ti.

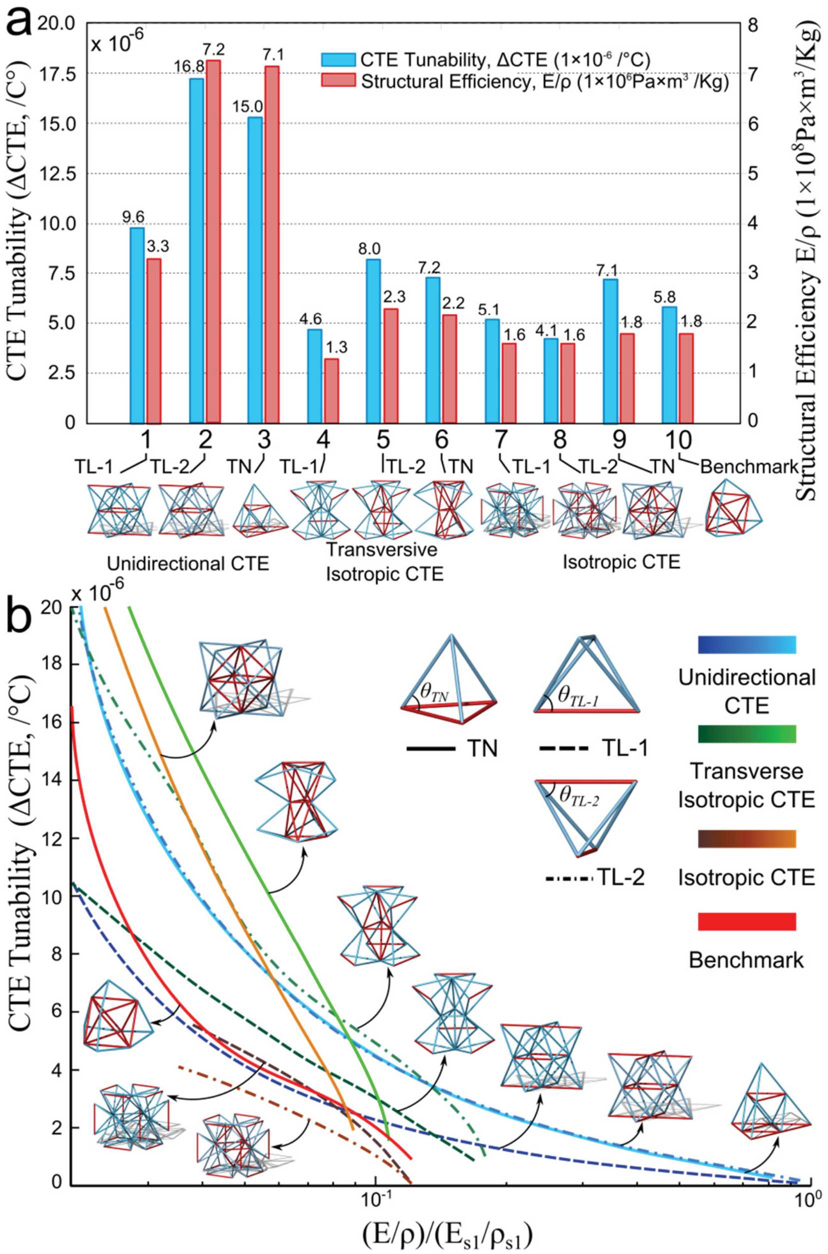

Figure 3-16: (a) Comparison of proposed and existing bi-material concepts for given bar thickness ratio of 0.04 on the basis of (i) CTE tunability ($\Delta CTE = \text{Max}\ CTE - \text{Min}\ CTE$) shown as blues bars for Young’s modulus of 1GPa in the CTE tunable direction, and (ii) specific stiffness (Young's modulus/Density: E/ρ) for prescribed CTE of 6.5×10^{-6}/℃, in red. (b) CTE tunability plotted versus structural efficiency. The relative specific stiffness and CTE tunability

are plotted in the vertical direction for unidirectional and isotropic CTE concepts, and in the horizontal direction for other concepts. The thermoelastic properties of a benchmark isotropic concept [3] is also shown in purple for comparison.

For Figure 3-16a, the ΔCTE bars are calculated for all concepts under a given stiffness value (1 GPa), while bars of structural efficiency are all derived from concepts with equal CTE (6.5×10^{-6}/℃), a value lower than the CTE of their base materials: Al/Ti). This allows for a consistent comparison of their thermo-elastic performance. The bars are arranged in order of increasing number of CTE tunable principal directions, from unidirectional to isotropic concepts. Evidently, with increasing number of CTE tunable directions, there is a penalty in both ΔCTE and structural efficiency. The decrease in ΔCTE is due to the presence and increasing size of monomaterial cores, as previously observed. The drop in structural efficiency, however, is attributed to the distribution of load bearing bars along the CTE tunable directions, thus resulting in a more uniform load capacity, but with lower effective stiffness along a specific direction. For unidirectional and transverse-isotropic concepts, TL-2 unit cells provide the best ΔCTE and specific stiffness values, followed closely by TN concepts, while both performing significantly better than TL-1. However, for isotropic concepts, the TN thermo-elastic performance exceeds that of TL-2, due to the reduced performance of the TL-2 core.

The Pareto-front curves shown in Figure 3-16b are generated from a parametric study of the unit cells, where the skewness angle and the thickness-to-length ratio are the active variables for given materials (Al/Ti). The curve shapes emphasize the trade-offs between the two metrics plotted: an attempt of increasing structural efficiency results in a reduced ΔCTE. This common trend demonstrates that the desired deformation that a large CTE tunability would require is generally antagonist to the high specific stiffness that is distinctive of a structurally efficient architecture. Here we notice that unidirectional concepts excel in structural efficiency along their CTE tunable direction; but for increasing ΔCTE, their specific stiffness drops. Transverse-isotropic unit cells are unable to attain the highest level of specific stiffness, but, within their attainable range, they generally provide higher ΔCTE compared to unidirectional concepts. Finally, for isotropic concepts, including S-concept [3], there is a sacrifice in both ΔCTE and structural efficiency, except for the isotropic TN unit cell, which maintains performance similar to its transverse-isotropic counterpart. Overall, Figure 3-16a and b provides a comprehensive comparison of the thermo-elastic performance of the concepts here examined, bearing in mind that no CTE directionality is ultimately superior to the rest as the direction of CTE tunability is entirely dependent on the application requirements. Other structural properties, such as yield and buckling strength, have been evaluated for specific concepts, as examples, and their expressions are provided in Supplementary Material Section 3.8.4.

In summary, this work has added to the body of the existing literature three fundamental aspects. The first is on the concepts and their mechanisms of thermal deformation. Three groups (low-CTE, intermediate-CTE, high-CTE) are introduced for the tetrahedral building block to tune the effective CTE at values that can be lower, in between, or higher than the constituent material CTEs. For the low-CTE group, three specific mechanisms are identified for a bi-material tetrahedron: two with stationary-lines, and the third with a stationary-node, the only one known in the literature. The second novel feature of this work is a systematic method to rationally assemble building blocks into compound units, such as the nine here introduced, that can attain desired magnitude and directionality of thermal expansion in three-dimensional lattices. The third is a path forward for resolving the trade-off between CTE tunability and specific stiffness, which has led to the assembly of building blocks into stiff and strong, yet high CTE tunable spatial lattices with application across the spectrum of length scale.

3.7 Conclusions

This chapter has investigated thermal expansion of spatial bi-material lattices built from tetrahedral building blocks with the twofold goal of providing a fundamental understanding of their mechanisms of thermal expansion, and a systematic method to program their CTE while achieving high values of structural efficiency. The material length vector and thermal displacement vector are first defined to assess thermal expansion of truss concepts, and then used to examine all the possible material permutations that can occur in the struts of a dual-material tetrahedron. Drawing from concepts of crystallography and tessellation, a scheme has been presented to understand the relationships between CTE tunability of tetrahedral building blocks, structural symmetry of unit cells, independent elements in the CTE tensor, and effective thermoelastic properties of periodic truss, which can be built from single units as well as more complex assembly of compound units. The results establish underlying principles governing tailorable thermal expansion in dual-material lattice materials, where desired CTE magnitude and spatial CTE directionality can be programmed a priori to satisfy given CTE requirements, such as unidirectional, transverse isotropic, or isotropic. Closed-form expressions for predicting and tuning CTE performance are validated through computational and experimental studies on proof-of-concept prototypes. Results illustrated in maps have been discussed within the context of structural efficiency and CTE tunability, two properties that are generally in conflict at a degree dependent on the unit cell type. This work has also shown that three-dimensional lattices can be systematically assembled with high specific stiffness to attain large CTE tunability over a substantial range of temperature, thus appealing to a large palette of applications where low mass, thermal stability and thermal actuation are primary goals.

3.8 Supplementary material

3.8.1 Additional concepts and stiffness mismatch of materials

Figure 3-17 depicts two dual-material tetrahedra with CTE tunability that can be used to generate six supplementary unit cells with given CTE behaviour. The first tetrahedron (Figure 3-17a) has low-CTE tunability in the vertical direction with shear thermal deformation during expansion. The second tetrahedron, intermediate tetrahedron, is able to obtain the effective CTE of a value between the CTEs of the two components only. The additional concepts shown in Figure 3-17 can not only obtain transverse isotropic and isotropic CTE, as with concepts shown in Figure 3-7 and Figure 3-8, but also orthotropic CTE, as shown in Figure 3-17b. The unit cell shown in Figure 3-17b has CTE tunability in both the x_1 and x_3 directions with different magnitudes. With the x_2 direction exhibiting no CTE tunability, the concept overall demonstrates orthotropic CTE tunability.

The effective CTE of the dual-material tetrahedra shown in Figure 3-17a and e ($\mathbf{M}$ direction) can be expressed respectively as:

$$\alpha_{z-\mathrm{L4H2}} = \frac{16\alpha_{s1}\cos^2\theta - \alpha_{s2}}{16\cos^2\theta - 1}, \theta \in \left(15^\circ, 75^\circ\right), \tag{3-29}$$

$$\alpha_{z-\mathrm{L3H3}} = \frac{4\alpha_{s1}\cos^2\theta + \alpha_{s2}}{4\cos^2\theta + 1}, \theta \in \left(36^\circ, 72^\circ\right). \tag{3-30}$$

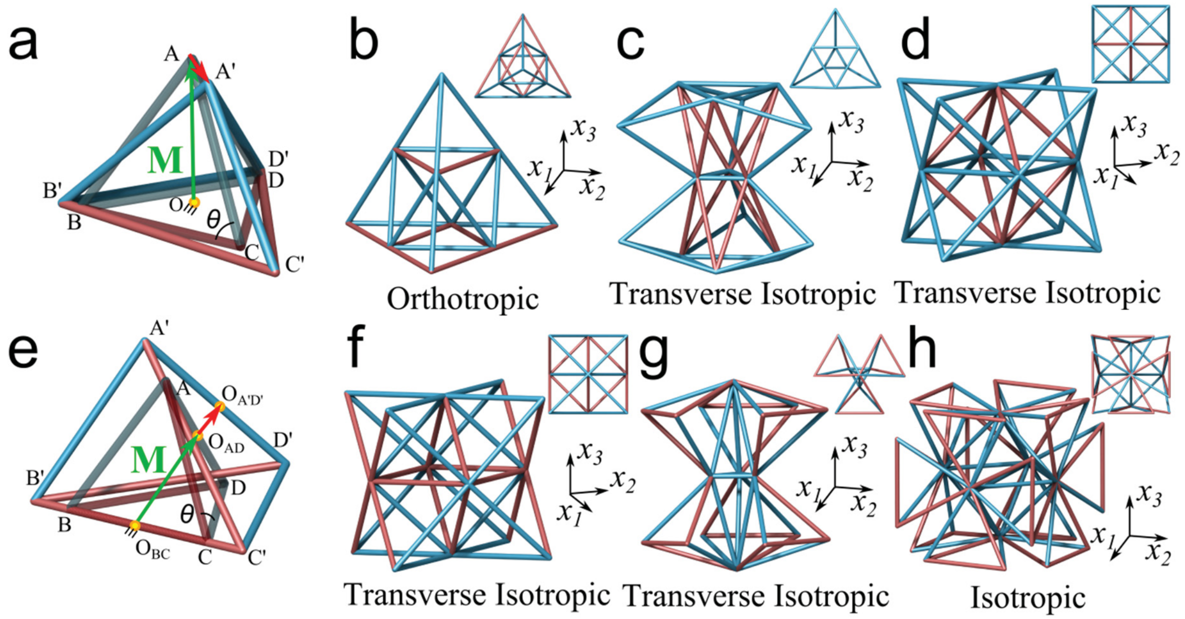

Figure 3-17: Dual-material tetrahedra along with compound unit cells (a): tetrahedron with low-CTE (four low-CTE bars and two high-CTE bars, L4H2); (b) to (d): unit cells constructed from the low-CTE tetrahedron shown in (a); (e): tetrahedron with intermediate CTE (L3H3); and (f) to (h): unit cells assembled from the intermediate-CTE tetrahedron shown in (e).

Figure 3-18 shows unit cells with transverse isotropic CTE governed by the deviation angle, γ , and the skew angle, θ . The decrease of γ and increase of θ allow the connection of unit cells (Figure 3-18a-d) in the out-of-plane principal direction via only stationary lines or stationary nodes. In contrast with concepts shown in Figure 3-7, which have no CTE tunability in the vertical direction, concepts in Figure 3-18 have CTE tunability in all three principal directions. Comparison of concepts depicted in Figure 3-18c and d shows the effects of γ and θ on the packing factor, φ . Differences in the packing factor are controlled by the need of the inner octahedron to thermally expand without touching adjacent cells (Figure 3-18k and l). A packing factor of 50% could be obtained for tessellation in Figure 3-18A2k. In contrast, dissimilar skew angles for the concept in Figure 3-18A2d results in a tessellation with higher packing factors, i.e. 100%.

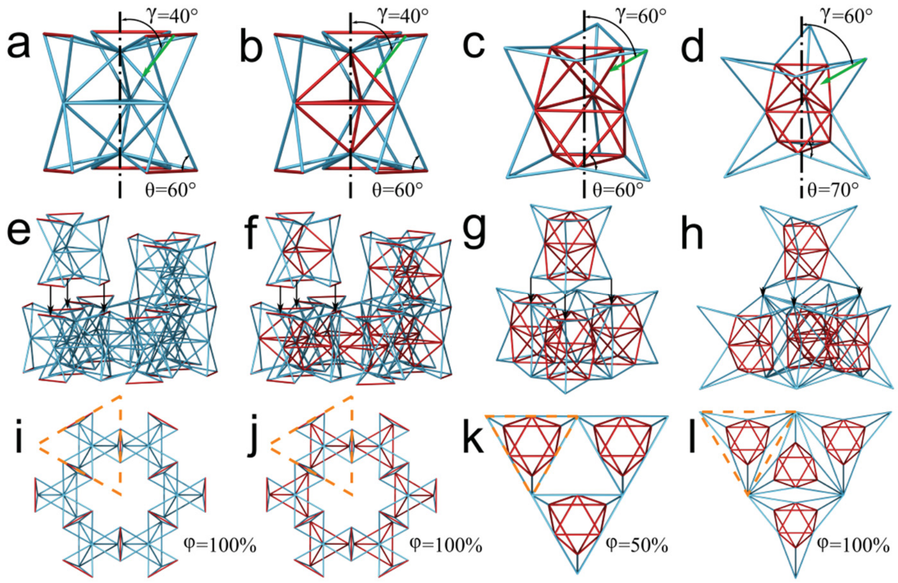

Figure 3-18: Low-CTE unit cells with transverse isotropic CTE tunability: (a) TL-1 concept, (b) TL-2 concept, (c) and (d) TN concepts. (e) to (h) show an axonometric view of the unit cell assembly; (i) to (l) are the top view of assembly. θ, γ, and φ are skew angle, deviation angle, and packing factor respectively. Dash yellow line indicates the compound unit cell within the assembly.

In the following we assess the effect of the stiffness mismatch of materials and joint assumption.

Figure 3-19 visualizes the effective CTE in the vertical direction for rigid-jointed TL-2 and TN concepts with unidirectional CTE tunability, here chosen for demonstrative purposes. Both the skew angle and the Young's modulus ratio E_{s1}/E_{s2} of the components (i.e. Young's moduli of high-CTE material over low-CTE material) play a role in the effective CTE but to a different extent. The effect of the stiffness mismatch of materials is secondary compared to that caused by a change in the skew angle, i.e. the interplay of structures. The former has a non-negligible influence only at low values of the skew angle (e.g. below $\theta = 55°$ for TL-2 concept, and below $\theta = 40°$ for TN concept). If the low-CTE material has a larger Young's modulus (i.e. $E_{s1} < E_{s2}$), an increase in E_{s1}/E_{s2}, i.e. the Young's modulus ratio of the components, reduces the effective CTE to a lower value; this phenomenon is caused by the high-CTE elements inducing a larger compensation of thermal expansion with increased stiffness. In contrast, if the high-CTE material has a larger Young's modulus (i.e. $E_{s1} > E_{s2}$), the impact of the stiffness mismatch of materials on the effective CTE is negligible.

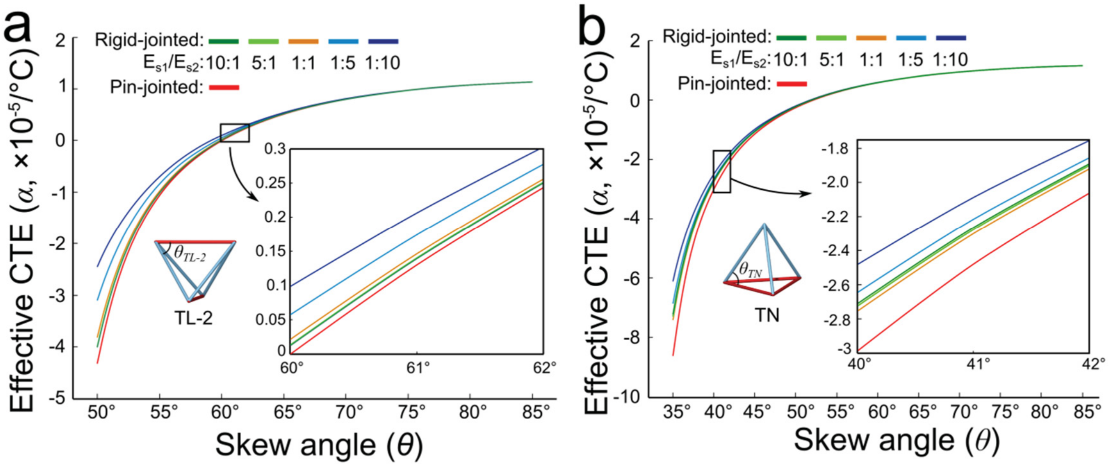

Figure 3-19: CTE dependence of TL-2 and TN concepts with unidirectional CTE tunability, on stiffness mismatch of materials (i.e. Young's modulus ratio of high-CTE material over low-CTE material: E_{s1}/E_{s2}), skew angle, and joint assumption.

3.8.2 Testing setup and testing samples

Figure 3-20 shows the schematic of the experimental set-up built to test the thermal expansion of specimens. It consists of a heating chamber and a DIC system. The heating chamber with dimensions of 200(L)×200(W) ×150(H) mm is made of glass to provide an unobstructed view for DIC measurements. Testing samples were set on the copper plate with thermal transfer grease (Fuchs Lubricants Co., US) between the two.

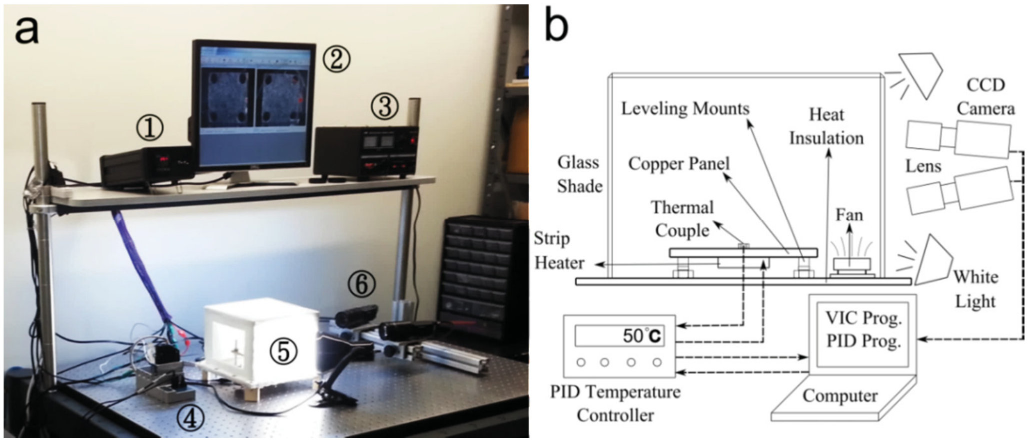

Figure 3-20: Experimental set-up used to measure thermal expansion: (a) (1) PID controller; (2)

Computer; (3) Power source; (4) DAQ system; (5) Heating chamber; and (6) CCD cameras, and (b) schematic of the apparatus.

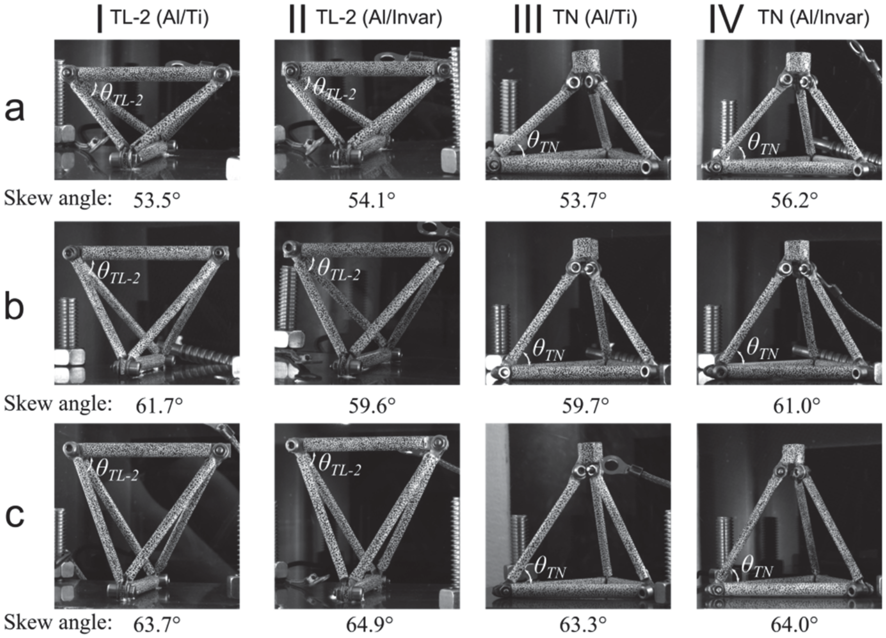

Figure 3-21: Thermal testing experiments for tetrahedra with stationary lines (I with Al/Ti and II with Al/Invar) and tetrahedra with stationary nodes (III with Al/Ti and IV with Al/Invar). Samples with three skew angles of roughly 55° (a), 60° (b), and 65° (c) are tested.

Twelve physical samples (Figure 3-21) were tested to validate the thermoelastic properties of the building blocks. Four sets, each of three samples, were constructed: two sets consisted of Al6061 and Ti-6Al-4V (Figure 3-21-I and III), and the other two were made from Al6061 and Invar (Figure 3-21-II and IV). Each set of material combinations included one of two configurations consisting of stationary lines or stationary nodes, at three skew angles (Figure 3-21a to c). This ensures that each building block was tested using two different material combinations and three different skew angles.

Table 3-6 tabulates the CTEs of building blocks obtained both from theory and experiments for given pair of materials. The joint-to-length ratio (averaging about 29%), referring to the length ratio of a copper flake (made of copper with CTE of 16×10^{-6}/℃) to a bar, characterizes the impact of flakes in the measured values of CTEs. Considering the joint impact, the absolute error goes no higher than 0.84×10^{-6}/°C.

Sample	Measured CTE in the vertical direction $(\times 10^{-6}/^{\circ}\mathrm{C})$	Predicted CTE in the vertical direction $(\times 10^{-6}/^{\circ}\mathrm{C})$	Absolute error $(\times 10^{-6}/^{\circ}\mathrm{C})$	Joint to length ratio (%)
TN (Al/Ti, $\theta = 53.7^{\circ}$)	3.62 ± 0.56	3.97	-0.35	30.8
TN (Al/Ti, $\theta = 59.7^{\circ}$)	7.65 ± 0.45	7.35	0.30	27.6
TN (Al/Ti, $\theta = 63.3^{\circ}$)	8.42 ± 0.39	8.77	-0.35	26.5
TN (Al/Invar, $\theta = 56.2^{\circ}$)	-3.60 ± 0.61	-3.48	-0.12	30.4
TN (Al/Invar, $\theta = 61.0^{\circ}$)	0.97 ± 0.54	0.13	0.84	29.2
TN (Al/Invar, $\theta = 64.0^{\circ}$)	1.69 ± 0.25	1.73	-0.04	28.3
TL-2 (Al/Ti, $\theta = 53.5^{\circ}$)	-11.58 ± 0.32	-11.61	0.03	32.0
TL-2 (Al/Ti, $\theta = 61.7^{\circ}$)	3.70 ± 0.41	4.49	-0.79	30.0
TL-2 (Al/Ti, $\theta = 63.7^{\circ}$)	6.47 ± 0.68	6.08	0.39	28.6
TL-2 (Al/Invar, $\theta = 54.1^{\circ}$)	-26.2 ± 0.49	-26.8	0.60	31.0
TL-2 (Al/Invar, $\theta = 59.6^{\circ}$)	-10.40 ± 0.64	-9.98	-0.42	27.0
TL-2 (Al/Invar, $\theta = 64.9^{\circ}$)	-2.50 ± 0.35	-2.26	-0.24	26.2

Table 3-6: Predicted and experimentally measured CTE values for TN and TL-2, accompanied by their standard deviation, along with the joint length ratio, i.e. the length ratio of a copper flake to a bar, of each testing sample.

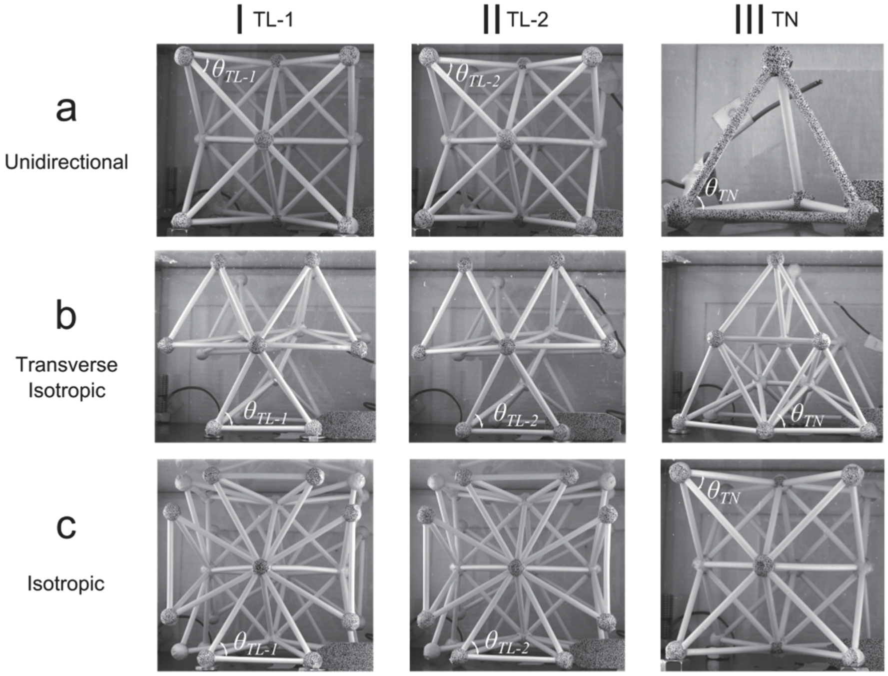

Figure 3-22: Thermal testing experiments for nine compound units with an identical skew angle of 60°.

The nine samples of compound units are shown in Figure 3-22. Randomly distributed black and white pattern is painted on the surface of ABS connection balls for DIC testing.

3.8.3 Calculation of elastic stiffness for truss members

Using the standard mechanics approach here, the microscopic strain tensor, ε_{ij}, at any point within the representative volume element (RVE) can be linearly expressed by the macroscopic strain tensor $\overline{\varepsilon_{kl}}$ through the local structural tensor M_{ijkl}:

$$\varepsilon_{ij} = M_{ijkl}\overline{\varepsilon_{kl}} . \tag{3-31}$$

From the constitutive relation, we have:

$$\sigma_{ij} = C_{ijpm} \cdot \varepsilon_{pm} , \tag{3-32}$$

where σ_{ij} is the microscopic stress tensor and C_{ijpm} is the stiffness matrix of the component. The effective stress matrix can be simply defined by a volumetric average through integrating the microscopic stress over the RVE and dividing by the RVE volume:

$$\overline{\sigma_{ij}} = \frac{1}{V_{RVE}} \int_{V_{RVE}} \sigma_{ij} dV_{RVE} , \tag{3-33}$$

where V_{RVE} is the volume of the RVE. Substituting Eqs. (3-31) and (3-32) into Eq. (3-33) results in

$$\overline{\sigma_{ij}} = \frac{1}{V_{RVE}} \int_{V_{RVE}} E_{ijpm} M_{pmkl} dV_{RVE} \overline{\varepsilon_{kl}} , \tag{3-34}$$

where E_{ijpm} is the elastic properties of solid components. From Eq. (3-34) the effective stiffness matrix $\overline{C_{ijkl}}$ is defined as

$$\overline{C_{ijkl}} = \frac{1}{V_{RVE}} \int_{V_{RVE}} E_{ijpm} M_{pmkl} dV_{RVE} . \tag{3-35}$$

Since the RVEs of dual-material unit cells consist of discrete members, the volumetric average through integration simplifies to become a mere summation. The relation between the effective strain of the k^{th} truss member, $\overline{\varepsilon_{pm}^{(k)}}$, and the local axial strain along the bar member, $\varepsilon^{(k)}$, is given by [49]:

$$\varepsilon^{(k)} = N_{ij}^{(k)} \overline{\varepsilon_{ij}^{(k)}}, \tag{3-36}$$

where $N_{ij}^{(k)}$ is the linear transformation operator from the local to global coordinates of the k^{th} member:

$$N_{ij}^{(k)} = \begin{bmatrix} l^2 & m^2 & n^2 & mn & nl & lm \end{bmatrix}^{(k)}, \tag{3-37}$$

where (l, m, n) are the direction cosines of the member. Furthermore, the local stress-strain relation is given by:

$$\sigma^{(k)} = E_s^{(k)} \varepsilon^{(k)}, \tag{3-38}$$

where $E_s^{(k)}$ is the Young's modulus of the solid component of the k^{th} unit cell member. The relation between the effective stress of the lattice, $\overline{\sigma_{ij}^{(k)}}$, and the local stress in the lattice member, $\sigma^{(k)}$, is given by:

$$\overline{\sigma_{ij}^{(k)}} = \left(N_{ij}^{(k)}\right)^{\mathrm{T}} \sigma^{(k)}, \tag{3-39}$$

where T denotes transposition. By substituting Eqs. (3-36) and (3-38) into Eq. (3-39), we can obtain the effective stress via a summation:

$$\overline{\sigma_{ij}} = \frac{1}{V_{RVE}} \sum_{k=1}^{k} \left(N_{ij}^{(k)}\right)^{\mathrm{T}} E_s^{(k)} N_{pm}^{(k)} A^{(k)} L^{(k)} \overline{\varepsilon_{pm}}, \tag{3-40}$$

where $A^{(k)}$ and $L^{(k)}$ are the cross-sectional area and length of the k^{th} member, respectively. From Eq. (3-40) we can extract the macroscopic stiffness tensor component as follows:

$$\overline{C_{ijpm}} = \frac{1}{V_{RVE}} \sum_{k=1}^{k} \left(N_{ij}^{(k)} \right)^{\mathrm{T}} E_s^{(k)} N_{pm}^{(k)} A^{(k)} L^{(k)} , \tag{3-41}$$

For ease of representation of the constitutive equations, we introduce vector notation for the tensors. We write the effective stiffness tensor as:

$$\boldsymbol{C} = \boldsymbol{N}^{\mathrm{T}} \boldsymbol{R} \boldsymbol{N} , \tag{3-42}$$

where $\boldsymbol{N}$ is the transformation operator for a lattice with M sets of struts, i.e. sharing the same directional orientation, size/volume and solid component:

$$\boldsymbol{N} = \begin{bmatrix} l_1^2 & m_1^3 & n_1^2 & m_1 n_1 & n_1 l_1 & l_1 m_1 \\ \cdots & \cdots & \cdots & \cdots & \cdots & \cdots \\ l_M^2 & m_M^3 & n_M^3 & m_M n_M & n_M l_M & l_M m_M \end{bmatrix}, \tag{3-43}$$

where $\left(l_i, m_i, n_i \right)$ are the directional cosines of the i^{th} set of struts with axes x_1, x_2, and x_3, respectively. $\boldsymbol{R}$ is given by:

$$\boldsymbol{R} = \begin{bmatrix} r_1 & & & & \\ & \ddots & & 0 & \\ & & r_i & & \\ & 0 & & \ddots & \\ & & & & r_M \end{bmatrix}, \tag{3-44}$$

with

$$r_i = \frac{E_{si} A_i L_i}{V_{RVE}} . \tag{3-45}$$

Here we examine the three unit cells with unidirectional CTE tunability (Figure 3-6a-c) for demonstration purposes. The coordinate systems defined for these concepts are depicted in Figure 3-23. As shown in Figure 3-23, struts sharing cross sectional area and component, parallel and equally distant from each other can be considered as one set of struts. Since TL-1 and TL-2 concepts have identical strut location, they both use the coordinate system shown in Figure 3-23a.

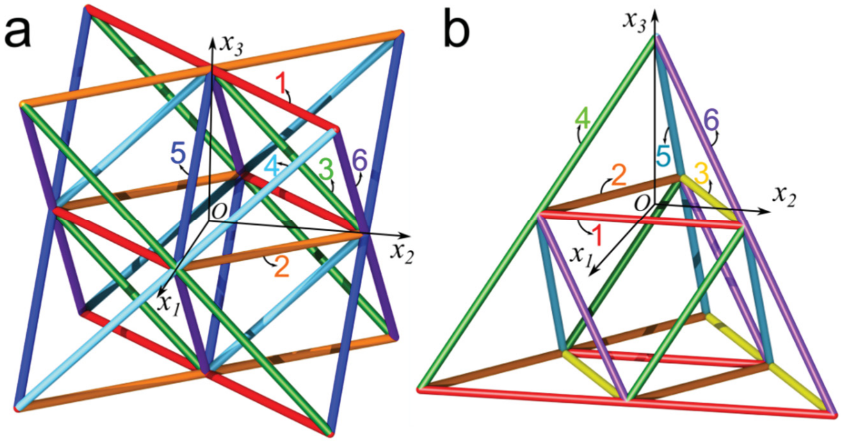

Figure 3-23: The coordinate system defined for (a) TL-1 and TL-2 concepts, and (b) TN concept. Different sets of trusses are marked in different colours and numbered accordingly.

For the topologies shown in Figure 3-6a-c, we summarized all the directional cosines, element length, and the effective Young's modulus of each set of struts, r_i, in Table 3-7 (for TL-1 and TL-2 concepts) and Table 3-8 (for TN concept).

Truss Set No.	1	2	3	4	5	6
l	$\sqrt{2}/2$	$\sqrt{2}/2$	0	0	$-\sqrt{2}\cos\theta$	$\sqrt{2}\cos\theta$
m	$\sqrt{2}/2$	$-\sqrt{2}/2$	$-\sqrt{2}\cos\theta$	$\sqrt{2}\cos\theta$	0	0
n	0	0	ξ	ξ	ξ	ξ
Length	l_1	l_1	$\dfrac{l_1}{2\cos\theta}$	$\dfrac{l_1}{2\cos\theta}$	$\dfrac{l_1}{2\cos\theta}$	$\dfrac{l_1}{2\cos\theta}$
r for TL-1	$\dfrac{2E_1\pi a^2\cos\theta}{l_1^2\xi}$	$\dfrac{E_2\pi a^2}{l_1^2\xi}$	$\dfrac{E_2\pi a^2}{l_1^2\xi}$			
r for TL-2	$\dfrac{2E_1\pi a^2\cos\theta}{l_1^2\xi}$		$\dfrac{E_2\pi a^2}{l_1^2\xi}$			

Table 3-7: Unit vector components, lengths, and effective Young's moduli of TL-1 and TL-2 concept truss members.

Truss Set No.	1	2	3	4	5	6
l	0	$\frac{\sqrt{3}}{2}$	$\frac{\sqrt{3}}{2}$	$-\frac{\sqrt{3}}{3}\cos\theta$	$\frac{2\sqrt{3}}{3}\cos\theta$	$-\frac{\sqrt{3}}{3}\cos\theta$
m	1	$-\frac{1}{2}$	$\frac{1}{2}$	$\cos\theta$	0	$-\cos\theta$
n	0	0	0	$\sqrt{3}\zeta/3$	$\sqrt{3}\zeta/3$	$\sqrt{3}\zeta/3$
Length	l_1	l_1	l_1	$\frac{l_1}{2\cos\theta}$	$\frac{l_1}{2\cos\theta}$	$\frac{l_1}{2\cos\theta}$
r	$\frac{4E_1\pi a^2\cos\theta}{l_1^2\zeta}$			$\frac{2E_2\pi a^2}{l_1^2\zeta}$		

Table 3-8: Unit vector components, lengths, and effective Young's moduli of TN concept truss members.

By substituting the values of directional cosines into Eq. (3-42), we obtain the macroscopic stiffness tensor for the TL-1, TL-2, and TN concepts with unidirectional CTEs as shown in Eqs. (3-26)-(3-28).

3.8.4 Yield and buckling strength

Tetrahedral building blocks were chosen in this study because of their high structural efficiency, which includes strength/mass, in addition to stiffness/mass. For this reason, here we also examine the overall strength performance, and we do so by adopting notation and terminology used in Supplementary Material Section 3.8.3. In this section, the yield and buckling strength of the three concepts with unidirectional CTE tunability are derived as examples for other concepts. From Eq. (3-39), we can obtain:

$$\overline{\sigma_{ij}}^{(k)} A^{(k)} = \left(N_{ij}^{(k)}\right)^{\mathrm{T}} \sigma^{(k)} A^{(k)} = \left(N_{ij}^{(k)}\right)^{\mathrm{T}} f^{(k)} \qquad (3\text{-}46)$$

where $f^{(k)}$ is the axial load of the k^{th} bar. Considering the same simplification steps discussed earlier, the stretching forces vector, $\boldsymbol{f}$, of struts can be defined as,

$$\boldsymbol{f} = \{f_1 \quad \cdots \quad f_i \quad \cdots \quad f_N\}^{\mathrm{T}} \qquad (3\text{-}47)$$

where f_i is the axial load of the i^{th} set of struts. Thus, we have

$$\boldsymbol{S}\bar{\boldsymbol{\sigma}} = \boldsymbol{N}^{\mathrm{T}}\boldsymbol{f} \tag{3-48}$$

with

$$S = \begin{bmatrix} S_1 & & & & \\ & \ddots & & 0 & \\ & & S_i & & \\ & 0 & & \ddots & \\ & & & & S_N \end{bmatrix} \tag{3-49}$$

S_i is the area occupied by one strut in the i^{th} set. From Eq. (3-42), we have

$$\boldsymbol{I} = \boldsymbol{N}^{\mathrm{T}}\boldsymbol{RNC}^{-1} \tag{3-50}$$

where $\boldsymbol{I}$ is a unit matrix. Thus, we have

$$\boldsymbol{N}^{\mathrm{T}}\boldsymbol{f} = \boldsymbol{S}\bar{\boldsymbol{\sigma}} = \boldsymbol{N}^{\mathrm{T}}\boldsymbol{RNC}^{-1}\boldsymbol{S}\bar{\boldsymbol{\sigma}} \tag{3-51}$$

So the stretching forces vector, $\boldsymbol{f}$, can be derived as

$$\boldsymbol{f} = \boldsymbol{RNC}^{-1}\boldsymbol{S}\bar{\boldsymbol{\sigma}} \tag{3-52}$$

Taking the yield strength of a strut as σ_Y, and the Euler buckling strength as σ_E, the ultimate force a strut can carry is [50]

$$f_{ij} = \begin{cases} \sigma_Y \pi a^2, & \text{yield by tension} \\ -\sigma_Y \pi a^2, & \text{yield by compression} \\ -\sigma_E \pi a^2, & \text{buckling by compression} \end{cases} \tag{3-53}$$

The force carried by each strut can be computed according to Eq. (3-52). If any component of vector $\boldsymbol{f}$ reaches f_{ij} defined in Eq. (3-53), the corresponding global stress would be equal to the strength of the lattice material. The Euler buckling load of the struts is given by $P_E = n^2\pi^3 a^4 E_s / \left(4l^2\right)$ while the plastic yielding load is $P_Y = \pi a^2 \sigma_Y$, with n determined by supporting conditions at strut ends. Thus, the critical aspect ratio is given by

$$l_{cr} = \frac{n\pi a}{2}\sqrt{\frac{E_s}{\sigma_Y}} \tag{3-54}$$

Under compression, if the length of the strut is larger than the critical length, then the strut will buckle and the buckling strength is given by

$$\sigma_E = \frac{n^2\pi^2 E_s a^2}{4l^2} \tag{3-55}$$

The initial yield surfaces under general macroscopic loadings are composed of the envelope of, at most, twelve super-planes in the stress space, and represented as follows for the TN concept:

$$\left\{\begin{array}{c}
-\frac{(2\cos\theta+1)}{2\cos\theta}\sigma_1 + \frac{3(2\cos\theta+1)}{2\cos\theta}\sigma_2 + \frac{2\cos\theta(2\cos\theta+1)}{4\cos^2\theta-3}\sigma_3 + \frac{2(2\cos\theta+1)}{\sqrt{3-4\cos^2\theta}}\sigma_{12} \\
\frac{(2\cos\theta+1)}{\cos\theta}\sigma_1 - \frac{2\cos\theta(2\cos\theta+1)}{\zeta^2}\sigma_3 - \frac{\sqrt{3}(2\cos\theta+1)}{\zeta}\sigma_{23} - \frac{(2\cos\theta+1)}{\zeta}\sigma_{13} - \frac{\sqrt{3}(2\cos\theta+1)}{\cos\theta}\sigma_{12} \\
\frac{(2\cos\theta+1)}{\cos\theta}\sigma_1 - \frac{2\cos\theta(2\cos\theta+1)}{\zeta^2}\sigma_3 + \frac{\sqrt{3}(2\cos\theta+1)}{\zeta}\sigma_{23} - \frac{(2\cos\theta+1)}{\zeta}\sigma_{13} + \frac{\sqrt{3}(2\cos\theta+1)}{\cos\theta}\sigma_{12} \\
\frac{3(2\cos\theta+1)}{\zeta^2}\sigma_3 + \frac{3\sqrt{3}(2\cos\theta+1)}{2\cos\theta\zeta}\sigma_{23} - \frac{(2\cos\theta+1)}{4\cos^2\theta\zeta}\sigma_{13} \\
\frac{3(2\cos\theta+1)}{\zeta^2}\sigma_3 + \frac{(2\cos\theta+1)}{2\cos^2\theta\zeta}\sigma_{13} \\
\frac{3(2\cos\theta+1)}{\zeta^2}\sigma_3 - \frac{3\sqrt{3}(2\cos\theta+1)}{2\cos\theta\zeta}\sigma_{23} - \frac{(2\cos\theta+1)}{4\cos^2\theta\zeta}\sigma_{13}
\end{array}\right\}$$

$$= \begin{cases} \rho^*\sigma_Y, & \text{yield by tension} \\ -\rho^*\sigma_Y, & \text{yield by compression} \\ -\rho^*\sigma_E, & \text{buckling by compression} \end{cases} \tag{3-56}$$

The yield criterion in the stress space for TL concepts is:

$$\left\{\begin{array}{l}
\dfrac{\cos\theta+1}{\cos\theta}\sigma_1+\dfrac{\cos\theta+1}{\cos\theta}\sigma_2-\dfrac{2\cos\theta\left(\cos\theta+1\right)}{\xi^2}\sigma_3+\dfrac{2\left(\cos\theta+1\right)}{\cos\theta}\sigma_{12}\\
\dfrac{\cos\theta+1}{\cos\theta}\sigma_1+\dfrac{\cos\theta+1}{\cos\theta}\sigma_2-\dfrac{2\cos\theta\left(\cos\theta+1\right)}{\xi^2}\sigma_3-\dfrac{2\left(\cos\theta+1\right)}{\cos\theta}\sigma_{12}\\
-\dfrac{\cos\theta+1}{2\cos^2\theta}\sigma_1+\dfrac{\cos\theta+1}{2\cos^2\theta}\sigma_2+\dfrac{\cos\theta+1}{\xi^2}\sigma_3-\dfrac{\cos\theta+1}{\cos\theta}\dfrac{\sqrt{2}}{\xi}\sigma_{23}\\
-\dfrac{\cos\theta+1}{2\cos^2\theta}\sigma_1+\dfrac{\cos\theta+1}{2\cos^2\theta}\sigma_2+\dfrac{\cos\theta+1}{\xi^2}\sigma_3+\dfrac{\cos\theta+1}{\cos\theta}\dfrac{\sqrt{2}}{\xi}\sigma_{23}\\
\dfrac{\cos\theta+1}{2\cos^2\theta}\sigma_1-\dfrac{\cos\theta+1}{2\cos^2\theta}\sigma_2+\dfrac{\cos\theta+1}{\xi^2}\sigma_3-\dfrac{\cos\theta+1}{\cos\theta}\dfrac{\sqrt{2}}{\xi}\sigma_{13}\\
\dfrac{\cos\theta+1}{2\cos^2\theta}\sigma_1-\dfrac{\cos\theta+1}{2\cos^2\theta}\sigma_2+\dfrac{\cos\theta+1}{\xi^2}\sigma_3+\dfrac{\cos\theta+1}{\cos\theta}\dfrac{\sqrt{2}}{\xi}\sigma_{13}
\end{array}\right\}=\left\{\begin{array}{ll}
\rho^*\sigma_Y, & \text{yield by tension}\\
-\rho^*\sigma_Y, & \text{yield by compression}\\
-\rho^*\sigma_E, & \text{buckling by compression}
\end{array}\right. \qquad (3\text{-}57)$$

According to Eqs. (3-56) and (3-57), the yield surface of the lattice in the macroscopic $\left(\sigma_1,\sigma_2,\sigma_3\right)$ and $\left(\sigma_{12},\sigma_{23},\sigma_{13}\right)$ space is sketched in Figure 3-24.

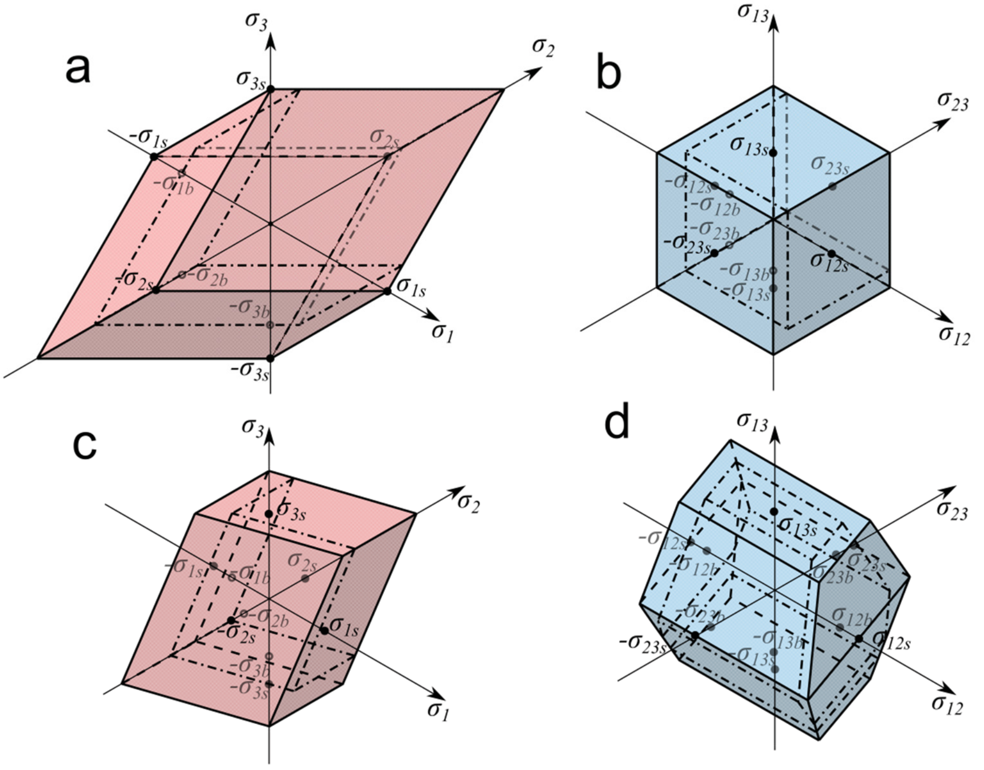

Figure 3-24: Yield (solid and dash line) and buckling (solid and dot dash line) surface in macroscopic $\left(\sigma_1,\sigma_2,\sigma_3\right)$ space: (a) for TN and (c) for TLs; and in $\left(\sigma_{12},\sigma_{23},\sigma_{13}\right)$ space: (b) for

TN and (d) for TLs. σ_{is} and σ_{ib} represent for equivalent uniaxial yield strength and buckling strength of the lattice material respectively.

3.9 References

1. Gilmore, D.G., *Spacecraft thermal control handbook: Fundamental technologies*. 2002, United States: Aerospace Press.
2. Yamamoto, N., E. Gdoutos, R. Toda, V. White, H. Manohara, and C. Daraio, *Thin films with ultra-low thermal expansion.* Advanced Materials, 2014. **26**(19): p. 3076-3080.
3. Steeves, C.A., S.L. dos Santos e Lucato, M. He, E. Antinucci, J.W. Hutchinson, and A.G. Evans, *Concepts for structurally robust materials that combine low thermal expansion with high stiffness.* Journal of the Mechanics and Physics of Solids, 2007. **55**(9): p. 1803-1822.
4. Ding, Z., C. Yuan, X. Peng, T. Wang, H.J. Qi, and M.L. Dunn, *Direct 4d printing via active composite materials.* Science Advances, 2017. **3**(4): p. e1602890.
5. Ge, Q., A.H. Sakhaei, H. Lee, C.K. Dunn, N.X. Fang, and M.L. Dunn, *Multimaterial 4d printing with tailorable shape memory polymers.* Scientific Reports, 2016. **6**: p. 31110.
6. Boatti, E., N. Vasios, and K. Bertoldi, *Origami metamaterials for tunable thermal expansion.* Advanced Materials, 2017. **29**: p. 1700360.
7. Zhang, Q., J. Wommer, C. O'Rourke, J. Teitelman, Y. Tang, J. Robison, G. Lin, and J. Yin, *Origami and kirigami inspired self-folding for programming three-dimensional shape shifting of polymer sheets with light.* Extreme Mechanics Letters, 2017. **11**(Supplement C): p. 111-120.
8. Breger, J.C., C. Yoon, R. Xiao, H.R. Kwag, M.O. Wang, J.P. Fisher, T.D. Nguyen, and D.H. Gracias, *Self-folding thermo-magnetically responsive soft microgrippers.* ACS Applied Materials & Interfaces, 2015. **7**(5): p. 3398-3405.
9. Stoychev, G., N. Puretskiy, and L. Ionov, *Self-folding all-polymer thermoresponsive microcapsules.* Soft Matter, 2011. **7**(7): p. 3277-3279.
10. Tibbits, S., *Design to self-assembly.* Architectural Design, 2012. **82**(2): p. 68-73.

11. Mao, Y., Z. Ding, C. Yuan, S. Ai, M. Isakov, J. Wu, T. Wang, M.L. Dunn, and H.J. Qi, *3d printed reversible shape changing components with stimuli responsive materials.* Scientific Reports, 2016. **6**: p. 24761.
12. Miller, W., C. Smith, D. Mackenzie, and K. Evans, *Negative thermal expansion: A review.* Journal of materials science, 2009. **44**(20): p. 5441-5451.
13. Sleight, A.W., *Negative thermal expansion materials.* Current Opinion in Solid State and Materials Science, 1998. **3**(2): p. 128-131.
14. Korthuis, V., N. Khosrovani, A.W. Sleight, N. Roberts, R. Dupree, and W.W. Warren, Jr., *Negative thermal expansion and phase transitions in the zrv2-xpxo7 series.* Chemistry of Materials, 1995. **7**(2): p. 412-417.
15. Mary, T.A., J.S.O. Evans, T. Vogt, and A.W. Sleight, *Negative thermal expansion from 0.3 to 1050 kelvin in zrw2o8.* Science, 1996. **272**(5258): p. 90-92.
16. Ito, T., T. Suganuma, and K. Wakashima, *A micromechanics-based analysis for tailoring glass-fiber-reinforced thermoplastic laminates with near-zero coefficients of thermal expansion.* Composites Science and Technology, 2000. **60**(9): p. 1851-1861.
17. Ashby, M.F., *Materials selection in mechanical design*. Fourth ed. 2011, Oxford: Butterworth-Heinemann.
18. Hopkins, J.B., K.J. Lange, and C.M. Spadaccini, *Designing microstructural architectures with thermally actuated properties using freedom, actuation, and constraint topologies.* Journal of Mechanical Design, Transactions of the ASME, 2013. **135**(6): p. 061004.
19. Jefferson, G., T.A. Parthasarathy, and R.J. Kerans, *Tailorable thermal expansion hybrid structures.* International Journal of Solids and Structures, 2009. **46**(11-12): p. 2372-2387.
20. Miller, W., D.S. Mackenzie, C.W. Smith, and K.E. Evans, *A generalised scale-independent mechanism for tailoring of thermal expansivity: Positive and negative.* Mechanics of Materials, 2008. **40**(4–5): p. 351-361.
21. Lim, T.-C., *Anisotropic and negative thermal expansion behavior in a cellular microstructure.* Journal of materials science, 2005. **40**(12): p. 3275-3277.
22. Palumbo, N., C. Smith, W. Miller, and K. Evans, *Near-zero thermal expansivity 2-d lattice structures: Performance in terms of mass and mechanical properties.* Acta Materialia, 2011. **59**(6): p. 2392-2403.

23. Wei, K., H. Chen, Y. Pei, and D. Fang, *Planar lattices with tailorable coefficient of thermal expansion and high stiffness based on dual-material triangle unit.* Journal of the Mechanics and Physics of Solids, 2016. **86**: p. 173-191.

24. Wu, L., B. Li, and J. Zhou, *Isotropic negative thermal expansion metamaterials.* ACS Applied Materials & Interfaces, 2016. **8**(27): p. 17721-17727.

25. Grima, J.N., D. Attard, and R. Gatt, *Truss‐type systems exhibiting negative compressibility.* physica status solidi (b), 2008. **245**(11): p. 2405-2414.

26. Vandeperre, L.J. and W.J. Clegg, *Tailoring strains through microstructural design.* MRS Online Proceedings Library, 2003. **785**: p. D11.4.1.

27. Lehman, J. and R.S. Lakes, *Stiff, strong, zero thermal expansion lattices via material hierarchy.* Composite Structures, 2014. **107**: p. 654-663.

28. Sigmund, O. and S. Torquato, *Design of materials with extreme thermal expansion using a three-phase topology optimization method.* Journal of the Mechanics and Physics of Solids, 1997. **45**(6): p. 1037-1067.

29. Ai, L. and X.L. Gao, *Metamaterials with negative poisson's ratio and non-positive thermal expansion.* Composite Structures, 2017. **162**: p. 70-84.

30. Wang, Q., J.A. Jackson, Q. Ge, J.B. Hopkins, C.M. Spadaccini, and N.X. Fang, *Lightweight mechanical metamaterials with tunable negative thermal expansion.* Physical Review Letters, 2016. **117**(17): p. 175901.

31. Lakes, R., *Cellular solids with tunable positive or negative thermal expansion of unbounded magnitude.* Applied Physics Letters, 2007. **90**(22): p. 221905.

32. Lehman, J. and R. Lakes, *Stiff, strong zero thermal expansion lattices via the poisson effect.* Journal of Materials Research, 2013. **28**(17): p. 2499-2508.

33. Lim, T.-C., *Negative thermal expansion in transversely isotropic space frame trusses.* Physica Status Solidi (b), 2013. **250**(10): p. 2062-2069.

34. Ai, L. and X.L. Gao, *Three-dimensional metamaterials with a negative poisson's ratio and a non-positive coefficient of thermal expansion.* International Journal of Mechanical Sciences, 2018. **135**: p. 101-113.

35. Qu, J., M. Kadic, A. Naber, and M. Wegener, *Micro-structured two-component 3d metamaterials with negative thermal-expansion coefficient from positive constituents.* Scientific Reports, 2017. **7**: p. 40643.

36. Wadley, H.N.G., *Multifunctional periodic cellular metals.* Philosophical Transactions of the Royal Society A: Mathematical, Physical and Engineering Sciences, 2006. **364**(1838): p. 31-68.
37. Kim, T., H.P. Hodson, and T.J. Lu, *Fluid-flow and endwall heat-transfer characteristics of an ultralight lattice-frame material.* International Journal of Heat and Mass Transfer, 2004. **47**(6): p. 1129-1140.
38. Xu, H. and D. Pasini, *Structurally efficient three-dimensional metamaterials with controllable thermal expansion.* Scientific Reports, 2016. **6**: p. 34924.
39. Palumbo, N.M.A., *Trusses with reduced thermal expansion: Their design, and mass and stiffness penalties*. 2013, University of Exeter: UK. p. 260.
40. Watts, S. and D.A. Tortorelli, *Optimality of thermal expansion bounds in three dimensions.* Extreme Mechanics Letters, 2017. **12**(Supplement C): p. 97-100.
41. USDOD, *Military handbook - mil-hdbk-5h: Metallic materials and elements for aerospace vehicle structures*. 1998, U.S.: U.S. Department of Defense.
42. Liot, F.c., *Thermal expansion and local environment effects in ferromagnetic iron-based alloys-a theoretical study*, in *Department of Physics, Chemistry and Biology*. 2009, Linoping University: Sweden. p. 61.
43. Nye, J.F., *Physical properties of crystals: Their representation by tensors and matrices*. 1985, Oxford, UK: Clarendon Press.
44. Takezawa, A. and M. Kobashi, *Design methodology for porous composites with tunable thermal expansion produced by multi-material topology optimization and additive manufacturing.* Composites Part B: Engineering, 2017. **131**: p. 21 - 29.
45. Arabnejad, S. and D. Pasini, *Mechanical properties of lattice materials via asymptotic homogenization and comparison with alternative homogenization methods.* International Journal of Mechanical Sciences, 2013. **77**(0): p. 249-262.
46. Vigliotti, A., V.S. Deshpande, and D. Pasini, *Non linear constitutive models for lattice materials.* Journal of the Mechanics and Physics of Solids, 2014. **64**(0): p. 44-60.
47. Hollister, S.J. and N. Kikuchi, *A comparison of homogenization and standard mechanics analyses for periodic porous composites.* Computational Mechanics, 1992. **10**(2): p. 73-95.

48. Hualin, F. and Y. Wei, *An equivalent continuum method of lattice structures.* Acta Mechanica Solida Sinica, 2006. **19**(2): p. 103-113.

49. Mohr, D., *Mechanism-based multi-surface plasticity model for ideal truss lattice materials.* International Journal of Solids and Structures, 2005. **42**(11–12): p. 3235-3260.

50. Fan, H.L., D.N. Fang, and F.N. Jing, *Yield surfaces and micro-failure mechanism of block lattice truss materials.* Materials & Design, 2008. **29**(10): p. 2038-2042.

Link between chapter 3 and chapter 4

In the previous chapter, the thesis proposed routes to systematically engineer thermally responsive architected materials that are built from nine dual-material tetrahedral building blocks that are stiff and strong with desired magnitude and spatial directionality of thermal expansion. Chapter 4 exemplifies the design methodology through the application to a set of three-dimensional lattices, such as the dual-material Octet-truss, which are proven to not only be stiffer and stronger than any other existing concepts, but also offer a highly tunable CTE. Pretension snap-fits were used to fabricate all the three versions of the Octet cell, which resolve the trade-off between CTE tunability and structural efficiency, and extends the pin-jointed concept in Chapter 3 to bonded-joint lattices. Via a combination of numerical simulations and physical experiments on 3D fabricated prototypes, this work demonstrates how the Octet lattice can generate a large range of CTE values, including negative, zero, or positive, with no loss in structural efficiency. The novelty and simplicity of the proposed design, as well as the ease in fabrication, make this bi-material architecture well-suited for a wide range of applications, including satellite antennae, space optical systems, precision instruments, thermal actuators, and MEMS.

Chapter 4

Structurally efficient three-dimensional metamaterials with controllable thermal expansion

Chapter 4: Structurally efficient three-dimensional metamaterials with controllable thermal expansion

Hang Xu, and Damiano Pasini*

Department of Mechanical Engineering, McGill University, 817 Sherbrooke Street West,
Montreal, Quebec, Canada H3A 0C3, Canada

*Corresponding author: (damiano.pasini@mcgill.ca)

Scientific Reports, 2016. 6: p. 34924.

4.1 Abstract

The coefficient of thermal expansion (CTE) of architected materials, as opposed to that of conventional solids, can be tuned to zero by intentionally altering the geometry of their structural layout. Existing material architectures, however, achieve CTE tunability only with a sacrifice in structural efficiency, i.e. a drop in both their stiffness to mass ratio and strength to mass ratio. In this work, we elucidate how to resolve the trade-off between CTE tunability and structural efficiency and present a lightweight bi-material architecture that not only is stiffer and stronger than other 3D architected materials, but also has a highly tunable CTE. Via a combination of physical experiments on 3D fabricated prototypes and numeric simulations, we demonstrate how two distinct mechanisms of thermal expansion appearing in a tetrahedron, can be exploited in an Octet lattice to generate a large range of CTE values, including negative, zero, or positive, with no loss in structural efficiency. The novelty and simplicity of the proposed design as well as the ease in fabrication, make this bi-material architecture well-suited for a wide range of applications, including satellite antennas, space optical systems, precision instruments, thermal actuators, and MEMS.

4.2 Introduction

With an increase in temperature, most conventional materials expand with thermo-elastic distortions that can be difficult to accommodate. Materials with low coefficient of thermal expansion (CTE) are less sensitive to temperature changes and thus sought in several areas of engineering, such as precision instruments, scanning electron microscopes, flexible electronics, biomedical sensors, thermal actuators, and MEMS [1-3]. Low CTE materials are also particularly crucial in aerospace components, such as space-based mirrors [3] and satellite antennas [4], that are built on earth but operate in outer space where wide temperature swings may cause undesired shape and size shrinkage. Solid materials, such as Invar and other metallic alloys, with intrinsically low or negative thermal expansion exist [5], and are currently used despite their limitations. One of their drawbacks is the narrow range in which they can operate, which is problematic when large temperature swings, from -150°C to 150°C as in outer space, occur. The CTE of ceramics and other brittle solids, on the other hand, is low as well as insensitive to temperature variation [6, 7]; their brittleness, however, poses challenges because thermal stresses easily peak and lead to abrupt failure. In contrast, the ideal material would have CTE that could be tailored to vanish for the whole range of temperature it operates and would not be brittle, a condition currently unmet by all existing solids. One route to create a material with adjustable CTE is to engineer its structural architecture and purposefully tweak it to yield desired ranges of CTE, from positive to negative values including zero.

Recent works on mechanical metamaterials have shown that the CTE of periodic materials can be tuned by purposefully designing the architecture of their repeating unit and proper selection of the constituent materials [2, 3, 8-36]. It has been shown that low CTE can be obtained through a purely mechanical, and thus temperature-independent, mechanism [3], which can be in principle designed to make the material operate over a wide range of temperature. Existing mechanical metamaterials, however, have their limitations. The majority are two dimensional and can accommodate only in-plane thermal deformation [2, 3, 8-25, 28-30, 34, 35]. A handful are three-dimensional [9, 25-33]. Among those, some can generate a large range of CTE, i.e. their CTE tunability is high, but their structural efficiency, i.e. the specific stiffness and strength, is poor, since their architecture deform by bending when loaded [36], a deformation mechanism that is far from being structurally efficient. A very small set of architectures, on the other hand, are stretch dominated with high specific stiffness, but these concepts can generate only a narrow range of CTE and cannot yield a vanishing CTE. The trade-off between CTE tunability and structural efficiency is currently unresolved with current concepts achieving high CTE tunability only at the expense of a dramatic loss in their specific stiffness and specific strength [25, 32], and vice versa [9, 26-31, 33]. The goal of this work is to create a structurally efficient 3D architected material with highly tunable CTE including zero.

4.3 Mechanisms of thermal deformation in a tetrahedron

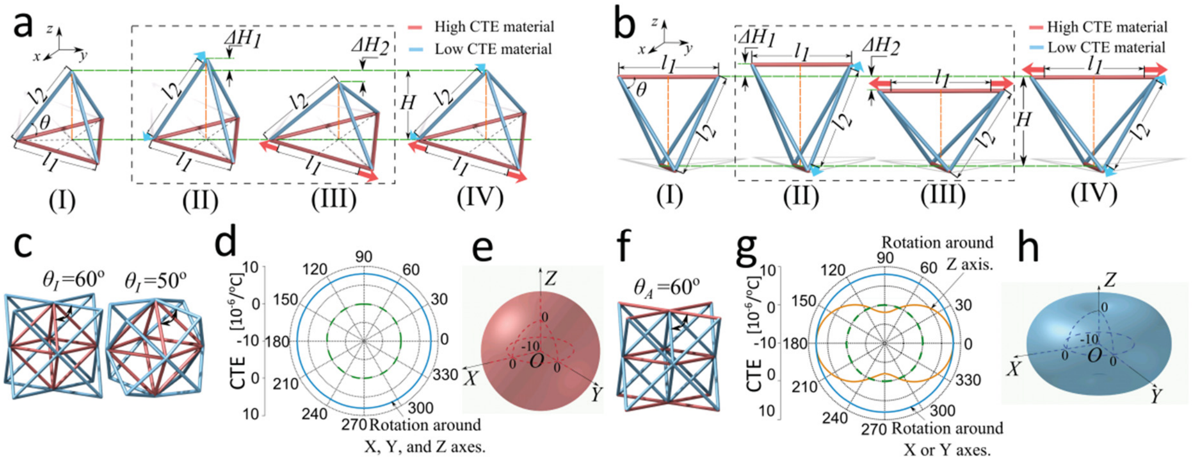

Figure 4-1: Thermal mechanisms a bi-material tetrahedron featuring either a stationary-node (a-I) or stationary-lines (b-I). II and III show visually uncoupled thermal expansions, one for the low-CTE material and the other for the high-CTE material; IV shows the overall thermal expansion of the tetrahedron. Application of bi-material tetrahedra to the Octet cells (c and f). (c) Iso-CTE Octet obtained by assembling 8 stationary-node tetrahedra with skew angle (θ_I) of 60° and 50° on a regular octahedron (red core). (d and e) isotropic CTE properties plotted in polar and spherical coordinates. (f) Aniso-CTE Octet (skew angle θ_A=60°) with directional CTE obtained with stationary-lines tetrahedra. (g and h) anisotropic CTE properties with low CTE in the *z*-direction. The green dashed line in (d) and (g) represents points with zero thermal expansion.

Since existing architected materials with high CTE tunability are bend-dominated and have thus low specific stiffness and strength, here we start off our investigation by considering a stretch-dominated lattice, the Octet truss, known for its structural efficiency, superior to that offered by most of the other existing lattices. The Octet lattice is obtained by replicating along periodic directions a unit cell that consists of a regular octahedron surrounded on each of its eight faces by a tetrahedron. We first focus on the thermal deformation mechanisms of its main building block, the tetrahedron, and show later how they can be used in an Octet lattice to generate high

CTE tunability, equally low in all directions or along preferential directions. A bi-material tetrahedron can undergo two mechanisms of thermal deformation by simply switching the position of the constituent materials. The first mechanism results in stationary-nodes (Figure 4-1a) [9, 28-31, 33-35], and can be used in an Octet cell to generate thermal expansion isotropy. The second mechanism that we identify here for the first time resorts to stationary-lines that appear in a bi-material tetrahedron upon thermal expansion (Figure 4-1b). This mechanism can be applied to obtain an Octet lattice with zero CTE in a specific direction, a thermal behavior that is often required at the interface between dissimilar materials, especially in transition components, or adapter elements, in need to tolerate a thermal-expansion mismatch in a given direction [17]. We recall that the unit cell of the Octet truss, here chosen for its high structural efficiency, contain eight tetrahedra that can be used to create thermal expansion mechanisms with either stationary lines or stationary nodes. A systematic strategy that uses the tetrahedron as the building block of the repeating unit is currently developed in a parallel work to rationally design a rich variety of bi-material lattices with programmable thermal expansion.

Figure 4-1a and 1b show the thermal expansion mechanisms with a stationary node and stationary lines respectively. The members with higher CTE, α_1, are shown in red and those with lower, but still positive, CTE, α_2, in blue. With a temperature increase, two modes of deformation occur simultaneously in the tetrahedron of Figure 4-1a-I, although visualized uncoupled in Figure 4-1a-II and III. The blue elements tend to heighten the tetrahedron (ΔH_1 in Figure 4-1a-II), whereas its top vertex is retracted by the red elements (ΔH_2 in Figure 4-1a-III). If the CTE of the constituent materials, α_1 and α_2, or alternatively the skew angle, θ, are carefully chosen, as shown in Figure 4-1b-IV, the height increase of the tetrahedron can be counteracted, a condition that leaves the position of the top vertex unaltered. This point is designated as a stationary-node [35], which implies that its position in the tetrahedron does not change during thermal deformation. An alternative scheme of thermal deformation, introduced here, consists of stationary-lines that can appear in a tetrahedron during thermal deformation (Figure 4-1b). With this mechanism, the minimum distance (marked as H in Figure 4-1b) between the top and bottom struts (red) of the tetrahedron, which have identical CTE, remain constant upon heating. For stationary lines to appear, the struts with high CTE (red) should be rationally designed in the tetrahedron so as to be skewed (Figure 4-1b), as opposed to those in a stationary-node mechanism, which all lie in the base plane of the tetrahedron (Figure 4-1a). In a stationary-line layout, the relative position of the struts, including the angle between struts and the minimum distance (H) between the top and bottom struts are preserved upon heating. Similarly to Figure 4-1a, Figure 4-1b-II and III show the deformation modes for a stationary-line tetrahedron; here to ease the understanding, the deformations are shown as uncoupled, although in practice they are not, as they occur at the same instant. Figure 4-1 (b-II)) shows the height increase, ΔH_1, caused by the thermal expansion of the blue elements, whereas Figure 4-1 (b-III) visualizes the height decrease ΔH_2 induced by the greater expansion of the horizontal red beams. The height increase, ΔH_1, of the blue elements (Figure 4-1b-II) is thus compensated by a height decrease, ΔH_2, (Figure 4-1b-III) induced by the greater expansion of the red members. As a result, the overall CTE of the tetrahedron in the vertical direction (Figure 4-1b-IV) can be controlled through either an educated choice of the constituent materials, in particular by selecting the CTE (α_1 and α_2) of the two constituent materials, or a tailored selection of the skew angle, θ, between the struts shown in Figure 4-1.

4.4 Generation of Octet bi-materials with high CTE tunability

Low CTE tetrahedra with either a stationary-node (Figure 4-1a-I) or stationary-lines (Figure 4-1b-I) can be used to generate more complex 3D unit cells that in turn can tessellate periodic lattices with low CTE in desired directions. Here we chose three examples as shown in Figure 4-1c and 1f, all applied to an Octet cell but potentially applicable to other cell topologies containing tetrahedra. Figure 4-1c shows two Octets with a stationary-node, one with skew angle θ_I=60° and the other with θ_I=50°, and Figure 4-1f illustrates an Octet with stationary-lines for θ_A=60°. The Octet in Figure 4-1c, namely Iso-CTE Octet, has a regular octahedron as its core, surrounded by eight stationary-node tetrahedra on its faces. Upon heating, each of the vertices of the eight tetrahedra remains stationary, and can guarantee an isotropic CTE, as shown by the plots in Figure 4-1d and e. On the other hand, the Aniso-CTE Octet in Figure 4-1f has stationary-lines tetrahedra assembled in an Octet cell that results in thermal expansion anisotropy. In this case, upon heating, the relative position of the planes, where the red struts of the eight tetrahedra lie, remain unaltered, thereby leading to a potentially zero thermal deformation in a specific direction (see Figure 4-1e and h). Whereas the thermal expansion of the Iso-CTE Octet is isotropic, its mechanical properties are almost isotropic, as opposed to the Aniso-CTE Octet, which is both mechanically and thermally anisotropic.

4.5 Results

Manufacturing, simulations, and testing

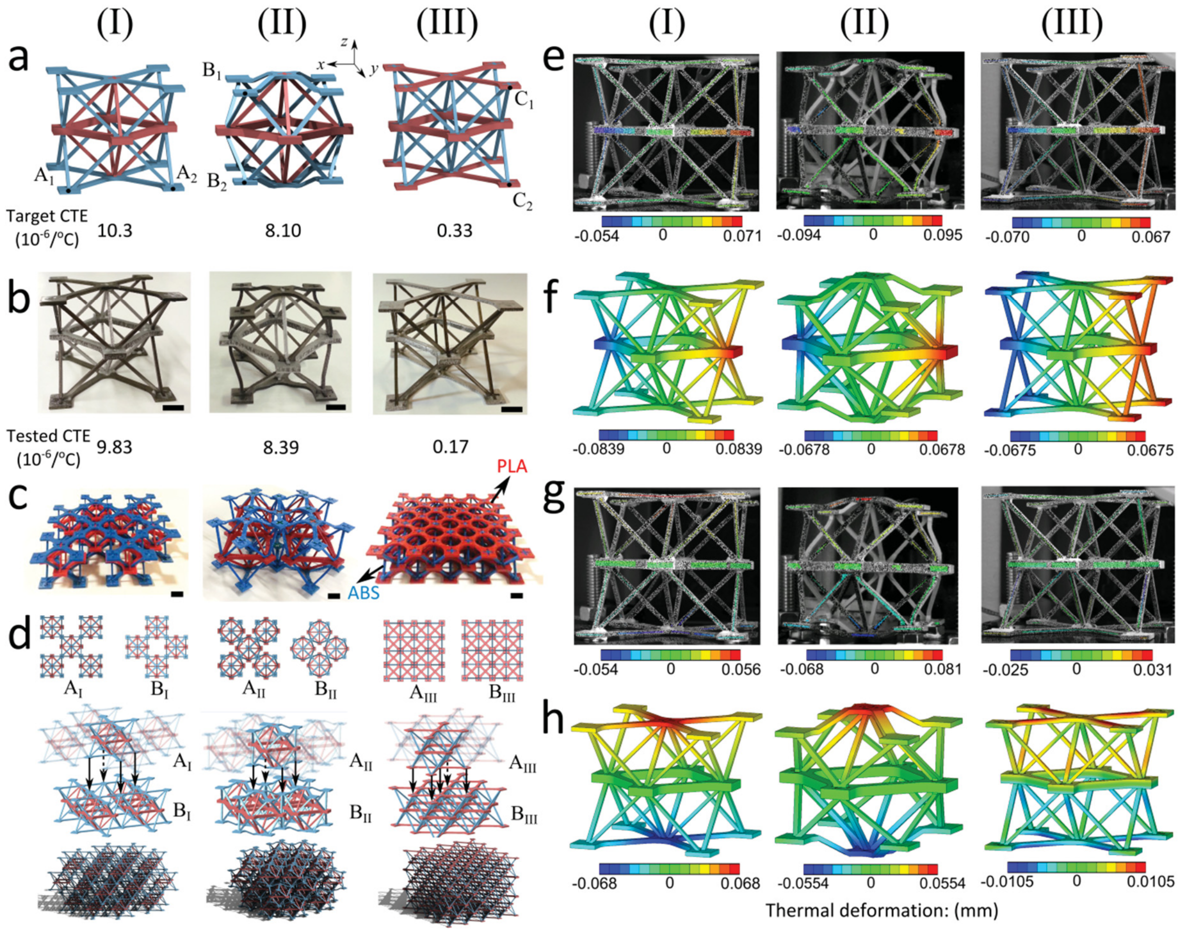

Figure 4-2: Design embodiments for Iso-CTE Octet and Aniso-CTE Octet: (a-I) Topologies for Iso-CTE Octet (θ_I=60°) with A_1 and A_2 used as corresponding nodes for the CTE measurement in the *x*-direction, (a-II) Iso-CTE octet (θ_I=50°) with B_1 and B_2 used as corresponding nodes for the CTE measurement in the *z*-direction, and (a-III) Aniso-CTE Octet (θ_A=60°), with C_1 and C_2 as corresponding nodes for the CTE measurement in the z-direction; (DIC tested CTEs obtained by evaluating the average of 100 CTE measurements between pairs of corresponding nodes). (b)

Cells manufactured from Al6061 (high-CTE) and Ti-6Al-4V (low-CTE); Design target and tested CTEs given for Iso-CTE Octet and Aniso-CTE Octet in the *z*-direction. (c) 3D printed low-CTE lattices showing one layer of the bi-material lattice: PLA (poly lactic acid) in red with high CTE, and ABS (acrylonitrile butadiene styrene) in blue with low CTE. (d) Top and isometric views of two layers showing the stacking sequence as well as the overall lattice assembly for each bi-material concept. Thermal displacement maps for horizontal deformation (e: DIC and f: FEA) and vertical deformation (g: DIC and h: FEA). (Scale bar: 10 mm).

The concepts shown in Figure 4-1 elucidate the two thermal expansion mechanisms of a tetrahedron and show their application to three Octet cells, where the skew angle can be tuned to yield negative, zero, or positive, CTE in either all directions or a specific direction. We now demonstrate their thermal tunability with physical experiments on fabricated prototypes and examine the robustness of our findings by performing numeric simulations. The embodiment of each Octet cell (Figure 4-1) is shown in Figure 4-2a with manufactured prototypes in Figure 4-2b, each targeting a specific CTE value of design. Each Octet cell is an assembly of laser cut pieces from Al6061 (23×10^{-6}/°C) and Ti–6Al–4V (11.5×10^{-6}/°C) alloy sheets with pretension snap-fit joints, similar to simple snap-fit joints [37]. (See Methods Section 4.8 and Supplementary Material Section 4.9). The thermal properties are tested on a single unit cell with experimentally measured CTE values, reported in Figure 4-2b, that enable a quantitative validation of the computational results. The feasibility of the overall lattice assembly is demonstrated in Figure 4-2c and d, where geometric models and 3D printed prototypes for each version of the Octet cell show the overall in-plane and out-of-plane tessellation. For CTE measurements, a 3D digital image correlation (DIC) set-up with a temperature controlled heating chamber (Methods Section 4.8 and Supplementary Material 4.9) is used to assess the CTE of each version of the Octet cell. Results from experiments (Figure 4-2e and g) and their counterpart simulations (Figure 4-2f and h) are quantitatively in good agreement. The results in Figure 4-2e-I to h-I show that for the Iso-CTE Octet with θ_I =60°, the thermal expansion along both the *x*- and *z*-direction is low and positive (9.83×10^{-6}/°C), which is below the CTE value of the inner Al6061 octahedron (21×10^{-6}/°C), and below that (11.5×10^{-6}/°C) of its constituent material Ti-6Al-4V. In addition, the effective CTE of the Iso-CTE Octet can be further reduced to 8.39×10^{-6}/°C by changing the skew angle from θ_I =60° to 50° (Figure 4-2e-II to h-II). On the other hand, for the Aniso-CTE Octet, the CTE measurement in Figure 4-2g-III shows no change appears in the vertical distance between the horizontal bars; in addition, the CTE value in the *z*-direction is almost zero (0.171×10^{-6}/°C), and much lower than the CTE in the horizontal direction (Figure 4-2e-III to h-III). We note that the maximum and minimum CTE values obtained with FEA and DIC differ slightly. The reason for the discrepancy is attributed to the testable zone on a given strut where DIC can provide reliable measurements. Points outside this zone, which is smaller than that analyzed with FEA, cannot be measured. Other factors of the DIC technique that can play a role in explaining the difference between experiment and computational results include the size and curvature of the testing sample subset, and the light contrast used during the experiments. (See Methods Section 4.8 and Supplementary Material Section 4.9).

4.6 Discussion

To establish and compare the thermomechanical merit of the Octet lattice bi-materials here presented, we now resort to two sets of charts. The first set (Figure 4-3) compares the Octet concepts with two 3D benchmarks existing in the literature [9, 32] for a representative value of relative density of 0.05 and assuming Al6061 and Ti–6Al–4V as the constituent materials (Material properties in Table 4-1 and Table 4-2 of Supplementary Material Section 4.9); the second set (Figure 4-4) compares them with other classes of materials in a given range of relative density. Figure 4-3a illustrates the CTE trends with respect to the skew angle for our versions of the Octet, along with those of the two benchmarks, the H-concept [32] (bend-dominated) and the S-concept [9] (stretch-dominated). The former has low structural efficiency but high CTE tunability, as opposed to the latter, which is structurally efficient but with relatively poor CTE tunability. CTE tunability is here measured by ΔCTE, which is the difference between the upper and lower CTE limit (obtained from the *y*-axis of Figure 4-3a) that each unit cell can yield with a change in either its skew angle or the constituent materials. We recall here that these are two, among others, of the most promising geometric variables that can be controlled to further boost the CTE tunability. The higher the CTE tunability of a concept, the larger ΔCTE. The results obtained for each concept via asymptotic homogenization [38] and validated via experiments for given geometries, show that the Aniso-CTE Octet has the highest CTE tunability. The CTE in the *z*-direction ranges from -366×10^{-6}/°C (not visible in Figure 4-3a) to 10.9×10^{-6}/°C, values that result in a tunability $\Delta\mathrm{CTE}_{(\theta)}=376.9\times10^{-6}$/°C. For larger skew angles, the CTE of the Aniso-CTE

Octet monotonically increases to reach that of Ti-6Al-4V. The H-Concept, on the other hand, has a highly tunable CTE, which can also reach negative values; as shown in Figure 4-3a; its effective CTE first decreases before rising up again for increasing skew angles. The CTE tunability of the Iso-CTE Octet is more than double that of the S-Concept, which has CTE that reaches the minimum of 0.273×10^{-6}/°C for θ_I =42° and its max of 11.3×10^{-6}/°C for θ_I =65°. Figure 4-3b shows a comparison of the CTE tunability of the concepts here under investigation, with those of Ti-6Al-4V. Besides their ΔCTE represented by the height of each column, the red and blue gradients specify CTE ranges of positive and negative values with white indicating zero. The Iso- and Aniso-CTE Octet are the only concepts that can obtain near-zero CTE. The H-Concept can provide a negative CTE range, whereas the ΔCTE of the S-Concept is narrow with min and max values that are both positive. The octet concepts presented in this work have a large CTE tunability including vanishing CTE obtained from common materials, such as Al and Ti alloys, which have both positive CTE.

To assess the structural efficiency of the bi-material Octet lattices, we plot in Figure 4-3c and d the effective elastic modulus and yield strength in all the relevant directions for the low range of relative density 0.02 to 0.30. The plot of the shear properties is included in the Supplementary Material Section 4.9. The properties of the H-Concept and the S-Concept are also visualized to allow a comparison of their specific stiffness and strength, represented by the slope of a given point on a curve. We note that for ρ^* below 0.1, the relation between the Young's modulus and the relative density of the bi-material Octet lattice is not linear – as one would expect to be for a single material lattice. The reason for this is that the unit cell contains struts made of two materials with dissimilar relative density. As expected, the results show that all stretch dominated concepts have a better structural efficiency, with the Aniso-CTE Octet being the best for stiffness and strength in the *z*-direction. For relative density above 0.1, the Iso-CTE Octet with θ_I =60° performs worse than the S-Concept, because the joints of the latter are modelled as ideal, i.e. weightless, as opposed to those of the Octet cells, which are modelled with their actual manufactured geometry. By comparing the two versions of the Iso-CTE Octet, one with θ_I =50° and the other with 60°, we observe that the former can provide a lower CTE at the expense of a reduction in structural performance. In summary, the Aniso-CTE Octet has the best mechanical performance, whereas the Iso-CTE Octet outperforms the structural performance of the S-Concept and the H-Concept.

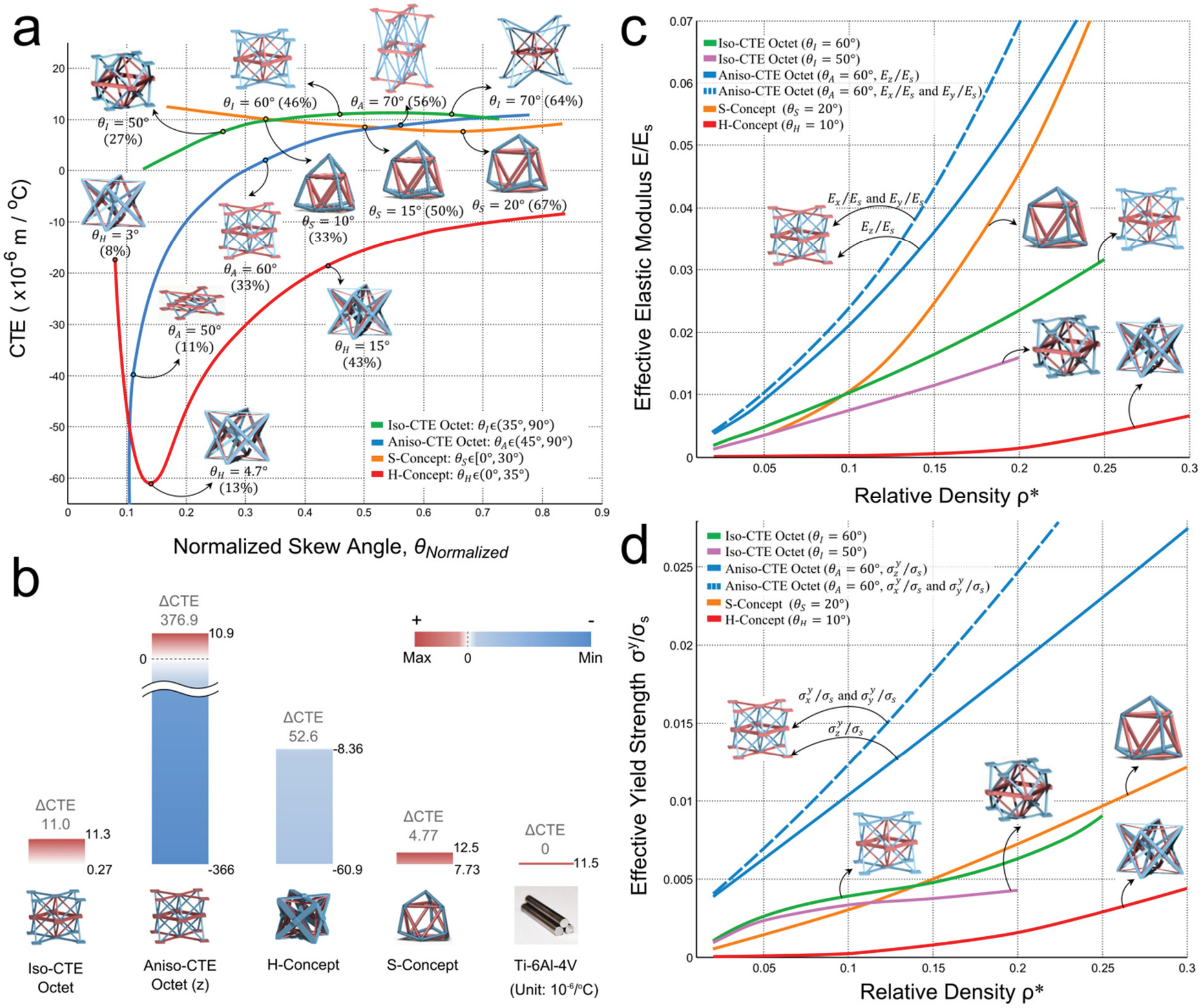

Figure 4-3: (a) Thermal properties of the Octet bi-materials and benchmark concepts (S-concept [9] and H-concept [32]) plotted with respect to the normalized skew angle, $\theta_{Normalized}$. Shown in bracket below each pictorial, $\theta_{Normalized}$ is calculated as $\theta_{Normalized} = (\theta_{Model} - \theta_{min}) / (\theta_{max} - \theta_{min})$, where θ_{Model} is the skew angle of a concept, and θ_{min} and θ_{max} are respectively the minimum and maximum skew angle that a concept can provide without its cell topology degenerates. (b) Histogram showing the CTE tunability (ΔCTE) as well as the max and min CTE for the selected concepts compared to a low CTE solid material, i.e. Ti-6Al-4V. (c) Effective stiffness and (d) effective strength plotted with respect to relative density ρ^*. Note $\rho^* = \rho_{lattice} / \rho_{solid\ composite}$ where

$\rho_{lattice}$ is the actual density of the bi-material unit cell and $\rho_{solid\ composite}$ is the density of the solid bi-material with volume fraction of the constituent materials. Note that the maximum relative density of the Iso-CTE Octet does not reach 0.3; it is 0.2 for θ_I =50°, and 0.25 for θ_I =60°, because above these values the size of the joints become unfeasibly larger than the cell members, which means that the cell is unfeasible.

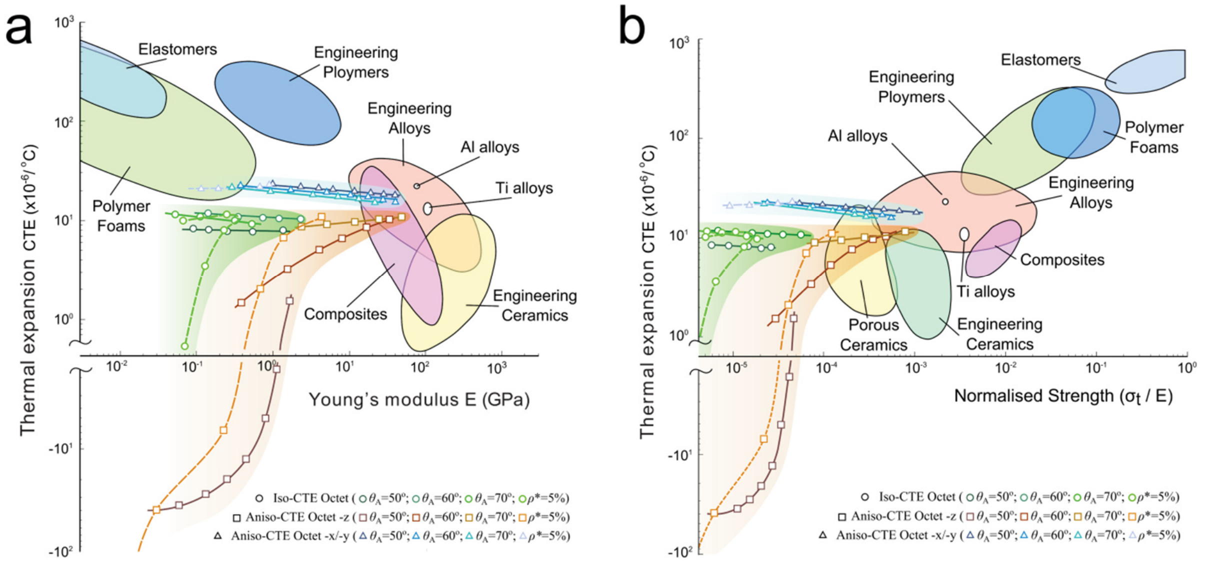

Figure 4-4: (a) CTE plotted against Young's modulus [39]; and (b) CTE versus normalized strength (ultimate strength for Metals and Polymers; modulus of rupture for Ceramics; tensile strength for Composites) [40]. The points for the Octet cells are obtained by varying either the skew angle for a given relative density (0.05) or vice versa. Relative density ranges considered in the charts for the Octet lattice concepts: $0.02<\rho^*<0.25$ for the Iso-CTE Octet, and $0.02<\rho^*<0.60$ for the Aniso-CTE Octet.

We finally resort to material property charts to visualize the thermomechanical performance of the two Al6061-Ti-6Al-4V Octet concepts and compare it with that of other classes of materials. Figure 4-4a and b show respectively Young's modulus and normalized strength plotted versus the CTE. The Octets with high CTE tunability achieve unprecedented combinations of properties that cannot be obtained with other classes of materials [39, 40]. By spanning the skew angle of the Iso-CTE Octet, the CTE can range from near-zero ($<1\times10^{-6}$/°C) to that of Ti-6Al-4V. The CTE of the Aniso-CTE Octet in the vertical direction can be theoretically changed from negative infinity to the CTE of Ti-6Al-4V. The Aniso-CTE Octet has CTE in the horizontal direction approximately equal to the Al6061 CTE, but possesses Young's modulus and normalized strength that can be tailored by purposefully changing relative density and skew angle. Figure 4-4 shows that for a given CTE, the Young's modulus and normalized strength of the Aniso-CTE Octet in the *z*-direction are higher than those of the Iso-CTE Octet. On the other hand, for given Young's modulus or normalized strength, the Aniso-CTE Octet can obtain a lower CTE in the *z*-direction, which make it an ideal candidate for applications which require thermal stability in prescribed directions.

4.7 Conclusions

To conclude, this study has presented, built, and thermally tested Octet lattice bi-materials (Al6061-Ti-6Al-4V) that can be tuned to cover a substantial range of CTEs, which include zero, in given spatial directions without jeopardizing their structural efficiency. Several variables defining the unit cell geometry govern the macroscopic thermo-mechanical properties of the bi-material lattices here investigated. The focus of this chapter has been on a subset of parameters, i.e. skew angle and strut thickness controlling relative density, which were selected as considered to play a crucial role in the CTE as well as specific stiffness and strength of the lattices. Other factors, such as the strut diameter ratio of the constituent materials and other topological variables, can be studied and used to achieve further CTE tuning. We also note that the conclusions drawn in this work on the thermomechanical performance of the bi-material octet lattice apply to the cases here investigated. Prototypes were built via snap-fit with pretension joints from either tetrahedra with stationary-node to provide CTE isotropy, or tetrahedra with stationary-lines to achieve CTE anisotropy. Results experimentally tested and validated via numeric simulations show that by introducing material architecture even common materials can render unprecedented combinations of thermomechanical properties. The novelty and the simplicity of the proposed 3d design as well as the ease in fabrication, make structurally efficient lattices with tunable coefficient of thermal expansion well-suited for a wide range of applications, such as satellite antennas, space optical systems, space-based mirrors, precision instruments, thermal actuators, and MEMS. The thermal expansion mechanism introduced in this chapter for the stationary-line tetrahedron, can also be exploited to create other multifunctional 3d architectures with high structural performance and desired directional properties, including thermal conductivity, acoustic bandgap, and electrical conductivity.

4.8 Methods

4.8.1 Sample fabrication

Pretension snap-fits were used to fabricate all the three versions of the Octet cell. Laser cut elements were bended to allow skew angle variation as needed, prior to snap-fitting of diagonal elements. Pretension provided by wedge resistance was used to fasten diagonal elements into cross-shaped holes. The connection between different elements was further reinforced with epoxy glue. The metal fabrication process is summarized schematically in Figure 4-5 with further explanatory details given (Supplementary Material Section 4.9).

4.8.2 DIC measurements

Digital Image Correlation was used to measure the small deformation of each lattice member and provide a full-field displacement map describing the thermal deformation behavior [3, 16, 18, 35]. A high contrast black and white speckle pattern with proper dot density was painted on each member of the lattice samples. The lattice was then placed into a heating chamber which rose the temperature up to approximately 125°C starting from an initial temperature of 25°C (Supplementary Material Section 4.9). The temperature was measured via thermocouples and collected in a data acquisition system. A proportional–integral–derivative controller (PID) was used to control the temperature. Digital images were captured with two charge-coupled-device (CCD) cameras and were controlled by a computer program (Vic-Snap 8 [41]). VIC-3D [42] was used to track the motion of speckle patterns to obtain the thermal deformation. The accuracy of the DIC system was evaluated by tested CTEs from standard metal alloy sheets (Al6061 and Ti-6Al-4V). The displacement noise was evaluated by taking multiple stationary images with time separation of 100ms. The noise was less than 2µm, while the expected displacement range was ~100-150µm.

4.8.3 Finite element simulations and asymptotic homogenization

Full 3D models of the testing samples were simulated by performing finite element simulations (ANSYS 14.5 [43]). All models were meshed using 10-node tetrahedral elements and simulated under a thermal load of 100°C. The effective CTEs were calculated by measuring the linear expansion between either the stationary-nodes or the stationary-lines (Figure 4-2a). For each cell topology, including the H-Concept and the S-Concept, asymptotic homogenization theory was combined with finite element analysis to calculate the thermomechanical effective properties. For thermal expansion analysis in steady state, the properties including effective stiffness, yield strength, and CTEs in all three orthogonal directions were calculated with respect to the relative density and the skew angle. Thermal properties calculated numerically were further validated for selected samples via experimentally obtained thermal measures. On the role played by the joints in the deformation of the simulated versus manufactured lattices, we recall that the Octet lattice is a pin-jointed structure that is stretch dominated, i.e. its slender members carry axial forces only. Making the joints of the Octet rigid makes no difference in the deformation modes. Whereas the computational analysis has considered both types of joints (pin and rigid), the manufactured lattices are built with rigid joints that are snap-fit to allow proper connection between struts of dissimilar materials.

4.9 Supplementary material

4.9.1 Manufacturing: pretension snap-fit method

Figure 4-5 shows the pretension snap-fit technique used to build the bi-material Octet cell. First, the structural elements were laser cut from metal sheets. For the regular Octet with either θ_I =60° or θ_A =60°, inclined elements were snap-fitted without bending and then attached to the horizontal panels. For irregular Octet-trusses, both the beam elements and interlayer panels require bending. To avoid rebound deformation, sheet metal hot extrusion processes can be used to alter the skewness angle. Since the snap-fit connections are between Al6061 (high CTE) and Ti-6Al-4V (low CTE), when heated, the cross-shaped grooves on the aluminum panels have a larger expansion than the titanium inserts, which loosens the joints, weakens the low CTE mechanism, and might cause the whole structure to fall apart. To avoid joint loosening, wedges with steep slopes (15°) were designed on both skewed elements and horizontal panels. When inserted, the wedged forces provided by the oblique-wedge clamping constrained the joints. Moreover, high-strength high-temperature-resistant epoxy glue (LePage Gel Epoxy Syringe Glue with working temperature up to 150°C) was used to fill in and cement Al6061 and Ti-6Al-4V elements. Epoxy providing a much larger CTE (45-65×10^{-6}/°C compared with Al6061 and Ti-6Al-4V) can increase the fastening force and prevent the joints from loosening. The wedges can be either laser cut or fine finished by CNC. We emphasize that joints made of Al6061 and Ti-6Al-4V can also be vacuum brazed with TiBrazeAl-580 foil (Al-12Si foil and Cu foil, Titanium Brazing, Inc.).

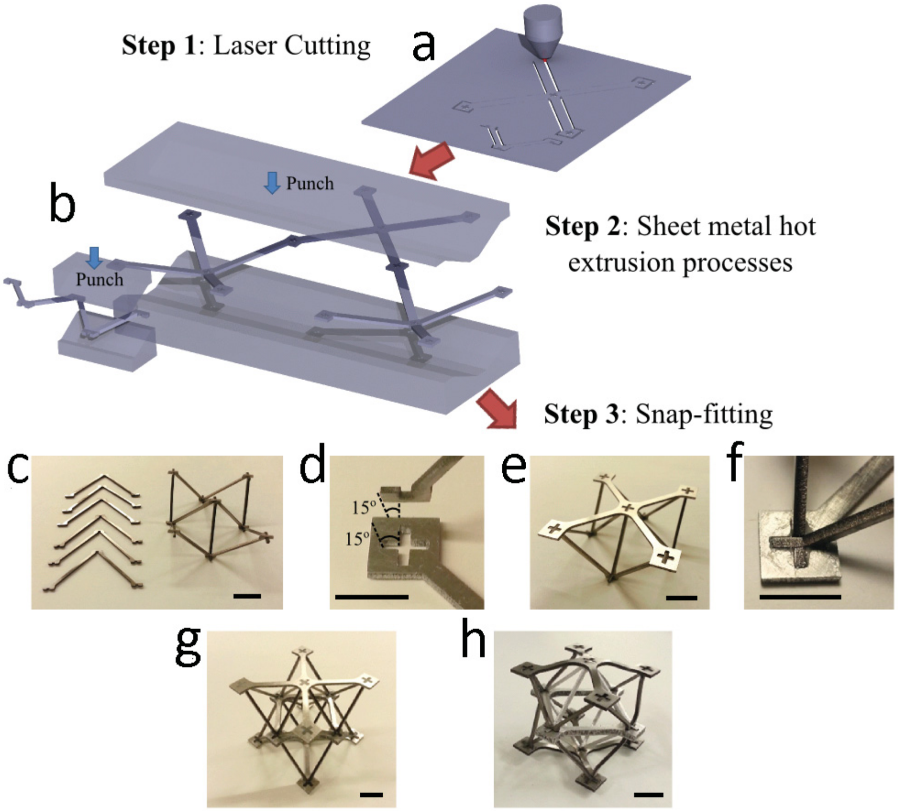

Figure 4-5: Pretension snap-fit manufacturing process. (a) Laser cutting; (b) Sheet metal hot extrusion processes to impose a given skew angle; (c) Snap-fitting of diagonal elements; (d) Wedge for pretension; (e) Snap-fitting of horizontal elements; (f) Joint reinforcement via Epoxy Glue; (g) Octet cell assembly from unbended elements; and (h) Octet cell assembly from slightly bended elements. (Scale bar: 10 mm)

4.9.2 Assembly and tessellation rules

Figure 4-6 shows possible tessellations for Octet cells at given skew angles. A packing density of 100% could be obtained for all Aniso-CTE Octets (Figure 4-6a). In contrast, dissimilar skew angles for the Iso-CTE Octet result in tessellations with lower packing factors, i.e. 50% for concepts in Figure 4-6b, c, and d, and 100% for the concept in Figure 4-6e. Differences in the packing factor are controlled by the need of the inner octahedron to thermally expand without touching adjacent cells as shown in Figure 4-6c-II.

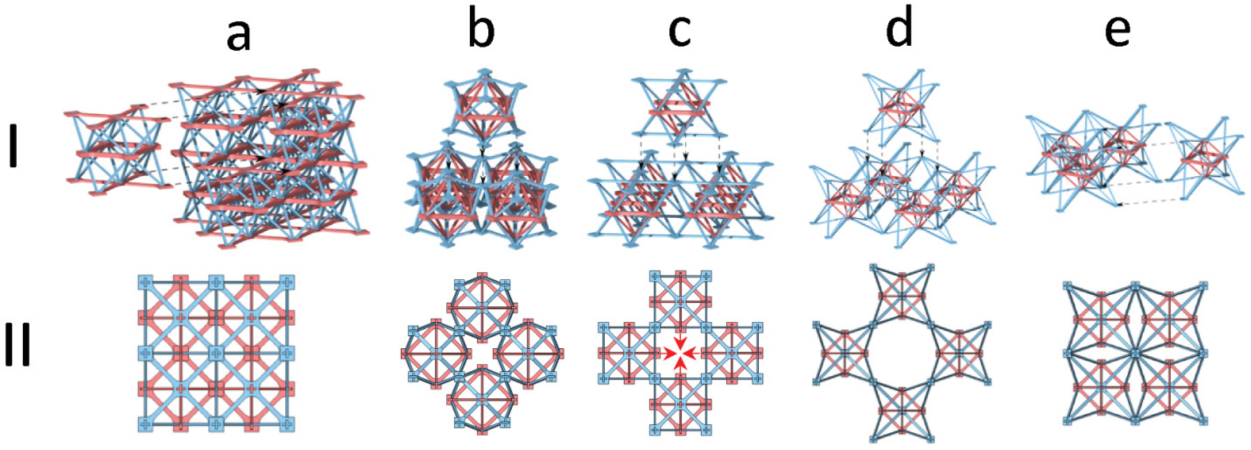

Figure 4-6: Tessellations of bi-material Octet cells (a) Aniso-CTE Octet with θ_A=60°, (b) Iso-CTE Octet with θ_I=50°, (c) Iso-CTE Octet with θ_I=60°, (d) and (e) are Iso-CTE Octet with θ_I=70°. Assembly in axonometric view (I) and top view (II).

4.9.3 Experiment to test thermal expansion

Figure 4-7 shows the schematic of the experimental set-up built to test the thermal expansion of the Octet cells. It consists of a heating chamber and a DIC system. The former with dimensions of 200(L)×200(W)×150(H) mm is made of glass to provide an unobstructed view for DIC measurements. A 200 Watt strip heater was placed under the copper plate in the heating chamber. The copper plate is supported by four leveling mounts which were used for horizontal adjustment. The temperature was controlled by a feedback system, which included a K-type thermocouple attached to the copper plate and a proportion integration differentiation (PID) (OMEGA CN7800) temperature controller. The controllable temperature range was from 25°C to 200°C. The temperature-time data in the PID controller were imported through a RS-485 interface. A NI cDAQ 9174 data acquisition system was used to collect the other three thermocouples from different locations in the chamber and to measure the temperature heterogeneity. A fan in the chamber mixed the air to provide a uniform ambient temperature. The temperature inhomogeneity was regulated within 5% of the real-time temperature through the application of a rotational air fan. Testing samples were covered by a black and white pattern and were set on the copper plate with thermal transfer grease between the two. The thermal strain was measured by DIC using images that were captured through two CCD cameras (Grasshopper 5.0 MP with Fujinon HF25SA-1 lens). Using the DIC correlation software, Vic-3D (Correlate Solution Inc.), virtual extensometers were placed on the reference image and tracked through the images to measure the displacement between pairs of pixel subsets. The strain field was obtained from the relative displacement between these pairs of subsets. The average CTE was calculated from thermal strain and temperature change.

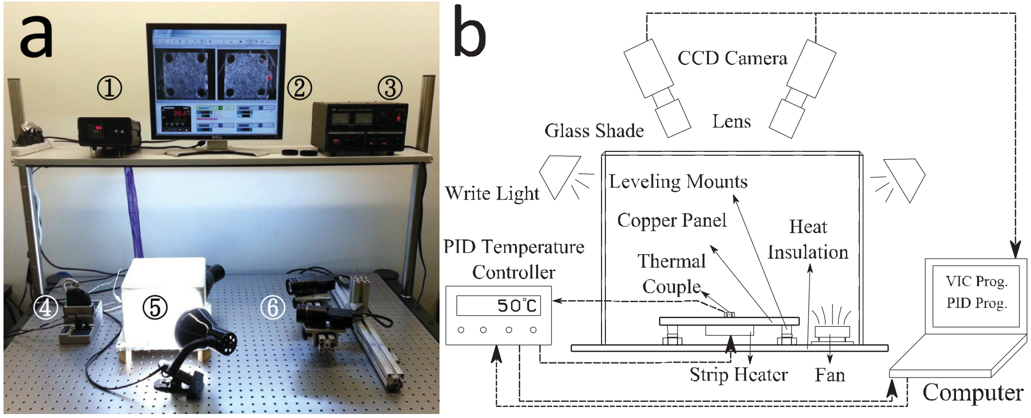

Figure 4-7: Experimental set-up used to measure thermal expansion (photograph (a) (1 PID controller; 2 Computer; 3 Power source; 4 DAQ system; 5 Heating chamber; and 6 CCD cameras) and schematic picture (b)).

To evaluate the accuracy of the CTE testing system, we choose Al6061 (Ta Chen International Inc.) and Ti-6Al-4V (RTI International Metals, Inc.) as two standard materials. The CTEs of these two standard materials were tested by both our DIC experimental set-up and a commercial thermal expansion instrument (TA Q400, TA Instruments, Inc.). The comparison of the measured CTEs shown in Table 4-1 shows the accuracy of our experimental set-up.

Material	DIC	Commercial instrument
Al6061	22.6×10^{-6}/°C	23.0×10^{-6}/°C
Ti-6Al-4V	12.0×10^{-6}/°C	11.5×10^{-6}/°C

Table 4-1: The measured CTEs of Al6061 and Ti-6Al-4V by DIC and TA Q400

Material	Young’s Modulus	Poisson’s Ratio
Al6061	70.75Gpa	0.35
Ti-6Al-4V	113.8GPa	0.34

Table 4-2: The mechanical properties of Al6061 and Ti-6Al-4V

4.9.4 Shear modulus of low-CTE octet truss

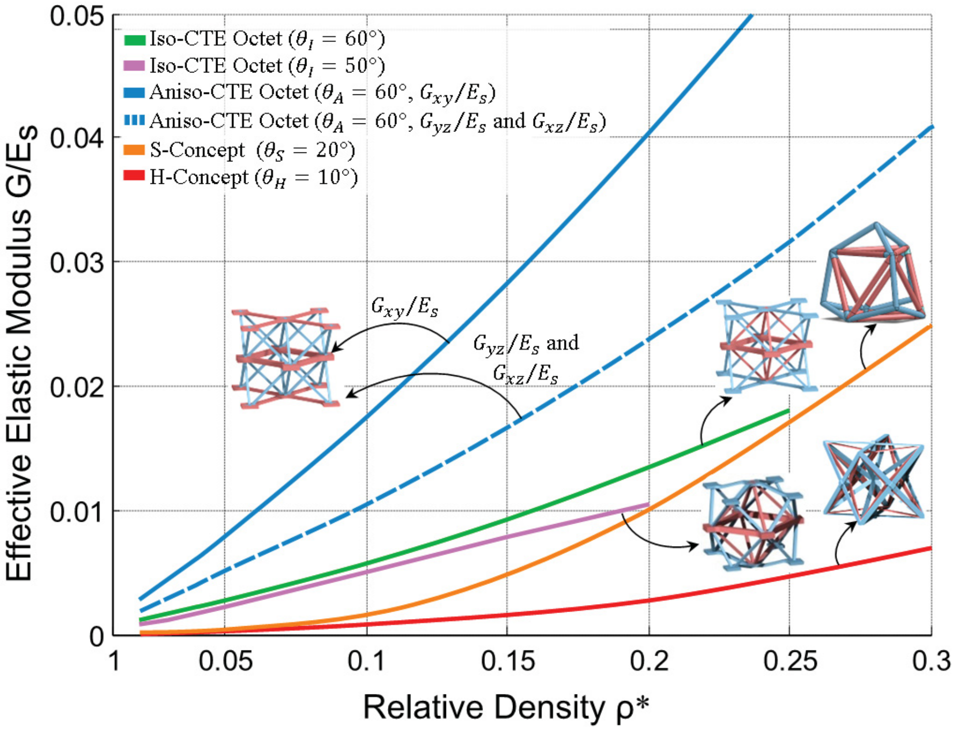

Figure 4-8: Effective shear modulus plotted with respect to relative density $\rho*$

4.10 References

1. Werner, M.R. and W.R. Fahrner, *Review on materials, microsensors, systems and devices for high-temperature and harsh-environment applications.* IEEE Transactions on Industrial Electronics, 2001. **48**(2): p. 249-257.
2. Toropova, M.M. and C.A. Steeves, *Adaptive bimaterial lattices to mitigate thermal expansion mismatch stresses in satellite structures.* Acta Astronautica, 2015. **113**(0): p. 132-141.
3. Yamamoto, N., E. Gdoutos, R. Toda, V. White, H. Manohara, and C. Daraio, *Thin films with ultra-low thermal expansion.* Advanced Materials, 2014. **26**(19): p. 3076-3080.

4. Gilmore, D.G., *Spacecraft thermal control handbook: Fundamental technologies*. 2002, United States: Aerospace Press.
5. Liu, Z.-K., Y. Wang, and S. Shang, *Thermal expansion anomaly regulated by entropy.* Scientific Reports, 2014. **4**: p. 7043.
6. Thieme, C., H. Görls, and C. Rüssel, *Ba1−xsrxzn2si2o7 - a new family of materials with negative and very high thermal expansion.* Scientific Reports, 2015. **5**: p. 18040.
7. Sun, Y., Y. Chen, C. Ding, G. Yang, Y. Ma, and C. Wang, *One-dimensional al4o4c ceramics: A new type of blue light emitter.* Scientific Reports, 2013. **3**: p. 1749.
8. Jefferson, G., T.A. Parthasarathy, and R.J. Kerans, *Tailorable thermal expansion hybrid structures.* International Journal of Solids and Structures, 2009. **46**(11-12): p. 2372-2387.
9. Steeves, C.A., S.L. dos Santos e Lucato, M. He, E. Antinucci, J.W. Hutchinson, and A.G. Evans, *Concepts for structurally robust materials that combine low thermal expansion with high stiffness.* Journal of the Mechanics and Physics of Solids, 2007. **55**(9): p. 1803-1822.
10. Lakes, R., *Cellular solid structures with unbounded thermal expansion.* Journal of Materials Science Letters, 1996. **15**(6): p. 475-477.
11. Lehman, J. and R. Lakes, *Stiff lattices with zero thermal expansion and enhanced stiffness via rib cross section optimization.* International Journal of Mechanics and Materials in Design, 2013. **9**(3): p. 213-225.
12. Sigmund, O. and S. Torquato, *Composites with extremal thermal expansion coefficients.* Applied Physics Letters, 1996. **69**(21): p. 3203-3205.
13. Hopkins, J.B., K.J. Lange, and C.M. Spadaccini, *Designing microstructural architectures with thermally actuated properties using freedom, actuation, and constraint topologies.* Journal of Mechanical Design, Transactions of the ASME, 2013. **135**(6): p. 061004.
14. Qi, J. and J.W. Halloran, *Negative thermal expansion artificial material from iron-nickel alloys by oxide co-extrusion with reductive sintering.* Journal of Materials Science, 2004. **39**(13): p. 4113-4118.
15. Grima, J.N., P.S. Farrugia, R. Gatt, and V. Zammit, *A system with adjustable positive or negative thermal expansion.* Proceedings of the Royal Society A: Mathematical, Physical and Engineering Science, 2007. **463**(2082): p. 1585-1596.

16. Berger, J., C. Mercer, R.M. McMeeking, and A.G. Evans, *The design of bonded bimaterial lattices that combine low thermal expansion with high stiffness.* Journal of the American Ceramic Society, 2011. **94**: p. s42-s54.
17. Toropova, M.M. and C.A. Steeves, *Bimaterial lattices with anisotropic thermal expansion.* Journal of Mechanics of Materials and Structures, 2014. **9**(2): p. 227-244.
18. Gdoutos, E., A.A. Shapiro, and C. Daraio, *Thin and thermally stable periodic metastructures.* Experimental Mechanics, 2013. **53**(9): p. 1735-1742.
19. Lim, T.-C., *Anisotropic and negative thermal expansion behavior in a cellular microstructure.* Journal of materials science, 2005. **40**(12): p. 3275-3277.
20. Palumbo, N., C. Smith, W. Miller, and K. Evans, *Near-zero thermal expansivity 2-d lattice structures: Performance in terms of mass and mechanical properties.* Acta Materialia, 2011. **59**(6): p. 2392-2403.
21. Vandeperre, L.J. and W.J. Clegg, *Tailoring strains through microstructural design.* MRS Online Proceedings Library, 2003. **785**: p. D11.4.1.
22. Ha, C.S., E. Hestekin, J. Li, M.E. Plesha, and R.S. Lakes, *Controllable thermal expansion of large magnitude in chiral negative poisson's ratio lattices.* physica status solidi (b), 2015. **252**(7): p. 1431 - 1434.
23. Grima, J.N., P.S. Farrugia, R. Gatt, and V. Zammit, *Connected triangles exhibiting negative poisson's ratios and negative thermal expansion.* Journal of the Physical Society of Japan, 2007. **76**(2): p. 025001.
24. Hirota, M. and Y. Kanno, *Optimal design of periodic frame structures with negative thermal expansion via mixed integer programming.* Optimization and Engineering, 2015. **16**(4): p. 1-43.
25. Lakes, R., *Cellular solids with tunable positive or negative thermal expansion of unbounded magnitude.* Applied Physics Letters, 2007. **90**(22): p. 221905.
26. Lehman, J. and R. Lakes, *Stiff, strong zero thermal expansion lattices via the poisson effect.* Journal of Materials Research, 2013. **28**(17): p. 2499-2508.
27. Lehman, J. and R.S. Lakes, *Stiff, strong, zero thermal expansion lattices via material hierarchy.* Composite Structures, 2014. **107**: p. 654-663.
28. Lim, T.-C., *Negative thermal expansion structures constructed from positive thermal expansion trusses.* Journal of Materials Science, 2012. **47**(1): p. 368-373.

29. Miller, W., D.S. Mackenzie, C.W. Smith, and K.E. Evans, *A generalised scale-independent mechanism for tailoring of thermal expansivity: Positive and negative.* Mechanics of Materials, 2008. **40**(4–5): p. 351-361.

30. Lim, T.-C., *Negative thermal expansion in transversely isotropic space frame trusses.* Physica Status Solidi (b), 2013. **250**(10): p. 2062-2069.

31. Aboudi, J. and R. Gilat, *Micromechanical analysis of lattice blocks.* International Journal of Solids and Structures, 2005. **42**(15): p. 4372-4392.

32. Spadaccini, C. and J. Hopkins, *Lattice-structures and constructs with designed thermal expansion coefficients*. 2013, Google Patents: US.

33. Palumbo, N.M.A., *Trusses with reduced thermal expansion: Their design, and mass and stiffness penalties*. 2013, University of Exeter: UK. p. 260.

34. Wei, K., H. Chen, Y. Pei, and D. Fang, *Planar lattices with tailorable coefficient of thermal expansion and high stiffness based on dual-material triangle unit.* Journal of the Mechanics and Physics of Solids, 2016. **86**: p. 173-191.

35. Steeves, C.A., C. Mercer, E. Antinucci, M.Y. He, and A.G. Evans, *Experimental investigation of the thermal properties of tailored expansion lattices.* International Journal of Mechanics and Materials in Design, 2009. **5**(2): p. 195-202.

36. Spadaccini, C. *Additive manufacturing and architected materials*. 2014 DOE NNSA SSGF Annual Program Review 2014; Available from: http://www.krellinst.org/ssgf/conf/2014/video/cspadaccini.

37. Dong, L., V. Deshpande, and H. Wadley, *Mechanical response of ti–6al–4v octet-truss lattice structures.* International Journal of Solids and Structures, 2015. **60**: p. 107-124.

38. Arabnejad, S. and D. Pasini, *Mechanical properties of lattice materials via asymptotic homogenization and comparison with alternative homogenization methods.* International Journal of Mechanical Sciences, 2013. **77**(0): p. 249-262.

39. Ashby, M.F., *Materials selection in mechanical design*. Third ed. 2005: Butterworth-Heinemann.

40. Ashby, M.F., *Materials selection in mechanical design*. Fourth ed. 2011, Oxford: Butterworth-Heinemann.

41. Correlated Solutions, Inc. (2009). Vic-Snap 8: A digital image collection program, Columbia, USA. URL http://www.correlatedsolutions.com/
42. Correlated Solutions, Inc. (2012). VIC-3D: A system for measuring and visualizing both strain and movement, Columbia, USA. URL http://www.correlatedsolutions.com/
43. ANSYS 14.5 (2012). ANSYS: a commercial finite element method software package, Pennsylvania, USA. URL http://www.ansys.com/

Chapter 5

Conclusions and future work

Chapter 5: Conclusions

5.1 Summary of the main results

The existing CTE tunable concepts of architected materials fail to simultaneously meet the following requirements imposed by a range of engineering applications: i) high structural efficiency and ii) wide, ideally unbound, obtainable CTE range covering large negative to positive, including zero, CTEs. The high structural efficiency, e.g. stiffness to mass ratio with small deformation when mechanically loaded, and ample freedom to tune the effective CTE, e.g. sufficient deformation can be obtained to adjust the thermal expansion of components leading to zero effective CTE, are two conflicting requirements, which current available concepts are unable to ideally reconcile. In this context, this thesis has provided the following insights on the CTE tunability of structurally efficient architected materials:

- In Chapter 2, stretch-dominated bi-material unit cells with low- and high-CTE have been proposed as diamond-shaped building blocks of hierarchical lattices with the goal of improving CTE tunability. The presented hierarchical bi-material lattices can be designed to attain a theoretically unbounded range of thermal expansion without (i) impact onto elastic moduli and (ii) severe penalty in specific stiffness. Through simulations, derived closed-form expressions and experiments on fabricated proof-of-concepts, this thesis has shown that hierarchical lattices (HL) including those made of self-repeating unit cells, i.e. fractal-like HL, can be tailored to concurrently provide high specific stiffness and theoretically unbounded CTE tunability with CTE values ranging from large positive, zero to large negative. Results show that the achievable range of CTE can be enlarged by 66% through the addition of one order of hierarchy alone, and that for a given CTE range the specific stiffness can be at least 1.4 times larger than that of existing stretch-dominated concepts.

- Dual-material concepts that expand or contract as desired upon changes in temperature exist but have their limitations. One upon which we have focused in Chapter 2 is the trade-off caused by the inherent thermo-elastic coupling that they feature, a condition that makes desired changes in thermal expansion penalize elastic stiffness, and vice versa. The introduced hybrid-type HLs can be exploited to decouple initially coupled thermo-elastic properties in different order of structural hierarchies so as to provide the individual property tailoring that current concepts have not been proven to attain yet. The hallmark of fractal-like and hybrid-type HL is that they can reduce the penalty that an increase in ΔCTE will generate on the elastic properties, so as to obtain the best compromise out of them.

- Thermal expansion can be problematic in manifold applications that require thermal stability, yet it can also be purposely exploited to meet specific directional requirements of thermal deformation. Opportunities to tailor thermal expansion in architected materials exist, but design options that are stiff and provide full directional authority on thermal expansion are currently limited by the structural characteristics of existing concepts. In Chapter 3, we have reported routes to systematically engineer thermally responsive lattice materials that are built from dual-material tetrahedral units that are stiff and strong. Drawing from concepts of vector analysis, crystallography, and tessellation, a scheme has been presented for three-dimensional lattices to program desired magnitude and spatial directionality, such as unidirectional, transverse isotropic, or isotropic, of thermal expansion. Demonstrations on thermal expansion and mechanical properties include theoretical, computational, and experimental studies of nine representative concepts, from tetrahedral building blocks to compound unit cells that can tessellate structurally efficient lattices with tunable magnitude and prescribed directionality of thermal expansion.

- In a solid, a change in temperature can cause the material to change in shape, length, area and volume. In Chapter 3 we have shown that via the application of the material length vector (ML) and thermal displacement vector (TD), it is possible to draw a simple analogy between the thermal deformation triggered in a solid material and that appearing in a bi-material building block. The ML and TD vectors can also express the CTE of an assembly of building blocks and even the CTE of tessellations of compound units. Concepts in both 2D and 3D have been given as examples to show the handiness of using vectors to visualize and analyze thermal expansion of a periodic truss built from single units, as well as a more complex assembly of compound units.

- In Chapter 3, we have also considered a tetrahedron building block made of six rods, each made of a material with either low or high CTE, but both positive. In total, there are eleven arrangements with all the possible material permutations that can appear by simply switching the position of high- and low-CTE rods. For two monomaterial tetrahedra, the thermal expansion is uniform; as there is no thermal mismatch, no opportunity exists to tailor the CTE. For the remaining nine tetrahedra, on the other hand, CTE tunability is possible as the effective CTE can be adjusted in one or more directions yielding effective CTEs that can be classified into three groups: 1) lower than, 2) between, and 3) higher than the CTEs of both the component materials. This chapter has thus also studied the relation that each of these tetrahedra has with the CTE along its principal axes and has provided a foundational basis to understand other, more complicated, truss-like materials.

- Chapter 4 has exemplified the design methodology presented in Chapter 3 through the application to a set of three-dimensional dual-material Octet-trusses, which are proven to not only be stiffer and stronger than any other existing concepts, but also offer a highly tunable CTE. Chapter 4 has presented, built, and thermally tested Octet lattice bi-materials that can be tuned to cover a substantial range of CTEs, which include zero, in given spatial directions without jeopardizing their structural efficiency. In contrast with Chapter 3, all metallic and plastic prototypes in Chapter 4, either laser cut or 3D printed, are built via snap-fit with pretension rigid joints, which are more practical than pin-jointed or ball-and-stick rigid-jointed models in Chapter 3. Prototypes have been built from either tetrahedra with stationary-nodes to provide CTE isotropy, or tetrahedra with stationary-lines to achieve CTE anisotropy. Several variables defining the unit cell geometry govern the macroscopic thermo-mechanical properties of the bi-material lattices here investigated. The focus of this chapter has been on a subset of parameters, i.e. skew angle and strut thickness controlling relative density, which were selected to play a crucial role in the CTE as well as specific stiffness and strength of the lattices. Results experimentally tested and validated via numeric simulations have shown that by introducing material architecture even common materials can render unprecedented combinations of thermomechanical properties.

In summary, we engineered several strategies for the development of architected materials that can simultaneously meet the two conflicting requirements in engineering applications, i.e. high structural efficiency and large CTE tunability. Firstly, structural hierarchy decouples thermos-elastic properties and allows stretch-dominated architected materials to exhibit unbounded CTE tunability. A scheme is then presented for architected materials to program desired magnitude and spatial directionality of thermal expansion, such as unidirectional, transverse isotropic, or isotropic CTE. As an exemplification of the scheme, we have elucidated how to resolve the trade-off between CTE tunability and structural efficiency, and presented Octet concepts that are not only stiffer and stronger than other 3D architected materials, but also offer a highly tunable CTE.

5.2 Original contribution

The following list summarizes the main findings achieved during the present study:

- Stretch-dominated architected materials, for the first time, have been tailored to provide theoretically unbounded CTE tunability via structural hierarchy. For a given concept, a large CTE tunability indicates ample freedom to tune the effective CTE of a unit cell, an asset that can also release the dependence on the CTE ratio of the constituents.

- Structural hierarchy has been applied to decouple physical properties of architected materials that are in conflict. Hierarchical architected materials can achieve both high CTE tunability and high structural efficiency. Hence, a better trade-off between thermal and mechanical performances can be provided.

- The material length vector and thermal displacement vector have been defined to assess thermal expansion of building blocks and their assembly, as well as the CTE of tessellations of compound units. Concepts in both 2D and 3D have been given as examples to show the handiness of using vectors to visualize and analyze the thermal expansion of a periodic truss.

- All the possible material permutations that can occur in the struts of a dual-material tetrahedron have been for the first time examined for linear thermal expansion control.

The relationship that each of these tetrahedra has with the CTE along its principal axes provides a foundational basis to understand other, more complicated, truss-like materials.

- Drawing from concepts of crystallography and tessellation, a scheme has been presented to understand the relationships between CTE tunability of tetrahedral building blocks, structural symmetry of unit cells, independent elements in the CTE tensor, and the effective thermoelastic properties of a periodic truss, which can be built from single units or a more complex assembly of compound units. The results establish underlying principles governing tailorable thermal expansion in dual-material lattice materials, where desired CTE magnitude and spatial CTE directionality can be programmed a priori to satisfy given CTE requirements, such as unidirectional, transverse isotropic, or isotropic.
- A set of three-dimensional dual-material Octet-trusses, with either anisotropic or isotropic CTE tunability, have been fabricated via pretension snap-fit technique. They are proven to not only be stiffer and stronger than any other existing concepts, but also offer a highly tunable CTE.

5.3 Future work

In this work, architected materials have been engineered to concurrently attain high structural efficiency and CTE tunability with desired magnitude and directionality. Hierarchical architectures have been applied to amplify the CTE tunability and decouple the conflicting physical properties. Several innovative fabrication methods, such as pretension snap-fit technique, have been developed to implement these microstructures and their associated mechanisms into engineering material. These contributions provide a platform to further explore CTE controllable architected materials, through combined experimental, analytical, and numerical studies. The following guidelines are therefore proposed as a continuation to this work:

- While the hierarchical architected materials here presented show promise for planar lattices, the strategy can also be applied to 3D hierarchical concepts. Nevertheless, their potential will always be confronted with the capabilities of current practices. For example, while the concepts are scale independent and material selection free, increasing the order of structural hierarchy has to account for the limits that a given manufacturing process poses. Furthermore, the fabrication of 3D hierarchical structures can be highly time consuming. However, given the fast development of multiple material additive manufacturing, we can infer that higher level of hierarchy in dual material lattices might be achieved in the near future.

- The hierarchical architectures have been applied to decouple the thermal expansion impact from elastic stiffness adjustments in Chapter 2. The strategy presented in this work can pave the way to the multifunctional design of bi-material hierarchical lattices with properties that can be independently tuned and exploited to the most of their potential. It can thus be extended to potentially address other conflicting properties to finally generate trade-off solutions for multifunctional applications, including thermal expansion control, MEMS, biomedical sensors and space optical systems.
- Though the scheme presented in Chapter 3 can engineer a class of architected materials with proposed magnitude and directionality of CTE, it can be extended to develop other, more complicated, truss-like materials providing unique CTE tunability. For example, extra building blocks, e.g. bi-material pyramids, can be considered to construct potential concepts with innovative thermal expansion performance (e.g. orthotropic CTE tunability) independently or jointly with tetrahedral building blocks.
- Despite considerable potential of large CTE tunability, all spatial specimens in Chapter 3 provide only small thermal deformation due to the restriction of the material and craftwork. Spatial bi-material lattices can be engineered to become thermally-responsive architected materials with given thermal expansion directionality upon prescribed changes of temperature. This task may require exploring 3D printable polymers with distinct CTEs as base components. The class of potential architected materials takes one step closer to meeting the demands of thermally functional materials that are stiff and strong and can be engineered to provide customized directions and levels of large deformation.

- In Chapter 4, a subset of geometric parameters that govern the macroscopic thermomechanical properties of the bi-material lattices have been investigated. This subset includes skew angle and strut thickness, which play a crucial role in the CTE as well as the specific stiffness and strength of the lattices. Other factors, such as the strut diameter ratio of the constituent materials and other topological variables, can be studied and used to achieve further CTE tuning. The additional conclusions drawn from the consideration of comprehensive parameters allow better understanding of thermal-mechanical performance of architected materials with CTE tunability.

5.4 Publications

5.4.1 Refereed journals

- Xu, H., Farag A., Pasini D., Routes to Program Thermal Expansion in Three-dimensional Lattice Metamaterials Built from Tetrahedral Building Blocks, Journal of the Mechanics and Physics of Solids, 2018. 117: p. 54-87.

- Xu, H., Farag A., Pasini D., Multilevel hierarchy in bi-material lattices with high specific stiffness and unbounded thermal expansion. Acta Materialia, 2017. 134: p. 155-166.

- Xu, H. and Pasini D., Structurally Efficient Three-dimensional Metamaterials with Controllable Thermal Expansion. Scientific Reports, 2016. 6: p. 34924.

- Wang Y, Xu H., Pasini D, Multiscale Isogeometric Topology Optimization for Lattice Materials, Computer Methods in Applied Mechanics and Engineering, 2017. 316: p. 568-585.

5.4.2 Conference abstracts

- Xu, H. and Pasini D., Bi-material Lattice with High Stiffness and Strength for Low Thermal Expansion, in ICCS 18th. 2015: Lisbon.

- Xu, H. and Pasini D., A Class of Low CTE 3D Lattices That are Stiff and Strong, in MRS 2015 Fall. 2015: Boston.

- Xu, H., Liu L., and Pasini D., Multifunctional Lattices with Low Thermal Expansion and Low Thermal Conductivity, in APS 2016. 2016: Baltimore.

- Xu, H. and Pasini D., Stiff and Strong Octet Lattice with Tunable Coefficient of Thermal Expansion, in ICTAM 2016. 2016: Montreal.

5.4.3 Poster presentations:

- Xu, H. and Pasini D., A Class of Low CTE Lattices Materials That are Stiff and Strong, in 12th CREPC Symposium. 2017: McGill University.

- Xu, H. and Pasini D., Bi-material Lattice with High Stiffness and Strength for Low Thermal Expansion, in MIAE. 2015: McGill University.

- Xu, H. and Pasini D., A Class of Low CTE Lattices Materials That are Stiff and Strong, in MERS. 2015: McGill University.